

**ELECTRON THERMAL TRANSPORT IN THE MADISON SYMMETRIC TORUS**

by

**THEODORE MATHIAS BIEWER**

A dissertation submitted in partial fulfillment of  
the requirements for the degree of

**DOCTOR OF PHILOSOPHY**

**(PHYSICS)**

at the

**UNIVERSITY OF WISCONSIN-MADISON**

2002

# Electron Thermal Transport in the Madison Symmetric Torus

Theodore M. Biewer

Under the supervision of Assistant Professor Cary B. Forest

At the University of Wisconsin-Madison

## **Abstract**

Due to diagnostic improvements and the development of the MSTFit equilibrium reconstruction code, it has become possible for the first time to accurately characterize the transport behavior of MST plasmas over the sawtooth cycle. Magnetic fluctuations in the MST reversed-field pinch, which rise sharply at the crash, play a significant role in the transport of heat and particles. The RFP configuration is a good test bed for studying magnetic fluctuation induced transport since the overlapping magnetic tearing mode islands create a large radial region in which the magnetic flux surfaces are destroyed and field lines wander stochastically. The measured electron thermal conductivity in this stochastic region agrees with Rechester-Rosenbluth like predictions from a fluctuating magnetic field.

Time evolving profiles are measured to understand electron heat and particle transport in the MST. In particular, electron temperature, electron density, and current density profiles have been measured during a “Standard” plasma sawtooth cycle. The MHD activity during the sawtooth cycle is examined as an *a priori*, time-evolving condition that is affecting the plasma equilibrium and consequently the transport of heat and particles. The cause of the MHD behavior is not central to this thesis. Rather, the effects of the fluctuations on transport are considered. The current density peaks up as the sawtooth crash is approached. This current peaking pushes the plasma farther away from the Taylor minimum-

energy state and causes (possibly dynamo driven) tearing instabilities to grow. At the crash the current density profile broadens, resulting in a flatter  $\beta$ -profile, and a plasma that is closer to a Taylor minimum-energy state. Another effect of the peaking current density is to broaden the q-profile. Lower q-shear results in a more stochastic magnetic field in the region where tearing mode islands overlap. Greater field stochasticity leads to enhanced transport of heat and particles by the electrons, and the electron temperature is observed to drop. After the sawtooth crash, the current density broadens, the q-profile peaks, the q-shear is increased in the region of overlapping islands, the field stochasticity is reduced, and the electron heat transport falls.

Experiments are also carried out in a number of different discharge conditions, and the results from these experiments are compared to the Standard plasma results. Time evolved measurements of thermodynamic profiles have been obtained in a variety of MST discharges (PPCD,  $F=-0.22$ ,  $F=0$ ,  $F=+0.02$ ,  $F=+0.03$ ), leading to the first measurement of radially resolved, time evolving heat transport in the MST.  $m=0$  modes are reduced in  $F=0$  plasmas, and confinement is observed to improve, but degrades rapidly as  $F$  is raised above zero.

## Acknowledgments

Sometimes the road was only a lane . . . And as you rode along in the warm, keen air you had a sensation that the world was standing still and life would last forever. Although you were pedaling with such energy, you had a delicious feeling of laziness.

--W. Somerset Maugham, *Cakes and Ale*

There is no way to properly estimate the appreciation I owe to those who shaped and supported my life over the past eight years as I endeavored to produce this piece of work and to graduate from the University of Wisconsin with a Ph.D. Foremost in my mind are friends and family, without whom life would be a dreary process indeed. My parents always offered kind words and a solid home to escape the worst of the Wisconsin winters to. My brothers Ben, Matt, and John, though far afield, prompted the occasional inquiry that expanded my own insight. My sister Jan kept me firmly grounded in the intricacies of life as they unfold in another, and provided a steady source of admiration that at times seemed my sole reassurance.

Riding my bike across the hills and prairies of Wisconsin has been a true pleasure and has helped me to rekindle my love of the sport. To that end I owe Marty Broeske a big, blonde “thank you very much” for all the hand-me-down gear I wouldn't have been able to afford as a lowly graduate student. The early morning Odd Ones made every ride (even the suicidal) enjoyable. I owe John Wright, though he was always late, a special debt for teaching me how to swim (properly) and spin. And I'd be remiss if I didn't thank my “biking mom,” Jackie Pinkowski for all the good grub and hospitality. Truly, age is a state of mind, and I hope to stay as active and generous as she has been.

To Jay K. Anderson, one of the true greats in the sport of life, I can only offer humble gratitude and whatever refreshing beverages lie within my power to procure. Without his tireless efforts to keep our advisor preoccupied, I would not have been able to get any work (or at least serious goofing off) done. Besides MSTFit, I have profited greatly from countless hours of advice on physics and equally many hours of enjoyment of that magical beverage, beer. As the road unwinds and I find myself parked on many a distant barstool, I'm sure that more than once I'll tip a glass in his honor. Cheers.

A considerable number have been tippled already in my years as a student, both with Jay and in the presence of many mentioned here. To protect the innocent, I won't name all names, but the guilty must be brought to trial: Anyone who's heard the demo tape for "The Drunkards'" is immediately culpable, let alone my fellow band members, David Isaac and Nathan Miczo. Though not a drop of Orange Duck Beer has yet been brewed, the future follows a long and uncertain path. I can't begin to count all the money I've lost along the way playing poker, though I'm sure a good share of it has found its way into the pockets of Jay Anderson, Diane Demers, Alex Hansen, Nick Lanier, Larry Smith, and David Beaudry. Many a Thursday night I've lost more than a dollar to Bruce Broker over a Sheephead game.

But you know what they say about cards, luck, and love. It was shortly after meeting Christine Rehder that I watched my luck at cards slip away, leaving me with a happy portent for the future. Though I can't remember the vintage of wine we shared on a cloudless night above an empty vineyard, I do still treasure the cork as manifest of all the calm, quiet, laughing moments.

Of course, there are so many other people that must be given their due, fellow graduate students, postdocs, and scientists, without whom I'd still be wandering the halls of MST-land: my officemates (past and present) Jay, Eduardo Fernandez, Paul Fontana, Susana Castillo, Darren Craig, Derek Baver, Karsten McCollam, Art Blair, Uday Shah, and Jianxin

Lei. I also thank Jim Chapman and Brett Chapman for the experience I gained as part of their extended run campaigns, and for their tutelage on plasma physics. Those campaigns would not have been as useful without the efforts of Nick Lanier, Steve Terry and Jim Reardon, or as fun without the friendly ear of Diane Demers. Grateful appreciation is paid to Gennady Fiksel, John Sarff, and Weixing Ding, scientists who contributed directly and indirectly to my exploration of the physics of the MST. Extra special thanks goes to the computer hackers, Larry Smith and Paul Wilhite, for not erasing all my data.

I must draw attention to Daniel Den Hartog for his advice in tackling the problems of the ruby laser Thomson scattering system, which he originally designed and built. In that vein, I offer thanks to Matt Stoneking and Don Holly for their help in keeping the system working. And of course, without the cheerful guidance of the Great John Laufenberg, I am certain the MST device itself would have ended as a smoldering heap long ago.

Finally, I show my appreciation to the members of my dissertation committee, Dave Anderson, Paul Terry, and Clint Sprott; and to my advisors (at one time or another), Stewart Prager and Cary Forest. Besides being a great teacher, the advice I've received from Dr. Prager has always proved beneficial. His efforts to promote the MST community have been tireless, doubtless accounting for the success of the program. I am happy to say that I was part of the MST plasma physics group during these past years. The vigilance of Dr. Forest has approached legendary status in the few short years that he has been a professor at the UW. His enthusiasm for experimental physics and learning is contagious, and I would not have finished my degree without its influence.

This work was appreciatively funded by the United States Department of Energy,  
particularly the Magnetic Fusion Science fellowship program,  
and ultimately the U.S. taxpayer.

“So long, and thanks for all the fish!” --Douglas Adams

## Contents

<b>Abstract</b> .....	i
<b>Acknowledgments</b> .....	iii
<b>Contents</b> .....	vi
<b>List of Tables</b> .....	xi
<b>List of Figures</b> .....	xii
<b>Chapter 1: Introduction</b> .....	1
<b>1.1 Overview of the Madison Symmetric Torus</b> .....	3
<b>1.2 Overview of this Thesis</b> .....	8
<b>References</b> .....	10
<b>Chapter 2: The MST Thomson Scattering Ruby Laser System</b> .....	11
<b>2.1 Thomson Scattering as a High Temperature Plasma Diagnostic</b> .....	11
<b>2.2 Overview of the MST Ruby Laser TS System</b> .....	14
2.2.1 The JK-Lasers Ruby Laser Head.....	16
2.2.2 The Support Structure and Optics .....	19
2.2.3 The Light Detection System.....	23
2.2.4 Electronics and Digitization Systems.....	26
<b>2.3 Alignment</b> .....	29
2.3.1 Central Laser Chord Alignment .....	30
2.3.2 Alignment of the Fiberoptic Collecting Bundle.....	31
2.3.3 Edge Laser Chord Alignment.....	33
<b>2.4 Calibration</b> .....	35

2.4.1 Instrument Transfer Function Measurement.....	35
2.4.2 Wavelength Channel Relative Sensitivity Calibration.....	37
2.4.3 Raman Scattering Absolute Density Calibration.....	38
2.4.4 Timing Sequence Check.....	39
<b>2.5 Thomson Scattering Data Analysis.....</b>	<b>41</b>
2.5.1 Error Bars .....	43
<b>2.6 Summary .....</b>	<b>45</b>
<b>References.....</b>	<b>46</b>
<b>Chapter 3: Measurements through the Sawtooth Cycle in Standard Plasmas.....</b>	<b>49</b>
<b>3.1 Sawteeth in MST Standard Discharges.....</b>	<b>49</b>
<b>3.2 The MSTFit Equilibrium Reconstruction Code.....</b>	<b>55</b>
<b>3.3 Temperature Profile Evolution .....</b>	<b>56</b>
3.3.1 Electron Temperature.....	56
3.3.2 Ion Temperature .....	61
<b>3.4 Density Profile Evolution.....</b>	<b>66</b>
3.4.1 Electron Density .....	66
3.4.2 Comments about $Z_{\text{eff}}$ and Ion Density .....	70
3.4.3 Neutral Density.....	71
<b>3.5 Current Profile Evolution.....</b>	<b>73</b>
3.5.1 Flux Loop Constraints.....	74
3.5.2 MSE Diagnostic Constraints .....	76
3.5.3 FIR Polarimeter Constraints.....	79
3.5.4 HIBP Diagnostic Constraints .....	80
3.5.5 Mirnov Coil-set Constraints .....	82
3.5.6 MSTFit Reconstructed Current Density.....	85

<b>3.6 Magnetic Modes and Mode Rotation</b> .....	87
3.6.1 Mode Fluctuation Amplitudes.....	88
3.6.2 Mode Velocities .....	94
<b>3.7 The Radial Electric Field</b> .....	95
<b>3.8 Summary</b> .....	100
<b>References</b> .....	101
<b>Chapter 4: Transport through the Sawtooth Cycle</b> .....	105
<b>4.1 Energy Confinement Time</b> .....	105
4.1.1 Total Energy Confinement Time.....	105
4.1.2 Electron Energy Confinement Time.....	111
<b>4.2 Particle Confinement Time</b> .....	112
<b>4.3 Electron Heat and Particle Fluxes</b> .....	115
4.3.1 Particle Flux .....	115
4.3.2 Power Deposition Profiles.....	116
4.3.3 Heat Flux .....	119
<b>4.4 Thermal Conductivity Coefficients</b> .....	123
4.4.1 Measured Electron Conductivity Profiles .....	123
4.4.2 Electron Conductivity through the Sawtooth Cycle.....	124
<b>4.5 Particle Diffusion Coefficients</b> .....	128
4.5.1 Measured Electron Diffusivity Profiles.....	128
4.5.2 Electron Diffusivity through the Sawtooth Cycle.....	131
<b>4.6 Summary</b> .....	134
<b>References</b> .....	135
<b>Chapter 5: Comparisons to Rechester-Rosenbluth Theory</b> .....	137

<b>5.1 Rechester-Rosenbluth Model for Thermal Transport in a Stochastic Field</b>	137
<b>5.2 DEBS Simulations of Standard Plasmas</b>	140
<b>5.3 Comparing Measured <math>\tau_e</math> to <math>\tau_{RR}</math> in Standard Plasmas</b>	149
<b>5.4 Implication for Ion Heating</b>	156
5.4.1 Ion Energy Confinement Time	156
5.4.2 Comments on Ion Thermal Conductivity Profiles	157
<b>5.5 Summary</b>	161
<b>References</b>	163
<b>Chapter 6: Comparisons to Other MST Plasmas</b>	165
<b>6.1 Introduction to the Experiments</b>	165
6.1.1 Overview	165
6.1.2 Experiment Sample Shots	168
<b>6.2 Stability of the Pressure Profile</b>	172
6.2.1 The Suydam Criterion	172
6.2.2 Measured Pressure Profiles	173
6.2.3 Current Density and q-Profiles	175
6.2.4 Discussion	179
<b>6.3 Anomalous Ion Heating</b>	182
6.3.1 Standard v. Non-Reversed Plasmas	182
6.3.2 Standard v. PPCD Plasmas	185
<b>6.4 Transport</b>	187
6.4.1 Zero-D: $\tau_e$ and Plasma $\tau$	187
6.4.2 One-D: $\tau_e$ through the Discharge	192
<b>6.5 Summary</b>	197
<b>References</b>	200

<b>Chapter 7: Conclusions</b> .....	203
<b>7.1 Summary and Conclusions</b> .....	203
<b>7.2 Future Work</b> .....	209
<b>Appendix A: Magnetic Mode Amplitudes and Velocities</b> .....	215
<b>A.1 Standard Plasmas</b> .....	216
<b>A.2 Non-Reversed Plasmas</b> .....	222
<b>A.3 <math>F=+0.02</math> Plasmas</b> .....	228
<b>A.4 <math>F=+0.03</math> Plasmas</b> .....	234
<b>A.5 PPCD Plasmas</b> .....	240

## List of Tables

<b>Table</b>	<b>page</b>
Table 2.1 Radial and poloidal locations of ruby laser Thomson scattering system views, including % sensitivity to perp. and parallel electron distribution functions. ....	22
Table 2.2 Spectrometer gratings and expected ranges of sensitivity. ....	23
Table 3.1 Comparison of different operating modes of the MST. ....	51
Table 5.1 Comparison of toroidally and poloidally calculated scaling factors from DEBS simulation to experiment. The radial scaling factors are the average of the toroidal and poloidal factors. ....	148
Table 5.2 The calculated stochasticity parameters for magnetic islands in Standard MST plasmas at $-1.75$ ms in the sawtooth cycle. ....	151
Table 6.1 Overview of the experimental conditions. Deuterium was the working gas in all experiments. ....	172
Table 6.2 Summary table of 0-D transport quantities. ....	197
Table 7.1 Summary table of 0-D transport quantities. ....	207

## List of Figures

<b>Figure</b>	<b>page</b>
Figure 1.1 Photograph of the MST from the South. ....	4
Figure 1.2 South View of the MST.....	5
Figure 1.3 MST Toroidal Magnetic Field System. ....	5
Figure 1.4 Poloidal projection of MST diagnostic sampling locations.....	6
Figure 2.1 Thomson scattering of light from a moving electron. ....	12
Figure 2.2 Wave vector diagram for Thomson scattering in the ruby laser system. ....	12
Figure 2.3 Ruby laser-head layout. ....	17
Figure 2.4 Side view of the ruby laser Thomson scattering system at 90 degrees toroidal of the Madison Symmetric Torus. To operate in “central” laser path mode, the lower steering mirror is removed along with the movable correction lenses. ....	20
Figure 2.5 Geometrical location of Thomson scattering viewing centers for both the edge and central laser paths.....	20
Figure 2.6 Top view of the ruby laser Thomson scattering system, showing a segment of the MST vacuum vessel. The spectrometer is shown in overlay at its two locations. The spectrometer is movable in order to reach the furthest inboard viewing locations with the fiber bundle. Only the top row of LA-APD modules is shown, in addition to the former location of the MCP detector.....	21
Figure 2.7 Geometrical coverage of ruby laser Thomson scattering views. Error bars indicate radial range (in $r/a$ space) of scattering volume on each view.....	22
Figure 2.8 Schematic of the TS spectrometer exit-plane arrangement of fiber optics. Vertical groupings correspond to separate LA-APD modules.....	24
Figure 2.9 Schematic setup of the TS spectrometer, showing the 2-tier layout of the LA- APD modules.....	25

Figure 2.10 Photograph of the TS spectrometer. The 2-tier, stadium style layout of the LA-APD modules, the exit-plane fixture, the larger area mirror, the spectrometer shutter, and the APD power distribution box are visible. ....	26
Figure 2.11 Schematic overview of the ruby laser TS system.....	27
Figure 2.12 Circuit schematic of the LA-APD module system. Eleven modules are connected in parallel in this fashion, though only one is shown. ....	28
Figure 2.13 Bench measured instrument transfer function for the TS spectrometer with APD modules for both the 1200 g/mm and 1800 g/mm gratings. Also shown is the extent of the region previously covered by the MCP in the 1200 g/mm configuration, as well as the location of the $H_{\beta}$ Balmer line. ....	37
Figure 2.14 Timing diagram of the ruby laser TS system. ....	40
Figure 3.1 Shot 69 from November 13 <sup>th</sup> , 2000 showing the presence of sawteeth in a Standard MST plasma.....	52
Figure 3.2 400 shot ensemble with respect to sawtooth crashes in “Standard” MST plasmas. The scale at the bottom shows the center locations of 0.5 ms time bins that are used in the following analysis.....	54
Figure 3.3 Comparison of splines to the Thomson scattering measured electron temperature profile at three time slices.....	57
Figure 3.4 The ratio of two thin-filter (Beryllium) soft x-ray signals gives an indicaton of the level of temperataure fluctuations in a Standard shot (Shot 17, 30-Mar-2001). ....	58
Figure 3.5 Surface and contour plots of the evolution of the electron temperature profile over a sawtooth cycle in Standard MST discharges. The 12 time slices can be seen, and the diagonal bar indicates the position of the sawtooth crash ( $t = 0$ ). ....	59
Figure 3.6 These three time slices represent the profiles away (-1.75 ms) from the sawtooth crash, just before the crash (-0.25 ms), and shortly after the crash (+0.75 ms). All three	

profiles shown are cubic splines, which are fit using MSTFit to the Thomson scattering $T_e(r)$ data points.....	60
Figure 3.7 The evolution of $T_e(0)$ (*) from Thomson scattering and $T_i(r/a \sim 0.3)$ (solid line) from Rutherford scattering over the sawtooth cycle in Standard MST discharges. The solid line is the ensemble average over $\sim 350$ plasma discharges.....	62
Figure 3.8 The MST Rutherford scattering diagnostic setup. Figure courtesy of Jim Reardon.....	63
Figure 3.9 Rutherford scattering measured ion temperature profiles for Standard plasmas - 1.75 ms (solid) before the sawtooth crash and 0.75 ms (dotted) after the crash. ....	64
Figure 3.10 Surface and contour plots of the RS measured ion temperature profile evolution over the sawtooth cycle in Standard plasmas.....	65
Figure 3.11 Comparison of the raw (line-integrated) data with the Abel-inverted MSTFit fit at $-1.75$ ms (solid) and $+0.75$ ms (dotted) during the sawtooth cycle of Standard plasmas. ....	67
Figure 3.12 Select profiles of electron density during Standard plasma discharges.....	67
Figure 3.13 Surface and contour plots of the electron density profile evolution over the sawtooth cycle for Standard plasmas.....	68
Figure 3.14 The FIR Interferometer/Polarimeter diagnostic on the MST, courtesy of Steve Terry and Nick Lanier. ....	69
Figure 3.15 The neutral particle density at $-1.75$ ms during Standard MST plasmas. Note that the neutral particle density is 3 orders of magnitude lower than the electron density in the core, but roughly equal in the extreme edge of the plasma. ....	73
Figure 3.16 Comparison of $F$ , $\square$ , and $I_p$ from measurements with MSTFit reconstructed values over the sawtooth cycle for Standard plasmas. ....	75
Figure 3.17 The MST motional Stark Effect diagnostic setup, courtesy of Jay Anderson. A diagnostic neutral beam, fired radially into the plasma experiences a changing magnetic	

field, because the equilibrium toroidal field peaks on-axis. The changing magnetic field appears to the neutral atoms as an electric field, which Stark-splits the lines of the neutral emission spectra. Measuring the spectral width of the Stark manifold then yields the magnetic field. ....77

Figure 3.18 The evolution of on-axis magnetic field over the sawtooth cycle in Standard plasmas. Since the original experiment the MSE spectrometer has been upgraded, and a high-time-resolution (100  $\mu$ s) MSE measurement of the on-axis field has become possible. ....78

Figure 3.19 5-chord Faraday rotation measurements at  $-1.75$  ms (solid) and  $+0.75$  ms (dashed) in Standard plasmas used to constrain the current density profile. ....79

Figure 3.20 The MST HIBP diagnostic setup including a poloidal cross-section of the MST, courtesy of Diane Demers. ....81

Figure 3.21 Trajectories of primary and secondary beam ions shown from a) a poloidal cross-section, and b) above, some of which c) intersect the energy analyzer entrance. Figure courtesy of Jay Anderson. ....82

Figure 3.22 Time evolution of the  $n=5$  and  $n=6$  toroidal mode fluctuation amplitudes for a Standard plasma. ....83

Figure 3.23 The on-axis value of  $q$  calculated from MSTFit should be high enough that the resonant surface of the observed, dominant magnetic mode is in the plasma. ....84

Figure 3.24 The MSTFit fit to the poloidal asymmetry factor at  $-1.75$  ms (solid) and  $+0.75$  ms (dotted), relative to the sawtooth crash. ....85

Figure 3.25 Current profile change in Standard plasmas from  $-1.75$  ms (solid) before the crash to  $+0.75$  ms (dotted) after the crash. ....86

Figure 3.26 On-axis current density evolution as measured by MSTFit equilibrium reconstruction of Standard plasmas. ....87

Figure 3.27 Sample n-spectra of the toroidal fluctuation amplitude at -1.75 ms and +0.25 ms. The dramatic increase of low-n fluctuations at the sawtooth is associated with m=0 activity. ....	89
Figure 3.28 Sample n-spectra of the poloidal fluctuation amplitude at -1.75 ms and +0.25 ms. Low n-modes remain small at the sawtooth since the poloidal coilset can't distinguish m=0 modes from equilibrium shifts. ....	89
Figure 3.29 n-spectra of m=0 (+ symbol), and m=1 (* symbol) mode fluctuation amplitudes at the wall of MST, measured at -1.75 ms in Standard plasmas. ....	93
Figure 3.30 Total magnetic fluctuation amplitude (summed over n) through the sawtooth cycle in Standard plasmas. ....	93
Figure 3.31 n=6 mode rotation velocity over the sawtooth crash during Standard plasmas. The y-axis is in km/s. ....	94
Figure 3.32 Radial electric field profile and the terms used in its calculation for a Standard plasma, -1.75 ms away from the sawtooth crash. ....	96
Figure 3.33 Comparison of HIBP measured radial electric field profile to that calculated from the ion momentum balance equation. ....	99
Figure 3.34 The mid-radius (~peak value) of the radial electric field as it evolves over the sawtooth cycle in Standard plasmas. ....	99
Figure 4.1 Comparison of the calculated Ohmic input power at the edge from the $\square$ -model (*) and from finite time-slice MSTFit (solid line). For comparison, the value of $\square^2$ from MSTFit integrated over the volume is also shown (+) with flat $Z_{\text{eff}}(r)=2$ . ....	108
Figure 4.2 The total energy confinement time over a sawtooth cycle. ....	110
Figure 4.3 The electron energy confinement time over the sawtooth cycle in Standard plasmas. ....	112
Figure 4.4 Particle confinement time through the sawtooth cycle. ....	114

Figure 4.5 Measured electron flux profile at -1.75 ms and +0.75 ms relative to the sawtooth crash in Standard discharges.....	116
Figure 4.6 The parameterized profile of effective $Z_{\text{eff}}$ in Standard plasmas away from the sawtooth crash. ....	118
Figure 4.7 The electron energy budget at -1.75 ms in the sawtooth cycle of Standard plasmas on linear and logarithmic scales (to show detail). ....	121
Figure 4.8 Electron heat flux (total: conductive and convective) -1.75 ms away and +0.75 ms after the sawtooth crash in Standard plasmas. ....	122
Figure 4.9 Measured electron thermal conductivity profiles at -1.25 ms (solid) and +0.75 ms (dashed) in Standard plasmas. ....	124
Figure 4.10 The q-profile at -1.75 ms in Standard plasmas, including island widths, which are derived from modeling in Chapter 5.....	125
Figure 4.11 Behavior of thermal conductivity over the sawtooth crash in Standard plasmas. ....	127
Figure 4.12 Total magnetic fluctuation amplitude as measured at the wall (summed over n) through the sawtooth cycle in Standard plasmas.....	127
Figure 4.13 A trajectory of the measured thermal conductivity over the sawtooth cycle shows that total magnetic fluctuation level is not sufficient by itself to explain the transport of heat in Standard plasmas.....	128
Figure 4.14 The electron diffusion coefficient derived from Fick's Law at -1.75 ms in Standard discharges. ....	130
Figure 4.15 The electron diffusion coefficient including temperature gradient effects in Standard discharges at -1.75 ms.....	131
Figure 4.16 Core-averaged values of the electron diffusivity for Standard plasmas.....	132
Figure 4.17 Edge-averaged values of the electron diffusivity for Standard plasmas. ....	133

Figure 4.18 Trajectory of edge-averaged electron diffusion coefficients over the sawtooth cycle in Standard plasmas.....	133
Figure 5.1 The experimental Lundquist number profile for Standard MST plasmas compared to the Lundquist number profile of the DEBS simulation.....	142
Figure 5.2 Comparison of the q-profiles from experiment (-1.75 ms before sawtooth crash) and from DEBS simulation at $S \sim 10^6$ .....	143
Figure 5.3 The behavior of the magnetic modes, as “measured” in the edge of the DEBS simulation, is qualitatively similar to the behavior observed in Standard MST plasmas (Figure 4.12). A full sawtooth cycle is shown. Since $\tau_{es}$ is between 1.0-0.5 s, the sawtooth period is between 3-6 ms, which is in approximate agreement with the MST period of 6 ms.....	144
Figure 5.4 The n-spectra of m=0 and m=1 modes in the edge of the DEBS simulation is qualitatively similar to the spectra of Standard MST plasmas (Figure 3.29).....	145
Figure 5.5 Radial fluctuation eigenfunctions as calculated by DEBS, scaled by the measured fluctuation amplitudes at the wall.....	146
Figure 5.6 Calculated scaling functions for m=1, n=6-11 radial eignemodes.....	149
Figure 5.7 Puncture plot of magnetic field lines in Standard plasmas between sawteeth from DEBS/MAL simulation. Figure courtesy of Ben Hudson.....	150
Figure 5.8 Profile of measured $\chi_e$ -1.25 ms away from the sawtooth crash in Standard plasmas, compared to the calculated Rechester-Rosenbluth expected conductivity from the measured fluctuation level.....	152
Figure 5.9 Linear scaling of core-averaged, measured thermal conductivity versus Rechester-Rosenbluth like thermal conductivity shows good agreement.....	154
Figure 5.10 Measured, core-averaged conductivity increases with stochasticity across various plasmas discharge types.....	155

Figure 5.11 Anomalous power required if the ions have a 10 ms energy confinement time. .....	157
Figure 5.12 Ion energy budget at -1.75 ms in Standard plasmas.....	159
Figure 5.13 Comparison between core&mid-radius and whole plasma of the amount of expected anomalous ion heating.....	160
Figure 6.1 Shot 69 from November 13 <sup>th</sup> , 2000 showing a typical “Standard” MST plasma. .....	169
Figure 6.2 Shot 80 from March 30 <sup>th</sup> , 2001 showing a typical “Non-Reversed” MST plasma. .....	169
Figure 6.3 Shot 51 from April 3 <sup>rd</sup> , 2001 showing a typical “F= +0.02” MST plasma....	170
Figure 6.4 Shot 69 from April 2 <sup>nd</sup> , 2001 showing a typical “F= +0.03” MST plasma: a small increase in F leads to a rapid degradation of the plasma. ....	170
Figure 6.5 Shot 50 from March 24 <sup>th</sup> , 2001 showing a typical “PPCD” MST plasma and the consequent reduction in magnetic fluctuations. Note that discharges were selected such that the last MHD burst occurs near ~15 ms. ....	171
Figure 6.6 The electron temperature profile away from the nearest sawtooth crash.....	174
Figure 6.7 The electron density profile away from the nearest sawtooth crash.....	174
Figure 6.8 The pressure profile away from the nearest sawtooth crash.....	175
Figure 6.9 The current profile away from the sawtooth crash.....	176
Figure 6.10 The safety factor profile away from the nearest sawtooth crash for all 5 plasma discharge types.....	177
Figure 6.11 Comparison of the measured pressure gradient (solid line) with the calculated Suydam pressure gradient limit (dashed line) to ideal interchange modes: a) Standard (F=-0.22) plasma (-1.75 ms), b) Non-Reversed (F=0) plasma (-1.75 ms), c) PPCD plasma (18 ms).....	179

Figure 6.12 Anomalous ion heating at the sawtooth crash in Standard plasma, as measured by Rutherford scattering (solid), compared to the Thomson scattering measured electron temperature (stars.) .....	183
Figure 6.13 The RS measured ion temperature (solid) remains flat throughout the sawtooth cycle, i.e. a lack of anomalous ion heating. The peak electron temperature (stars) is also shown.....	184
Figure 6.14 Comparison of equilibrium reconstructed profiles between Standard (solid) and Non-Reversed plasmas (dotted) shows a much flatter $\beta$ -profile.....	185
Figure 6.15 Electron and ion temperature profiles at 18 ms, during PPCD plasma discharges. ....	186
Figure 6.16 Electron and ion temperature evolution during PPCD discharges. ....	187
Figure 6.17 Total $\beta$ over the sawtooth cycle for Standard plasmas.....	188
Figure 6.18 Energy confinement time over a sawtooth cycle for $-0.22 < F < +0.03$ and during PPCD. Confinement improves at $F=0$ , but degrades rapidly for $F>0$ . The total energy confinement during PPCD is about a factor of 3 higher.....	189
Figure 6.19 Total $\beta$ over a sawtooth cycle for $-0.22 < F < +0.03$ plasmas, and during PPCD. ....	190
Figure 6.20 Magnetic fluctuation levels normalized to the equilibrium magnetic field for different discharge conditions.....	192
Figure 6.21 Profiles of electron thermal conductivity for different MST discharge types away from the sawtooth crash (where applicable). PPCD discharge is shown at 18 ms. ....	193
Figure 6.22 Electron thermal conductivity variation over the sawtooth cycle for $-0.22 < F < +0.02$ plasmas, and during PPCD plasmas.....	195
Figure 6.23 Measured, core-averaged conductivity increases with stochasticity across various plasmas discharge types.....	196

Figure A.1 Poloidal fluctuation amplitude spectrum for Standard plasmas. ....	216
Figure A.2 Toroidal fluctuation amplitude spectrum for Standard plasmas.....	217
Figure A.3 Poloidal fluctuation amplitudes at select times during F=-0.22 plasmas. ....	218
Figure A.4 Toroidal fluctuation amplitude at select times during F=-0.22 plasmas. ....	219
Figure A.5 Poloidally derived mode velocity spectrum (km/s) for Standard plasmas. ...	220
Figure A.6 Toroidally derived mode velocity spectrum (km/s) for Standard plasmas...	221
Figure A.7 Poloidal mode amplitude spectrum for Non-Reversed plasmas.....	222
Figure A.8 Toroidally derived mode amplitude spectrum for Non-Reversed plasmas. .	223
Figure A.9 Poloidal mode amplitudes for select times during F=0 plasmas. ....	224
Figure A.10 Toroidal mode amplitude at select times during F=0 plasmas. ....	225
Figure A.11 Poloidally derived mode velocity spectrum (km/s) for Non-Reversed plasmas. .....	226
Figure A.12 Toroidally derived mode velocity spectrum (km/s) for Non-Reversed plasmas. .....	227
Figure A.13 Poloidally derived mode amplitude spectrum for F=+0.02 plasmas. ....	228
Figure A.14 Toroidally derived mode amplitude spectrum for F=+0.02 plasmas.....	229
Figure A.15 Poloidal mode amplitude for select times during F=+0.02 plasmas.....	230
Figure A.16 Toroidal mode amplitude for select times during F=+0.02 plasmas. ....	231
Figure A.17 Poloidally derived mode velocity spectrum (km/s) for F=+0.02 plasmas..	232
Figure A.18 Toroidally derived mode velocity (km/s) for F=+-0.02 plasmas.....	233
Figure A.19 Poloidally derived mode amplitude spectrum for F=+0.03 plasmas. ....	234
Figure A.20 Toroidally derived mode amplitude for F=+0.03 plasmas. ....	235
Figure A.21 Poloidal mode amplitudes at select times for F=+0.03 plasmas.....	236
Figure A.22 Toroidal mode amplitudes at select times for F=+0.03 plasmas. ....	237
Figure A.23 Poloidally derived mode velocity spectrum (km/s) for F=+0.03 plasmas..	238
Figure A.24 Toroidally derived mode velocity spectrum (km/s) for F=+0.03 plasmas.	239

Figure A.25 Poloidally derived mode amplitude spectrum for PPCD plasmas.....	240
Figure A.26 Toroidally derived mode amplitude spectrum for PPCD plasmas. ....	241
Figure A.27 Poloidal mode spectrum at select times for PPCD plasmas. ....	242
Figure A.28 Toroidal mode spectrum at select times for PPCD plasmas.....	243
Figure A.29 Poloidally derived mode velocity spectrum (km/s) for PPCD plasmas. ....	244
Figure A.30 Toroidally derived mode velocity spectrum (km/s) for PPCD plasmas.....	245

**Ode on a Grecian Torus**

*Enormous donut, MST,  
you throw me into ecstasy,  
steely vacuum manifold,  
plasma in magnetic hold-  
reveal to me your MHD!*

--C. M. Farmer

I had been familiar with that street for years, and had supposed it was dead level: But it was not, as the bicycle now informed me to my surprise.

--Mark Twain, "Taming the Bicycle"

## **Introduction**

Plasma physics is the study of the fourth state of matter.<sup>1</sup> As temperature increases, a body passes through distinct phase transitions from solid to liquid to gas to plasma. By far, the majority of the matter in the universe is in the plasma state, making up both stars and the diffuse material that fills much of interstellar space. Fusion is the energy process that powers these stars, and is the ultimate goal of this scientific program. The goal of fusion research is to create miniature "stars" on earth and tap their fusion fire to produce usable energy. A star has to its advantage the tremendous force of gravity due to its great mass of particles. This force of gravity confines the plasma that results from the high-energy particles released by the fusion of atomic nuclei in the star. Without the benefit of such a large gravitational pressure, other means are sought to confine the fusion plasmas created in the laboratory. Because the plasma is made up of a collection of charged particles, i.e. electrons and nuclei, electric and magnetic fields can be used to confine the plasma. In a toroidal device, such as the Madison Symmetric Torus,<sup>2</sup> a helical magnetic field winds around the torus and comes back on itself, creating a kind of magnetic bottle, which facilitates heating the plasma to extremely high temperatures. By changing the structure of the magnetic and electric fields in the MST, the quality of confinement the plasma experiences is changed.

From this layperson's introduction evolves the complex history of this scientific research. Particle and thermal transport has long been a central issue in the drive to achieve

fusion in magnetically confined plasmas. In particular, when the confining magnetic fields themselves become stochastic, the transport of heat and particles from the plasma is enhanced. In 1978 Rechester and Rosenbluth<sup>3</sup> expanded the work of Callen<sup>4</sup> and published a *Physical Review Letter*, detailing the effect of a stochastic magnetic field on electron transport: “Electron Heat Transport in a Tokamak with Destroyed Magnetic Surfaces.” While the subject of that paper is the tokamak confinement device, the implications of their studies are generally valid for any magnetic confinement device. In particular the reversed-field pinch (RFP) confinement scheme is an ideal test-bed for heat transport in a stochastic magnetic field, since the magnetic topology of the RFP yields a large radial region of overlapping magnetic tearing mode islands.<sup>5-8</sup> Overlapping islands tend to destroy flux surfaces and cause magnetic field lines to wander stochastically.<sup>9</sup>

In typical MST plasma discharges, magneto-hydrodynamic (MHD) instabilities generally known as “sawteeth” are present. Sawteeth were first observed in an RFP on the ZT-40M experiment.<sup>10-12</sup> The sawtooth instability can be characterized by a rapid event, followed by a long period of recovery.<sup>5,14</sup> The time between sawtooth “crashes” is referred to as the sawtooth period. The sawtooth period in MST plasmas is typically very regular, and many sawtooth cycles are present within a given discharge. This thesis is not intended to be a study of the mechanisms that cause sawteeth. Because of the sharpness of the sawtooth crash, the sawtooth cycle is used as a type of clock, around which the dynamics of the plasma will be studied. This thesis can be heuristically divided into three parts: 1) phenomenological observations (measurements) of the behavior of the plasma through the sawtooth cycle (Chapter 3), 2) calculations of the underlying transport properties as they evolve through the sawtooth cycle of the plasma, based on those measurements (Chapter 4), and 3) comparisons of those transport calculations to a theoretical model of transport in a stochastic magnetic field (Chapter 5).

## 1.1 Overview of the Madison Symmetric Torus

The MST reversed-field pinch is a toroidal, magnetic plasma confinement device, with a circular cross-section and iron core (Shown schematically in Figure 1.2).<sup>2</sup> The iron core is used to drive Ohmic current in the established plasma via transformer action. The plasma acts as a single-turn, secondary winding, while the switchable 20 or 80 turn primary windings wrap around the iron core that links the MST plasma. The major and minor radii of the plasma confinement volume are  $R=1.5$  m and  $a=0.52$  m, respectively, giving an aspect ratio ( $R/a$ ) of approximately 3. The vacuum vessel of the MST is 5 cm thick aluminum and serves both as the primary toroidal field winding of the machine and as a stabilizing, close conducting shell. Besides diagnostic portholes, there are two functional “cuts” in the vacuum vessel that allow magnetic flux to enter and leave the MST. These cuts are nominal breaks in the conductivity of the vacuum vessel, but preserve the integrity of the vacuum seal. For the vacuum vessel to serve as the toroidal magnetic field coil, there is a conduction break, or “gap” in the poloidal cross-section on the inboard midplane. This gap runs toroidally around the MST, (hence the moniker “toroidal gap,”) and allows current to be driven poloidally in the vacuum vessel to produce the toroidal magnetic field, as shown in Figure 1.3. The “poloidal gap” is a conduction break in the toroidal cross-section, located beneath the iron flux core, and runs poloidally around the machine. Locations on the MST shell, e.g. portholes, are specified in toroidal degrees counter-clockwise (viewed from above) from the poloidal gap (at 0 degrees,) and poloidal degrees from the outboard midplane (opposite the toroidal gap), with positive degrees being on the upper half of the machine, negative degrees being on the lower. Because of these conventions, the MST is inherently a “left-handed” coordinate system.

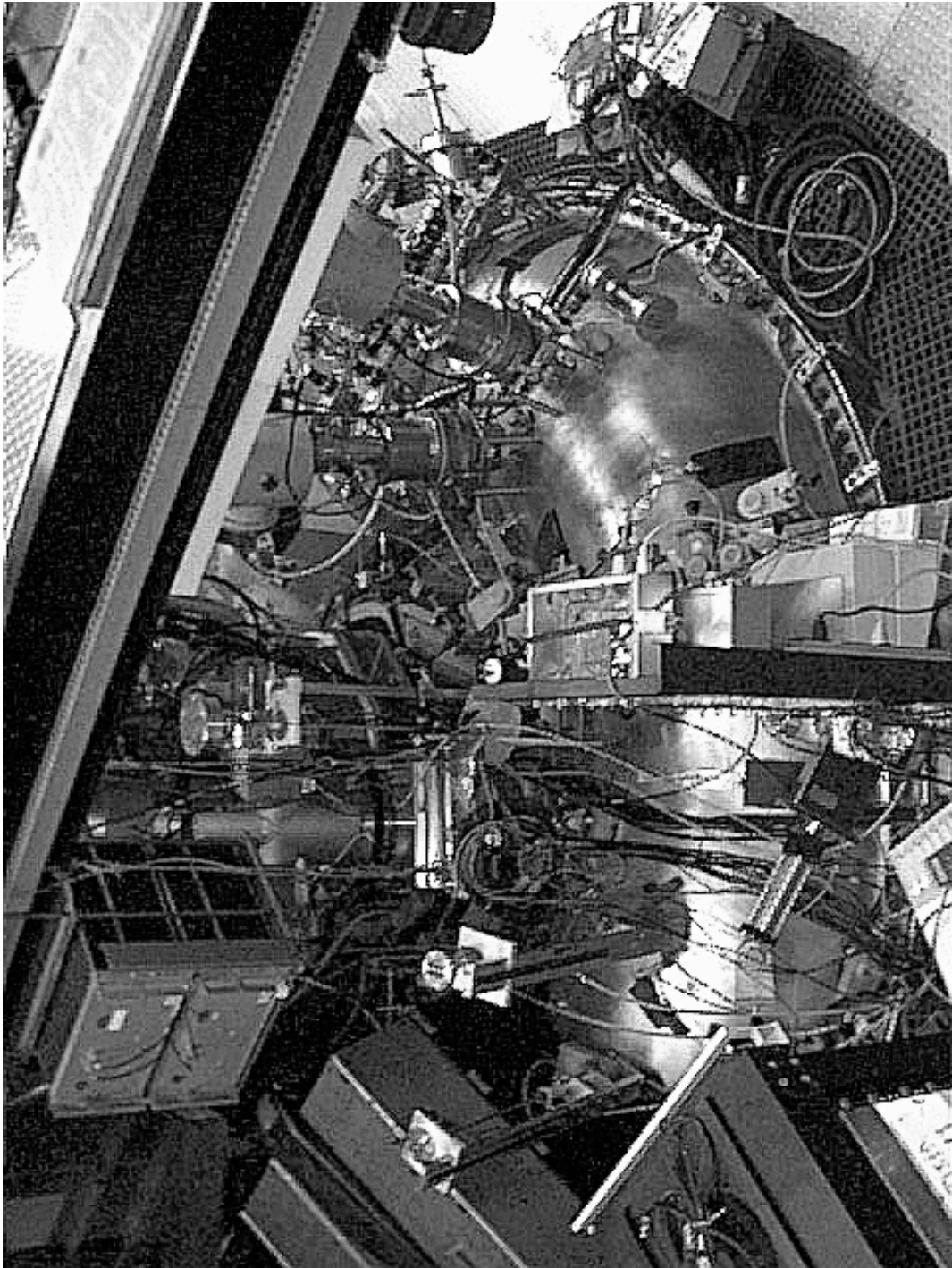


Figure 1.1 Photograph of the MST from the South.

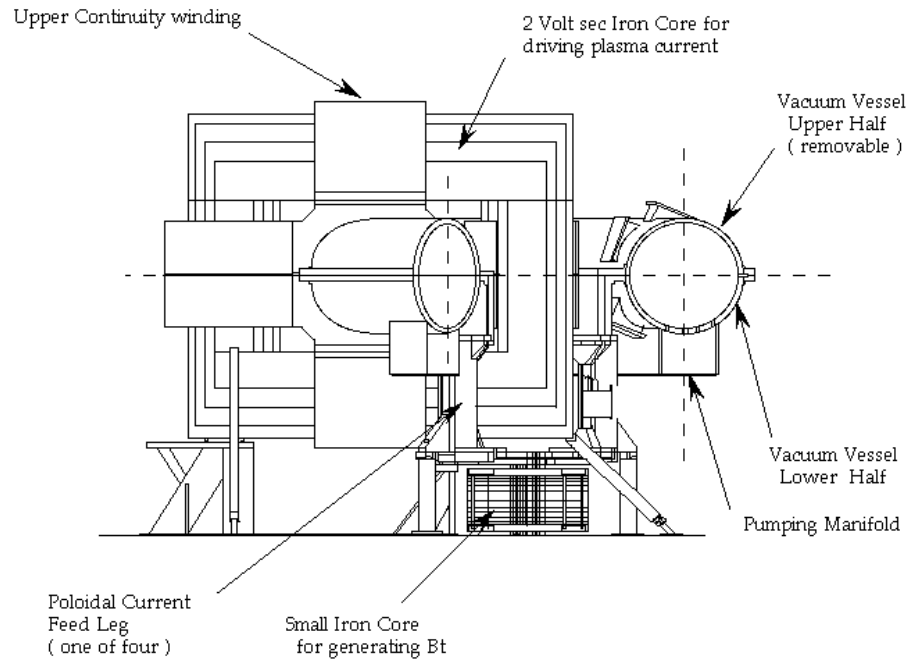


Figure 1.2 South View of the MST.

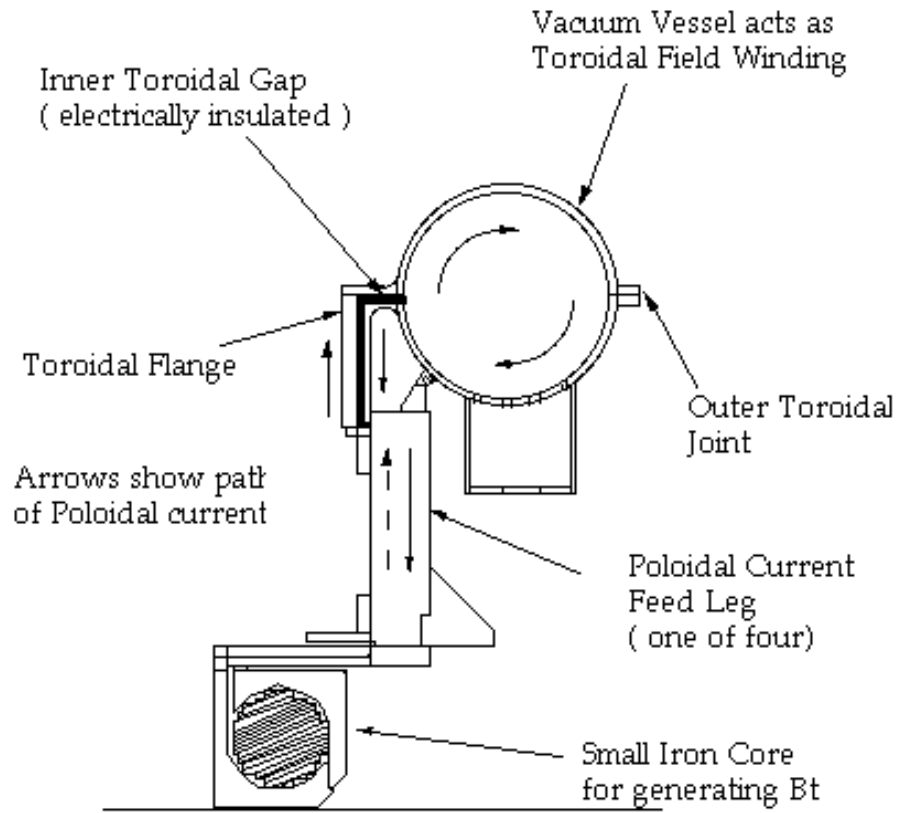


Figure 1.3 MST Toroidal Magnetic Field System.

Since the currents flowing in the vacuum vessel stabilize MHD instabilities, portholes, which interrupt these currents, are a source of symmetry breaking error fields. To minimize these non-axisymmetric perturbations to the plasma, portholes are kept small; this limits the etendue of light gathering optical systems, e.g. Thomson scattering. The biggest portholes are 4.5" in diameter, of which there are 4. More typical, however, are the 1.5" ports that are distributed about the MST. The MST vacuum is established by over 200 1" ports in the lower segment of the vacuum vessel, which open onto a pumping manifold connected to 3 turbo pumps and one cryogenic pump. Typical base pressure in the MST is on the order of  $10^{-7}$  Torr.

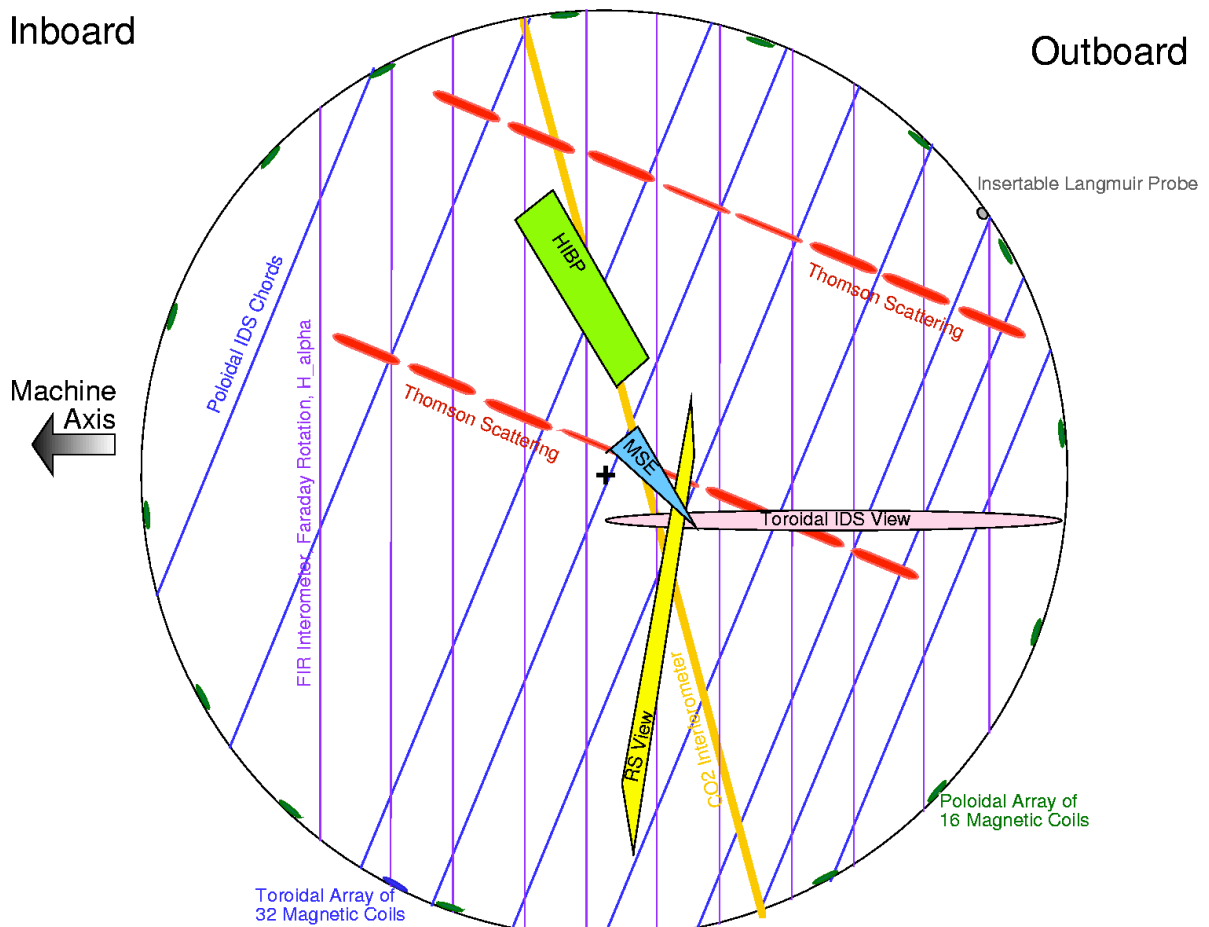


Figure 1.4 Poloidal projection of MST diagnostic sampling locations.

The MST has the diagnostics to make the measurements necessary to understand transport. Figure 1.4 shows the locations that are sampled by routine MST diagnostics, projected onto one poloidal plane. In the actual machine, the diagnostics are distributed toroidally about the device. The individual diagnostics will be discussed in somewhat more detail in later sections. Routine diagnostics on the MST include Thomson scattering, Rutherford scattering, ion Doppler spectrometry, FIR interferometry/polarimetry, two  $H_{\alpha}$  arrays, CHERS, MSE, HIBP, and arrays of magnetic pick-up coils. As discussed subsequently in this thesis, Thomson scattering is used to measure the electron temperature profile,  $T_e$ . Bulk ion temperature  $T_i$  can be measured with Rutherford scattering. Ion Doppler spectrometry (IDS) is used to measure line averaged impurity ion ( $C^V$ ) temperature and flow velocity (poloidal and toroidal). Charge exchange-recombination spectroscopy (CHERS) is similarly used to measure impurity ion temperatures (localized, rather than line averaged). Far-infrared interferometry (FIR) is used to measure profiles of electron density, which can be coupled with  $H_{\alpha}$  measurements to give an estimate of the electron source rate. FIR polarimetry is used to measure angles of Faraday rotation, and subsequently current density, when combined with the FIR density profile. The motional Stark effect (MSE) diagnostic gives a value of the on-axis magnetic field. Mirnov probes at the edge of the plasma, i.e. magnetic pickup coil arrays, allow the magnetic mode spectrum of the plasma to be inferred. A heavy-ion beam probe (HIBP) is used to measure the plasma potential profile, and consequently the radial electric field. Gathering these measurements under the banner of the equilibrium reconstruction code MSTFit creates a stage upon which to examine the plasma behavior and approach issues of transport as it varies through the sawtooth cycle.

## 1.2 Overview of this Thesis

In this thesis, time evolving profiles are measured to understand electron heat and particle transport in the MST. In particular, electron temperature, electron density, and current density profiles have been measured during a standard plasma sawtooth cycle. The MHD activity during the sawtooth cycle is examined as an *a priori*, time-evolving condition that is affecting the plasma equilibrium and consequently the transport of heat and particles. The cause of the MHD behavior is not central to this thesis. Rather, the effects of the fluctuations on transport are considered. As will be shown in the body of this thesis, the current density peaks up as the sawtooth crash is approached. This current peaking pushes the plasma farther away from the Taylor minimum-energy state and causes (possibly dynamo driven) tearing instabilities to grow.<sup>13</sup> At the crash the current density profile broadens, resulting in a flatter  $\beta$ -profile, and a plasma that is closer to a Taylor minimum-energy state. Another effect of the peaking current density is to broaden the q-profile. Lower q-shear results in a more stochastic magnetic field in the region where tearing mode islands overlap. Greater field stochasticity leads to enhanced transport of heat and particles by the electrons, and the electron temperature is observed to drop. After the sawtooth crash, the current density broadens, the q-profile peaks, the q-shear is increased in the region of overlapping islands, the field stochasticity is reduced, and the electron heat transport falls. The thesis covers the measurements necessary to test these assertions. Experiments are also carried out in a number of different discharge conditions, and the results from these experiments are compared to the Standard plasma results.

This thesis began with a cursory introduction to the Madison Symmetric Torus reversed-field pinch, where all of this research was conducted. After a short overview of Thomson scattering from high temperature plasmas, the ruby laser system that is used on the MST (Chapter 2) is described in detail. Following that description, and constituting the

original research of this thesis, are the results of the many experiments that have been done using the described Thomson scattering system and other diagnostics on the MST. Chapter 3 contains the analysis of experiments geared to examine how the equilibrium of “Standard” MST plasmas evolves over the course of the sawtooth cycle. Chapter 4 contains the results from transport studies of heat and particles in these plasmas, and Chapter 5 contains a comparison of the main transport results to the Rechester-Rosenbluth theoretical model for stochastic transport. Finally, in Chapter 6, MST “Standard” plasma discharges are compared to 4 other discharge types: Non-Reversed plasmas ( $F=0$ ),  $F\sim+0.02$  plasmas,  $F\sim+0.03$  plasmas, and PPCD plasmas. The main results are summarized in Chapter 7, and avenues of future work on those topics are outlined.

## References

1. F.F. Chen, *Introduction to Plasma Physics and Controlled Fusion*, Plenum Press, New York, NY, 1984.
2. R.N. Dexter, D.W. Kerst, T.W. Lovell, S.C. Prager, and J.C. Sprott, *Fusion Technology*, **19**, 131 (1991).
3. A.B. Rechester and M.N. Rosenbluth, *Phys. Rev. Lett.*, **40**, 38 (1978).
4. J.D. Callen, *Physical Review Letters*, **39** (24), 1540-1543 (1977).
5. S. Ortolani and D.D. Schnack, *Magnetohydrodynamics of Plasma Relaxation*, World Scientific Publishing, New Jersey (1993).
6. E.D. Held, J.D. Callen, C.C. Hegna, C.R. Sovenic, *Physics of Plasmas*, **8** (4), 1171-1179 (2001).
7. J.S. Sarff, "Control of Magnetic Fluctuations and Transport in the MST," PLP Report 1225, University of Wisconsin-Madison, (1999).
8. F. D'Angelo, R. Paccagnella, *Physics of Plasmas*, **3** (6), 2353-2364 (1996).
9. G.M. Zaslavsky and B.V. Chirikov, *Sov. Phys. Usp.*, **14**, 549 (1972).
10. G.A. Wurden, *Physics of Fluids*, **27** (3), 551-554 (1984).
11. D.A. Baker, C.J. Buchenauer, L.C. Burkhardt, et al., in *10<sup>th</sup> International Conference on Plasmas Physics and Controlled Nuclear Fusion Research*, London., Vol. 2, IAEA, Vienna (1984) 2-9.
12. K.A. Werley, R.A. Nebel, G.A. Wurden, *Physics of Fluids*, **28** (5), 1450-1453 (1985).
13. J.B. Taylor, *Rev. of Modern Physics*, **58** (3), 741-763 (1986).
14. F. Wagner and U. Stroh, *Plasma Phys. Control. Fusion*, **35**, 1321-1371 (1993).

. . . it was aimed down at a beautiful white Italian racing bicycle lying on its side. The bicycle was so full of magic and innocence, hiding there. It might have been a unicorn.

--Kurt Vonnegut, Jr., *Hocus Pocus*

## **The MST Thomson Scattering Ruby Laser System**

This chapter is intended to give a semi-technical description of the MST Thomson scattering ruby laser system; its alignment; its calibration; and the highlights of data analysis. Future generations of graduate students may find this useful, should they need to utilize the MST TS ruby laser system. The scientific aspects of this thesis are presented in subsequent chapters.

### **2.1 Thomson Scattering as a High Temperature Plasma Diagnostic**

The theory of Thomson scattering as a high temperature plasma diagnostic is well developed. A brief overview of the most salient points will be presented here, but readers interested in a more thorough description are encouraged to see the references.<sup>1,2,3</sup> Thomson scattering refers to the elastic scattering of light from a moving (free) electron. Specifically, the kinetic energy of the moving electron must be large compared to the energy of the incident photon. Comparing Compton and Thomson scattering, Compton scattered photons (usually x-rays) impart substantial energy to the electron, causing it to recoil. And Rayleigh scattering is essentially Thomson scattering off electrons bound in atoms. A cartoon depiction of a Thomson scattering process is shown in Figure 2.1. Figure 2.2 gives a wave

vector diagram of this process. In a single collision, the moving electron imparts its energy to the scattered photon, changing the wavelength of the scattered light. If the wavelength of the incident photon is well known, by measuring the wavelength of the scattered photon, the velocity of the electron can be deduced.

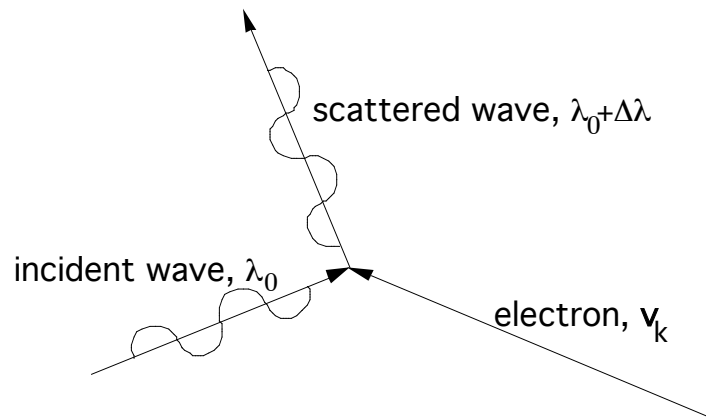


Figure 2.1 Thomson scattering of light from a moving electron.

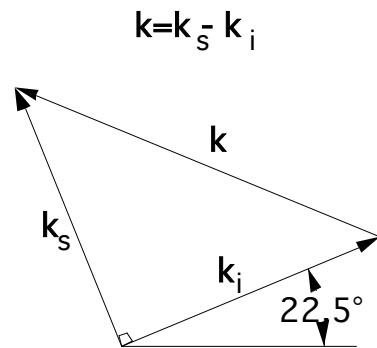


Figure 2.2 Wave vector diagram for Thomson scattering in the MST ruby laser system.

A plasma is a collection of electrons and ions. Statistically, the temperature of any body of matter (solid, liquid, gas, or plasma) is a representation of the distribution of velocities of the elements of that body. As such, the plasma has statistical electron and ion temperatures, which can be calculated if the particle velocity distribution functions are known. Laser light is extremely coherent, meaning that it consists of photons that have

essentially the same wavelength. Hence, by shining a laser through a high temperature plasma, the individual laser photons will Thomson scatter off individual electrons in the plasma, which have a distribution of velocities, to produce a spectrum of scattered light which has a distribution of wavelengths about the initial laser wavelength. In wavelength-space, Thomson scattering transforms the input delta-function into an output spectrum of wavelengths. The shape of the output spectrum is representative of the electron velocity distribution function. Hence, by measuring the Thomson scattered spectrum from a known laser line, the electron distribution function can be measured, allowing the electron temperature of the plasma to be calculated.

For most low-temperature plasmas, the electron velocity distribution is assumed to be Maxwellian. That is to say, the electron velocities are non-relativistic and are distributed according to Gaussian statistics. In terms of the relevant plasma parameters:

$$f_k(v_k) = n_e \left( \frac{m_e}{2\pi T_e} \right)^{1/2} e^{-m_e v_k^2 / 2T_e} . \quad (1)$$

Here  $n_e$  is the electron number density,  $T_e$  is the electron temperature,  $m_e$  is the mass of the electron,  $v_k$  is the velocity of an electron with wave-vector  $k$ , and  $f_k$  signifies the electron distribution function in for the wave-vector  $k$ . It is simple to rewrite this equation in terms of wavelength rather than wave-number, by using the “linear Doppler” approximation:

$$v_k \approx c \frac{\lambda_0 - \lambda}{\lambda_0} = c \frac{\lambda - \lambda_0}{\lambda_0} , \quad (2)$$

where  $c$  is the speed of light,  $\lambda_0$  is the incident (laser) wavelength,  $\lambda$  is the Thomson scattered wavelength, and  $\lambda - \lambda_0 = \lambda \frac{\lambda - \lambda_0}{\lambda_0}$ . The difference between the linear Doppler approximation and the full Doppler effect for light remains small even up to relativistic velocities, hence its validity

here. Making this substitution leads to a formulation for the non-relativistic electron distribution function, which can be directly fit to the Thomson scattered spectrum to find the electron temperature:

$$f(v) = n_e \left( \frac{m_e}{2\pi T_e} \right)^{3/2} e^{-m_e c^2 v^2 / 2T_e} = \frac{C_n}{C_D} e^{-v^2 / 2C_D^2}, \quad (3)$$

where  $C_n$  and  $C_D$  are fitting constants for the electron density and temperature, respectively.

As the electron temperature increases, a significant fraction of the electron velocities in the tail of the distribution function will be relativistic. In that case, Hutchinson suggests a “mildly relativistic” correction to the above distribution function:<sup>2</sup>

$$f_{\text{Hutch.}}^{\text{rel}}(v) = \left( \frac{v}{v_0} \right)^3 \frac{3}{2} \frac{v_0}{v_0 + v} f(v). \quad (4)$$

An even more accurate, “fully relativistic” correction is proposed by Sheffield:<sup>3</sup>

$$f_{\text{Shef.}}^{\text{rel}}(v) = \left( \frac{v}{v_0} \right)^3 \left[ \frac{7}{2} \frac{v_0}{v} + \frac{v^2}{v_0^2 2C_D^2} \right] f(v). \quad (5)$$

## 2.2 Overview of the MST Ruby Laser TS System

The MST Thomson scattering ruby laser system is relatively robust, and has generated useful data for over 15 years. The system consists of a JK Lumonics PDS1 (Plasma Diagnostic laser System) ruby laser-head, associated power supplies and chillers, mirrors and focusing optics, a beam dump, collection optics, a Jarrell-Ash MonoSpec-27

(Model 82-499) spectrometer, and light detectors with their associated electronics. Each of these elements will be discussed in the following sections. Over time, the system has evolved through minor and major technological upgrades, but the laser itself has remained the same. It is a single-pulse-per-plasma-shot unit, limited by the time it takes to pump the flashlamps and dissipate the excess heat. It can be operated in “double pulse mode,” however less than half the energy of a single pulse is released in either of the two pulses. Because the system historically has operated on the verge of signal-to-noise practicality, double pulsing the laser has not been an option. In fact, to improve the reliability of measurements, multiple shots are usually ensembled together. Before the latest upgrade, 10 plasma shots were required to make a single temperature measurement at a single radial location, usually at the center of the plasma. And changing viewing locations was a long and arduous chore, though it had been done in a limited sense.<sup>4</sup>

Hardware upgrades have improved the performance of the ruby TS system. A significant improvement came in 1997 with the addition of a movable fiber optic bundle, which defines the entrance aperture of the light gathering system.<sup>5</sup> This upgrade made it possible to change viewing geometries between shots, and opened up the possibility of measuring temperature profiles (with ensembling) in the matter of a few days. The capability of the system was further improved in 1998 by the addition of an alternate laser beam-line. This doubled the number of viewing locations that the MST Thomson scattering system has and expanded the radial range of coverage nearly to the plasma edge. Even with this improved flexibility of the system, it was still severely hampered by low light levels and an unacceptable signal-to-noise ratio in the edge region. In 2000 a major upgrade in the light detection system was implemented, greatly improving the light collection efficiency. With this upgrade from the 5-channel micro-channel plate (MCP) detector to the 11-channel large area-avalanche photodiode (LA-APD) array, it became possible to make statistically significant, single shot temperature measurements. The time required to measure a

temperature profile was reduced from days to hours, while at the same time the resolution of that measurement was increased by a factor of 3. The details of these measurements are the subjects of subsequent chapters. This chapter focuses on the MST Thomson scattering ruby laser system, as it exists after this last upgrade.

### 2.2.1 The JK-Lasers Ruby Laser Head

Figure 2.3 shows an overview of the laser-head. At the heart of the system are two ruby crystals, which are referred to as the “oscillator rod” and the “amplifier rod.” The oscillator rod is a manufactured ruby crystal, 4 inches in length and 3/8 inches in diameter. It resides in the oscillator-pumping chamber, which is a chilled water filled cavity. The walls are parabolic reflectors, which focus light from four broad-spectrum flashlamps to “pump” the electrons in the ruby into a metastable state for lasing. This pumping chamber rests between the “front” and “back” mirrors of the ruby laser resonant (hence “oscillator”) cavity. A Brewster plate polarizer is used to ensure that the emitted beam has horizontal polarization. Crossing this polarizer with a cylindrical Pockels cell allows the laser to be Q-switched, concentrating the energy of the laser into a 50 ns pulse. At the output of the pumping chamber is an aperture that is useful to select the TEM<sub>100</sub> mode of laser operation. Output laser pulses from the oscillator side of the laser-head are typically 250 mJ.

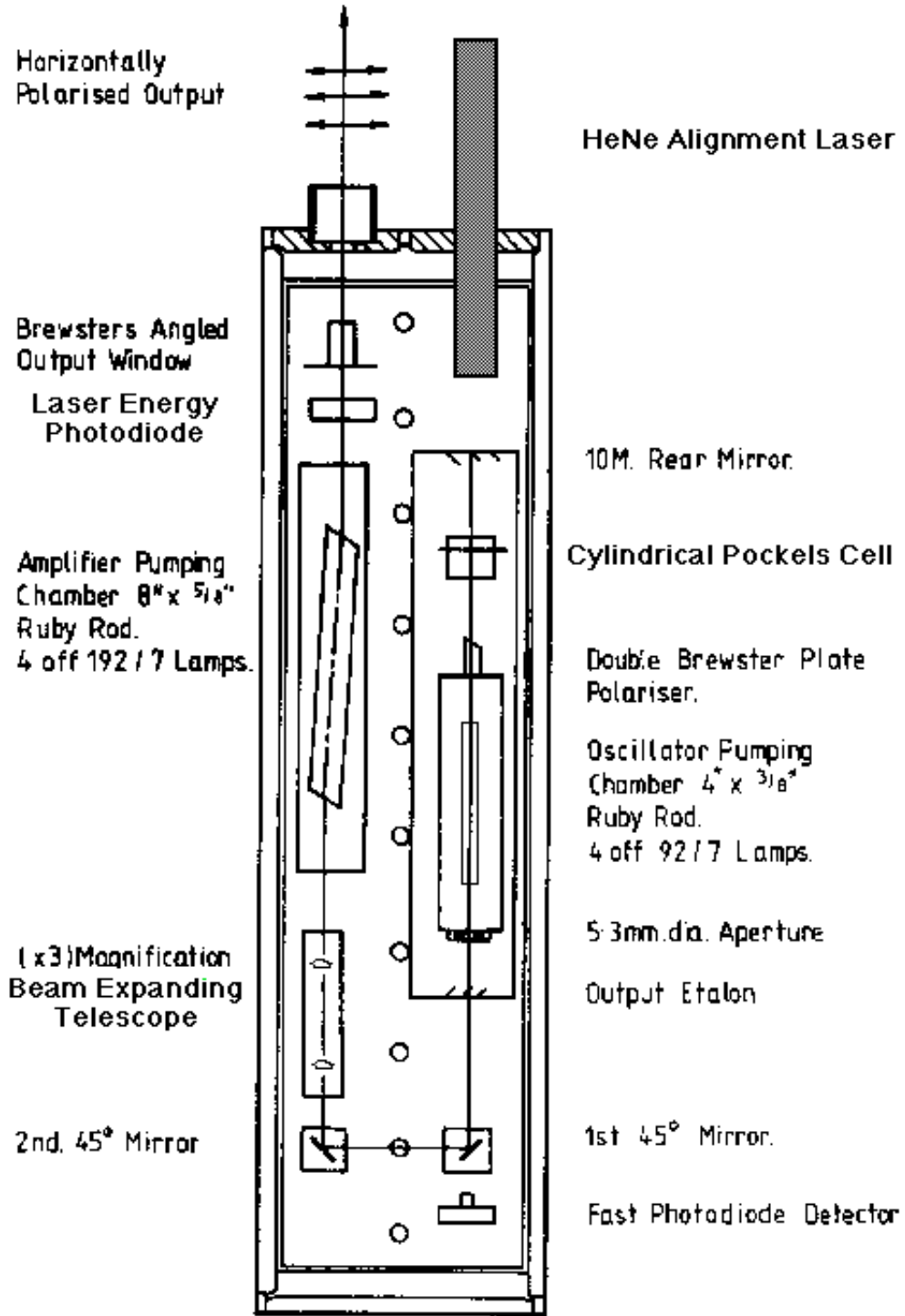


Figure 2.3 Ruby laser-head layout.

After exiting the oscillator cavity, the light encounters two 45-degree mirrors, steering the beam into the amplification side of the laser-head. At the first 45-degree mirror, a small fraction of the light passes through the mirror, striking what is called the “laser fast photodiode.” The signal from this photodiode is used to control the timing of the Thomson scattering data acquisition system. After the second 45-degree mirror, the light enters a “beam expanding telescope,” which has a magnification of 3. This is necessary since the oscillator and amplifier ruby rods have differing diameters, and to extract maximum amplification from the amplifier rod, the beam should fill its diameter. The amplifier rod has a diameter of 5/8 inches and a length of 6 inches. Similar to the oscillator rod, the amplifier rod resides in a chilled-water filled, pumping chamber with 4 flashlamps. On its way out of the laser-head, the light passes through a 45-degree partial mirror that reflects a small fraction of the laser onto another photodiode, called the “laser energy monitor.” The last element of the system is another Brewster angle polarizer, which serves two purposes: it ensures the horizontal polarization after amplification, and it acts as a physical barrier to dust particles moving up the laser path. This protects the surface of the amplifier rod. Dust is a major concern because of its potential to damage optical elements. To minimize the amount of dust, the entire laser-head is enclosed in a cabinet that is kept at positive pressure by the flow of filtered air. Laser pulses exiting the amplifier are typically on the order of 5 J when the system is well aligned.

Two charging supplies power the flashlamps, but they share one chilled water supply. The distilled, chilled water is circulated in a closed loop with a heat exchanger to an external chiller. It is necessary to cool the pumping chambers to maintain temperature uniformity for lasing, and to dissipate excess heat generated by the broadband flashlamps.

### 2.2.2 The Support Structure and Optics

The entire laser system is mounted to a movable cart, which is positioned in close proximity to the MST.<sup>6</sup> Once in position, the cart can be raised off its casters to prevent unwanted movement. The laser beam path is mated to the MST through an extension of the vacuum. There are two paths the laser can alternately be made to follow, but for simplicity, only the “central laser path” is considered for now. First, the beam is turned 157.5 degrees by reflection in a vertical plane from a turning mirror. This angle is set by the poloidal MST boxport, which holds the collection optics at an angle of 22.5 degrees. The air-to-vacuum interface is a lens with a focal length of 500 mm. This lens is at the end of a long pipe, which has both a bellows for mechanical isolation and a delrin segment for electrical insulation. These pipes are supported from the laser-head platform and weakly from a VAT valve at the entrance to the MST vacuum vessel. After passing through the lens, the beam is converging so that it reaches a maximum energy density near the geometrical center of the MST vacuum vessel. On the opposite side of where the beam enters the MST, there is a vacuum beam dump. Keeping the beam dump under vacuum eliminates the need for a second vacuum-to-air interface, which could increase the background scattered light. The spectrometer and collection fiber optics are located in a light-tight cabinet at the top of a pair of nearly vertical support beams, which attach to the laser cart. In this way, the entire Thomson scattering laser system remains mechanically and electrically isolated from the MST.

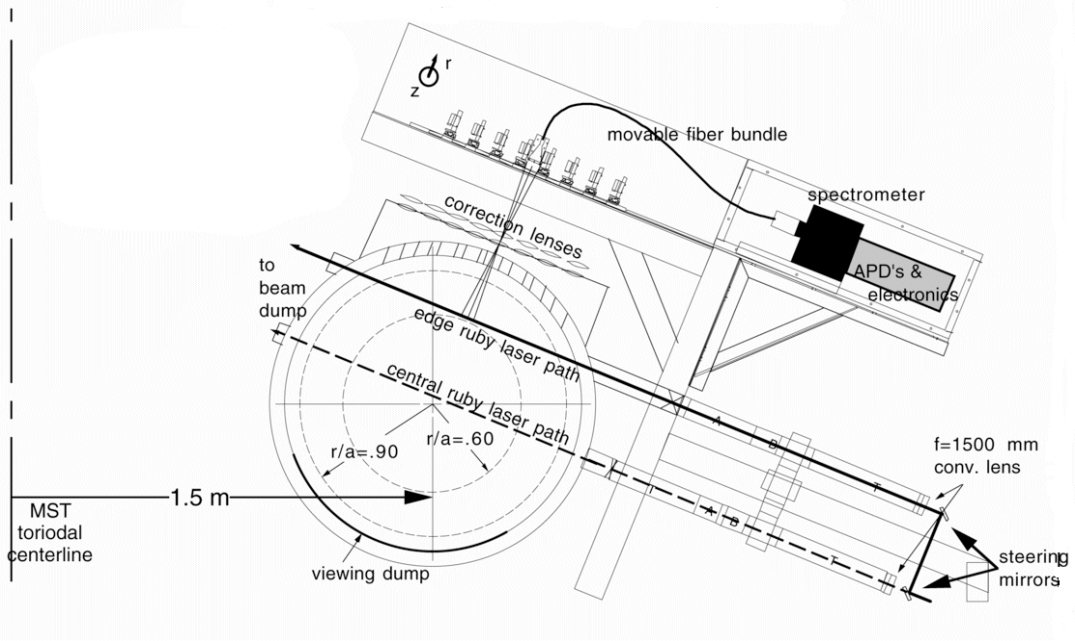


Figure 2.4 Side view of the ruby laser Thomson scattering system at 90 degrees toroidal of the Madison Symmetric Torus. To operate in “central” laser path mode, the lower steering mirror is removed along with the movable correction lenses.

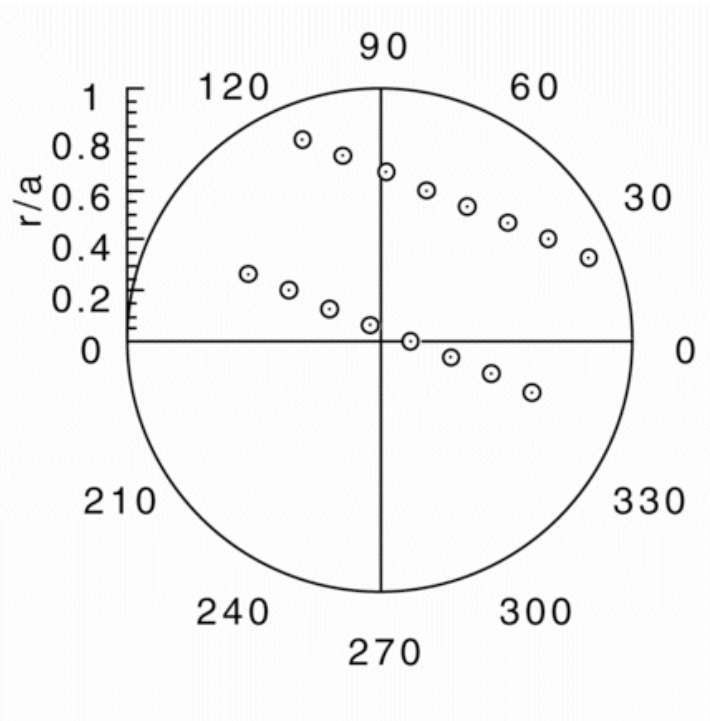


Figure 2.5 Geometrical location of Thomson scattering viewing centers for both the edge and central laser paths.

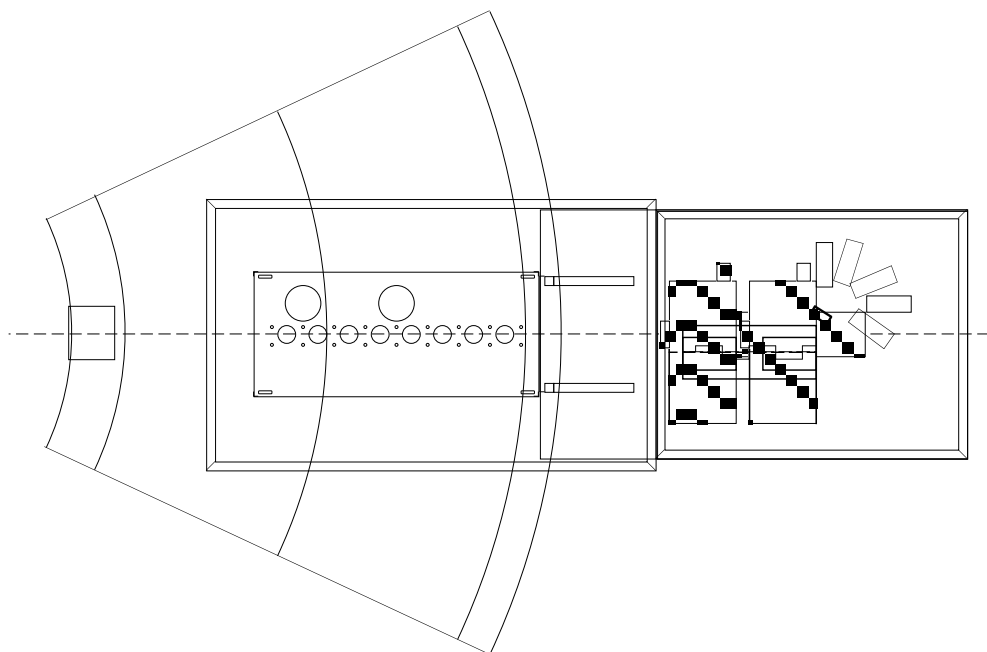


Figure 2.6 Top view of the ruby laser Thomson scattering system, showing a segment of the MST vacuum vessel. The spectrometer is shown in overlay at its two locations. The spectrometer is movable in order to reach the furthest inboard viewing locations with the fiber bundle. Only the top row of LA-APD modules is shown, in addition to the former location of the MCP detector.

The MST ruby laser system can be operated in two configurations, which are related to the regions of plasma volume that are of interest for a particular experiment. The Thomson scattering volume that is viewable by the system is the intersection between the laser beam and the viewing chord defined by the fiber optic bundle and collection lenses. In the “central laser path” configuration, there are 8 chords of measurement extending from  $r/a = -0.587$  to  $r/a = +0.627$ . Here the negative sign refers to chords that are inboard of the geometrical center of the MST vacuum vessel. See Figure 2.4. In the “edge laser path” configuration, a steering mirror is inserted into the beam line, directing the laser onto a more tangential path to the plasma. In “edge” configuration, because of the specific geometry of the TS system and the MST, it is no longer useful to refer to locations in terms of “inboard” or “outboard.” Suffice it to say that the radial locations that are measured cover a range from  $r/a = 0.625$  to  $r/a = 0.882$ , i.e. nearly to the edge of the plasma. Figure 2.7 gives an indication

of the extent of the radial coverage. Table 2.1 summarizes the radial and poloidal locations of all 16 Thomson scattering viewing chords.

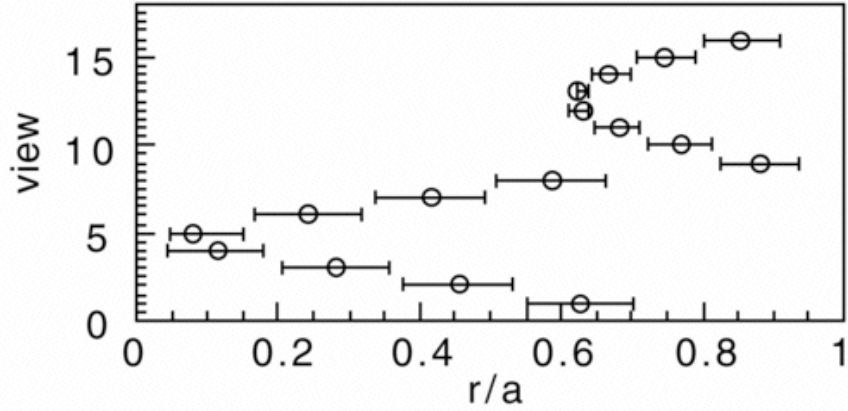


Figure 2.7 Geometrical coverage of ruby laser Thomson scattering views. Error bars indicate radial range (in  $r/a$  space) of scattering volume on each view.

View	$r/a$	$\phi$ (degrees)	% perp. Sens.	% parll. Sens.
1	0.627	-18.46	63.0	37.0
2	0.455	-16.93	77.0	23.0
3	0.283	-13.53	88.5	11.5
4	0.115	0	99.5	4.5
5	0.080	123.91	96.8	3.2
6	0.244	147.06	76.2	23.8
7	0.415	151.39	64.3	35.7
8	0.587	153.19	50.0	50.0
9	0.882	22.28	99.9	0.1
10	0.769	31.41	96.1	3.9
11	0.681	43.26	84.5	15.5
12	0.630	57.76	64.1	35.9
13	0.625	73.61	38.2	61.8
14	0.666	88.59	13.9	86.1
15	0.746	101.10	3.1	96.9
16	0.854	110.82	6.6	93.4

Table 2.1 Radial and poloidal locations of ruby laser Thomson scattering system views, including % sensitivity to perpendicular and parallel electron distribution functions.

Geometrically, the TS system covers a wide range of  $(r, \varphi)$  space. Since the toroidal and poloidal components of the magnetic field are also varying over this space, the sensitivity of the TS system to the parallel and perpendicular (to the magnetic field) electron distribution functions also varies. While it is generally believed that the parallel and perpendicular electron temperatures are equal in the MST, it may still be useful to examine the variation in directional sensitivity of the TS system. To this end, the equilibrium magnetic field profiles were found for a representative (so called “Standard” discharge in subsequent chapters) MST plasma using the equilibrium reconstruction code MSTFit. Since the geometry of the TS system is well known, it is straightforward to calculate from these field profiles the fractional sensitivity of each TS viewing chord to the parallel and perpendicular electron distribution functions. The results are shown in Table 2.1.

### 2.2.3 The Light Detection System

Grooves/mm	$T_e$ range
600	1-3 keV
1200	500-1500 eV
1800	100-700 eV

Table 2.2 Spectrometer gratings and expected ranges of sensitivity.

Thomson scattered photons are collected by a 3-inch diameter lens located in the boxport flange. This light is focused onto the movable fiber optic bundle and piped into the Jarrell-Ash Monospec-27 spectrometer. At the entrance to the fiber bundle are a cut-glass filter and a plastic polarizer that are both used to reduce non-Thomson scattered, background light. The spectrometer entrance aperture is set by a 0.072” slot attached to the end of the fiber bundle. The spectrometer uses one of three gratings to disperse the incoming light. Table 2.2 shows the range over which each grating is expected to be most sensitive.

The most recent upgrade to the Thomson scattering system required replacing the 5-channel micro-channel plate (MCP) detector with an 11-channel large area-avalanche photodiode (LA-APD) array. To do this the exit-plane mirror of the spectrometer was removed and a new exit-plane structure was fabricated. This new exit-plane structure consists of 2 bundles of fiber optics, which are fastened to a kinematic mount. These two bundles contain 7 (on the long-wavelength side) and 4 (on the short-wavelength side of the laser line) separate sub-bundles of fibers, each sub-bundle going to its dedicated LA-APD module. For each sub-bundle, the end at the exit-plane is a rectangular column of fibers, while the other end is circular, meeting a lens to focus its light onto the LA-APD detector. Because the plastic fibers (1mm ESKA-MEGA) used to construct this array slightly attenuate the light at the frequencies of interest, it is necessary to minimize the distance between the exit-plane and the LA-APD detector element. To do this a 2 tier, “stadium seating” arrangement was employed. See Figure 2.9.

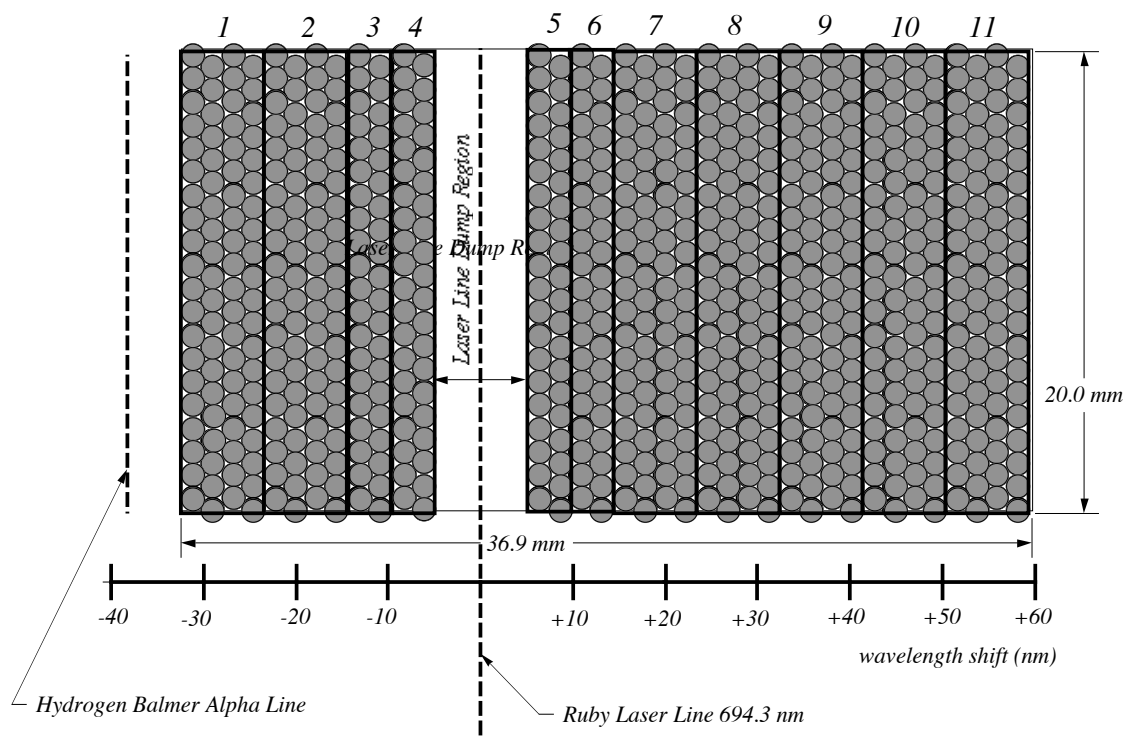


Figure 2.8 Schematic of the TS spectrometer exit-plane arrangement of fiber optics. Vertical groupings correspond to separate LA-APD modules.

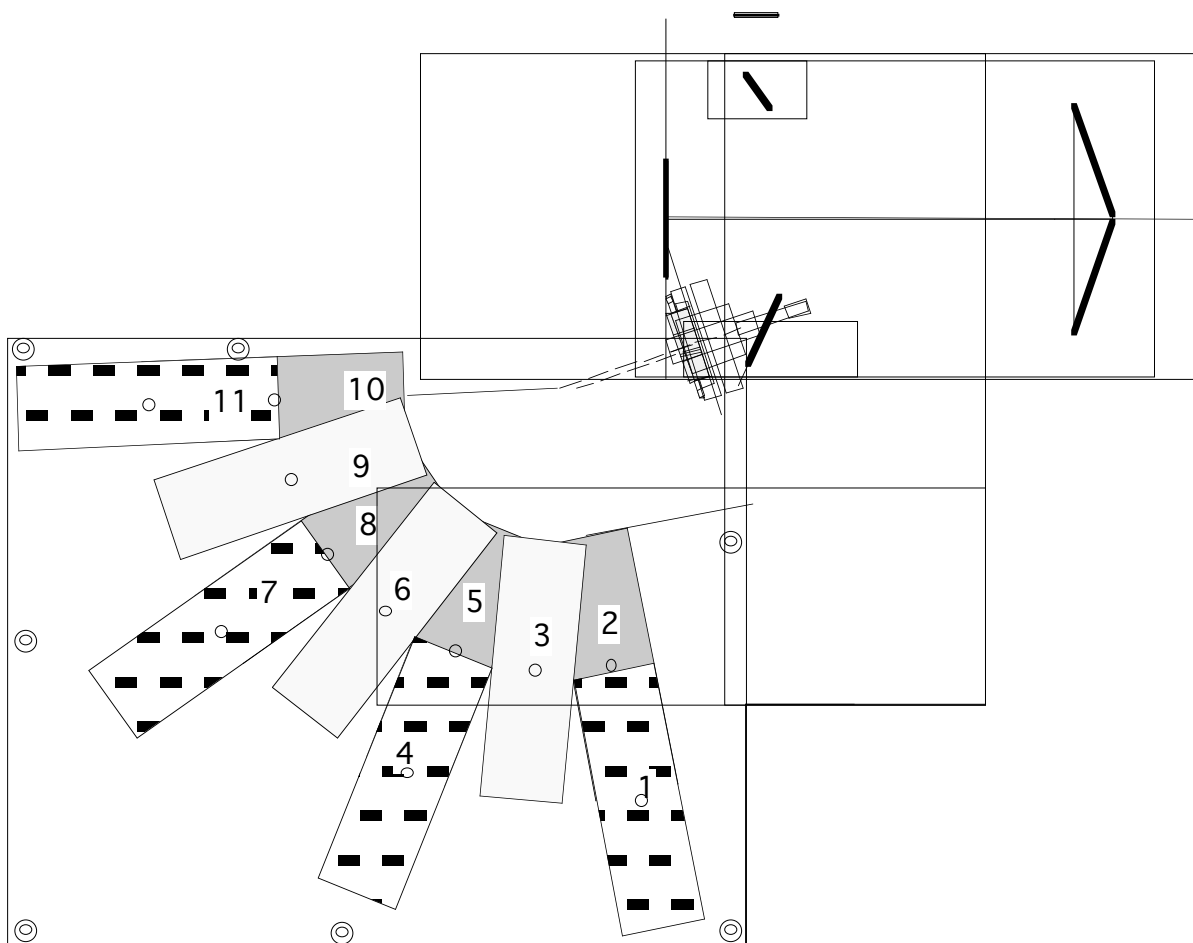


Figure 2.9 Schematic setup of the TS spectrometer, showing the 2-tier layout of the LA-APD modules.

The LA-APD modules themselves are commercially available units from Advanced Photonix, Inc. The photodiode has a 5 mm diameter active area. The APD is thermoelectrically cooled to maintain a high signal-to-noise ratio (SNR). The improvement in the SNR is due to the high quantum efficiency of the LA-APD compared to the MCP, about 85% vs. 3.5%. The main advantage of the MCP was its relatively high gain,  $10^6$ , as compared to the LA-APD gain of approximately 300.<sup>5</sup> Another difference between the APD modules and the MCP is that the APD's have a continuous signal output, whereas the MCP could only be gated on for a few microseconds. Because the APD's are always “on,” it was necessary to

install a fast-opening shutter in the spectrometer. This shutter remains closed during “start-up” of the plasma discharge to block out the intense background light. A photograph of the assembled spectrometer, exit-plane, and LA-APD array and shutter can be seen in Figure 2.10.

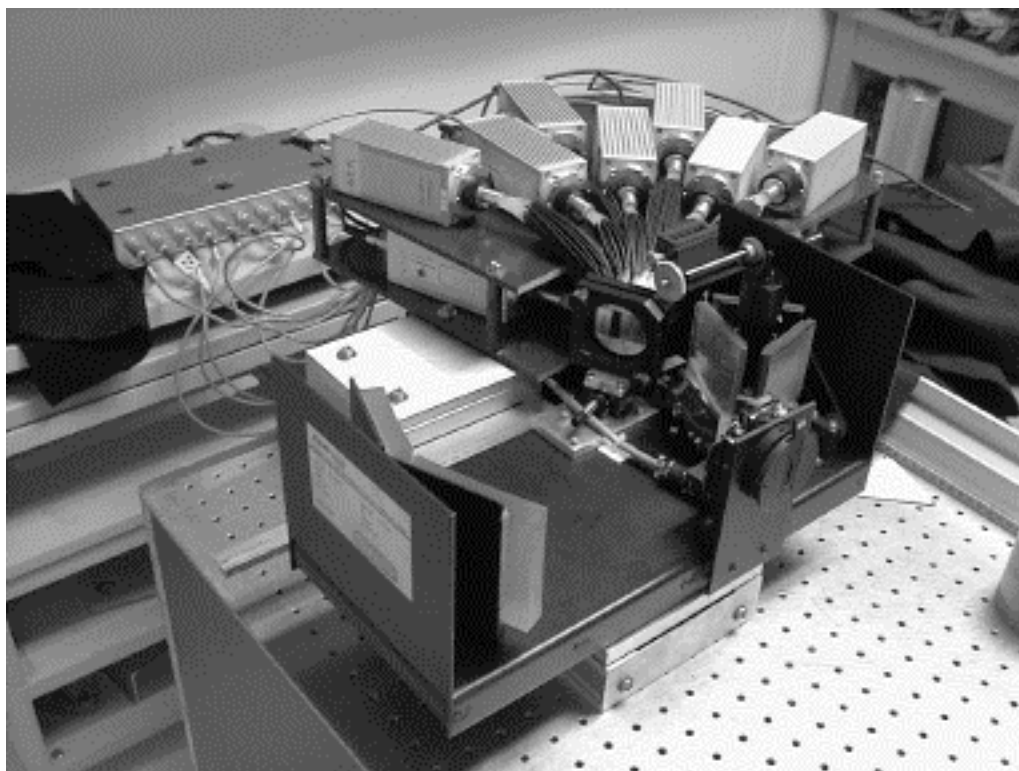


Figure 2.10 Photograph of the TS spectrometer. The 2-tier, stadium style layout of the LA-APD modules, the exit-plane fixture, the larger area mirror, the spectrometer shutter, and the APD power distribution box are visible.

#### 2.2.4 Electronics and Digitization Systems

An overview of the MST TS system is shown in Figure 2.11. Working back from the data acquisition system, Thomson scattering data is digitized using either 3 LeCroy 2249A or 3 LeCroy 2250L digitization modules. The main difference between the two types is that the 2250L's have 32-bit FIFO (fast in fast out) memory. This allows the modules to be re-

triggered with a minimum separation time of 9 ns. This feature is extremely important for double-pulse experiments, and is convenient when calibrating the system. Both types of modules integrate the charge delivered to their 12 parallel inputs as long as the module is gated on. They can be gated on for as long as 200 ns, but for our purposes a gate of 100 ns is preferred.

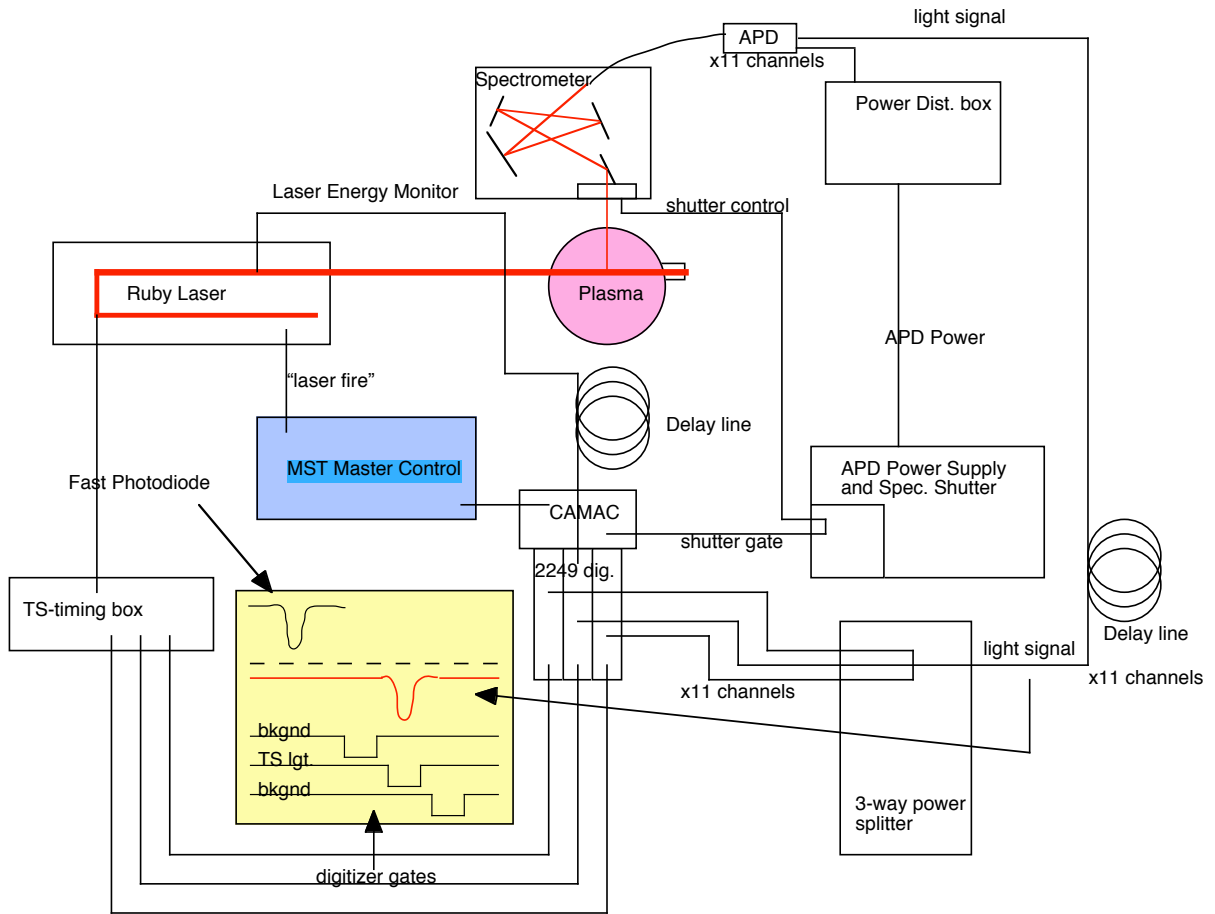


Figure 2.11 Schematic overview of the ruby laser TS system.

Three digitizers are used to capture: 1) the background light preceding the Thomson scattering signal, 2) the Thomson scattering signal, and 3) the background light following the Thomson scattering signal. To accomplish this the signals from the 11 LA-APD modules are triplicated using 11 zero-degree, 3-way power splitters, available commercially from Mini-

Circuits, Inc. The sensitivity of these power splitters ranges from 10 kHz to 2 GHz. One drawback of this scheme is the loss of “DC” background light from the plasma. This represents a possible source of error, not in the temperature, but in the  $\sqrt{N}$  uncertainty of the number of photons. The temperature is unaffected, since subtracting the average of the two digitized background signals from the digitized TS signal removes this DC background. In addition to the filtering done by the power splitters, each APD module signal cable is also filtered by an isolation transformer, used primarily to prevent internal ground loops. The iso-transformers used are simply integrated circuits (chip #8451-IP), which have a 3 ns rise time.<sup>7</sup>

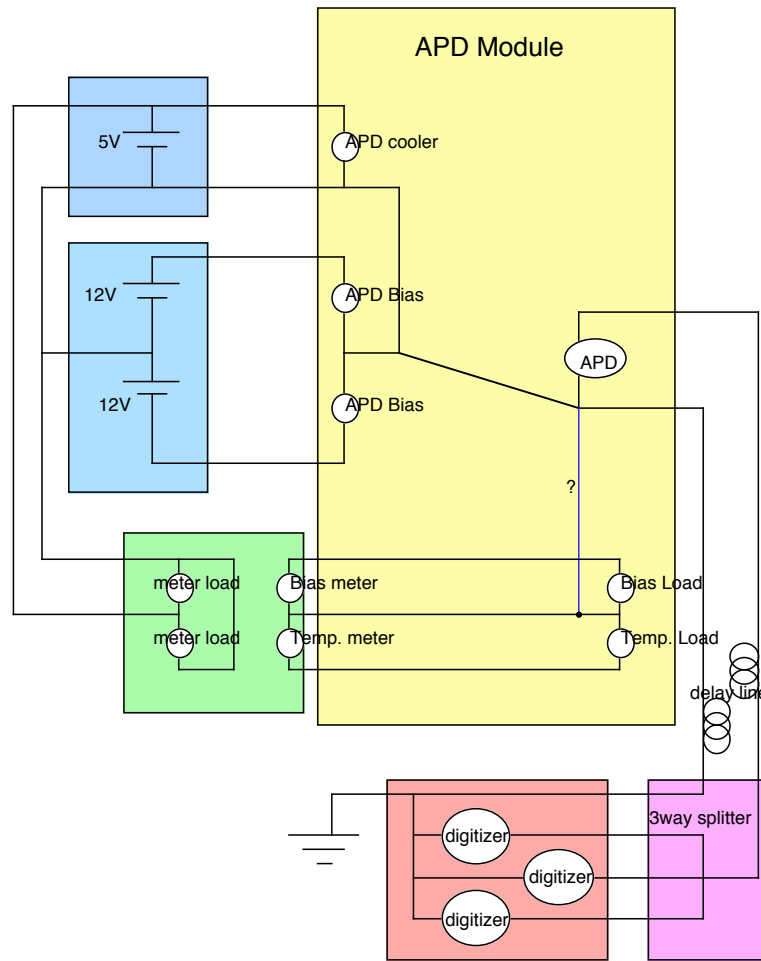


Figure 2.12 Circuit schematic of the LA-APD module system. Eleven modules are connected in parallel in this fashion, though only one is shown.

The LA-APD modules have already been discussed in the previous section. It may be useful, however, to give some information on their power requirements. A schematic is shown in Figure 2.12. The APD detector element itself is thermoelectrically cooled to reduce the inherent “dark current” noise. For this purpose a 5 V, 18 A power supply is used. Each module draws roughly 0.8 A when initially turned on, for a total current of about 9 A. Once the modules have cooled down, the current draw drops to 1/3 of that value. The 2500 V bias on the APD detector is maintained by a dual output, 3 A power supply, +12 V and -12 V. The maximum current drawn from these supplies is small. From the +12 V supply, 2 A are drawn, but only 0.5 A is drawn from the -12 V supply. The power from the supplies is carried over 26 feet of cable to a distribution box, where it is mitered out to the LA-APD modules. The bias and temperature of the individual modules is monitored at the power supplies. The operator simply selects the module of interest by a multi-position switch.

The final electronic element worth mentioning is the Thomson scattering timing box. This circuit is used to control the data acquisition by gating the digitizers. The laser “fast photodiode” pulse is used to trigger this circuit, which then delivers three independently adjustable (in width and delay) gate pulses to the digitizers. This is discussed in more detail in Section 2.4.4.

### **2.3 Alignment**

A detailed procedure for aligning the laser-head itself is outlined in the operator’s manual that accompanies the laser.<sup>8</sup> The Helium-Neon (HeNe) alignment laser should be co-linear with the ruby beam, and will be used throughout the alignment process. The alignment of the two lasers, along with the degree of divergence of the ruby beam, can be checked by comparing ZAP paper burn patterns from the exit of the laser and at a large distance away

(e.g. across the MST control room.) The burn mark diameters should be the same for a well-collimated beam. The divergence of the beam is adjusted via the “beam expanding telescope” located within the laser-head. Also, the HeNe spot should fall directly onto the ruby burn mark at a large distance if the two lasers are co-axial. If this is not the case, the HeNe pointing should be adjusted, which can be accomplished with the associated thumbscrews and a great deal of trial-and-error.

### 2.3.1 Central Laser Chord Alignment

Assuming a co-axial HeNe and well-collimated ruby, the alignment procedure begins by steering the HeNe beam with the “main turning mirror” through the MST tank and onto the beam dump. The beam dump alignment block should be inserted to the depth fixed by the attached spacing clamp. The alignment block is normally held out of the beam path by a similar, but longer, spacing clamp. Adjust the micrometer screws on the turning mirror until the HeNe is visibly striking the dark center of the beam dump alignment block. In this configuration the ruby beam will fall onto the beam dump in the proper location when the alignment block is retracted.

There are a series of 8 light baffles located in the beam line just after the entrance lens. These baffles reduce the amount of stray laser light (due to dust or imperfections on the optical surfaces) that enters the MST, and eventually the detection system. Effectively, they increase the signal-to-noise ratio by decreasing the ambient “pedestal” associated with non-Thomson scattered light that is detected, i.e. light not rejected by the spectrometer, filter, or polarizer. However, if a portion of the main ruby beam strikes any of these baffles, there can be an increase in the amount of pedestal light in the system. While the ruby is Q-switched, this can make an audible metallic “snap,” and is visible as heat damage to the stainless steel baffles. The laser beam should be aligned to pass through the baffles and directly enter the

MST. This can be accomplished by fine adjustments of the micrometer screws on the turning mirror. Take care that the beam still falls on the center of the beam dump alignment block after adjustment. If a larger adjustment is necessary, there are opposing set screws on the forward foot of the laser-head which can be used to bring the laser-head, the turning mirror, the light baffles, and the beam dump into better mutual alignment. Since the alignment of the baffles to the MST and the beam dump is fixed by the construction of the support hardware once the laser cart is in place, all the adjustment must come from the turning mirror and the laser-head. This procedure requires some patience.

### 2.3.2 Alignment of the Fiber Optic Collecting Bundle

Once the ruby beam has been steered through the MST vacuum vessel, the next step is to align the collection optics. This is accomplished through the use of 2-dimensional ( $z$  and  $r$  with respect to the MST minor axis) positioning stages, which are located on each of the 8 (per laser chord) viewing chords. The fiber optic collecting bundle rests in the viewing chord of interest by means of a dove-tailed receiving mount.

The Thomson scattering system alignment probe consists of a stainless steel block that is cut at 45-degrees to serve as a reflecting surface. This block can be inserted into the HeNe/ruby beam at various distance along the laser path to steer the beam through the boxport mounted collections lenses, simulating Thomson scattered rays of light. With the detector power OFF, remove the polarizer and filter from the front of the fiber bundle. Look with the eye through the collection lens of interest to see that the HeNe is indeed being reflected through that lens. Care should be taken, as with all laser applications, to avoid looking directly into the HeNe beam. Peripheral vision should be sufficient to assess whether or not the HeNe is indeed exiting through the collection lens of interest. Place the fiber bundle into the dove-tail mount and observe the location of the HeNe spot on the front

face of the bundle using a small, hand-held, diagnostic mirror. Be careful not to block the beam path with the diagnostic mirror.

Begin by adjusting the “radial” height of the fiber bundle until the HeNe spot achieves its tightest focus. A piece of tissue paper or notebook paper is useful to determine where the focus is best, since the HeNe spot is still visible to the eye on the back side of the paper. Find the tightest focus then lower the fiber bundle using the adjustment knob on the translation stage until the height of the plane of the paper is equal to the height of the plane of the front face of the bundle. Tighten the locking screw. Once this has been achieved, adjust the “z-direction” of the fiber bundle using the other adjustment knob until the HeNe spot falls directly onto the center of the fiber optic column in the face of the fiber bundle. Again, tighten the locking screw. Be careful to “take out the slack” in the adjustment screw by approaching the final resting position from the same direction every time. The spot will be much narrower than the height of the fiber optic column. This is because the HeNe is reflected from a single spot on the alignment probe. During normal plasma shots, Thomson scattered light will come from an extended volume of plasma along the beam path, and hence will fill the height of the fiber optic column. Repeat this process to roughly align each view chord of the central laser chord, i.e. views 1 through 8. Be certain to retract the TS alignment probe when finished.

To attain an even finer alignment of the collection optics, monitor the total number of TS collected photons while taking plasma shots at a fixed density. By moving the “z” translation stage in either direction, and taking 3 to 5 plasma shots at each adjustment, it should be possible to map out a peak in the number of TS collected photons. Set the “z” adjustment to the position where maximum signal was attained, and tighten the locking screw. The system should now be aligned and ready to take data. Repeat for each viewing chord.

### 2.3.3 Edge Laser Chord Alignment

Alignment of the edge laser chord requires first that the central laser chord be properly aligned, including collection optics. Begin by moving the laser beam dump to the edge laser chord, then proceed to steer the beam from the central laser chord through the edge laser chord. This is accomplished via two turning mirrors. The first turning mirror is inserted between the main turning mirror at the exit of the laser-head and the entrance lens to the central laser chord. The mirrored surface should be at 45-degrees to the path of the HeNe/ruby beam, directing the beam onto the second turning mirror which is located just before the entrance lens for the edge laser chord. The relative tilt of these two mirrors will control the vertical location of the HeNe spot on the beam dump alignment block. The HeNe should fall on the darkened center of the inserted alignment block. If it does not, it will be necessary to make further adjustments to the tilt of the two turning mirrors. Since the mirror tilt is held fixed by simple, locking thumb screws, achieving the correct tilt can take some time. It is useful to have a second person to observe the HeNe spot and call out directions while the mirrors are adjusted from below.

Similar to the central laser chord, the edge laser chord contains a series of eight light baffles to reduce the amount of ambient “pedestal” light that is seen by the detection system. Directly striking these baffles with the ruby beam can result in a higher amount of pedestal light. The edge and central laser chords are designed to be parallel to each other. Hence, if the central laser chord is aligned, the edge laser chord should also be fairly well aligned. Because there are slight imperfections in the support structure, it is usually necessary to adjust the alignment of the beam through the baffles and MST, onto the beam dump, using the main turning mirror micrometer screws. Be sure to write down the settings of the micrometer screws before beginning, so that re-aligning the central laser chord will be relatively simple, i.e. re-set the micrometer screws. As with the central laser chord, adjust

the micrometer screws until the HeNe passes through the edge laser chord baffles unobstructed and falls on the dark spot of the beam dump alignment block. It is again useful to write down the micrometer screw settings in the edge laser chord configuration.

With the HeNe/ruby beam traversing the MST and exiting into the beam dump along the edge laser path, it is parallel to the central laser chord, but has been translated by 30 cm towards the collection optics. For the scattering volume to be focused onto the fiber optic collecting bundle, it is necessary to add a “correction lens” at the proper location. For this purpose, a special mount has been constructed which holds the correction lens at the proper height above the collection lens. This mount fits over the bolt-heads, which secure an individual collection lens to the boxport. With the correction lens in place, and because of the slight adjustments to the beam path needed to traverse the edge chord, it is highly likely that the fiber optic collection bundle is no longer aligned with the HeNe/ruby beam. Unfortunately, there is no TS alignment probe on the edge laser chord to utilize during a “rough” alignment. Instead, the operator must rely on the approximate alignment afforded by a well-aligned central laser chord. To more finely align the fiber bundle it is necessary to monitor the total number of Thomson scattering collected photons during plasma shots of constant density. By making 1/2-turn adjustments to the “z” translation stage of each chord, it should be possible to map out a peak in the collected light signal, and hence to determine where proper alignment of the viewing chord is achieved. Note the number of turns required to bring an individual chord into alignment. Repeating the process on other chords should reveal a trend in the number of turns needed to bring chords into alignment. It may be necessary to extrapolate this trend to align the extreme edge-most chords (view chords 9, 10, 15, and 16.) The low density and high variability associated with these chords can make it impossible to find the peak in the TS signal.

The procedure for switching between the central and edge laser chords is then as follows: 1) Move the beam dump. 2) Insert or remove the first turning mirror for the edge or

central chord, respectively. 3) Turn the micrometer screws on the main turning mirror to the appropriate setting. 4) Insert or remove the collection lens' correction lens. And 5) rotate the adjustment knob of the “z” translation stage by the proper number of turns to bring the fiber optic bundle into alignment. Again, it is important to “take out the slack” in the micrometer screws and translation stages when making final adjustments, i.e. always approach the final resting position from the same direction.

## 2.4 Calibration

### 2.4.1 Instrument Transfer Function Measurement

Utilize a light source with a well-defined, narrow spectrum. A HeNe laser works well. Expand the HeNe beam so that it fills the entrance array of the fiber optic collection bundle, after removing the polarizer and cut-glass filter from the face of the fiber-bundle. It is absolutely necessary to reduce the light intensity from the HeNe beam using a calibrated set of neutral density (ND) filters. Excess light can damage the detectors. Rotate the grating on the spectrometer to bring the HeNe line (632.8 nm) onto the center of the second wavelength channel. Start with a high power ND filter, and reduce the filter power until the light level on the detector is on the same order as the number of Thomson scattered photon counts (including background) that are observed during normal operation of the TS laser system with plasma (~100 counts). Monitor the light level by manually triggering the data acquisition system and examining the data. The digitizer is saturated when the number of digitizer counts reaches 496 counts. If this is observed, increase the power of the ND filter. The calibration process is the same for all three gratings with a few caveats. First, the spectrometer dial reading is intended for a 1200 g/mm grating. Wavelength ranges of interest will be at approximately half (or 3/2) the number that is indicated on the

spectrometer dial due to the decreased (or increased) dispersion of the 600- g/mm (or 1800- g/mm) grating. And secondly, the appropriate neutral density power may be different between the 3 gratings since, e.g. the 600-g/mm grating compresses the spectrum though the number of photons/wavelength does not change.

Once the proper neutral density filter power has been established, rotate the grating to bring the HeNe line just off of the sensitive wavelength range of the detectors. Trigger the digitization module to record 100 samples. This can be accomplished by gating the digitizer 32 times at a rate of  $\sim 1$  Hz (to fill up the digitizer buffer with 32 samples) and then triggering the digitizer read out. Repeating this process 3 times will yield 3 stored data “shots” each containing 32 samples of “signal” and “background” for all wavelength channels. Since the HeNe presents a continuous light source, the “signal” and “background” counts should be statistically equivalent on any given wavelength channel. If they are not, there is most likely a problem in the 3-way power splitter for that wavelength channel. Assess and repair before proceeding.

If no problems exist then measure the instrument transfer function by taking  $\sim 100$  ( $=32*3$ ) samples at each wavelength setting, as indicated by the dial on the spectrometer. Rotate the spectrometer grating in 1 nm increments, measuring the light levels on all channels, until the entire wavelength range has been covered, i.e. the HeNe line has traversed channels 1 through 11 and the counts in each channel are roughly the same ambient level. It is important to measure the ambient background for a few nanometers beyond the point at which the HeNe line leaves the last channel. This background should be subtracted off each measurement to give a more accurate representation of the channel locations.

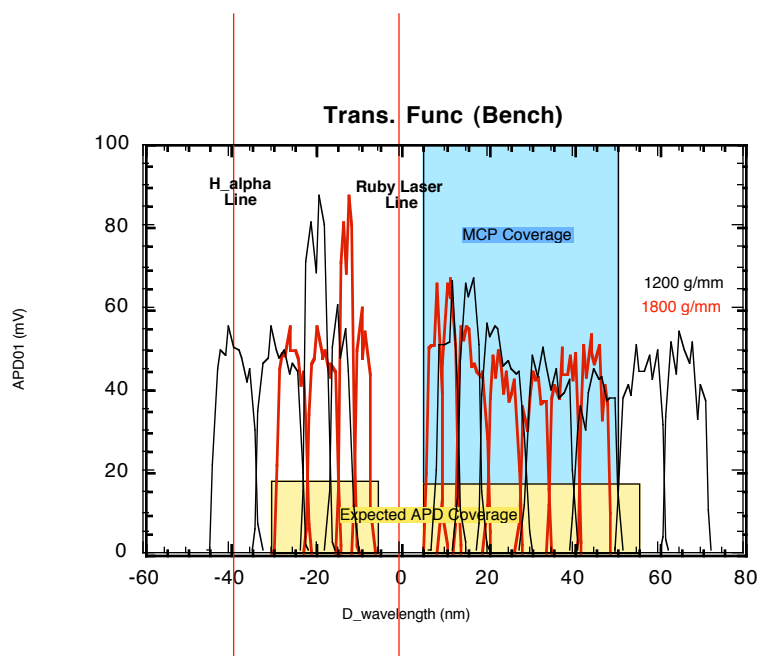


Figure 2.13 Bench measured instrument transfer function for the TS spectrometer with APD modules for both the 1200 g/mm and 1800 g/mm gratings. Also shown is the extent of the region previously covered by the MCP in the 1200 g/mm configuration, as well as the location of the  $H_{\alpha}$  Balmer line.

Because the HeNe line (632.8 nm) is 60 nm away from the ruby line (694.3 nm), there may be some concern over the grating dispersion at these two different wavelengths. Practically, it is correct to simply subtract for the wavelength difference when calculating the channel widths and centers from the measured instrument transfer function, and it is not necessary to correct for the difference in dispersion. The correction is small in comparison to systematic errors in reading the spectrometer wavelength grating setting dial. Spectral dispersion can also be neglected when using the 600-g/mm and 1800-g/mm gratings.

#### 2.4.2 Wavelength Channel Relative Sensitivity Calibration

This procedure is used to measure the relative wavelength channel normalization factors that are necessary to accurately calculate  $T_e$  from measured photon spectra. Begin

with a well-calibrated blackbody source of known spectral irradiance. Direct the light from this source so that it falls uniformly on the entrance face of the fiber-bundle with the polarizer and cut-glass filter in place. It will be necessary to reduce the intensity of the light with a set of well-calibrated neutral density filters. Monitor the light that is falling on each channel as outlined in Section 2.4.1 by triggering the data acquisition system. Reduce the light intensity from the blackbody source using ND filters until the number of observed digitizer counts in each channel is roughly the same as that observed during normal operation of the TS system with plasma. Once this is achieved, take 100 samples of the measured blackbody spectrum to reduce statistical uncertainty and better characterize the measurement.

By comparing the light levels measured in each channel with the light level that is predicted from the calibration sheets of the blackbody source, the relative channel normalization factors can be determined.

### 2.4.3 Raman Scattering Absolute Density Calibration

Thomson scattering systems can be used to measure the local electron density if properly calibrated, since the intensity of the measured light signal is directly related to the density of scattering centers. The outcome of this procedure is essentially a multiplicative factor which relates the measured area under the Thomson scattered spectrum to the electron density, for the viewing chord in question. In Section 2.4.2 the procedure for calibrating the wavelength channels relative to each other is outlined. The area of the measured spectra can be calibrated to a known density of scattering centers by filling the MST tank to a given pressure of Nitrogen gas.

Begin by backfilling the MST with Nitrogen gas, slowly raising the pressure in the tank to about 5 Torr. Monitor the pressure using a well calibrated, accurate gauge such as those made by Barritron. The pressure should be raised slowly (over a few hours) to avoid

stirring up hydrocarbon dust that litters the inside of the MST. Scattering from this dust can lead to erroneous measurements in the density calibration.<sup>9</sup> Once at pressure, allow any dust to settle by letting the MST stand over night. When a satisfactory amount of time has elapsed, operate the Thomson scattering system as during normal plasma discharges, measuring 10 shots for each viewing chord to generate a good statistical ensemble.

#### 2.4.4 Timing Sequence Check

The timing of events in the MST Thomson scattering system is entirely controlled by the measurement of the laser fast-photodiode output. This photodiode detects a small fraction of the photons that are emitted by the oscillator ruby rod during lasing. From that point onward, the majority of the timing is set by the time-of-flight physical separation of objects and by lengths of delay line. What is important is that the signal from the Thomson scattered photons arrives at the digitizer within the window of time that the digitizer is gated on to receive data. A properly timed sequence of events is shown schematically in Figure 2.14.

The “laser fire” trigger can be adjusted to occur nearly anywhere within the plasma discharge. The “laser fire” signal may be given manually, or via the CAMAC based, MST timing circuitry. A mechanical shutter is used to block the intense burst of plasma start-up light at the beginning of the discharge, which could damage the detectors. The first 3 ms after the plasma “breaks down” should be blocked. Moreover, the shutter has a finite opening time of 3 ms. Hence, TS measurements should not be attempted in the first 6 ms of the plasma lifetime. If the laser is being manually fired, e.g. without plasma, then the shutter can be set open by connecting a 9 V battery across the input gate.

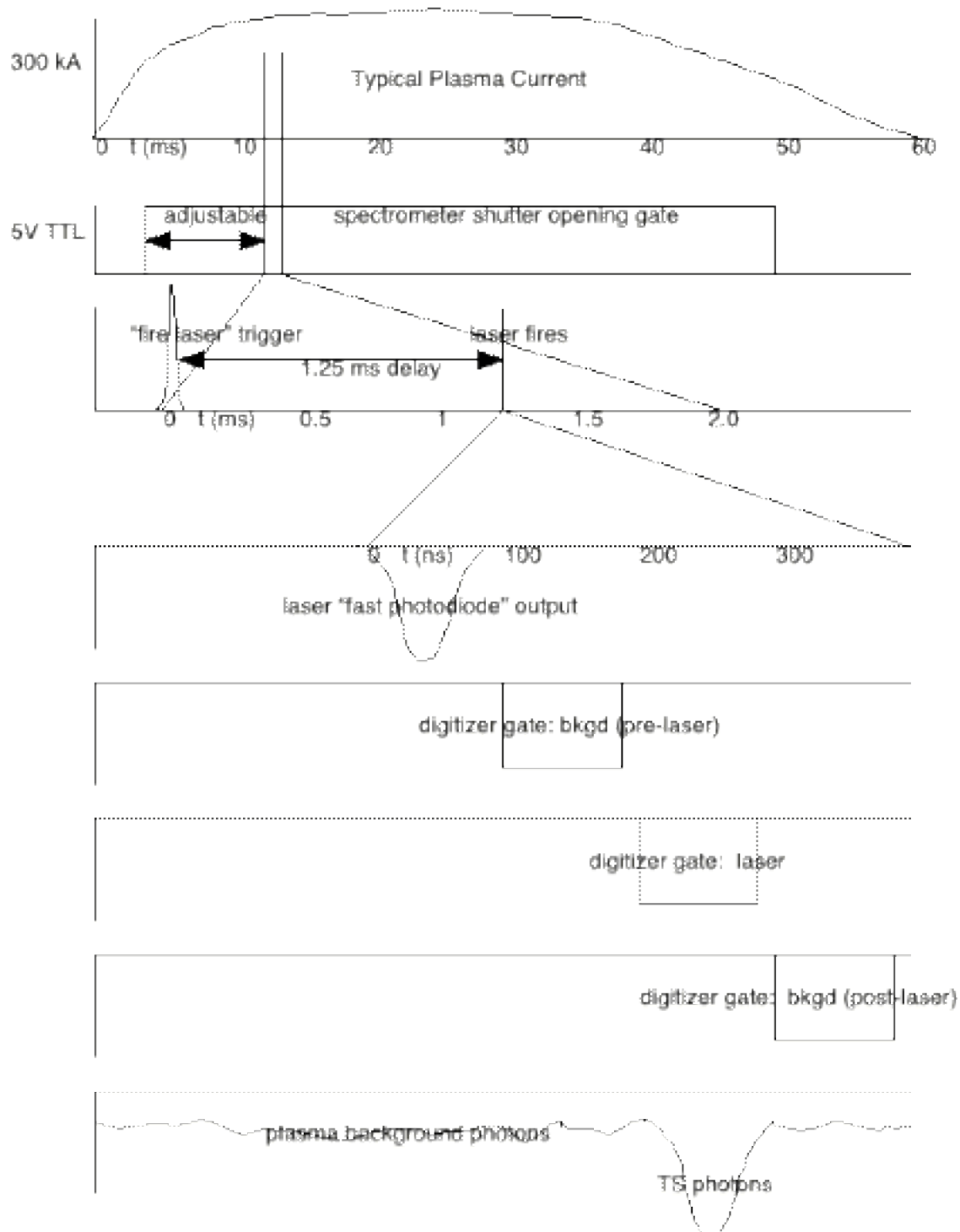


Figure 2.14 Timing diagram of the ruby laser TS system.

After “laser fire” is given to the laser, roughly 1.25 ms are required for the flash lamps to fire and pump the ruby rods. This is the source of the built in delay shown in Figure 2.14. Once the laser actually fires, delay lines set the majority of the timing. Besides adjusting the lengths of these cables, some (fine) adjustment is available in the width and delay of the three digitizer gate pulses. To this end, there are 6 adjustable potentiometers in the front of the Thomson scattering timing box. Each digitizer gate is independently adjustable in both delay and width. Begin by setting the three widths to 100 ns. This gives an adequate amount of flexibility for any jitter in the initial timing of the fast-photodiode triggering. Then adjust the delays of the digitizer gates such that they are non-overlapping, and that one of them wholly contains the Thomson scattered signal. Once these delays are set, further adjustment should not be necessary.

Since the signal from the laser energy monitor should also be digitized, it is necessary to check that it arrives within the window that the Thomson scattered photons are digitized. Adjust by adding or removing delay line, if necessary.

## **2.5 Thomson Scattering Data Analysis**

To streamline the analysis of Thomson scattering data a new processing code has been written. The old code was FORTRAN based and fragmented, but relatively robust. The precise method of fitting TS spectra used what is known as Newton-Raphson decomposition of the function given in Equation 61.<sup>10</sup> The new code is written in IDL, and has the un-ceremonial name TS\_CODE.PRO. The main improvements to this code are the addition of multiple fitting techniques, and increased versatility in spectrum sampling. Besides the Newton-Raphson method, there is also a Monte-Carlo based,  $\chi^2$  minimization using the AMOEBA function of IDL. For simplicity, this method is referred to as AMC (AMOEBA-Monte Carlo). The AMC method is extremely versatile, allowing an arbitrary

function as input. In this way, it is trivial to fit and compare the TS data to many different functional forms; e.g. a simple Maxwellian, a drifted Maxwellian, a mildly relativistic correction to a simple Maxwellian, and/or a fully relativistic correction to a simple Maxwellian. All of these fitting options, including the “traditional” Newton-Raphson decomposition, are available in the latest version of TS\_CODE.PRO.

Besides accommodating fits to other functional forms, the new processing code has greater versatility in other ways as well. When the 5-channel micro-channel plate (MCP) detector system was replaced by the 11-channel LA-APD detector system, the code was likewise upgraded to be able to process (at a keystroke) data of either 5 or 11 wavelength channels, on both the blue- and red-shifted sides of the laser centerline. The code was later updated to process an arbitrary number of wavelength channels (11 or less), allowing data channels from malfunctioning APD’s to be toggled-off. Moreover, the data storage system itself was upgraded from MDS to MDS-plus at the end of 2000. At a keystroke, the new TS code can process data from either storage system.

These aspects, though improving ease-of-use, are superficial when accurately measuring the electron temperature of MST plasmas. One addition to the code can be used to estimate the magnitude of systematic errors from mis-calibration, if a large dataset of discharges is available. This approach follows the development of Fajemirokun,<sup>11</sup> but the basic argument is presented here. Extracting the electron temperature (for a given functional form) from the raw spectral data requires an accurate measurement of the spectrometer/detector transfer-function. Essentially, the locations (in wavelength), widths, and sensitivities of each wavelength channel must be known. These calibration factors are measured as discussed above in Section 2.4. If the channel calibration factor of channel 3, for example, is mis-measured this introduces a systematic error in the calculated temperature. Suppose that channel 3 is “higher” than the fit curve in all discharges, yielding a somewhat larger fit temperature. By examining a large dataset of discharges, the code determines,

statistically, how much the calibration factor for channel 3 would need to be reduced to bring it into agreement with the fit temperatures. These multiplicative factors (which are denoted as “x-factors” in the code) can then be applied to any discharge using the nominally flawed calibration factors to presumably improve the accuracy of the fit temperature. Note that this technique is only valid if the dataset used to find the x-factors is much larger than the dataset that is used, ultimately, to calculate the fit temperature. For a more in-depth discussion of this process, the reader is again encouraged to see the references.<sup>11,12,13</sup> It is worth noting that the data presented in this thesis was processed with unity x-factors, i.e. no correction to the calibration data was made, i.e. the TS system is believed to have been well calibrated.

### 2.5.1 Error Bars

The number of photons detected from Thomson scattering of light off electrons obeys Poisson statistics, meaning that the error in the measurement of the number of photons is the square root of the number of measured photons.<sup>14,15</sup> In other words, if  $N$  is the number of TS photons detected, then  $\sqrt{N}$  is the error in that measurement. Since the signal increases faster than its error, the signal-to-noise ratio is improved by ensembling TS spectra. This will be discussed in more detail later. For the current discussion, it is sufficient to understand that finding the temperature from Thomson scattering means finding the best fit (with a fit error) to 11 wavelength channel measurements, each of which has its own associated error. The area under the TS spectrum is proportional to the electron density, and the previous statement applies to finding the area and its error as well. Since the TS system is not relied on to estimate the electron density, the area is of lesser concern. For simplicity only the electron temperature is discussed, though these statements are equally true for finding the area under the spectrum.

The AMC method of finding  $T_e \pm \Delta T_e$  is the most straightforward. An AMOEBA minimization finds the value of  $T_e$  that best fits the 11 channel  $N(\lambda)$  data. On the next iteration of a Monte-Carlo cycle, a random number,  $+1 \geq f_{\text{rand}} \geq -1$ , is calculated for each wavelength channel. The raw data is then modified,

$$N(\lambda) \rightarrow N(\lambda) + f_{\text{rand}}(\lambda) \Delta N(\lambda), \quad (6)$$

and a new  $T_e$  is calculated. In this manner, through 1000 iterations, the measured data is varied randomly within its error bar, and 1000  $T_e$ 's are fit. The reported value of  $T_e$  is then the average of the 1000 calculated fits, and  $\Delta T_e$  is the standard deviation of the 1000 calculated fits. The AMOEBA minimization routine accepts an arbitrary function as input, hence the versatility of using this method to fit given TS data to various functional forms.

Historically, Newton-Raphson decomposition (NR) has been used to fit the TS data to a simple Maxwellian distribution, yielding  $T_e$ .<sup>10</sup> To begin to find  $\Delta T_e$  a 5-point numerical derivative is calculated, estimating the variation in fit  $T_e$  with the variation of the  $N(\lambda)$  data. The square of this term is then multiplied by the square of the error in  $N(\lambda)$ , and summed over wavelength channels, resulting in the final  $\Delta T_e$ :

$$\Delta T_e = \sqrt{\sum_{\lambda} \Delta N(\lambda)^2 \left( \frac{\partial T_e}{\partial N(\lambda)} \right)^2}. \quad (7)$$

The exact manner that the 5-point numerical derivative is calculated depends inherently on the function (a simple Maxwellian) that is being fit to the data. For this reason, the NR method of finding  $T_e$  can only fit to a single functional form. The NR method is thus less versatile than the AMC method, but because the NR method is computationally quick and was the method used for many years, it is maintained in the new TS processing code.

Thomson scattering measurements suffer from a low signal-to-noise ratio (SNR). By ensembling the measured spectra from multiple discharges, the SNR can be improved. This is true because the number of scattered photons,  $N$ , increases faster than  $\sigma_N$ , which goes as  $\sqrt{N}$  since TS obeys Poisson statistics as discussed above. A simple calculation shows why this is true. Consider 50 measurements of  $N$ , which all yield  $N=100$ . Then for each measurement  $\sigma_N = \sqrt{N} = 10$ . Hence, in any single measurement  $\sigma_N/N = 10/100 = 10\%$ . Summing over 50 measurements,  $N=5000$ , and  $\sigma_N = \sqrt{N} \sim 70.7$ . Now  $\sigma_N/N \sim 70/5000 = 1.4\%$ . This, of course, gives the same SNR if 50 shots are averaged over, since  $\bar{N} = (\sum N)/50 = 5000/50 = 100$  and  $\sigma_{\bar{N}} = (\sqrt{\sum N})/50 \approx 70.7/50 \approx 1.4$ , yielding  $\sigma_{\bar{N}}/\bar{N} \sim 1.4\%$ .

## 2.6 Summary

This chapter has discussed in detail the mechanical setup and hardware utilized in the MST ruby-laser Thomson scattering system. It has discussed the alignment and calibration of this system. And it has briefly discussed the analysis of the data gathered by this system. It is now time to turn to the data itself and its role in the plasma physics of the MST. Before doing so, it is worth noting that though the ruby laser system has performed routinely on the MST, its single-point in space and time hindrances are beginning to limit the types of phenomena that can be studied. To address this limitation, a new multi-point, 100 Hz sampling rate, NdYg laser system is being implemented on the MST for Thomson scattering measurements. This new system will in many ways render the old ruby-system obsolete. In the meantime the ruby TS system remains the only way to make non-invasive measurements of  $T_e$  in the MST.

## References

1. D.J. Den Hartog, *An Energy Confinement Study of the MST Reversed Field Pinch Using a Thomson Scattering Diagnostic*, Ph.D. Thesis, University of Wisconsin-Madison (1989).
2. I.H. Hutchinson, *Principles of Plasma Diagnostics*, Cambridge Press, New York, 1987.
3. J. Sheffield, *Plasma Scattering of Electromagnetic Radiation*, Academic Press, New York, 1975.
4. M. Cekic, D.J. Den Hartog, G. Fiksel, S.A. Hokin, D.J. Holly, S.C. Prager and C. Watts, Poster presented from the *Bulletin of the American Physical Society*, Seattle (1992).
5. M.R. Stoneking, D.J. Den Hartog, M. Cekic and T. Biewer, "Proposal for Upgrading the MST Thomson Scattering Diagnostic," PLP Report 1181, University of Wisconsin-Madison, (1996).
6. D.J. Den Hartog and M. Cekic, *Meas. Sci. Technol.* **5**, 1115-1123 (1994).
7. Designed and built by D. Holly.
8. "Operator's Manual: Plasma Diagnostic Laser System (Model PDS 1)", J.K. Lasers Limited.
9. D.J. Den Hartog, Private communication.
10. D.J. Den Hartog and D.E. Ruppert, "Photon Counting Spectroscopy as Done with a Thomson Scattering Diagnostic," MST Group internal report, University of Wisconsin-Madison, (1993).
11. H. Fajemirokun, C. Gowers, P. Nielsen, H. Salzmman and K. Hirsch, *Rev. Sci. Instrum.*, **61** (10), 2849-2851 (1990).
12. R. Pasqualotto, A. Sardella, A. Intravaia and L. Marrelli, *Rev. Sci. Instrum.*, **70** (2), 1416-1420 (1999).
13. M.N.A. Beurskens, C.J. Barth, C.C. Chu and N.J. Lopes Cardozo, *Rev. Sci. Instrum.*, **70** (4), 1999-2011 (1999).

14. M.R. Stoneking and D.J. Den Hartog, *Rev. Sci. Instrum.* **68** (1), 914-917 (1997).
15. M.R. Stoneking and D.J. Den Hartog, "Maximum-Likelihood Fitting of Data Dominated by Poisson Statistical Uncertainties," MST Group internal report, University of Wisconsin-Madison (1996).



He dropped down the hills on his bicycle. . . . His bicycle seemed to fall beneath him, and he loved it.

--D.H. Lawrence, *Sons and Lovers*

## **Measurements through the Sawtooth Cycle in Standard Plasmas**

This chapter presents measurements of the behavior of basic plasma parameters over the sawtooth cycle in “Standard” MST plasma discharges. Direct profile measurements of time-evolving fundamental quantities, such as  $T_e$ ,  $n_e$ , and  $T_i$  were made in similar plasma discharges for the first time. These profiles, combined with Faraday rotation and on-axis MSE measurements, were then used to reconstruct the time evolving current density and magnetic field profiles over a sawtooth cycle. These data provide a self-consistent base, upon which to study the inferred transport mechanisms of particles and energy, throughout the sawtooth cycle. Additionally, calculations of the radial electric field are compared for the first time to measurements from the heavy-ion beam probe (HIBP) diagnostic, showing good agreement.

### **3.1 Sawteeth in MST Standard Discharges**

Sawtooth events are observed in most MST plasma discharge conditions, generating a periodic, sudden increase in the toroidal magnetic flux. These sudden increases, as seen in Figure 3.1, are phenomenologically referred to as “sawteeth,” based on the appearance they give to time traces of many signature plasma quantities. That is to say, a typical sawtooth

crash has a rapidly rising leading edge, followed by a slower decay to some equilibrium. Sawteeth were first observed in RFP plasmas on the ZT-40M experiment.<sup>1,2,3</sup> The time between MST sawteeth can vary considerably with basic plasma parameters, sometimes disappearing altogether. Even though the actual crash of the sawtooth is on a plasma magneto-hydrodynamic (MHD) timescale (10's of  $\mu$ s), the comparatively longer timescale of the sawtooth cycle (6 ms) represents slow changes in the equilibrium plasma. In this sense, the sawtooth cycle is an important, but slowly changing aspect of the plasma equilibrium.

The character of sawteeth in the MST can vary dramatically. The MST can be operated in a variety of modes, from an ultra-low  $q$  (safety factor) device in which the toroidal field does not reverse at the edge, to a deeply reversed RFP, by changing the combination of plasma current, plasma density, and toroidal field. In Chapter 6 this thesis will attempt to address some of the differences in confinement between operating modes of the MST, but Table 3.1 contains a brief list. The "Standard" MST plasma discharge has a field reversal parameter,  $F=B_T(a)/\langle B_T \rangle$ , which is shallow enough to avoid the spontaneous transition to the so-called "enhanced confinement" (EC) mode.<sup>4,5,37</sup> This transition threshold varies somewhat with plasma current. Experiments that have similar plasma current and number density are compared, approximately 380 kA and  $1.1 \times 10^{13}$  particles/cm<sup>3</sup>. At this current the MST can experience EC periods when  $F < -0.25$ , particularly at lower densities.<sup>6</sup> At shallow reversal parameter ( $F \sim 0$ ), the resonant surface for  $m=0$  modes begins to be excluded from the plasma, representing another change in the character of the sawteeth. Hence "Standard" RFP discharges occur in the MST for  $-0.25 < F < 0$  at this plasma current and density. The conditions presented here as the "Standard" MST plasma are:  $I_p \sim 380$  kA,  $n_e \sim 1.1 \times 10^{13}$  cm<sup>-3</sup>, and  $F \sim -0.22$ . The working gas for these experiments is deuterium.

Operating Mode	F	T <sub>e</sub>
PPCD	-1.0	800 eV
Enhanced Confinement	-0.3	???
“Standard”	-0.22	300 eV
Non-Reversed	0	350 eV
Ultra-Low q	+0.03	200 eV

Table 3.1 Comparison of different operating modes of the MST.

Characteristics of a “Standard” MST discharge are shown in Figure 3.1, including the presence of sawteeth. The sawtooth crash events are most readily seen in the third time trace, which is a measure of the voltage across the toroidal gap of the MST. Sudden increases in toroidal magnetic flux appear as “spikes” in the toroidal gap voltage. The sawteeth can also be seen in global plasma parameters, such as the top trace, which is the plasma current, the second trace, which is the line-averaged central electron density (from the CO<sub>2</sub> interferometer), and in the fourth trace, which is the field reversal parameter. As can be seen here, the plasma current ramps up to ~380 kA in roughly 10 ms, while in the same period of time the line-averaged density becomes constant at  $\sim 1 \times 10^{13} \text{ cm}^{-3}$ . The current and density are sustained for (roughly) an additional 25 ms during the plasma current “flattop” phase. Following the flattop, the plasma current ramps down as the stored charge is drawn down on the capacitor banks. Typical MST Standard discharges ramp-up, flattop, and ramp-down in a total of 60 to 70 ms. It should be noted that the sawtooth period in this discharge is roughly 5 to 6 ms.

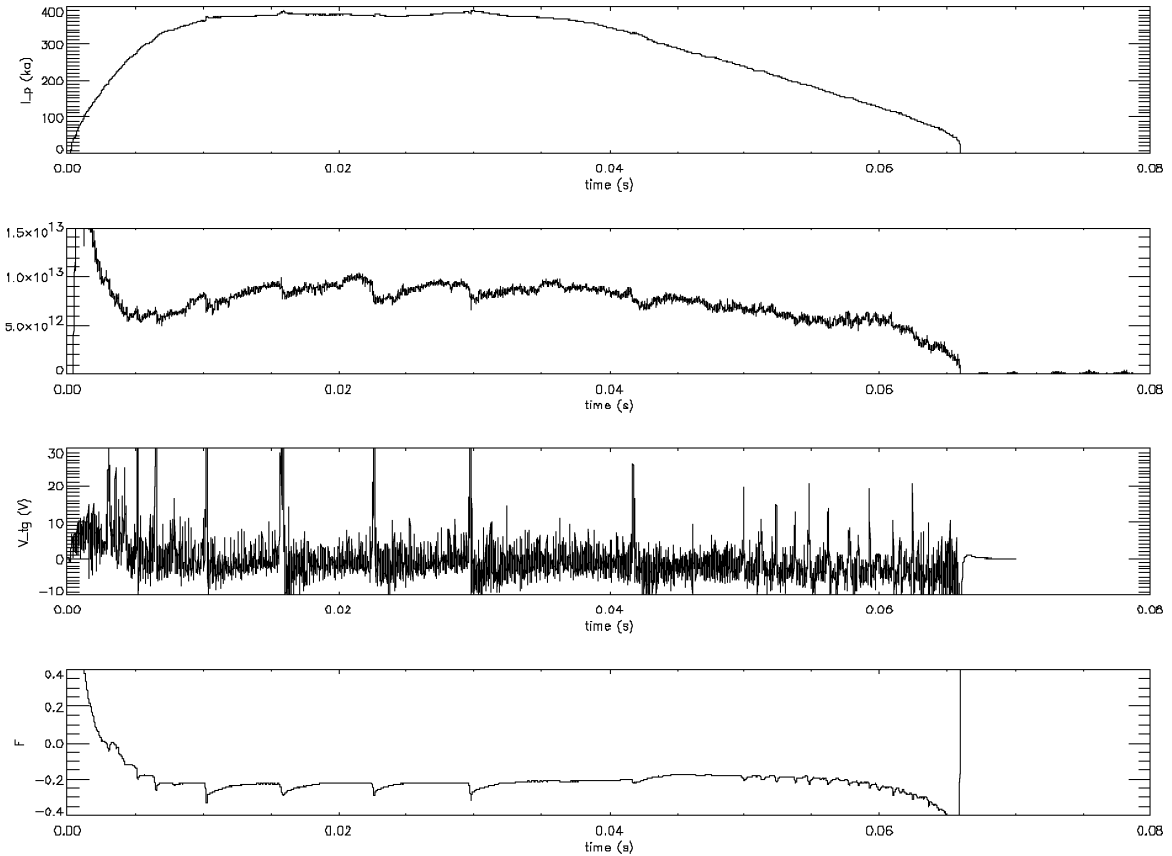


Figure 3.1 Shot 69 from November 13<sup>th</sup>, 2000 showing the presence of sawteeth in a Standard MST plasma.

Profile evolution has been measured by averaging over many similar discharges through a process called ensemble averaging. From the time trace of the toroidal gap voltage it is clear that there is a large amount of MHD activity, besides the sawteeth, as evidenced by the between-sawteeth level of fluctuations. In this thesis, changes in the plasma equilibrium over the sawtooth cycle are of primary interest. By averaging the basic plasma signals over many similar discharges, the background “noise” associated with high frequency MHD fluctuation activity can be reduced. The slowly varying equilibrium changes can be measured by using the time of the crash as a reference ( $t = 0$ ) time, and then averaging the different discharges together. This process is referred to as “sawtooth ensembling.” Whereas ensembling over many discharges is useful for revealing the equilibrium changes

associated with sawteeth, the primary reason for ensembling is one of necessity. The MST ruby laser Thomson scattering system measures the electron temperature at a single point in time and space during each plasma discharge. Hence, to build up a time evolving (on sawtooth period timescale)  $T_e$  profile for a given discharge condition requires hundreds of plasma discharges. In this experiment, the Thomson scattering laser is fired at 15 ms into the plasma discharge. This is during the flattop phase, but early in the discharge. The natural variation in the time that sawteeth occur enables the electron temperature to be measured throughout the sawtooth cycle. The time  $t=0$  is set in each discharge by selecting the peak of the toroidal-gap voltage spike:<sup>7</sup>

To conduct an ensemble over many sawtooth cycles we first identify the time in the cycle with which we may align the zero of the ensemble window time axis. For this purpose we identify the “sawtooth crash time”,  $t_c$ , defined as the point in the sawtooth cycle at which toroidal flux is generated most rapidly. We locate this point from the derivative of  $B_\parallel$  which appears as a voltage across the toroidal gap of the MST ( $V_{tg}$ ). An automated sawtooth selection code scans  $V_{tg}$  for spikes above a preset threshold and then locates those spikes more precisely through a parabolic fit to their local maxima. The extremely sharp nature of these spikes allows the identification of  $t_c$  to within a few  $\mu$ s.

The effect of ensembling discharges with respect to the sawtooth crash time is shown in Figure 3.2, which contains the same signals as Figure 3.1. The spike in the toroidal gap voltage is now clearly evident, as well as the effect on the field reversal parameter. The between-sawtooth MHD activity, as seen on the  $V_{Tg}$  trace, has averaged to zero. This analysis also shows that the plasma current and electron density (as measured by the  $CO_2$  interferometer) are slightly increasing. A possible explanation for this is that the data is taken soon after ramp-up and early in the flattop phase, i.e. within  $\pm 3$  ms of 15 ms into the discharge. This 6 ms window represents the entire sawtooth cycle in a 380 kA Standard

MST discharge. This window is divided up into 12 time slices. The reticule at the bottom of Figure 3.2 indicates the center of each bin. High time resolution signals, such as magnetic pickup coil data or the data from the combination FIR interferometer/polarimeter,<sup>8</sup> are ensembled to 0.1 ms bins. Raw data from the Thomson scattering system is ensembled to 0.5 ms bins. By choosing the bins in this way, the fast dynamics of the sawtooth crash itself ( $t=0$ ) are avoided. Right at the crash the plasma is probably not in thermodynamic equilibrium, hence the futility of attempting equilibrium calculations at that time. The following analysis is centered on these 12 time slices during the sawtooth cycle.

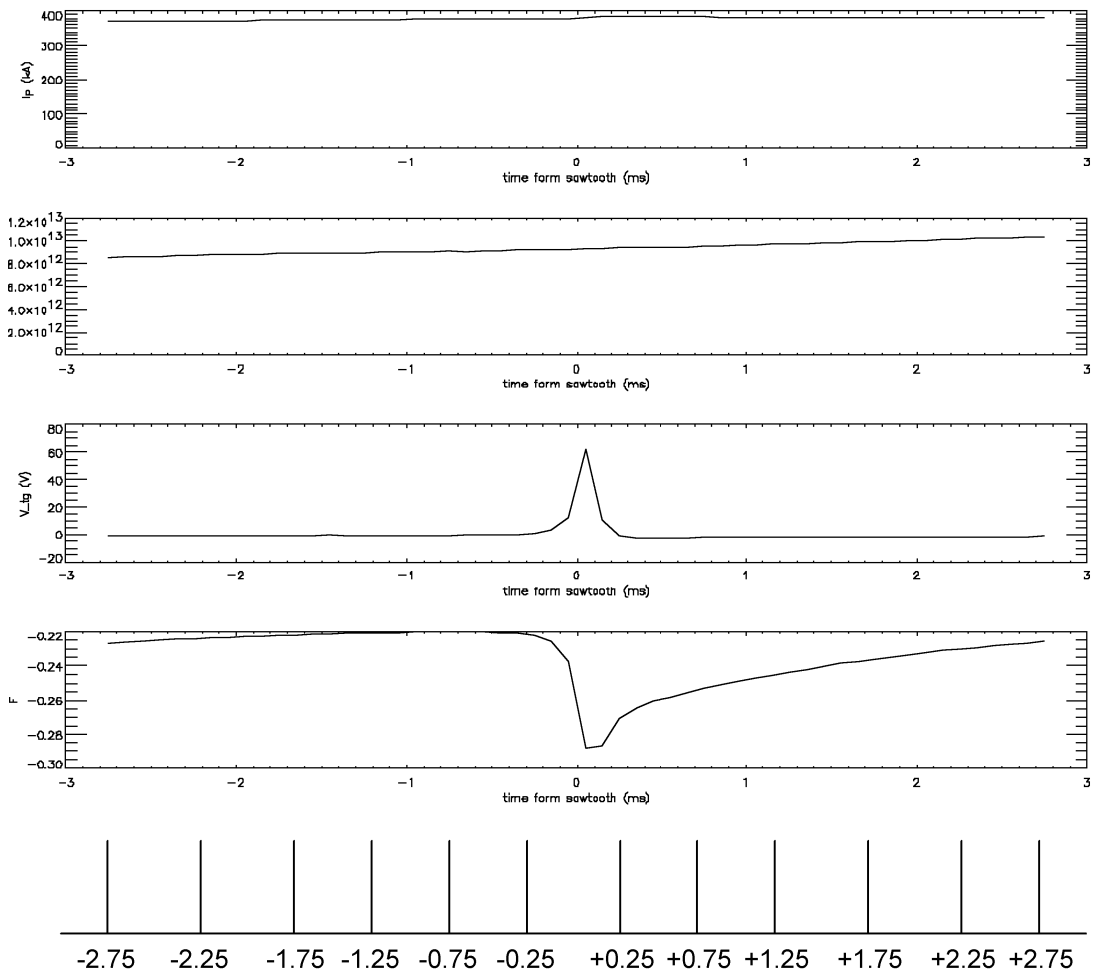


Figure 3.2 400 shot ensemble with respect to sawtooth crashes in “Standard” MST plasmas. The scale at the bottom shows the center locations of 0.5 ms time bins that are used in the following analysis.

### 3.2 The MSTFit Equilibrium Reconstruction Code

MSTFit is a toroidal geometry, equilibrium reconstruction and transport analysis code. The code has been discussed in detail elsewhere, but since it features prominently in this analysis, a short summary is given here.<sup>9</sup> MSTFit iteratively solves the Grad-Shafranov equation in the geometry of the MST reversed field pinch for the equilibrium electromagnetic fields. One aspect of the code is that measured MST data can be used to constrain the equilibrium reconstruction. The pressure profile, plasma current, and toroidal flux ( $F$  and  $\Psi$ ) are taken as input data to which the current profile is fit. The equilibrium can be further constrained by on-axis measurement of the magnetic field from the motional Stark effect (MSE) diagnostic and from profile measurements of Faraday rotation induced in the FIR polarimeter signals. To be consistent, flux surface geometry is used in the output of the reconstruction. This serves to provide a set of common reference points since the Shafranov-shift of the core-most flux surfaces can be as much as 6 cm, i.e. 10% compared to the minor radius. With the exception of the particle source term, all quantities are assumed to be symmetric poloidally along the flux surface. There appears to be a strong source of particles from the outboard midplane, resulting in a non-symmetric flux-surface profile for this quantity. All quantities are, however, assumed to be symmetric toroidally.

The transport analysis package associated with MSTFit utilizes the equilibrium fields, and particularly the current density profile. Primarily, it serves as a location to calculate a plethora of plasma quantities, based on the data that went into MSTFit. The electron temperature profile measured from Thomson scattering is combined with the electron density profile from FIR interferometry to get the pressure profile. A  $D_{\square}$  array (measuring deuterium Balmer line radiation), which is collinear with the FIR, can be used to measure the particle source rate. Majority ion temperature measurements from Rutherford scattering give an

indication of how thermal energy is distributed between the electrons and ions. This can be compared with impurity ion temperature measurements from charge exchange recombination spectrometry (CHERS) and/or ion Doppler spectroscopy (IDS). The IDS additionally gives information on the flow speeds of impurity ions, which when combined with the MSTFit calculated equilibrium magnetic fields yield a measurement of the electric field, as per the ion momentum balance equation. This can be confirmed with direct measurements of the plasma potential from the heavy-ion beam probe (HIBP) diagnostic. An emerging, but important element in the analysis is the ability to constrain the  $Z_{\text{eff}}$  profile from collinear measurements of NIR bremsstrahlung and  $D_{\alpha}$  emission. All of these measurements are brought together consistently within MSTFit. Some of these topics will be raised again later in the thesis.

### 3.3 Temperature Profile Evolution

#### 3.3.1 Electron Temperature

Electron temperature measurements are made on the MST with a ruby laser Thomson scattering (TS) system, as discussed in Chapter 2. This is a single point in time, single point in space diagnostic. Because of poor signal-to-noise statistics, the raw TS spectra are often added together (after the appropriate background subtraction), before a temperature is fit to the distribution. Hundreds of plasma discharges are necessary to build up enough data to accurately measure time resolved electron temperature profiles. As such, these profiles represent an average equilibrium at each time step. The on-axis evolution of the electron temperature has previously been studied,<sup>10</sup> but these are the first-ever measurements of time evolved temperature profiles in the MST, “Standard” or otherwise.

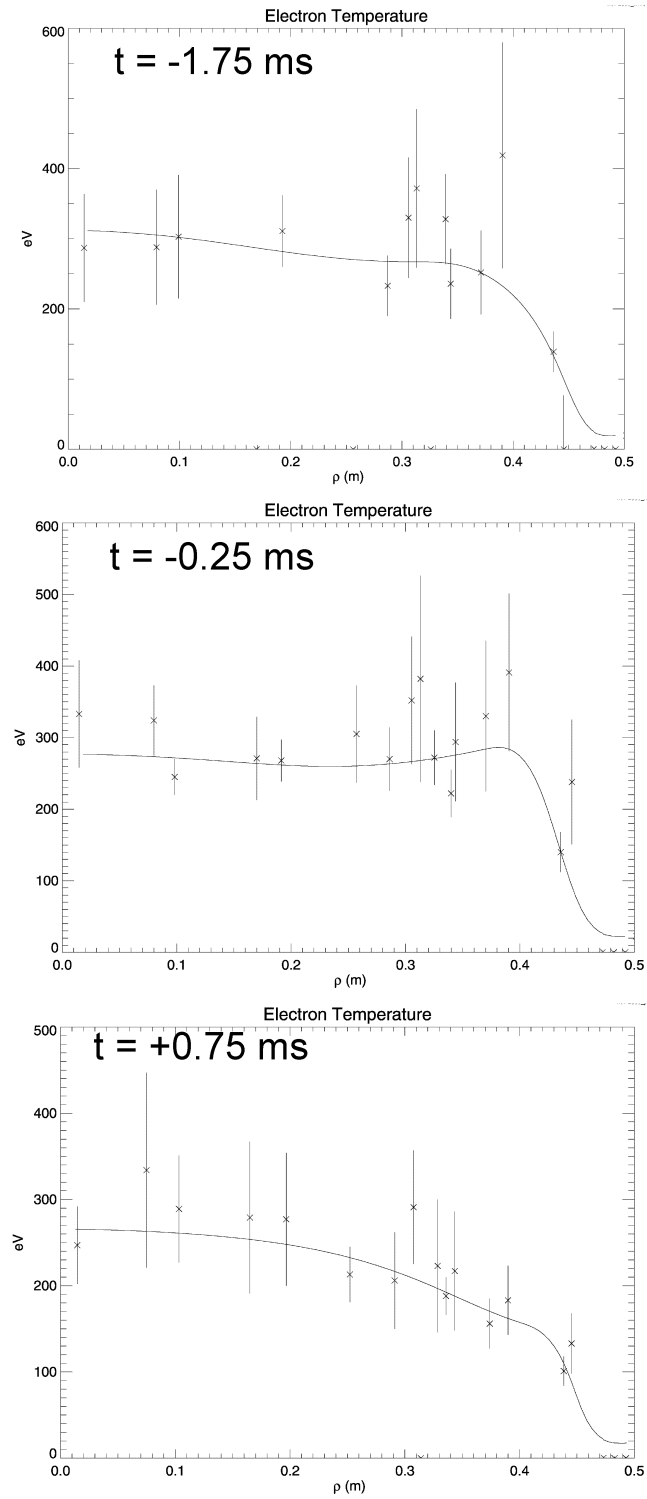


Figure 3.3 Comparison of splines to the Thomson scattering measured electron temperature profile at three time slices.

Using MSTFit splines to the Thomson data represents a further averaging of the actual temperature profile. Figure 3.3 shows how the spline fits compare to the raw TS data. At some radii the data is significantly above or below the fit curve. This may be the result of time variation of the electron temperature. At a given radius, in a given shot, away from the sawtooth crashes, the electron temperature does fluctuate, as suggested by the ratio of two soft x-ray filter chords, shown for a sample shot in Figure 3.4. Theoretically the ratio of soft x-ray signals from two filters of differing thickness can give an estimation of the electron temperature time evolution in a single shot.<sup>11</sup> The data shown below in Figure 3.5 is ensembled over many shots. Hence, high frequency fluctuations, like those in the electron density, should average out.

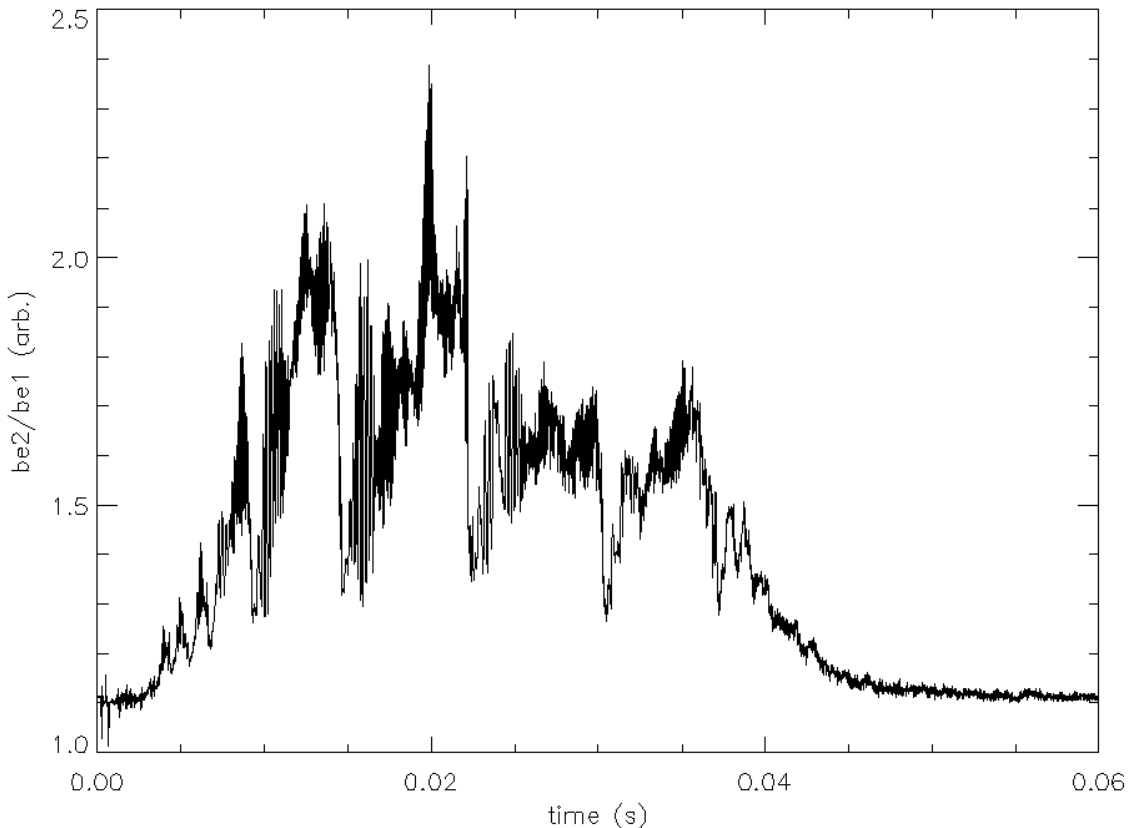


Figure 3.4 The ratio of two thin-filter (Beryllium) soft x-ray signals gives an indicaton of the level of temperataure fluctuations in a Standard shot (Shot 17, 30-Mar-2001).

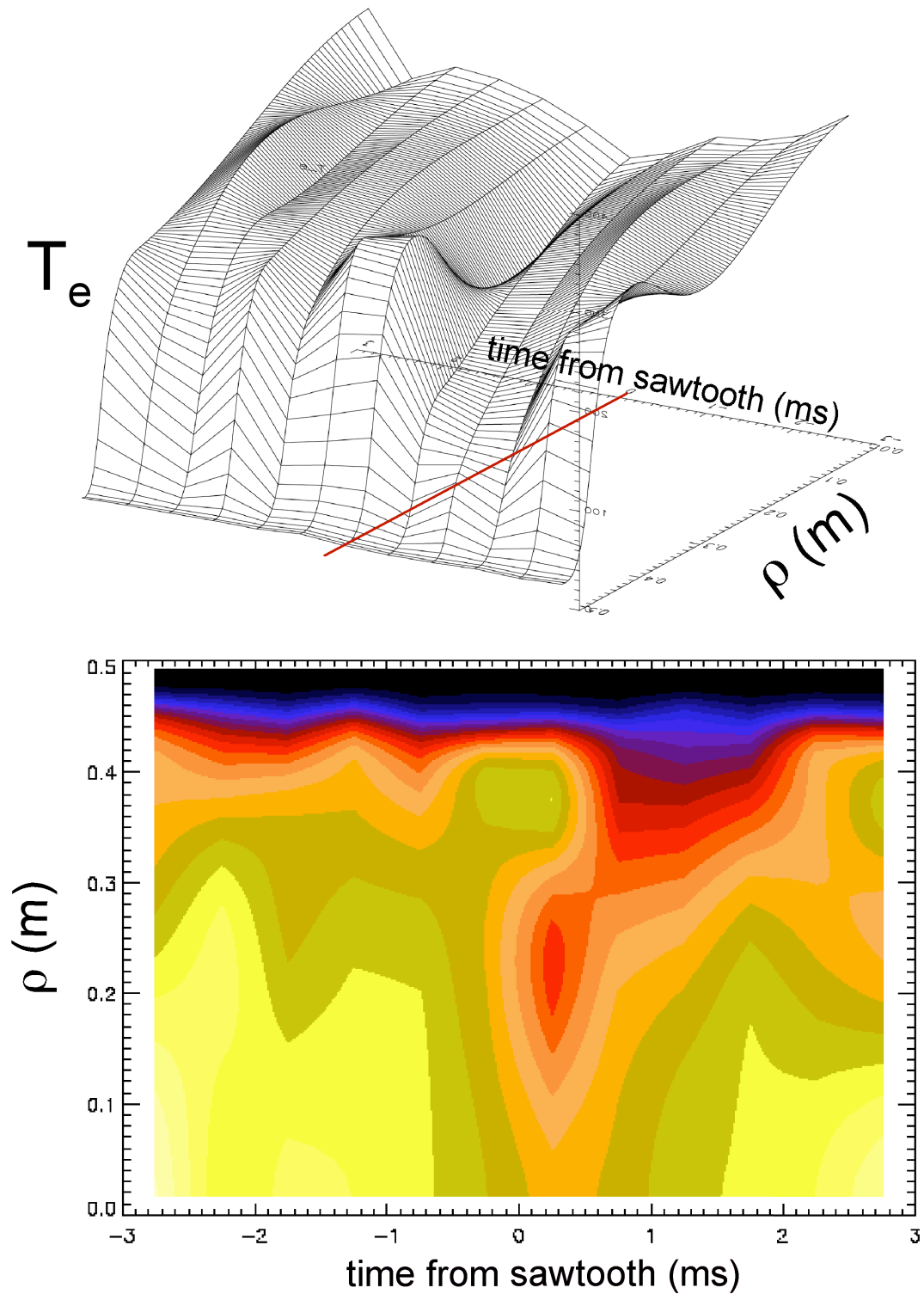


Figure 3.5 Surface and contour plots of the evolution of the electron temperature profile over a sawtooth cycle in Standard MST discharges. The 12 time slices can be seen, and the diagonal bar indicates the position of the sawtooth crash ( $t = 0$ ).

The evolution of the electron temperature profile over a sawtooth cycle in Standard MST discharges is shown in Figure 3.5. While there is still some scatter in the data, it is clear that the temperature drops across the entire profile after the sawtooth crash. Also of note is that the peak temperature appears to begin decreasing before the crash occurs, suggesting that there is some mechanism at work, which has thermodynamic implications. This drop has been observed to occur up to 2 ms before the sawtooth crash in MST.<sup>10</sup> Section 4.4 will show that there is a strong correlation between the drop in central electron temperature and the rise in magnetic tearing mode fluctuations. Experiments at the ZT-40M RFP suggest that the sawtooth crash may be a toroidally localized phenomena, and the finite rotation time (into the TS diagnostic field of view) must be considered.<sup>12</sup> Typical rotation speeds of MST plasmas, however, indicate that this is a small effect.

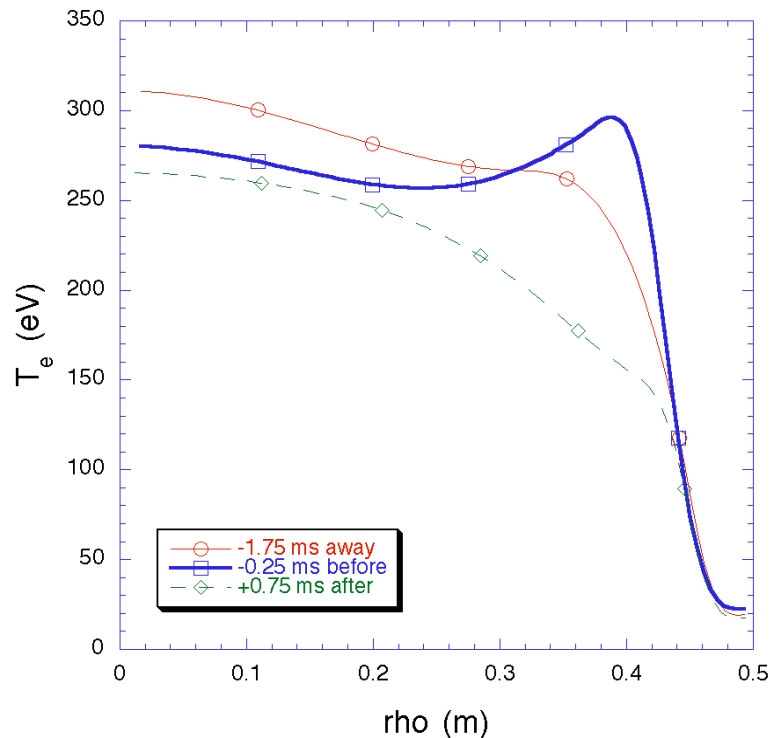


Figure 3.6 These three time slices represent the profiles away (-1.75 ms) from the sawtooth crash, just before the crash (-0.25 ms), and shortly after the crash (+0.75 ms). All three profiles shown are cubic splines, which are fit using MSTFit to the Thomson scattering  $T_e(r)$  data points.

### 3.3.2 Ion Temperature

The ion temperature evolution stands in contrast to the electron temperature evolution. Figure 3.7 shows how the central electron and (Deuterium) ion temperatures behave over a sawtooth cycle. The bulk-ion temperature is measured by the MST Rutherford scattering (RS) diagnostic.<sup>#</sup> The sampling volume of the RS measurement is quite broad, as shown in Figure 3.8, and in this case it is centered on a location that is approximately mid-minor-radius in the plasma. The ion temperature is calculated every 30  $\mu$ s in each plasma discharge, for a period of 3 ms. The active element of the RS system is a 30 keV diagnostic neutral beam which operates for 3 ms. By staggering the time that the neutral beam is “on” relative to the sawtooth crash, the ion temperature throughout the sawtooth cycle can be mapped out. The calculated ion temperatures are then binned to 100  $\mu$ s intervals in the ensembling process. Particularly significant in Figure 3.7 is the increase in bulk ion temperature immediately following the sawtooth crash and persisting for 2 to 3 ms, i.e. half the sawtooth cycle. Part of this increase may be a systematic rise as the ions heat through the discharge. The rapid increase in ion temperature at the crash is also observed in impurity ion temperatures as measured by the ion Doppler spectrometer (IDS) and charge exchange-recombination spectrometer (CHERS), both of which are sensitive to charge states of carbon in their typical configurations.<sup>13,14</sup> Bulk and impurity ions are heated to temperatures greater than the electron temperature near the crash, as has been observed in the MST previously.<sup>15</sup> Currently, the mechanism for this ion heating is not well understood.<sup>16-19</sup> Away from the sawtooth crash the ion temperature is roughly 80% the value of the electron temperature.

---

<sup>#</sup> Diagnostic operated by Jim Reardon and Gennady Fiksel.

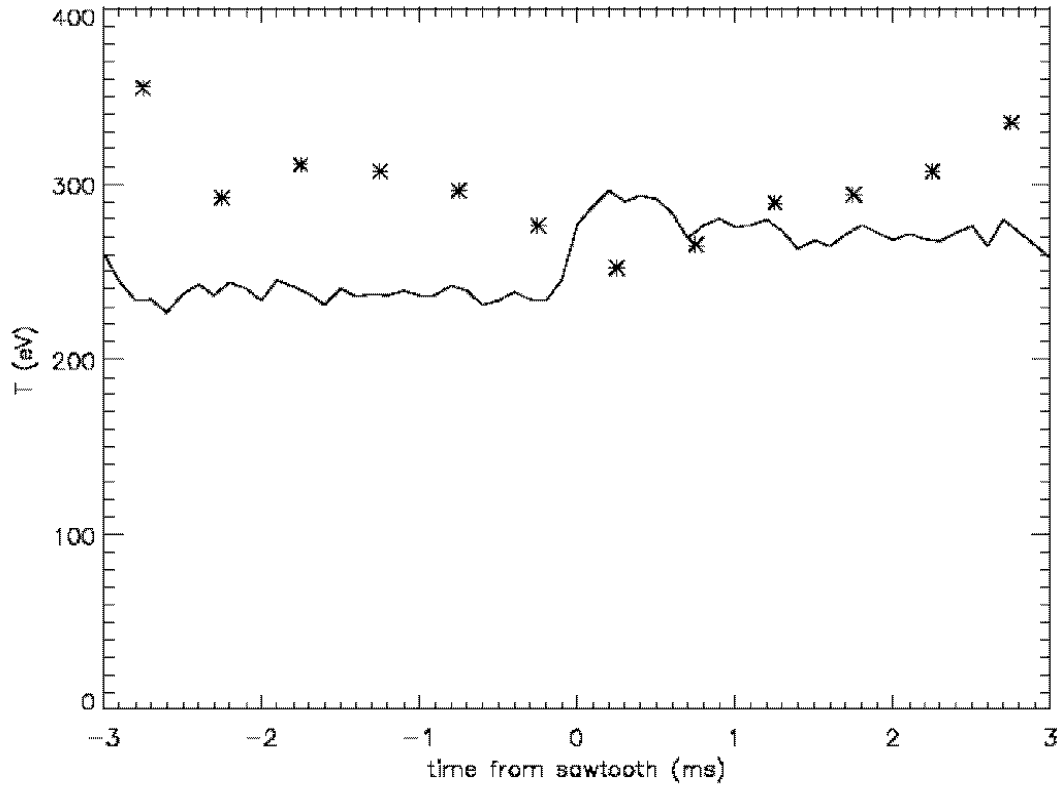


Figure 3.7 The evolution of  $T_c(0)$  (\*) from Thomson scattering and  $T_i(r/a \sim 0.3)$  (solid line) from Rutherford scattering over the sawtooth cycle in Standard MST discharges. The solid line is the ensemble average over  $\sim 350$  plasma discharges.

The MST Rutherford scattering system has the capability to measure the ion temperature profile. It is described in detail elsewhere, but is shown schematically in Figure 3.8.<sup>20</sup> By changing the angle and/or location of the neutral-particle energy analyzers, the sampling location of the RS system can be moved radially. This feature was not available at the time of the original experimental campaign (November 2000), but was added in March 2001. Great care was taken to repeat the experimental conditions of November 2000 in June 2001 and to use the enhanced functionality of the RS diagnostic to measure the bulk-ion temperature profile. The separate experiments are sufficiently similar that including the ion

temperature profile data is valid. This data does not affect the equilibrium quantities at all, but does play a role in the transport analysis.

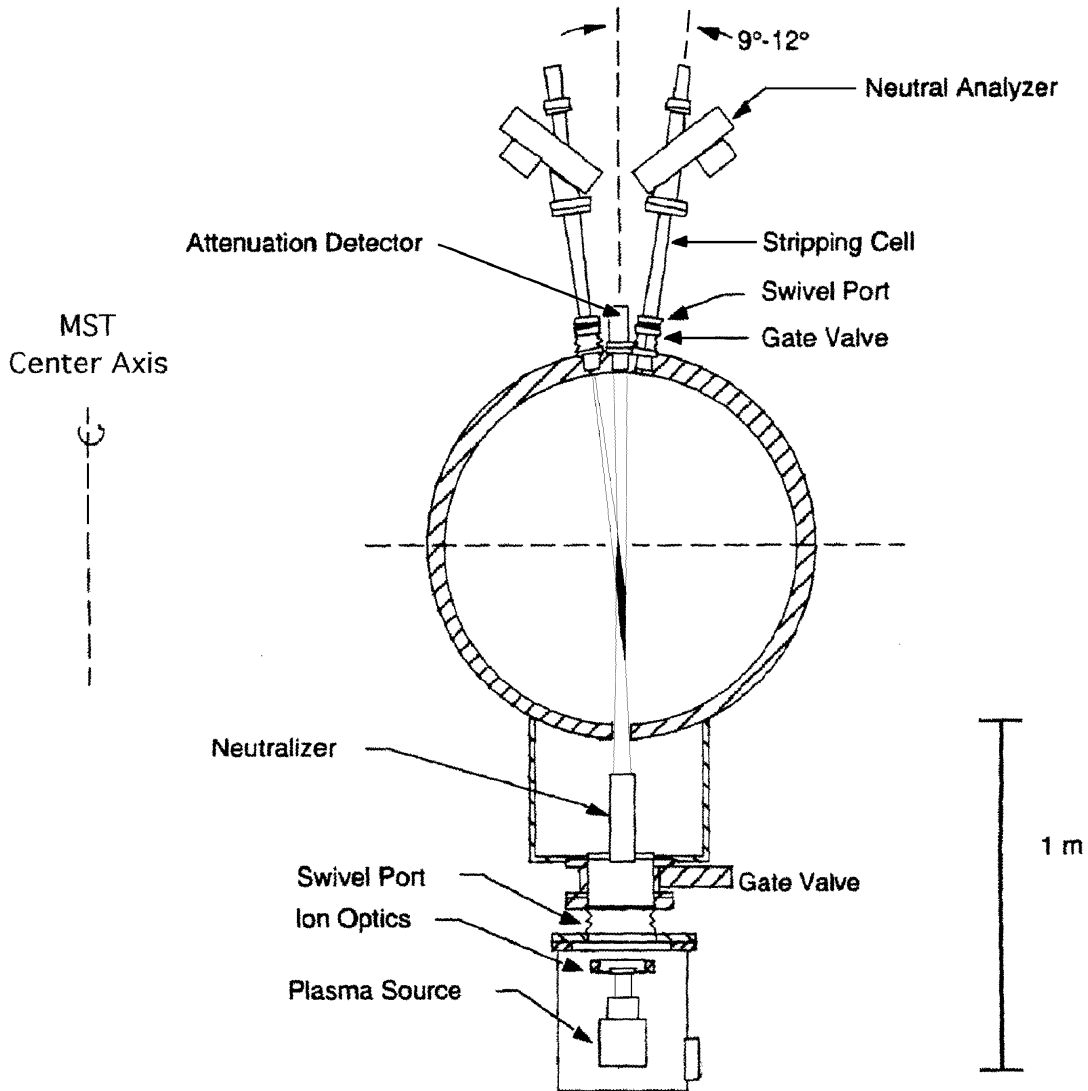


Figure 3.8 The MST Rutherford scattering diagnostic setup. Figure courtesy of Jim Reardon.

The bulk-ion temperature profile can be measured and its evolution studied. Figure 3.9 below shows RS measured ion temperature profiles at  $-1.75$  ms and  $+0.75$  ms from a

sawtooth crash. It is worth noting that these measurements are the first-ever radial profile measurements of bulk-ion temperature in Standard MST plasmas. Though the data is presented here, it is primarily the work of others.<sup>#</sup> Analogous to the Thomson scattering data, the 6-point ion temperature profiles are spline-fit in MSTFit in order to interpolate the ion temperature profile into regions that cannot be accessed with the Rutherford scattering diagnostic. The MSTFit spline is the solid line in Figure 3.9. Surface and contour plots of the evolution of these temperature profiles over the sawtooth crash are shown in Figure 3.10.

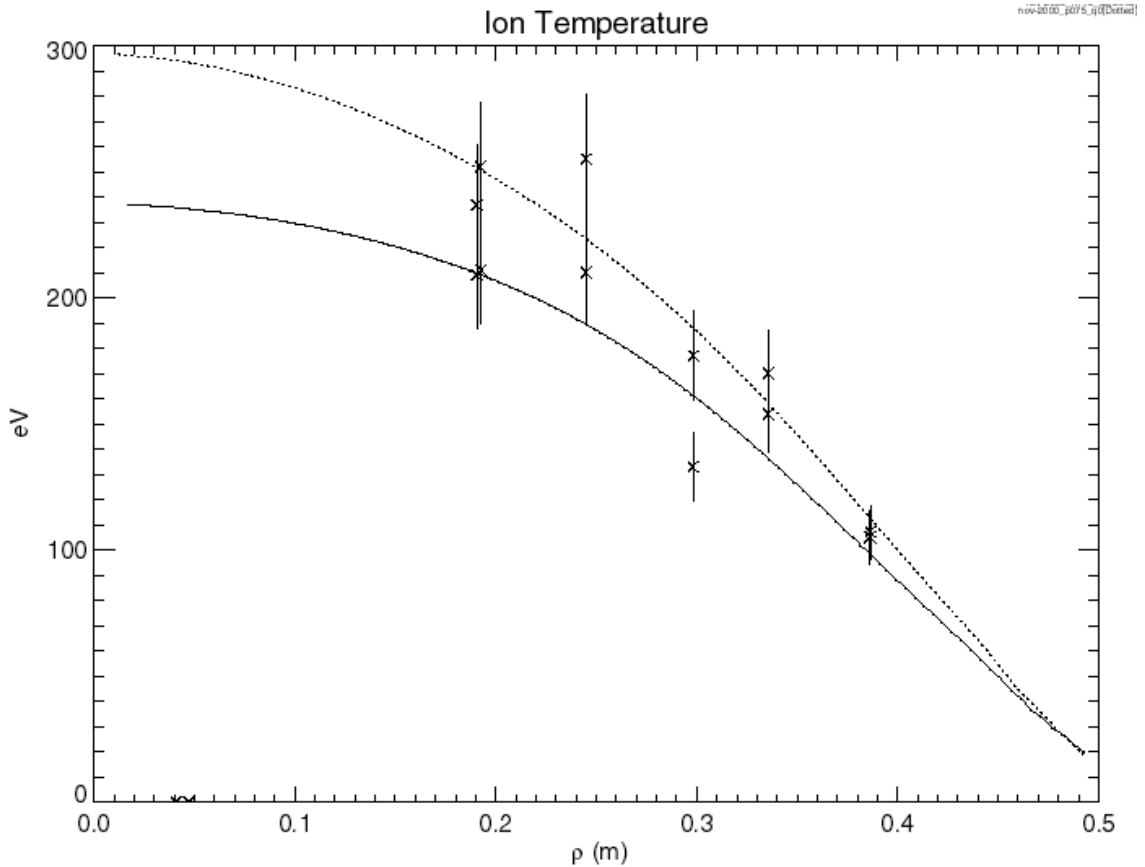


Figure 3.9 Rutherford scattering measured ion temperature profiles for Standard plasmas - 1.75 ms (solid) before the sawtooth crash and 0.75 ms (dotted) after the crash.

<sup>#</sup> Jim Reardon and Gennady Fiksel

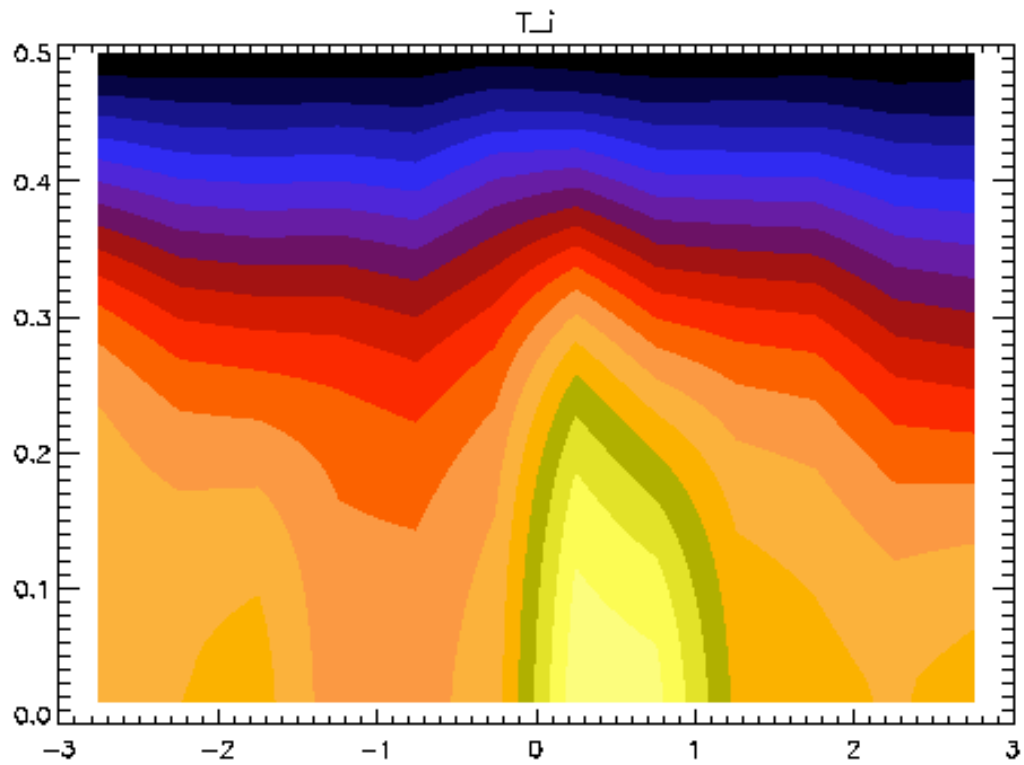
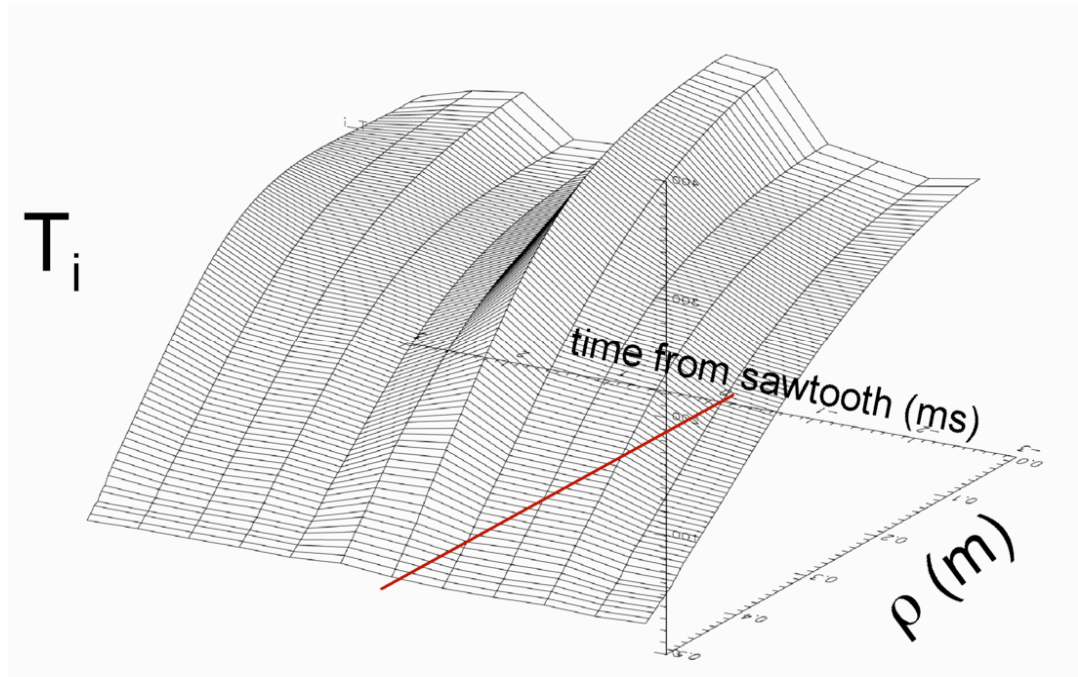


Figure 3.10 Surface and contour plots of the RS measured ion temperature profile evolution over the sawtooth cycle in Standard plasmas.

## 3.4 Density Profile Evolution

### 3.4.1 Electron Density

The electron density profile evolution has been measured with an 11-chord Far-Infrared (FIR) interferometer/polarimeter,<sup>#</sup> shown in Figure 3.14. This diagnostic is described in great detail elsewhere.<sup>8</sup> The diagnostic can be either operated as an interferometer or as a polarimeter. There are roughly 400 plasma discharges in this experiment. For half of those shots, the diagnostic was in “interferometer mode,” measuring the electron density. For the other half of the discharges, the diagnostic was operated as a high-time resolution polarimeter, measuring the Faraday rotation induced by the vertical magnetic field. The ensembled 11-chord FIR interferometer line-averaged density data is Abel inverted and mapped onto flux surface coordinates in MSTFit, as shown in Figure 3.11. The evolution of the density profile over the entire sawtooth cycle is shown in Figure 3.13. Figure 3.12 shows sample profiles of electron density at three times during the sawtooth cycle. At the sawtooth crash the electron density profile broadens significantly, and the central electron density drops, yielding a slightly hollow profile.

---

<sup>#</sup> Diagnostic operated by Steve Terry and Weixing Ding.

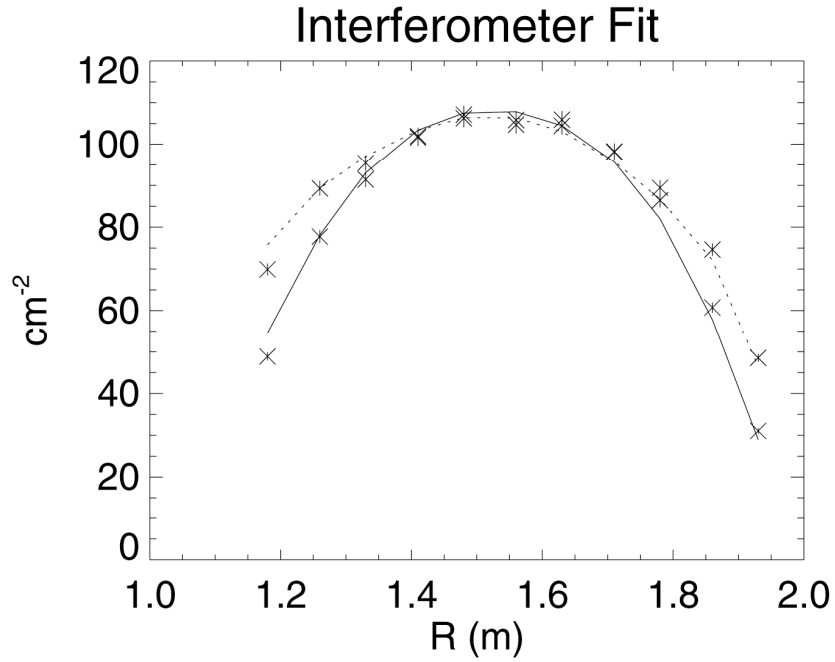


Figure 3.11 Comparison of the raw (line-integrated) data with the Abel-inverted MSTFit fit at  $-1.75$  ms (solid) and  $+0.75$  ms (dotted) during the sawtooth cycle of Standard plasmas.

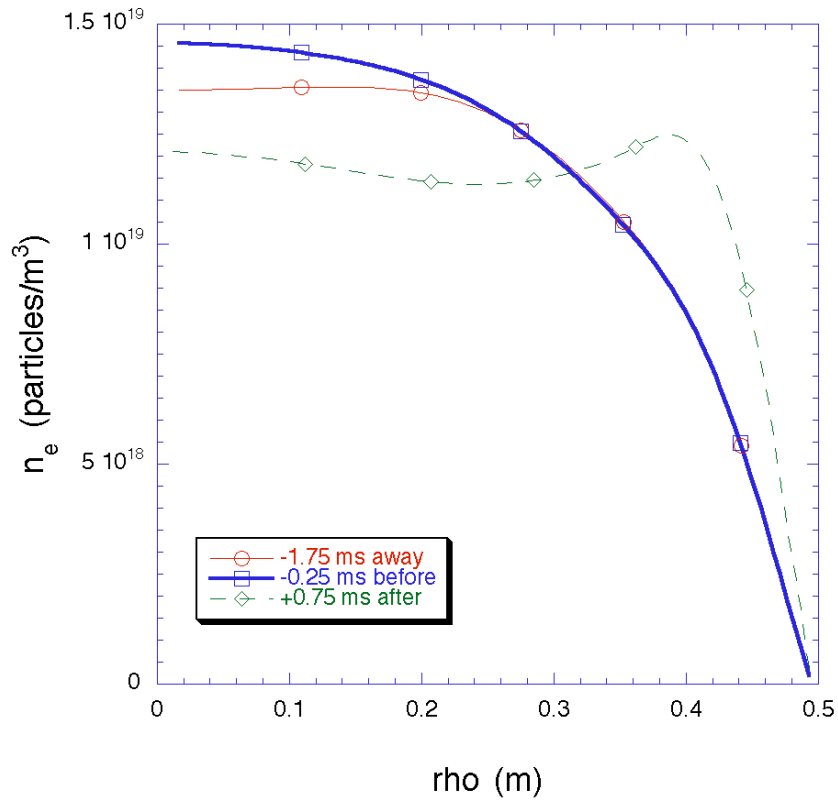


Figure 3.12 Select profiles of electron density during Standard plasma discharges.

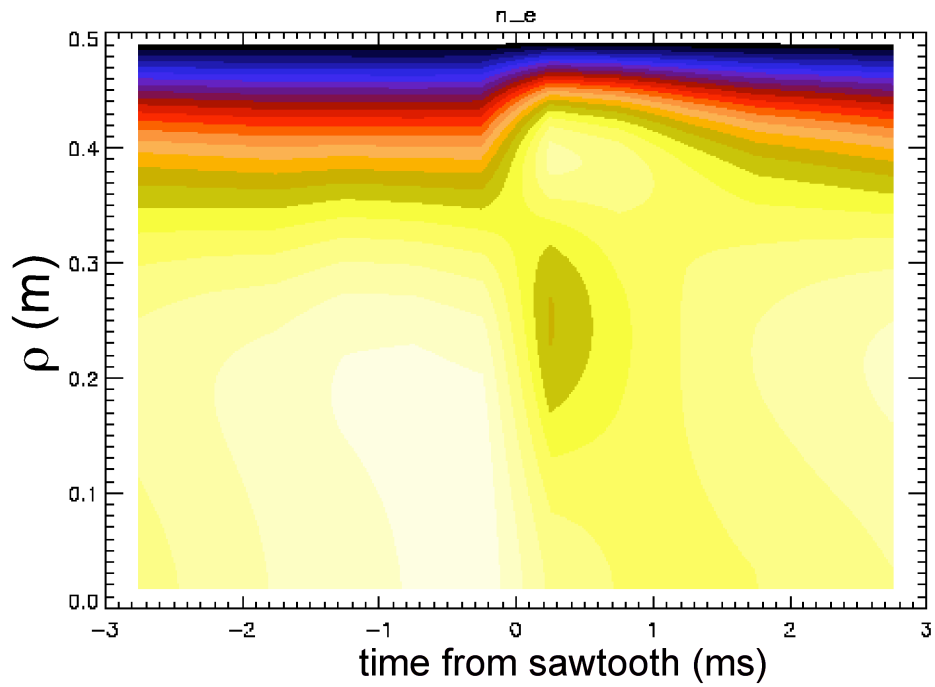
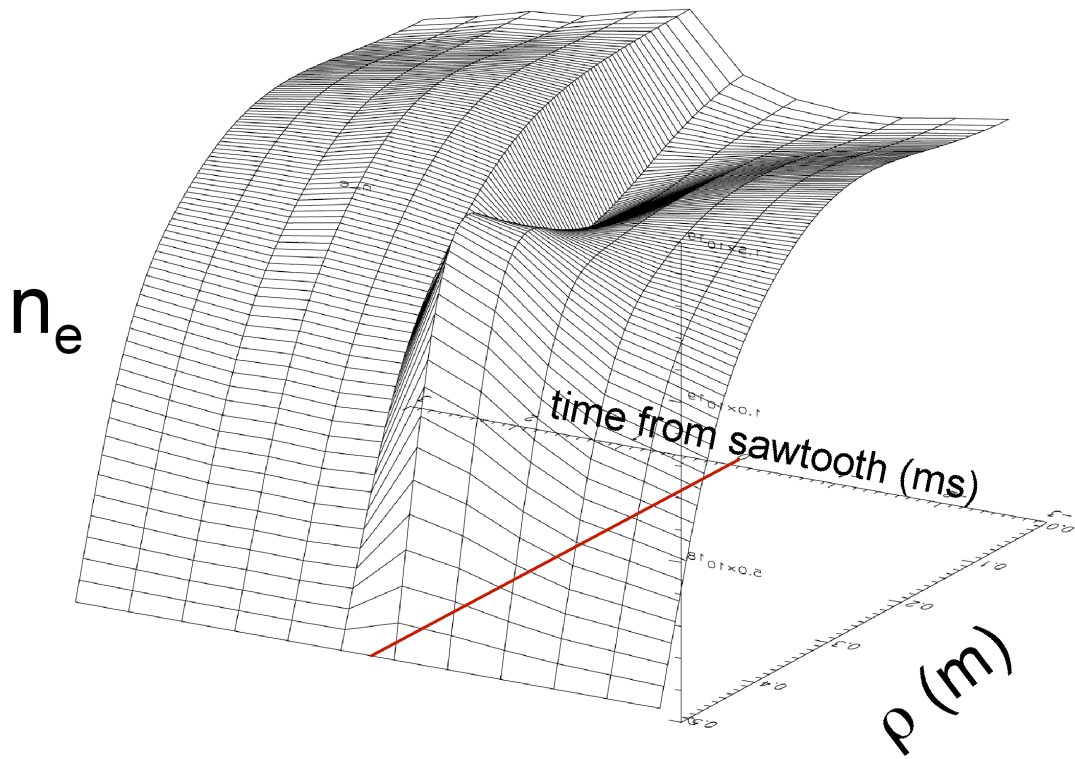


Figure 3.13 Surface and contour plots of the electron density profile evolution over the sawtooth cycle for Standard plasmas.

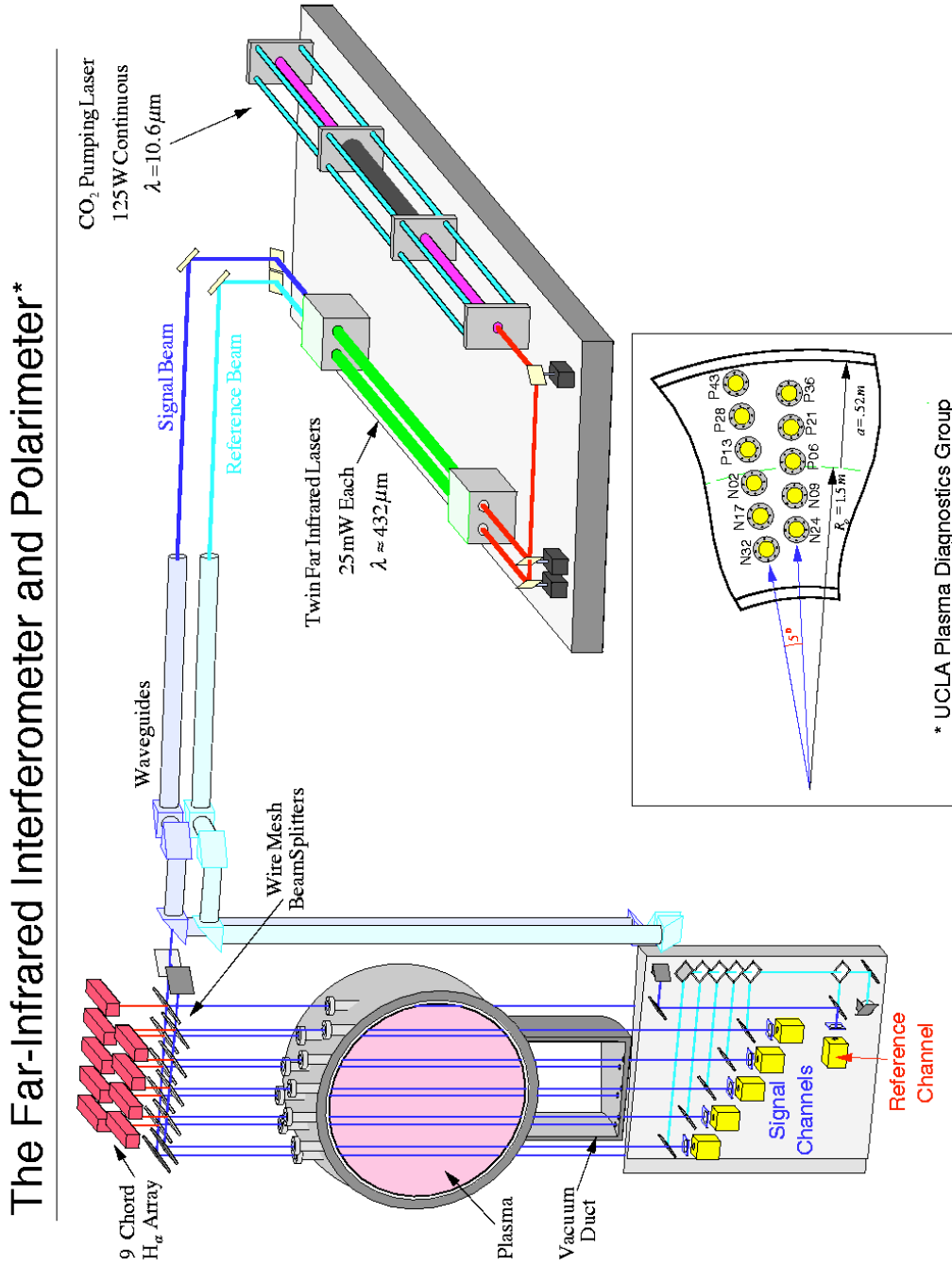


Figure 3.14 The FIR Interferometer/Polarimeter diagnostic on the MST, courtesy of Steve Terry and Nick Lanier.

### 3.4.2 Comments about $Z_{\text{eff}}$ and Ion Density

The bulk ion density profile is not systematically measured in the MST. In principle, since the Rutherford scattering (RS) system measures the energy spectrum of the ions to infer the ion temperature, the area under the ion energy spectrum could be used to give a localized measurement of the ion density at the sample volume location. This could be done in much the same way as the TS diagnostic could yield a local electron density measurement, if it were so calibrated. In the absence of impurities, overall charge neutrality requires that the electron and ion densities be equal, since deuterium (having a single charge state) is the working gas for these plasmas. The presence of impurities in the plasma, particularly high-Z impurities, will reduce the concentration of bulk ions necessary to balance the electron population. Typical MST discharges contain a nominal “ham sandwich” of impurities (to quote the local lingo), as born out by the abundance of spectroscopic lines: H, He, B, C, O, N, Al, . . . . If one could measure the relative concentrations of each of these species through their spectral line intensities, then it would be possible to estimate the  $Z_{\text{eff}}$  profile (as defined below) of MST plasmas through collisional radiative modeling (CRM), and to extract the bulk ion density. While these techniques are being discussed for use on the MST, they have not yet been implemented.<sup>9</sup>

One method of approximating the ion density is from the  $Z_{\text{eff}}$  profile. The  $Z_{\text{eff}}$  profile in the MST is inferred by equating the measured Ohmic input power deposition profile,  $\mathbf{E} \cdot \mathbf{j}$ , and then relating this to the  $|\mathbf{j}|^2$  profile.<sup>21</sup> Through neoclassical resistivity, an effective  $Z_{\text{eff}}(r)$  is implied (as will be discussed in more detail in Section 4.3). This profile can then be used, under a three-component plasma assumption, to estimate  $n_i(r)$ . Utilizing charge neutrality in the plasma,  $\sum n_i + Z_{\text{eff}} n_e = 0$ ,  $Z_{\text{eff}}$  is defined as:

$$Z_{\text{eff}} \equiv \frac{\sum Z_j^2 n_j}{n_e} = \frac{n_i + Z^2 n_z}{n_e}. \quad (8)$$

Defining the relations,

$$x_i = \frac{Z Z_{\text{eff}}}{Z-1} \quad \text{and} \quad x_z = \frac{Z_{\text{eff}}-1}{Z(Z-1)} = \frac{1-x_i}{Z}, \quad (9)$$

leads to the simplifications:

$$n_i = x_i n_e \quad \text{and} \quad n_z = x_z n_e. \quad (10)$$

Calculations of the effective  $Z_{\text{eff}}$  necessary to obtain the proper Ohmic input power indicate that the value is between 2 and 4. If the dominant impurity is Aluminum ionized to a  $Z=10$  charge state, then calculations for a three component plasma show that  $n_i \sim 0.78 n_e$  and  $n_{\text{Al}} \sim 0.012 n_e$ . Such a small concentration of Aluminum can be essentially neglected in transport studies, since a radial flux of this particle species would carry few particles and little heat from the plasma. For the analysis in Chapters 4 and 5, the simplifying approximation is made that

$$n_i(r) = 0.80 n_e(r). \quad (11)$$

### 3.4.3 Neutral Density

Transport analysis requires knowledge of particle sources and the neutral particle density. The neutral particle density is estimated from the measured  $D_{\square}$  emission and the

measured electron density profile.<sup>22</sup> The source rate is related to the particle density by the expression:

$$S(r) = n_e(r)n_N(r)\langle\sigma v\rangle_{e.i.i.r.} . \quad (12)$$

Here  $S(r)$  is the ionization rate of neutrals, measured from  $D_\alpha$  emission,  $\langle\sigma v\rangle_{e.i.i.r.}$  is the electron impact ionization rate, and  $n_N$  is the neutral particle density. Lanier argues that this rate is fairly constant for ion temperatures in excess of 20 eV, leading to the approximation:<sup>22</sup>

$$\langle\sigma v\rangle_{e.i.i.r.} \approx 3.0 \times 10^{-8} \frac{\text{cm}^3}{\text{s}} . \quad (13)$$

For the transport study presented in this thesis, neutral particles factor in when attempting to take into account heat (power) lost by the ions through charge-exchange with neutrals. This will be discussed in more detail in Section 5.4, but Figure 3.15 shows a neutral particle profile calculated from these expressions. The particle source profile,  $S(r)$ , will be shown when discussing particle transport in Section 4.2.

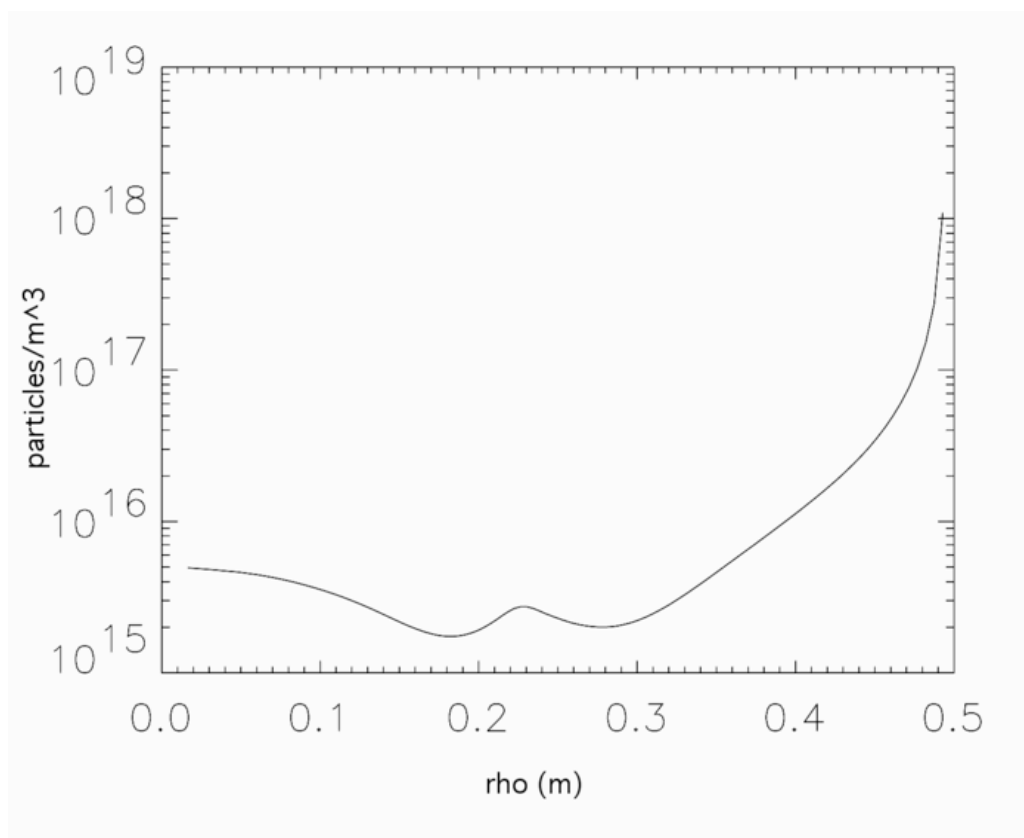


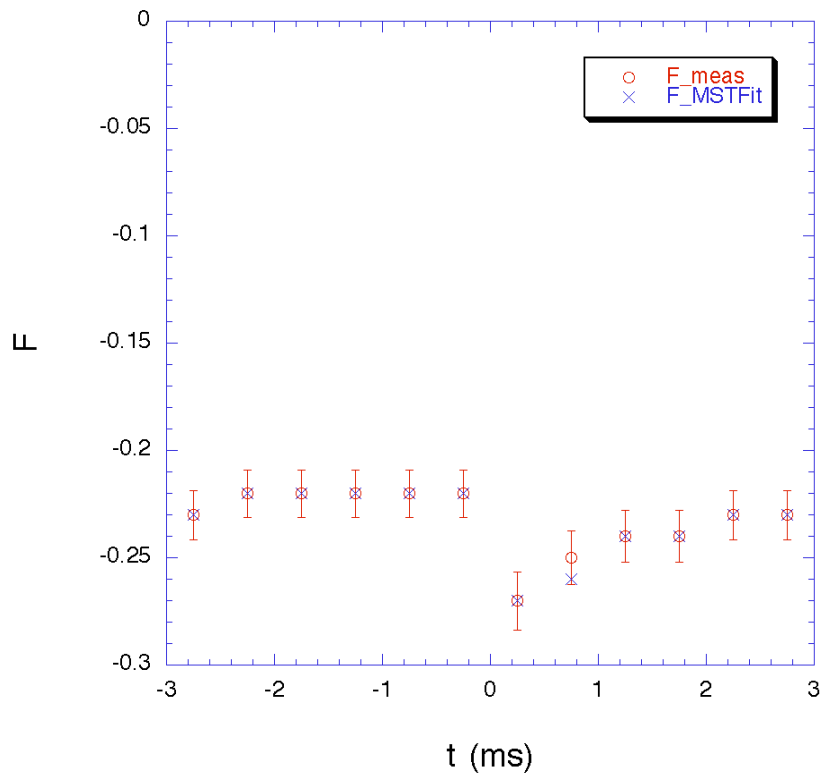
Figure 3.15 The neutral particle density at -1.75 ms during Standard MST plasmas. Note that the neutral particle density is 3 orders of magnitude lower than the electron density in the core, but roughly equal in the extreme edge of the plasma.

### 3.5 Current Profile Evolution

In the MST the current density profile is determined by fitting a solution of the Grad-Shafranov equation (valid throughout the volume) in MSTFit to a number of local measurements.<sup>9</sup> The current density profile is essential for the following transport analysis. The MST diagnostics which most directly affect the current density reconstruction are: a simple flux loop and internal Rogowski coils, the motional Stark effect diagnostic (MSE), the FIR polarimeter/interferometer, the heavy-ion beam probe (HIBP) diagnostic, and edge Mirnov coil arrays.

### 3.5.1 Flux Loop Constraints

A simple flux loop around the plasma column allows the total magnetic flux to be measured. The total plasma current is measured with a large internal Rogowski coil. With the total plasma current measured, the volume-integrated current density is constrained. Similarly, some information about the distribution of currents in the plasma can be found from the edge measured poloidal magnetic field, which when normalized by the volume-averaged magnetic field determines the RFP parameter  $\square$ . The reversal parameter,  $F$ , can similarly be found by normalizing the toroidal magnetic field at the wall (determined by a Rogowski coil measuring the current flowing poloidally in the shell) by the volume-averaged magnetic field. Figure 3.16 shows a comparison between the measured  $F$ ,  $\square$ , and  $I_p$  values with the MSTFit reconstructed values (ultimately derived from the reconstructed current density profile) through the sawtooth cycle.



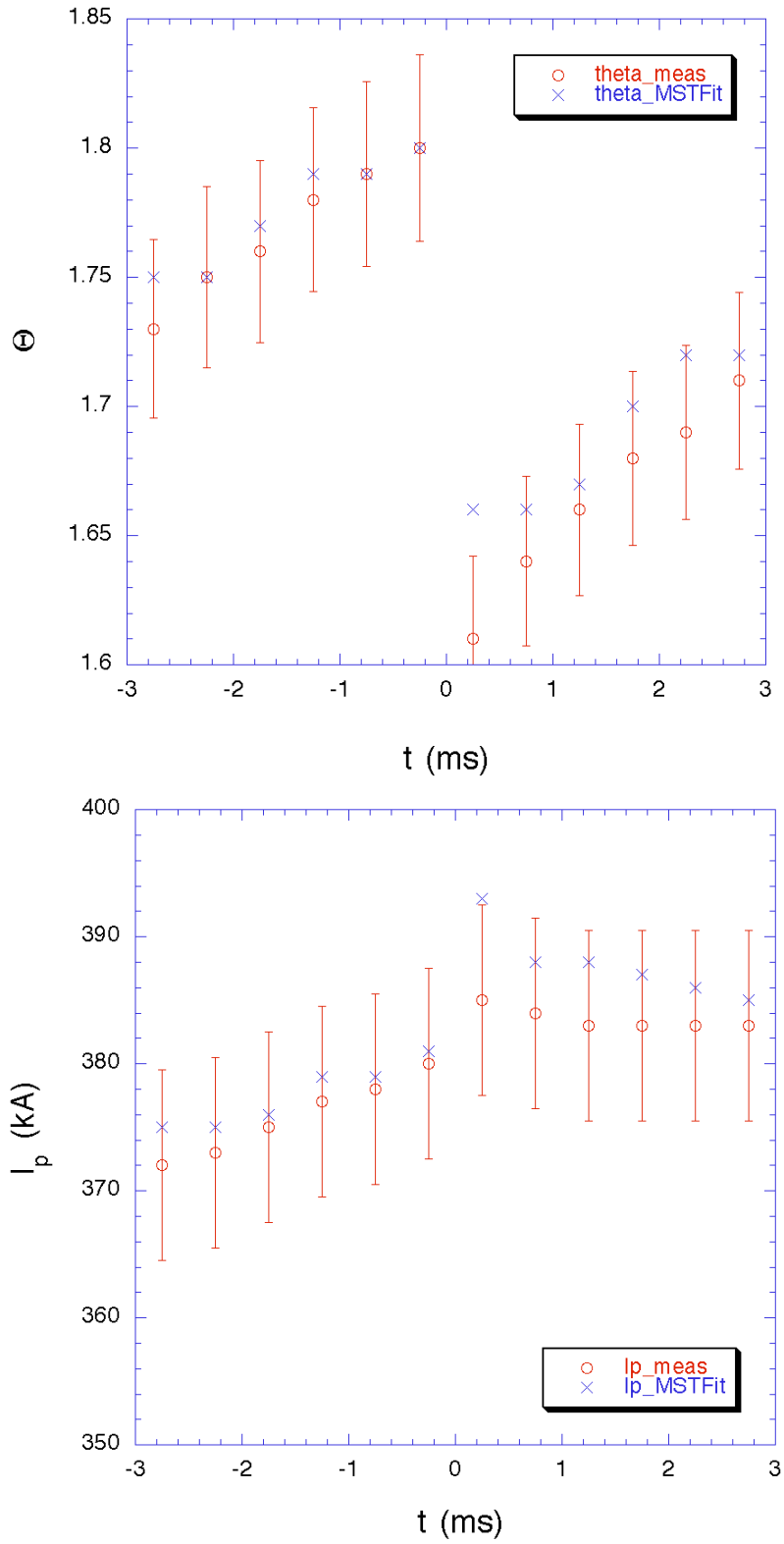


Figure 3.16 Comparison of  $F$ ,  $\theta$ , and  $I_p$  from measurements with MSTFit reconstructed values over the sawtooth cycle for Standard plasmas.

### 3.5.2 MSE Diagnostic Constraints

The on-axis magnetic field itself can be measured with the MSE diagnostic.<sup>#</sup> The MSE diagnostic on the MST is described elsewhere,<sup>23</sup> but is shown schematically in Figure 3.17 and will be summarized here. A diagnostic neutral beam, fired radially into the plasma experiences a changing magnetic field, because the equilibrium toroidal field peaks on-axis. The changing magnetic field appears to the neutral atoms as an electric field, which Stark-splits the lines of the neutral emission spectra. Measuring the spectral width of the Stark manifold then yields the magnetic field. The measurement is localized to the intersection of the collection optics line-of-site with the neutral beam trajectory. For the MST, this intersection occurs fairly close to the magnetic axis. The on-axis magnetic field value is a strong constraint on the core current density profile during the MSTFit reconstruction process.

---

<sup>#</sup> Diagnostic operated by Darren Craig and Gennady Fiksel.

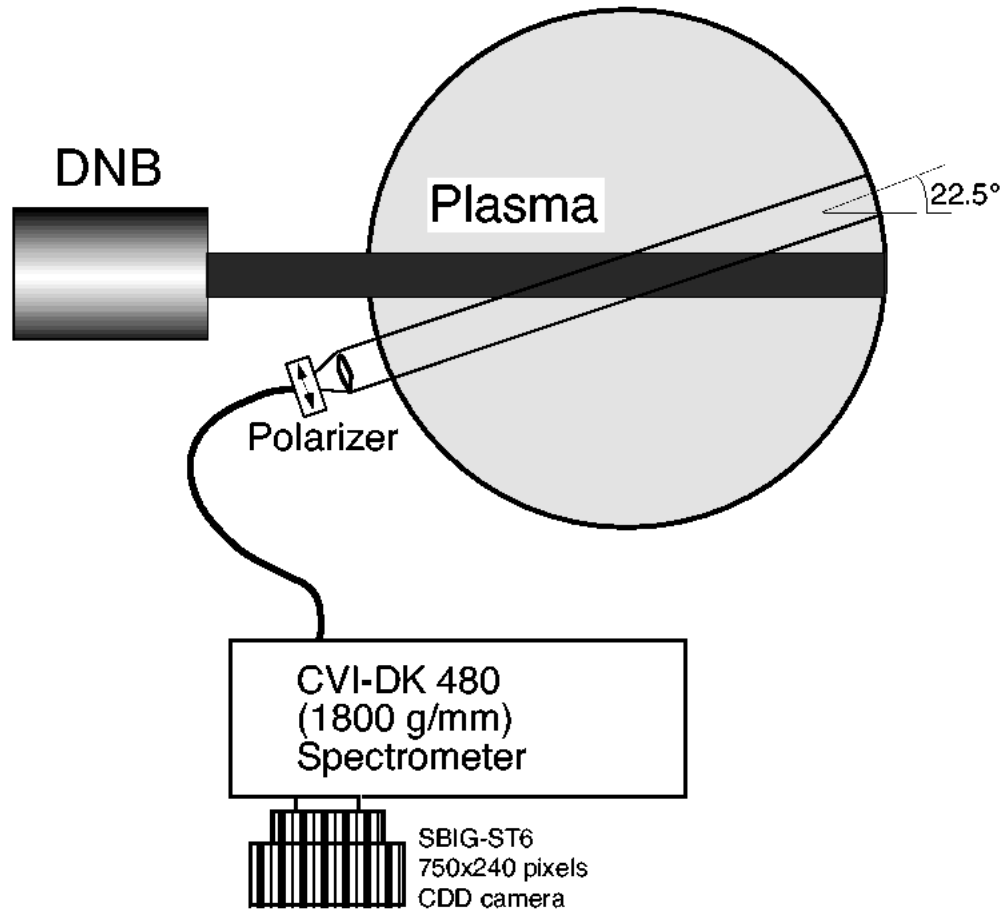


Figure 3.17 The MST motional Stark Effect diagnostic setup, courtesy of Jay Anderson. A diagnostic neutral beam, fired radially into the plasma experiences a changing magnetic field, because the equilibrium toroidal field peaks on-axis. The changing magnetic field appears to the neutral atoms as an electric field, which Stark-splits the lines of the neutral emission spectra. Measuring the spectral width of the Stark manifold then yields the magnetic field.

The time resolution of the MSE diagnostic is set by: 1) the duration of the diagnostic neutral beam, and 2) the time response of the spectrometer and its shutter. The neutral beam is active for a 3 ms window, which can be scanned to map out the entire sawtooth period ( $\sim 6$  ms). In November 2000 (the time of these Standard plasma experiments) the MSE spectrometer required roughly 1 ms of integration time in order to measure enough signal to accurately resolve the line separation. Because of this poor time resolution, the discharges

under analysis were divided into two bins: those containing sawteeth during the integration window, and those without. This gave some indication of how the on-axis magnetic field changed during the sawtooth crash, dropping from 0.347 T (no sawteeth) to 0.345 T (sawteeth). Figure 3.18 shows a comparison between the MSTFit reconstructed value of the local magnetic field at the location of the MSE measurement, to the MSE measured value used in the reconstruction. The MSTFit value is systematically higher than the measured MSE value, but the trend (decreasing at the sawtooth) is similar and the reconstruction falls within the 10% error bars of most time slices. Since the original experiment the MSE spectrometer has been upgraded, and a high-time-resolution (100  $\mu$ s) MSE measurement of the on-axis field has become possible,<sup>24</sup> but these exact experimental conditions have not been revisited.

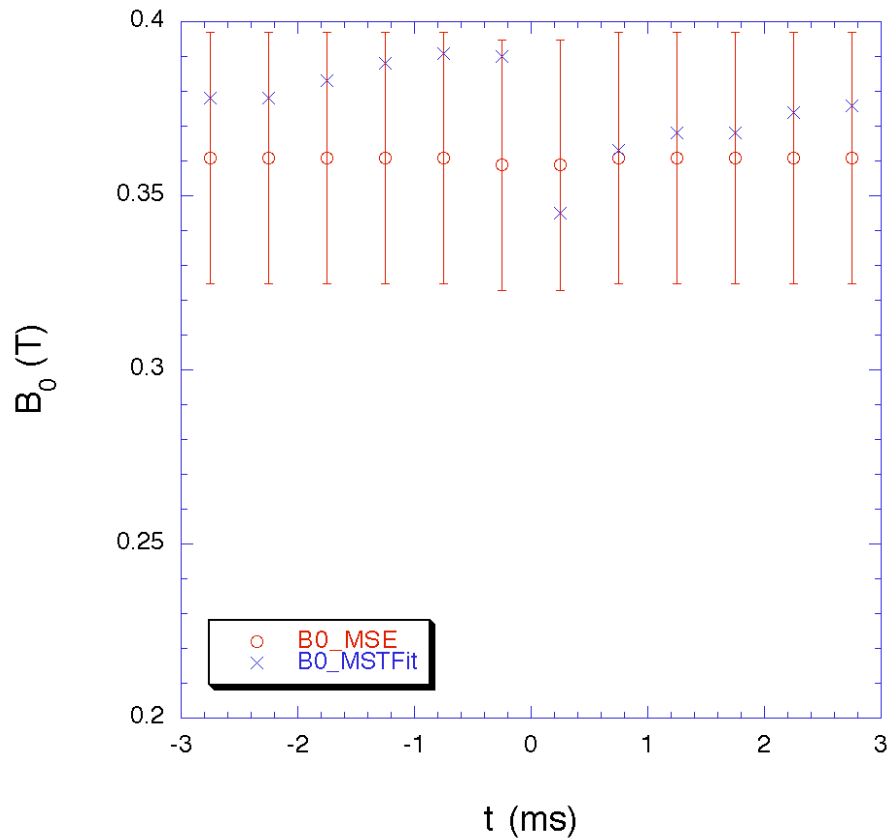


Figure 3.18 The evolution of on-axis magnetic field over the sawtooth cycle in Standard plasmas. Since the original experiment the MSE spectrometer has been upgraded, and a high-time-resolution (100  $\mu$ s) MSE measurement of the on-axis field has become possible.

### 3.5.3 FIR Polarimeter Constraints

The combination FIR interferometer/polarimeter<sup>8</sup> strongly constrains the current density profile in the core and mid-radius region, along with a weaker constraint at the edge. This diagnostic is operated for the UW-Madison MST group through collaboration with UCLA,<sup>#</sup> and is shown above in Figure 3.14. In polarimeter mode, the diagnostic measures the Faraday rotation induced by the current (through Ampere's Law) flowing in the dielectric plasma at 11 chordal locations. Combining the Faraday rotation data with the co-linearly measured electron density profile allows the current density profile to be locally constrained.

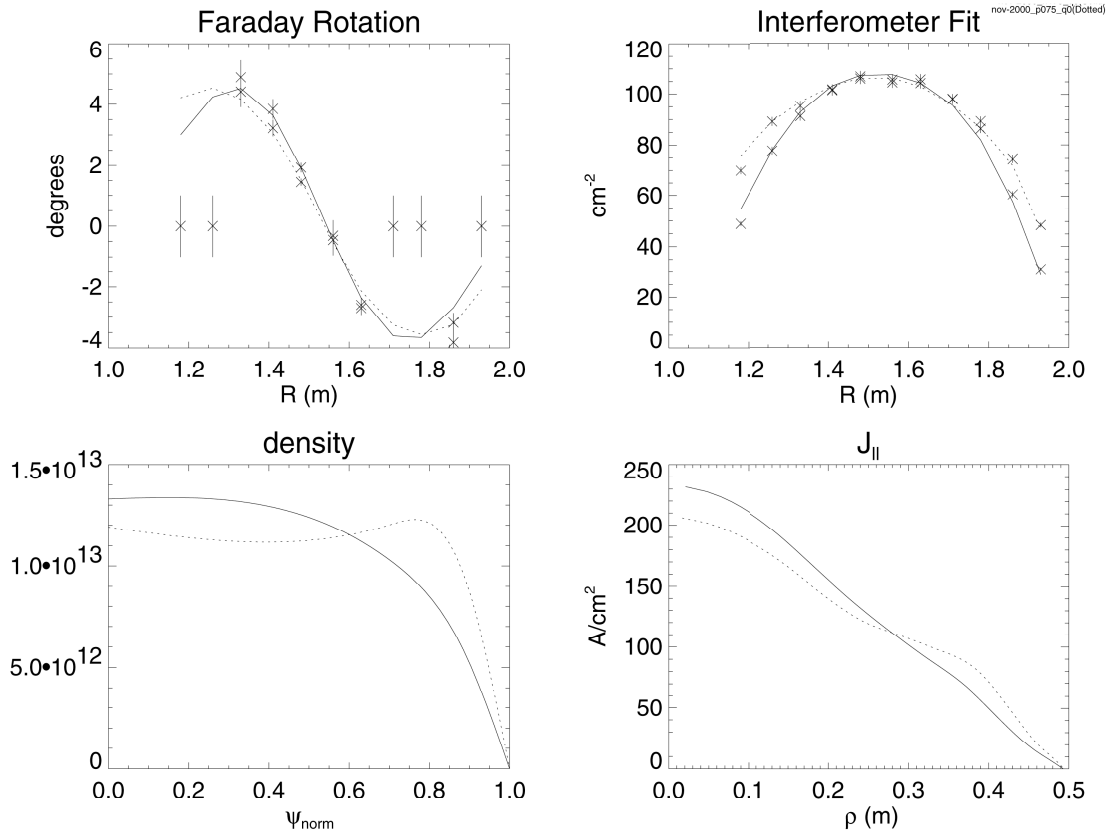


Figure 3.19 5-chord Faraday rotation measurements at  $-1.75$  ms (solid) and  $+0.75$  ms (dashed) in Standard plasmas used to constrain the current density profile.

<sup>#</sup> Diagnostic operated by Steve Terry and Weixing Ding.

At the time of this experiment, the FIR laser at the heart of this diagnostic was not optimized for full-power operation. As a result, the laser, which is normally split into 11 chords, was concentrated into 5 chords to boost signal levels. Hence only 5 chords of polarimetry data were measured in this Standard plasma experiment. This problem was later resolved, and the experimental conditions were repeated to measure 11-chord data (50 plasma discharges). While that data appeared to generally agree with the 5-chord data (200 plasma discharges), it was not incorporated in this analysis because of the lower signal-to-noise ratio resulting from fewer discharges.<sup>25</sup> The other experimental campaigns in this thesis utilize 11-chord polarimeter data.

#### 3.5.4 HIBP Diagnostic Constraints

The heavy-ion beam probe (HIBP) diagnostic<sup>26</sup> can indirectly constrain the current density profile, through the magnetic field profiles. This diagnostic is described in great detail elsewhere, but is schematically shown in Figure 3.20. The HIBP is operated collaboratively for the MST group by Rensselaer Polytechnic Institute.<sup>#</sup> Its primary objectives include a measurement of the radial profile of electrostatic potential, and hence the radial electric field, in the MST. A beam of relatively heavy ions (Na or K) is singly ionized, accelerated, and injected into the plasma. The beam interacts with the plasma, and doubly ionized beam particles (may) enter the “secondary energy analyzer.” The trajectories of primary and secondary beam-ions follow a complicated 3-dimensional path through the plasma, sampling large regions of the magnetic field from edge to core and back. The velocity (speed and direction) of the primary particles at the point of injection is well known, and the velocity of detected secondary particles can be determined from the energy analyzer

---

<sup>#</sup> Diagnostic operated by Diane Demers, Jianxin Lei, and Uday Shah.

settings and its geometrical acceptance angles. The MSTFit reconstructed equilibrium magnetic field profiles (derived from the current density profile) are constrained in such a way that trajectories of primary and secondary beam particles through those fields must match. Figure 3.21 below shows beam trajectories successfully exiting the MST for a particular magnetic field configuration.

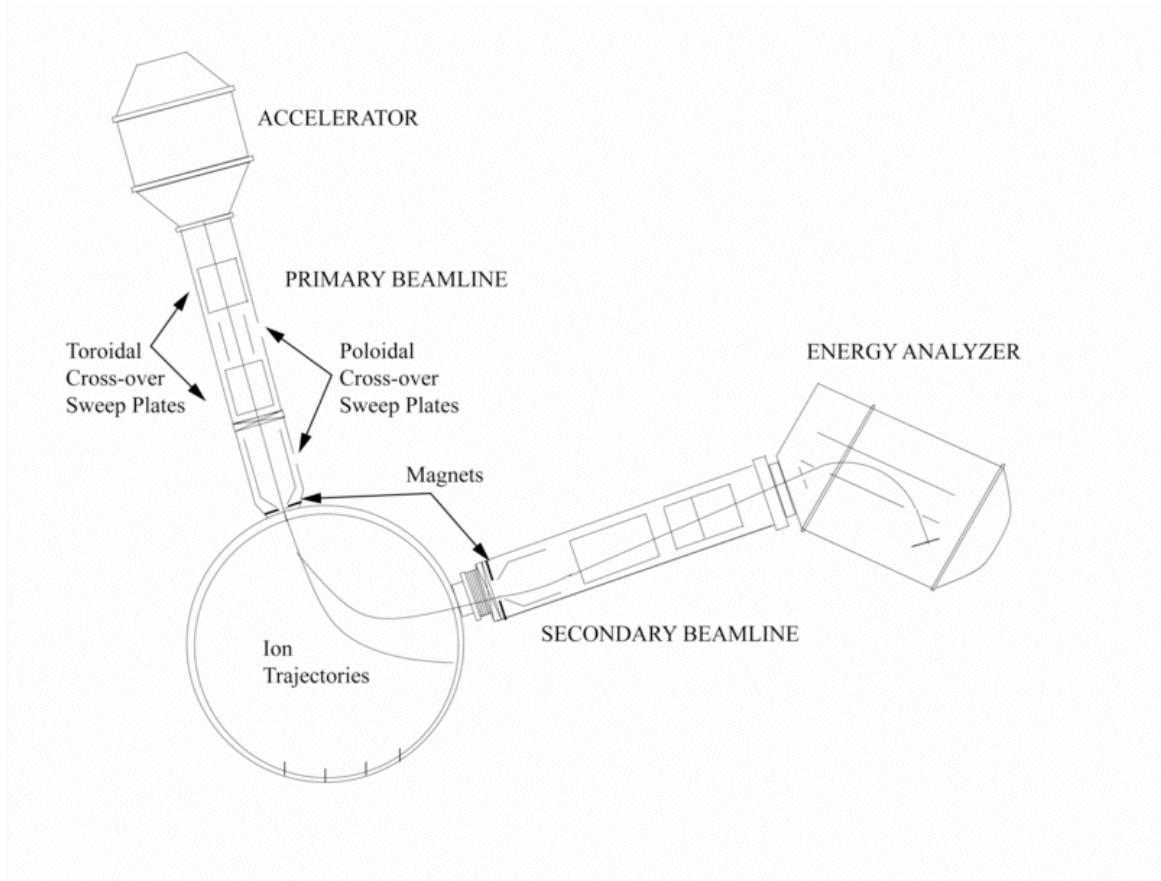


Figure 3.20 The MST HIBP diagnostic setup including a poloidal cross-section of the MST, courtesy of Diane Demers.

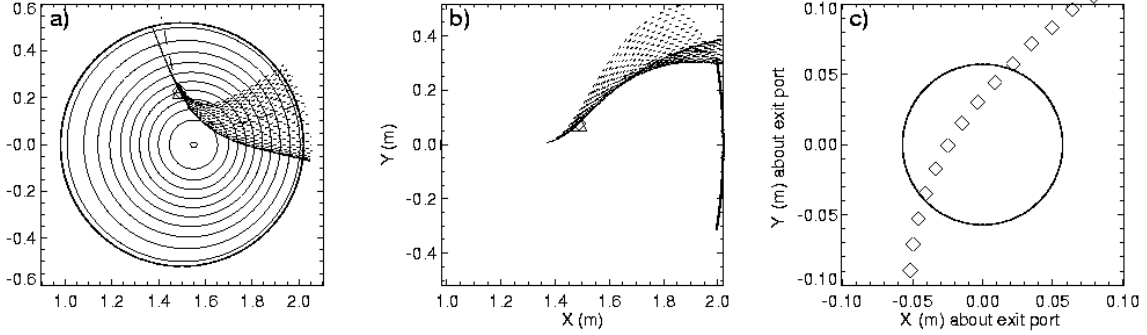


Figure 3.21 Trajectories of primary and secondary beam ions shown from a) a poloidal cross-section, and b) above, some of which c) intersect the energy analyzer entrance. Figure courtesy of Jay Anderson.

Though HIBP data was taken for these experiments, implementing it as a constraint on the equilibrium profiles proved problematic. These experiments were the first attempt to run the HIBP in this manner. Operational difficulties of the HIBP resulted in a small dynamic range of measurement for any given discharge. Consequently, data was sporadic, making ensembling essentially impossible. Data from single shots could be compared to the equilibrium established by other diagnostics, but it is unjustifiable to use single shot HIBP data on equal footing with other ensembled diagnostics to constrain the equilibrium. The experience gained from this experimental campaign will improve the systematic use of the HIBP diagnostic in future experiments. Despite these concerns, the radial electric field calculated from the HIBP measured potential profiles is in good agreement with the radial electric field inferred from ion momentum balance calculations, as will be shown in Section 3.7.

### 3.5.5 Mirnov Coil-Set Constraints

Detection of MHD modes also constrains the current density. Mirnov coil-sets at the edge of the plasma give important information about the spectrum of magnetic tearing modes

that are present in the MST. The toroidal array of coil-sets allows the toroidal mode number ( $n$ ) spectrum to be resolved. The presence of  $n=5$  or  $n=6$  modes at the pickup coils, suggests that the ( $m=1$ )  $n=5$  or  $n=6$  mode rational surface should be in the plasma (Figure 3.22). This constrains MSTFit to reconstruct a current density profile consistent with magnetic field profiles that imply a  $q(0) > 1/5$  or  $q(0) > 1/6$ , respectively. Figure 3.23 below shows a comparison between the dominant magnetic mode number (specifically the  $q$  value necessary for its resonant surface to be in the plasma) with the MSTFit reconstructed value of the on-axis  $q$  value through the sawtooth cycle. Except for the period of time after the sawtooth crash, when mode analysis indicates that the  $n=5$  mode should be in resonance, the MSTFit value is in good agreement with the magnetic mode data.

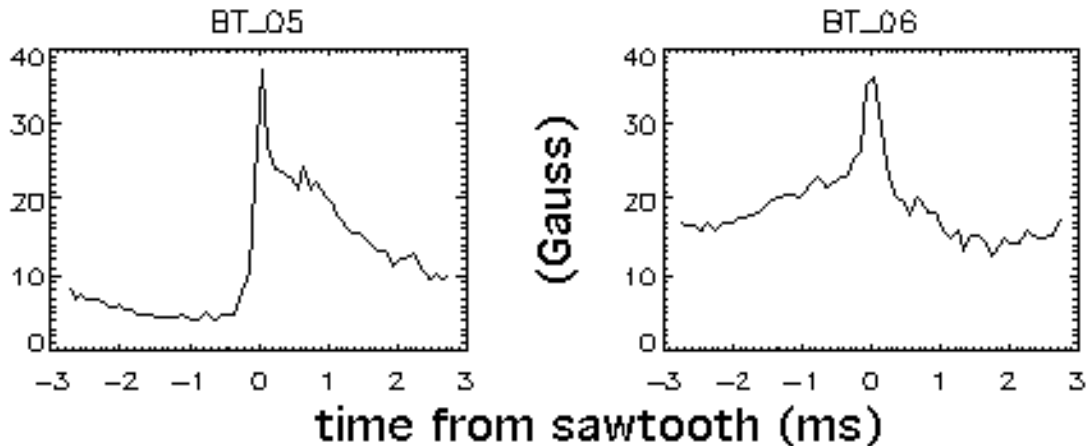


Figure 3.22 Time evolution of the  $n=5$  and  $n=6$  toroidal mode fluctuation amplitudes for a Standard plasma.

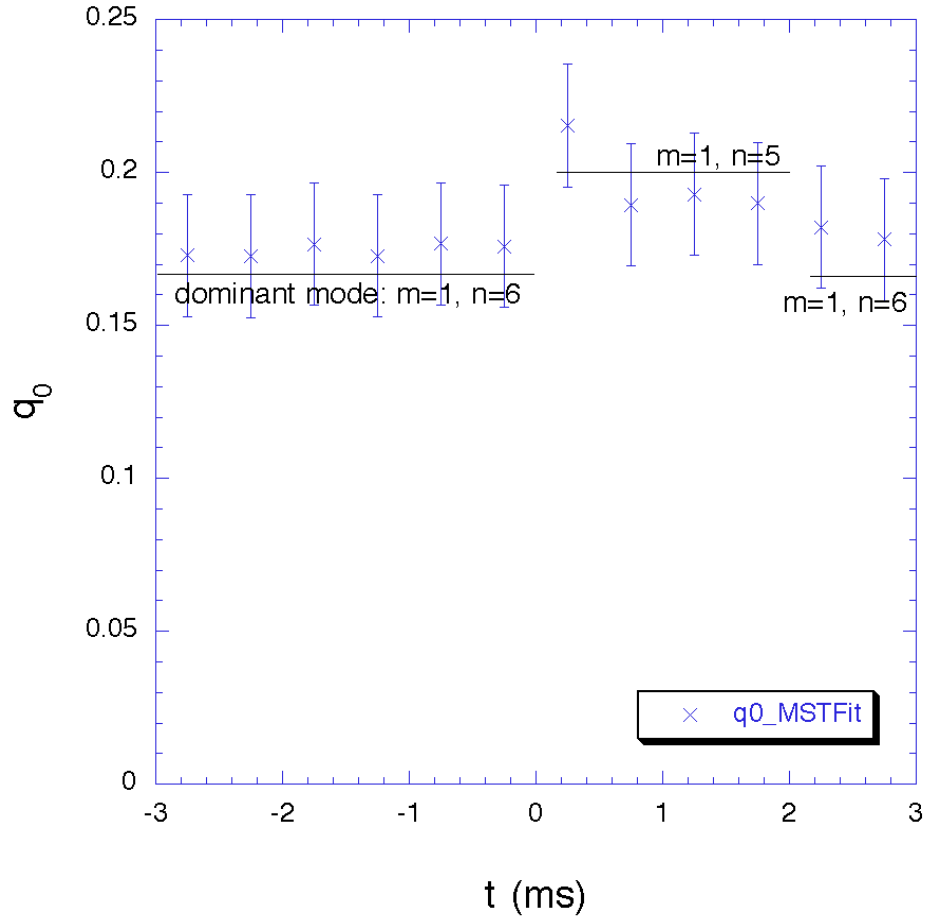


Figure 3.23 The on-axis value of  $q$  calculated from MSTFit should be high enough that the resonant surface of the observed, dominant magnetic mode is in the plasma.

The poloidal array of coil-sets will exhibit systematic amplitude changes, which must be consistent with an equilibrium Shafranov-shift. This is the so-called “poloidal asymmetry factor.” Though the poloidal array is not well calibrated, prohibiting the  $m$ -spectra from being well resolved, it nonetheless serves as a weak check on the reconstructed current density. The poloidal array data is plotted in Figure 3.24 for two different times in the sawtooth cycle;  $-1.75$  ms and  $+0.75$  ms, showing that the coil data is in rough agreement with the equilibrium Shafranov-shift that is reconstructed in MSTFit.

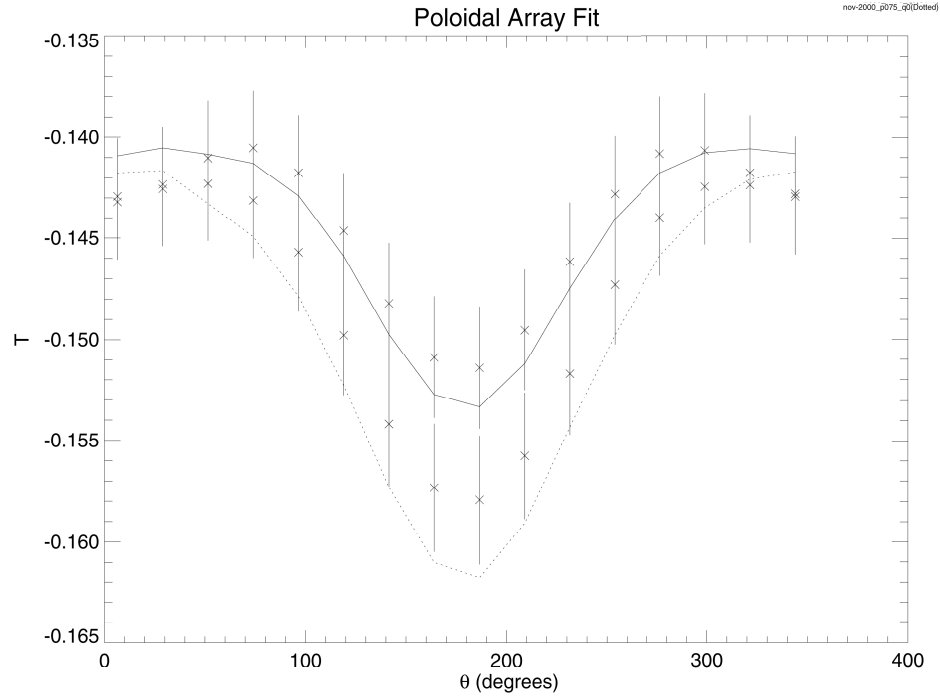


Figure 3.24 The MSTFit fit to the poloidal asymmetry factor at  $-1.75$  ms (solid) and  $+0.75$  ms (dotted), relative to the sawtooth crash.

### 3.5.6 MSTFit Reconstructed Current Density

Determining the current density profile is a  $\chi^2$  minimization of the available, above measurements. The agreement of the individual measurements to the collective, reconstructed current density has been shown above, and the current density profile itself revealed in some of the figures. Not shown above, but included in the equilibrium reconstruction is the effect of the pressure profile. Fortunately, a large portion of this experimental campaign was devoted to measuring just that. Once the equilibrium profiles are determined, it's straightforward to compute such basic plasma quantities as the safety factor profile ( $q$ ), and the  $\beta$ -profile.  $\beta$  can be defined as:

$$\beta = \frac{\mathbf{j} \cdot \mathbf{B}}{B^2}. \quad (14)$$

More insight into the physical meaning of  $\lambda$  can be had by considering that a constant  $\lambda$  (i.e. a flat  $\lambda$  profile) is the Taylor solution to the minimum energy state of an RFP plasma:<sup>27</sup>

$$\nabla \times \mathbf{B} = \lambda \mathbf{B}. \tag{15}$$

The  $q$  and  $\lambda$ -profiles are shown in Figure 3.25 for two different time slices: -1.75 ms away from the sawtooth crash and +0.75 ms after the crash. There is a slight change in the magnetic field profiles, but a large redistribution of current density, falling in the core and rising in the edge after the crash. The effect of this redistribution is to flatten the  $\lambda$ -profile, consistent with Taylor relaxation to a lower energy state, and to peak-up the  $q$ -profile in the core, consistent with the observation from the Mirnov coil-sets that the  $m=1, n=5$  mode becomes resonant and the 1,6 mode is stabilized (by being shifted closer to the wall and into a region of relatively higher  $q$ -shear).

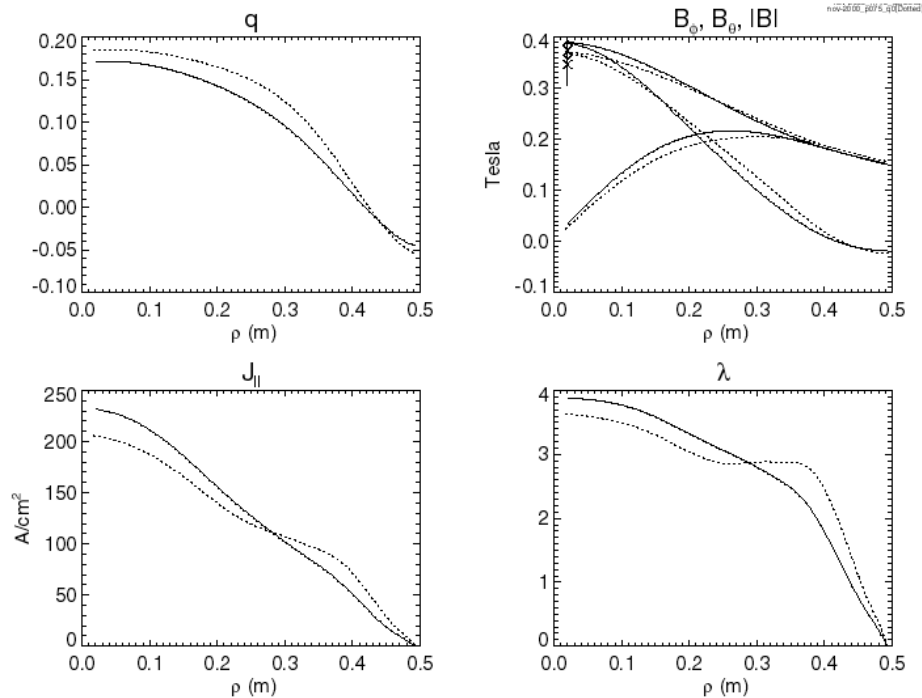


Figure 3.25 Current profile change in Standard plasmas from -1.75 ms (solid) before the crash to +0.75 ms (dotted) after the crash.

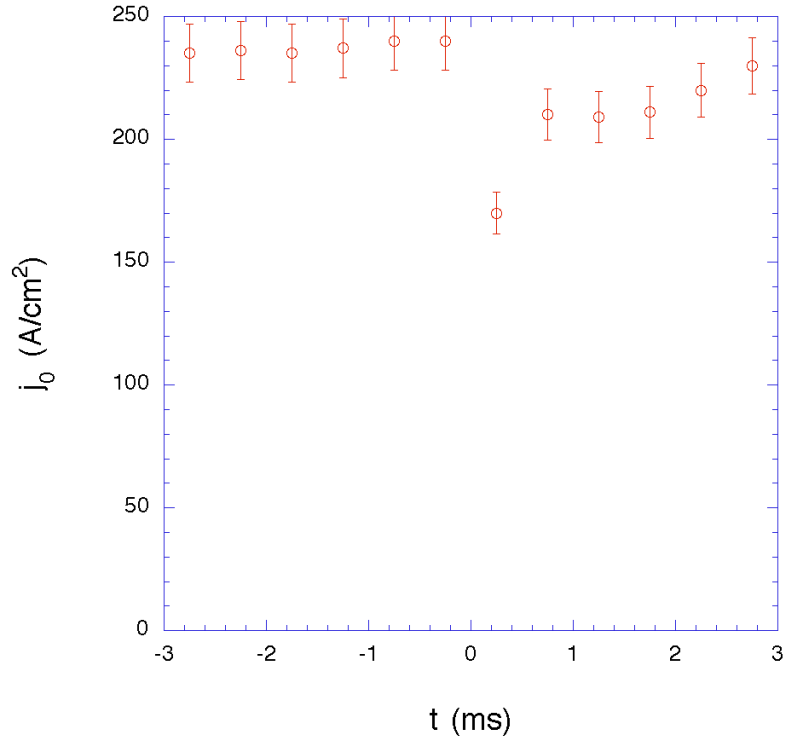


Figure 3.26 On-axis current density evolution as measured by MSTFit equilibrium reconstruction of Standard plasmas.

### 3.6 Magnetic Modes and Mode Rotation

The time dynamics of the mode spectrum are useful both to assess the overall level of magnetic fluctuations, and to examine which particular modes are in resonance at a give time, as discussed above. The experimentally observed presence of an  $m=1$ ,  $n=6$  fluctuation, for example, can serve as a constraint on the equilibrium  $q$  profile, i.e.  $q(0) \geq 1/6$ . The MST has 2 primary arrays of magnetic pick-up coil-sets, or so called Mirnov probes. The “poloidal array” is a 16-element array of equally spaced coil-sets running poloidally around the machine, located at 0 degrees toroidal, i.e. the gap. The “toroidal array” is a 64-element array of equally spaced coil-sets running toroidally around the machine, located at 241 degrees poloidal. Typically, because of digitizer shortage, only half of these coils are used,

run in either “even” or “odd” mode. These arrays can be used to resolve the amplitude, phase, and velocity of fluctuating magnetic tearing modes. The full spectra of magnetic modes are reproduced in Appendix A. Since the highest magnetic mode-number that can be resolved is approximately 1/2 the number of pick-up coils,  $n=15$  is the highest toroidal mode measured in the MST. For the analysis done here, higher- $n$  modes are not important, since by  $n=10$  the mode amplitudes have diminished significantly, almost even to the level of digitizer bit-noise.

### 3.6.1 Mode Fluctuation Amplitudes

The toroidal fluctuation  $n$ -spectra at  $-1.75$  ms and  $+0.25$  ms are shown in Figure 3.27. The broad- $n$  increase in fluctuations at the sawtooth is clear. Resolving the poloidal,  $m$ -spectra is a bit more complicated. Because of the equilibrium Shafranov shift, resolving low  $m$ -number modes is difficult. Low  $m$ -number modes have the same appearance in the pick-up coils as the Shafranov shift. This “poloidal asymmetry factor” is discussed elsewhere, but the essence is that low- $m$  modes cannot be resolved from the poloidal array in the MST.<sup>28</sup>

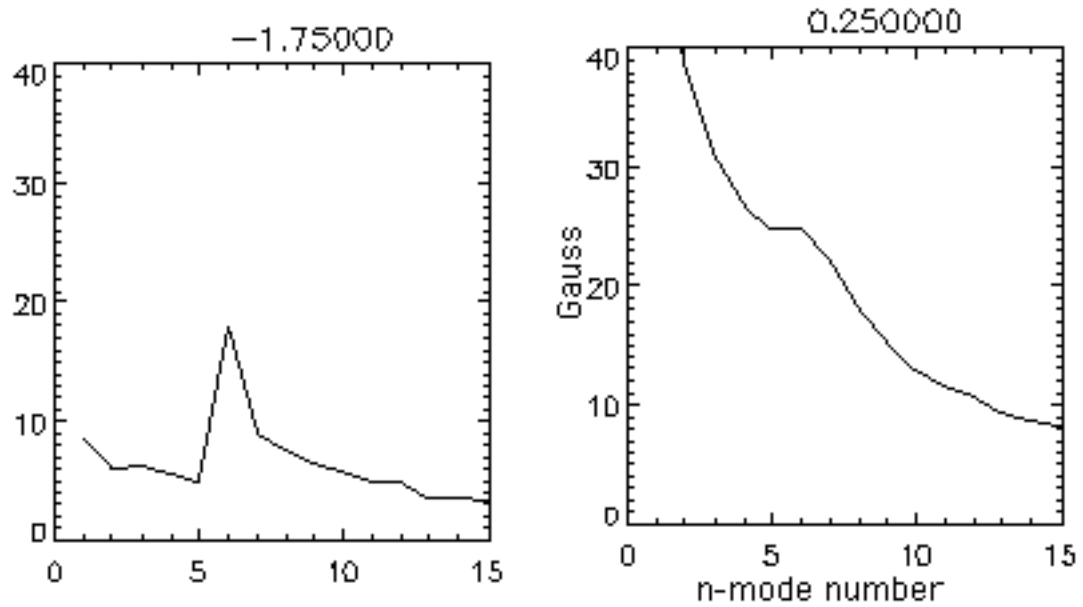


Figure 3.27 Sample n-spectra of the toroidal fluctuation amplitude at -1.75 ms and +0.25 ms. The dramatic increase of low-n fluctuations at the sawtooth is associated with  $m=0$  activity.

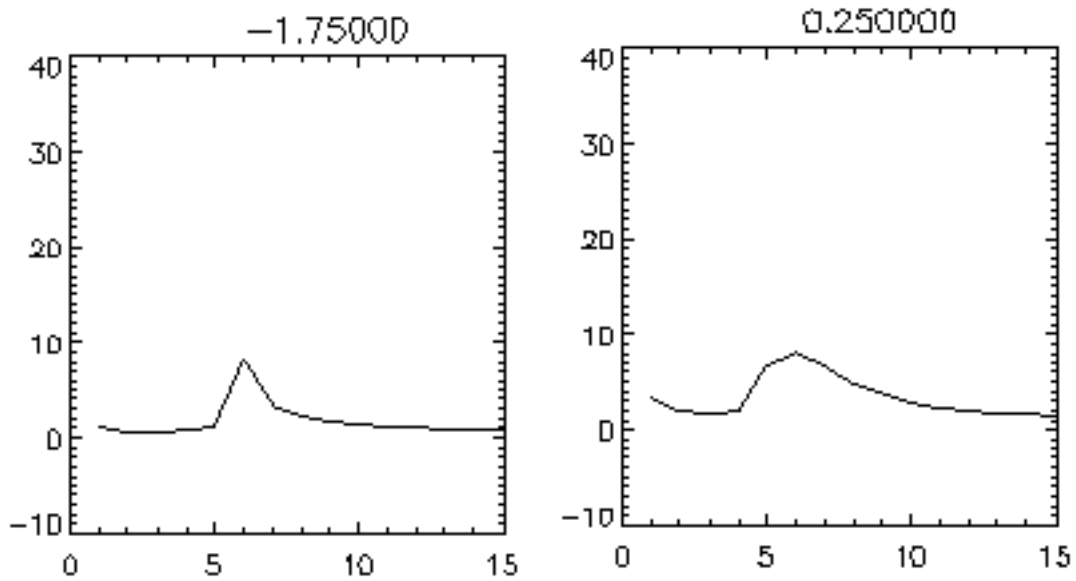


Figure 3.28 Sample n-spectra of the poloidal fluctuation amplitude at -1.75 ms and +0.25 ms. Low n-modes remain small at the sawtooth since the poloidal coilset can't distinguish  $m=0$  modes from equilibrium shifts.

The m-spectrum can, in principle, be extracted by comparing the poloidal and toroidal fluctuation amplitudes of the toroidal array. The total fluctuation amplitude of any mode is simply given by:

$$\tilde{B}(n) = \sqrt{\tilde{B}_p^2(n) + \tilde{B}_T^2(n) + \tilde{B}_r^2(n)}. \quad (16)$$

Here each  $\tilde{B}_x(n)$  is the measured poloidal, toroidal, or radial fluctuation amplitude for a given  $n$  (all  $m$ ) measured by the toroidal array. At the wall, where the pickup coil-sets are located,  $\tilde{B}_r(n)|_a = 0$ , because the MST wall appears perfectly conducting to the plasma, i.e. the resistive shell time ( $\sim 1$  s) is much larger than the fluctuation period ( $\sim 0.1$  ms).<sup>7</sup> Moreover, because the MST plasma is limited by graphite tiles approximately 1 cm from the wall, there is a thin vacuum region between the plasma and the wall, implying that  $\tilde{j}_r|_a = 0$ , which leads from Ampere's law to the relationship:

$$0 = \tilde{j}_r|_a = \frac{1}{\mu_0} \hat{r} \cdot (\nabla \times \tilde{B})_a = \frac{1}{\mu_0} (k_p \tilde{B}_T - k_T \tilde{B}_p)_a = \frac{1}{\mu_0} \left( \frac{m}{a} \tilde{B}_T - \frac{n}{R} \tilde{B}_p \right). \quad (17)$$

Hence, for the toroidal and poloidal fluctuation amplitudes at the wall:

$$\tilde{B}_T(m, n) = \frac{n}{m} \frac{a}{R} \tilde{B}_p(m, n). \quad (18)$$

Substituting, it is found that

$$\tilde{B}(m, n) = \sqrt{1 + \left( \frac{na}{mR} \right)^2} \tilde{B}_p(m, n), \quad (19)$$

where now the explicit  $m$  dependence has been drawn out. Keep in mind that the fluctuation amplitudes measured by the toroidal array contain all  $m$ 's. This expression becomes infinite for  $m=0$  modes unless  $\tilde{B}_p(0,n) \equiv 0$ , asserting that the measured poloidal fluctuation amplitude from the toroidal array is only sensitive to  $m=1$  or higher  $m$ -number modes. Another way of expressing this fact, is that poloidal magnetic fluctuations ( $\tilde{B}_p$ ) aren't measurable for  $m=0$  with a toroidal set of coils that are all at the same poloidal angle. The contribution of higher  $m$ -number modes to the  $\tilde{B}_p$  spectra can be neglected for MST Standard plasmas by considering their resonance condition. For  $m=2$  modes to be resonant the plasma requires  $n \geq 12$ , since  $q(0) \sim 1/6 = 2/12$  during most of the sawtooth cycle. Yet it is observed that the  $n > 10$  mode fluctuation amplitudes (toroidal and poloidal) are small, approaching digitizer resolution. The situation is even worse for  $m > 2$  modes. These constraints justify the approximation that  $m \geq 2$  modes are negligible:

$$\begin{aligned} \tilde{B}_p(n) &= \sum \tilde{B}_p(m,n) \\ &= \tilde{B}_p(0,n) + \tilde{B}_p(1,n) + \tilde{B}_p(2,n) + \dots \\ &\approx 0 + \tilde{B}_p(1,n) + 0 + \dots \end{aligned} \quad (20)$$

Hence the total  $m=1$  fluctuation amplitude spectrum at the wall can be found by substituting:

$$\tilde{B}(m=1,n) \approx \sqrt{1 + \left(\frac{na}{R}\right)^2} \tilde{B}_p(n). \quad (21)$$

The  $m$ -other (i.e.  $m=0, 2, 3, \dots$ ) can then easily be found from:

$$\tilde{B}(m \neq 1,n) = \sum \tilde{B}_p(m,n) \approx \tilde{B}(1,n) \approx \sqrt{\tilde{B}_T^2(n) + \tilde{B}_p^2(n)} \approx \sqrt{1 + \left(\frac{na}{R}\right)^2} \tilde{B}_p(n). \quad (22)$$

Practically, as discussed above, since the contribution from higher m-number modes is small (even for m=2):

$$\tilde{B}(m = 0, n) \approx \tilde{B}(\text{other}, n) \approx \sqrt{\tilde{B}_T^2(n) + \tilde{B}_P^2(n)} \approx \sqrt{1 + \left(\frac{ha}{R}\right)^2} \tilde{B}_P(n). \quad (23)$$

These expressions translate the measured toroidal and poloidal fluctuation amplitude spectra from the toroidal array into the total m=0 and m=1 fluctuation amplitude spectra (at the wall). Figure 3.29 shows the n-spectra for m=0 and m=1 calculated in this way at -1.75 ms in the sawtooth cycle. Figure 3.30 shows the sum over n of the fluctuation amplitude as it evolves over the sawtooth cycle for m=0 and m=1 modes. Clearly the m=0 component of the fluctuation spectrum dominates for most of the sawtooth cycle.

One caveat to these expressions is that the measured poloidal and toroidal fluctuation amplitude spectra from the toroidal array are calculated assuming cylindrical symmetry, rather than toroidal symmetry. Hence due to curvature effects, a calculated n-mode will consist of an actual n-mode and components of both actual  $n \pm 1$  modes (reduced by a factor approximately equal to the aspect ratio,  $a/R_0 \sim 0.33$ ).<sup>29</sup> This, however, is a small correction, and is of little concern in the analysis that follows.

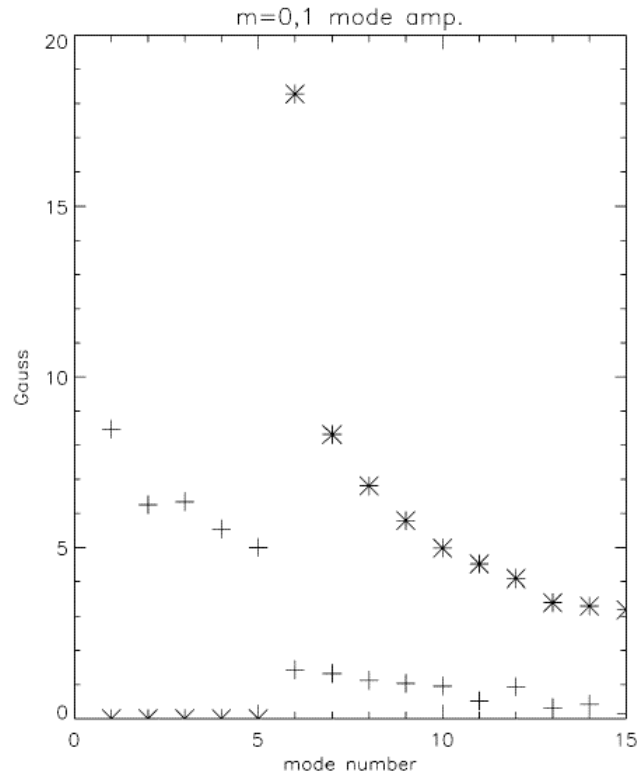


Figure 3.29 n-spectra of m=0 (+ symbol), and m=1 (\* symbol) mode fluctuation amplitudes at the wall of MST, measured at -1.75 ms in Standard plasmas.

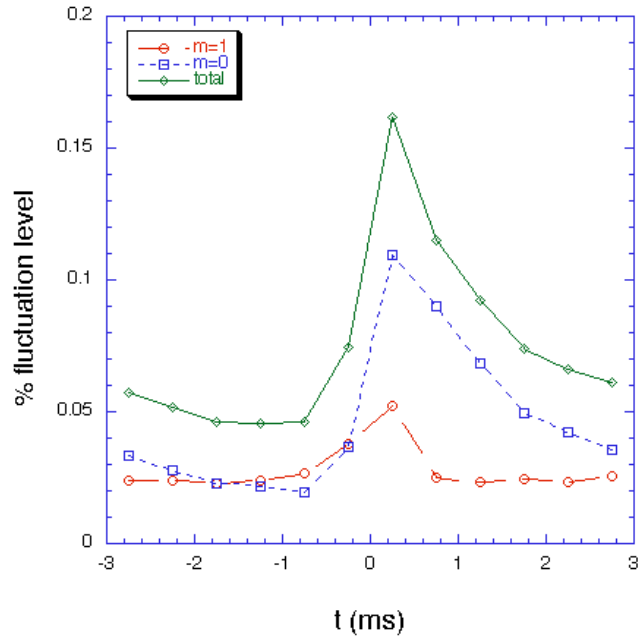


Figure 3.30 Total magnetic fluctuation amplitude (summed over n) through the sawtooth cycle in Standard plasmas.

### 3.6.2 Mode Velocities

The mode velocity of the magnetic modes is useful for estimating the radial electric field. Both the amplitude and phase of each  $n$ -mode is measured with the toroidal array for both poloidal and toroidal fluctuations. From the phase information, since the location of the coil-sets is well known, it is straightforward to calculate the toroidal rotation velocity of each mode. The toroidal mode velocity can be calculated from either the toroidal or poloidal phase, and should yield identical results (since the coil-sets run toroidally.) In practice, digitizer errors (bit noise) and signal noise can distort the phase measurement in either coil-set, leading to differences between the toroidal mode velocity as calculated from the (toroidally running) poloidal coil-set or the (toroidally running) toroidal coil-set. Since the overall amplitude of the toroidal signals is generally higher, the susceptibility to noise-induced errors in the mode velocity is lower. For that reason, the mode velocity is generally taken from the toroidal coils sensitive to toroidal fluctuations. Figure 3.31 shows the rotation velocity of the  $n=6$  mode over the sawtooth crash. The full mode rotation spectrum is reproduced in Appendix A.

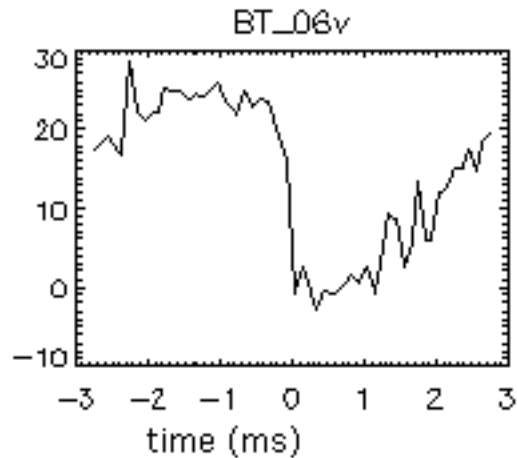


Figure 3.31  $n=6$  mode rotation velocity over the sawtooth crash during Standard plasmas. The y-axis is in km/s.

### 3.7 The Radial Electric Field

An equation relating the radial electric field, plasma rotation, and plasma pressure can be derived from considering the balance of ion momentum. For convenience, the relation is simply stated here:

$$E_r = v_{\theta,i} B_{\phi} - v_{\phi,i} B_{\theta} + \frac{\partial_r p_i}{en_i}. \quad (24)$$

$E_r$  is the radial electric field,  $v_{\theta}$  and  $v_{\phi}$  are the poloidal and toroidal ion flow velocities,  $B_{\theta}$  and  $B_{\phi}$  are the poloidal and toroidal magnetic fields,  $p_i$  is the ion pressure, and  $n_i$  is the ion number density. The ion pressure is calculated from the product of the ion temperature and ion density. The bulk ion temperature profile is measured via Rutherford scattering. The ion density profile is inferred as discussed above.

Besides the ion pressure gradient term, the other two terms above contain products of components of the ion flow velocity and components of the magnetic field. The components of the magnetic field are known from the equilibrium reconstructions. The ion flow velocity components are not as well known. Experiments in RFP's have shown that the impurity ion flow speed is strongly coupled to the magnetic mode rotation speed.<sup>30-32</sup> Hence, the mode rotation speed is representative of the toroidal bulk ion flow speed, assuming that impurity ions and bulk ions flow together. As discussed in the previous section, the rotation velocity of each mode can be individually resolved in the MST for  $n=1-15$ . From the  $q$ -profile representation of the magnetic fields, where each mode is resonant can be estimated, and thereby a plot of toroidal velocity (actually mode speed) vs. radius can be generated. This is shown by the + symbols in Figure 3.32(e). The solid line is an interpolation of this data,

which is used in the calculation of  $E_r$ . A spline interpolation is used between the  $n=6$  and  $n=10$  points. Outside of this range, a linear interpolation is used to the average slope inside of this range. Even though the Mirnov coils on the MST can theoretically resolve modes up to  $n=15$ , the mode amplitudes themselves for  $n>10$  become so small that the signals are on the order of the digitizer bit-noise. For this reason, calculations of mode velocities for  $n>10$  are highly suspect. Data is shown for  $n=11-15$  simply for the sake of comparison.

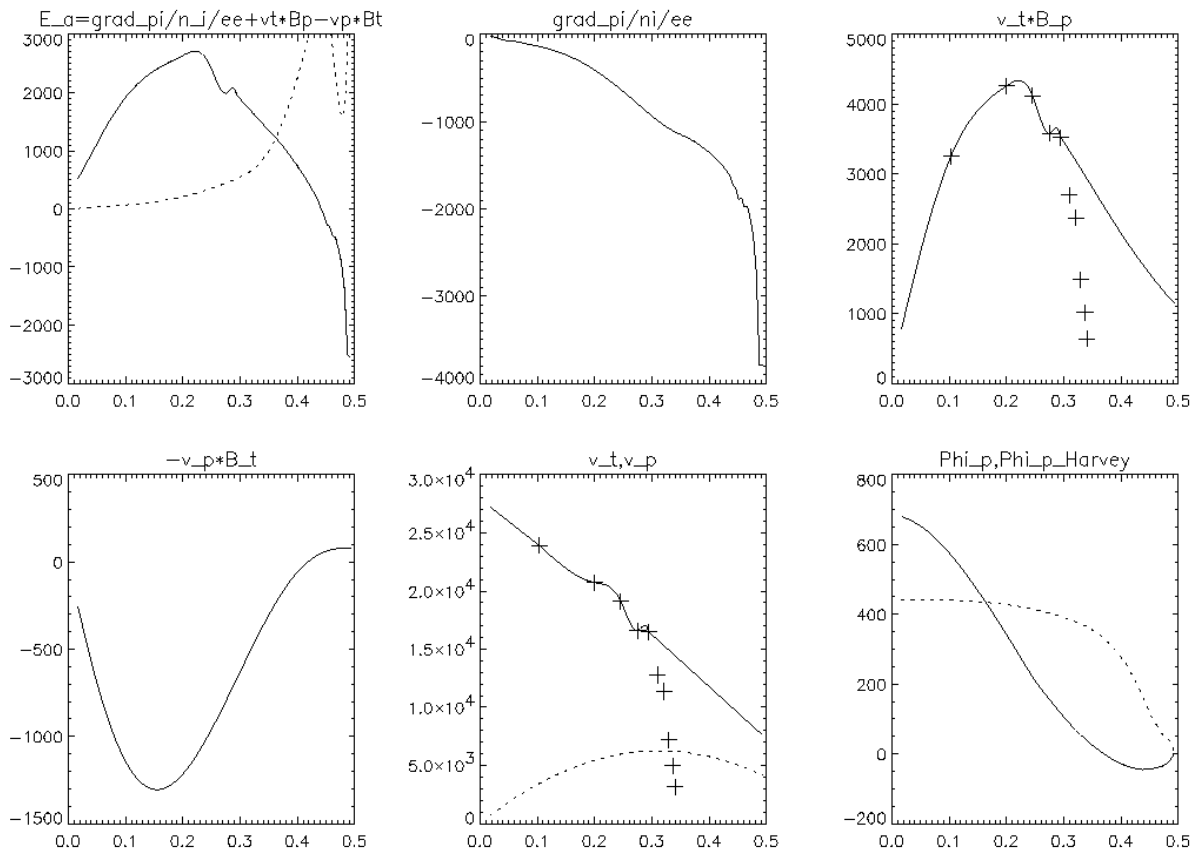


Figure 3.32 Radial electric field profile and the terms used in its calculation for a Standard plasma, -1.75 ms away from the sawtooth crash.

The poloidal flow is difficult to assess. Experiments have measured that the poloidal flow of impurity ions at the outboard edge of the MST is small ( $\sim 5$  km/s) and positive (in usual MST conventions.)<sup>33</sup> Geometrically, the poloidal flow must go to zero at the core. In this analysis, the flow has been modeled as the sum of two terms: 1) a linearly increasing

function from the core to the edge, and 2) an inverted parabola, peaked in the center of the plasma and zero at the core and edge. The result is shown as the dashed line in Figure 3.32(e), and reasonably represents the poloidal flow in the MST. The contribution to the radial electric field for the  $v_{\phi}B_{\phi}$  term is small in any case, since where  $B_{\phi}$  is large  $v_{\phi}$  must (geometrically) be small.

The solid line in Figure 3.32(a) shows the radial electric field, calculated as the sum of the terms in  $E_r$  equation, which are individually shown in Figure 3.32(b, c, and d). Note that the scales are different in each plot.  $E_r$ , as calculated by this method, is negative in the edge, increases rapidly, becomes positive, peaks near  $r \sim 0.2$  m, and finally decreases to zero in the core (as it must, geometrically.) In the RFX experiment measurements of  $E_r$  in the edge show the same profile dependence.<sup>34</sup> Since any electric field is by definition the force on a positive unit test charge, a negative  $E_r$  implies that ions are forced radially inwards and electrons outwards, which is the case at the edge of MST. If  $E_r$  is interpreted as resulting from an imbalance in the flux of electrons and ions, (i.e. that  $E_r$  is an ambipolar electric field,) then it would appear that there is an abundance of electrons in the edge, i.e. that the electrons are better confined in the edge of MST than the ions are. The converse is true in the center of the plasma where  $E_r$  is positive. Ions are in abundance, and being forced out by an ambipolar radial electric field, i.e. ions are better confined than electrons near the core of the MST. Perhaps a more accurate statement would be that electrons are poorly confined near the core of the MST, especially compared to ions. This is supported intuitively and experimentally. First, intuitively, because the ions are more massive than the electrons, they are much less mobile, and hence less susceptible to confinement degrading processes like magnetic tearing mode fluctuations. Secondly, though it was not involved at all in this calculation, the electron pressure profile is experimentally observed to be flat in the region that  $E_r$  is positive. A flat electron pressure profile indicates that electrons are poorly confined, since a gradient cannot be sustained. Indeed, most of the electron pressure gradient

appears in the edge, again where this calculation predicts that electrons are better confined than ions.

A direct measurement of the radial electric field has been made in the region of  $0.1 < r < 0.3$  m using a heavy-ion beam probe (HIBP) on the MST. These measurements indicate that  $E_r \sim +2600$  V/m over that region (see Figure 3.33), which is in rough agreement with calculations based on the ion momentum balance equation for  $E_r$ . There are a number of caveats on these measurements. The MST HIBP measures plasma potential, and relies on MSTFit equilibrium reconstructions to locate the sample volume of the measurement. This is a 3-D calculation. By “sweeping” the injection angle of the HIBP beam, the potential can be measured at different locations within the plasma. MSTFit reconstructions are then used to find the different sample locations, yielding an average potential gradient over this region. These calculations consistently indicate that the mid-plasma  $E_r$  in rotating Standard discharges is on the order of a few kV/m,<sup>35</sup> which agrees with the ion momentum balance formalism.

For comparison, the dashed line in Figure 3.32(a) is the ambipolar radial electric field expected from Harvey’s formalism for magnetically confined plasmas.<sup>36</sup> Clearly, it predicts a quite different behavior than that from the ion momentum balance equation. Since  $E_r$  is the negative gradient in the potential, the curves in Figure 3.32(a) can be integrated to estimate the potential profile up to a constant offset, as shown in Figure 3.32(f). Even if MSTFit is not used to find the sample volumes, the raw HIBP potential data indicates that as the beam is swept in injection angle, (which presumably corresponds to some change in radial sampling location) there is a steep change in potential. The solid line is the potential profile from the ion momentum balance calculation, and is quite peaked. This shape is in agreement with the raw HIBP sweep data. The potential profile from the Harvey formalism is very flat. Sweeping the HIBP beam in such a plasma would yield little change in measured potential, for a given sweep range, which is inconsistent with the HIBP sweep data.

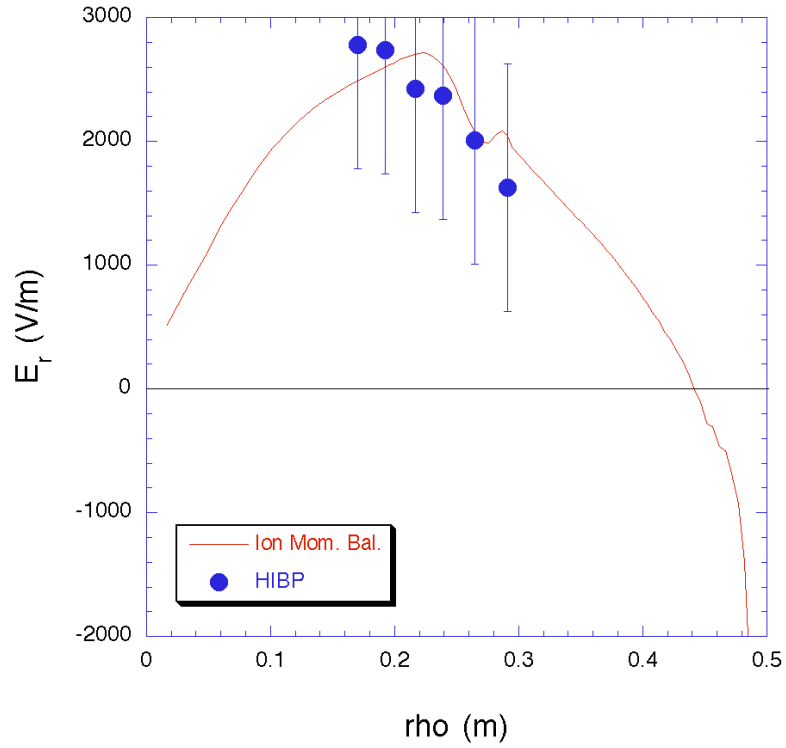


Figure 3.33 Comparison of HIBP measured radial electric field profile to that calculated from the ion momentum balance equation.

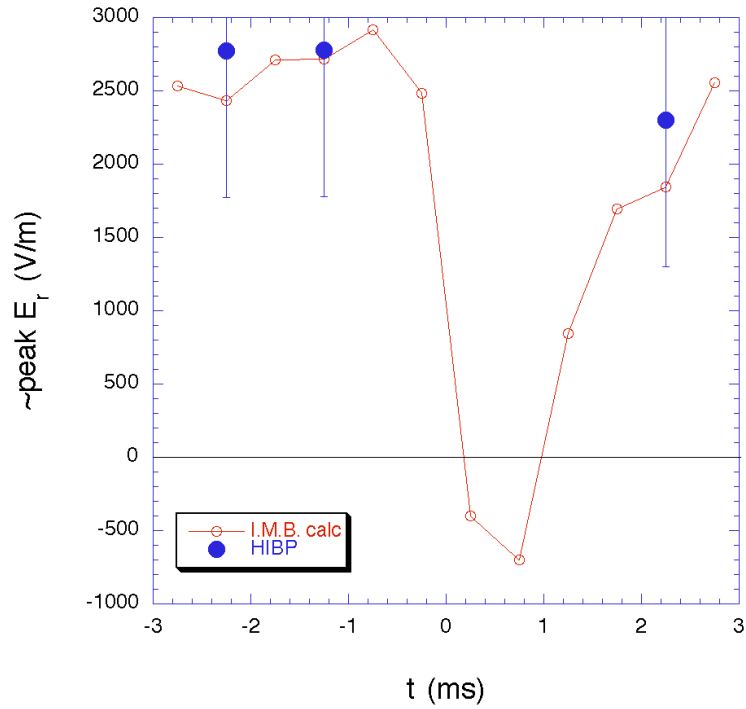


Figure 3.34 The mid-radius (~peak value) of the radial electric field as it evolves over the sawtooth cycle in Standard plasmas.

### 3.8 Summary

Diagnostic upgrades and additions have expanded the ability of experimentalists to accurately characterize the dynamics of plasmas in the MST. Time evolved profiles over the sawtooth cycle of the electron temperature and electron density have been shown for “Standard” MST plasmas, defined as  $I_p \sim 380$  kA,  $n_{e0} \sim 1.1 \times 10^{13}$  particles/cm<sup>3</sup>, and  $F \sim -0.22$ . Profiles of the majority ion temperature have also been shown for several times during the sawtooth crash. Whereas the electron temperature is observed to decrease up to a ms before the sawtooth crash, the ion temperature is observed to increase dramatically at the crash, to temperatures above the electron temperature. The causes of these variations will be examined in Chapters 4 and 5.

The development of the MSTFit equilibrium reconstruction code plays no small role in interpreting and understanding the implications of this data. A consistent set of measurements (some for the first time) have been made during Standard MST plasmas, allowing (also for the first time) the time dependence of the current density profile through the sawtooth cycle to be characterized. The current density profile evolution plays a major role in understanding the energy-budget of the plasma, since MST plasmas are Ohmically heated. Implications for heat and particle transport will be examined further in Chapter 4.

Charged particle transport is highly susceptible to the presence of electric fields. Quasi-neutral plasmas will establish radial electric fields in response to the ambipolar movement of electrons and ions, which have differing mobilities. The radial electric field has been measured for the first time in the MST using the HIBP diagnostic. It agrees well with the calculated radial electric field that is expected from ion momentum balance.

## References

1. G.A. Wurden, *Physics of Fluids*, **27** (3), 551-554 (1984).
2. D.A. Baker, C.J. Buchenauer, L.C. Burkhardt, et al., in *10<sup>th</sup> International Conference on Plasmas Physics and Controlled Nuclear Fusion Research*, London., Vol. 2, IAEA, Vienna (1984) 2-9.
3. K.A. Werley, R.A. Nebel, G.A. Wurden, *Physics of Fluids*, **28** (5), 1450-1453 (1985).
4. B.E. Chapman, M. Cekic, J.T. Chapman, C.S. Chiang, D.J. Den Hartog, N.E. Lanier, S.C. Prager, M.R. Stoneking, Poster from the *Bulletin of the American Physical Society*, Denver, Colorado (1996).
5. R. Gatto, P.W. Terry, C.C. Hegna, submitted to *Nuclear Fusion*, (2001).
6. B.E. Chapman, Private communication.
7. J.T. Chapman, *Spectroscopic Measurements of the MHD Dynamo in the MST Reversed Field Pinch*, Ph.D. Thesis, University of Wisconsin-Madison (1998).
8. D.L. Brower, Y. Jiang, W.X. Ding, S.D. Terry, N.E. Lanier, J.K. Anderson, C.B. Forest, D.H. Holly, *Review of Scientific Instruments*, **72** (1), 1077-1080 (2001).
9. J.K. Anderson, *Measurement of the Electrical Resistivity Profile in the Madison Symmetric Torus*, Ph.D. Thesis, University of Wisconsin-Madison (2001).
10. M. Cekic, J.S. Sarff, D.J. Den Hartog, S.C. Prager, "Magnetic Fluctuation Induced Energy Transport During Sawtooth Events in the MST Reversed-Field Pinch," MST Group internal report, University of Wisconsin-Madison.
11. B.E. Chapman, Private communication.
12. R.B. Howell, J.C. Ingraham, G.A. Wurden, P.G. Weber, C.J. Buchenauer, *Physics of Fluids*, **30** (6), 1828 (1987).
13. H. Ji, H. Toyama, K. Miyamoto, S. Shinohara, and A. Fujisawa, *Phys. Rev. Lett.* **67** (1), 62-65 (1991).

14. D.J. Den Hartog, D. Craig, "Isotropy of ion heading during a sawtooth crash in a Reversed-Field Pinch," MST Group internal report, University of Wisconsin-Madison (2000).
15. S. Hokin, A. Almagri, M. Cekic, B. Chapman, N. Crocker, D.J. Den Hartog, G. Fiksel, J. Henry, H. Ji, S. Prager, J. Sarff, E. Scime, W. Shen, M. Stoneking and C. Watts, *Journal of Fusion Energy*, **12** (3), 281-287 (1993).
16. P.G. Carolan, A.R. Field, A. Lazaros, M.G. Rusbridge, H.Y.W. Tsui, and M.V. Bevir, *Proceedings of the 14<sup>th</sup> European Conference on Controlled Fusion and Plasma Physics*, Madrid, EPS, Petit-Lancy, **2**, 469 (1987).
17. G.A. Wurden, P.G. Weber, K.F. Schoenberg, et al., in *15<sup>th</sup> European Conference on Controlled Fusion and Plasmas Physics*, Vol. 12B, 533 (European Physical Society, Dubrovnik, 1988).
18. A. Ejiri, K. Miyamoto, *Plasma Physics and Controlled Fusion*, **37**, 43-56 (1995).
19. J.M. McChesney, P.M. Bellan, R.A. Stern, *Physics of Fluids B*, **3** (12), 3363-3378 (1991).
20. J.C. Reardon, T.M Biewer, B.E. Chapman, D. Craig, and G. Fiksel, Poster from the *Bulletin of the American Physical Society*, Long Beach, California (2001).
21. W.A. Houlberg, *Nuclear Fusion*, **27** (6), 1009-1020 (1987).
22. N.E. Lanier, *Electron Density Fluctuations and Fluctuation-Induced Transport in the Reversed-Field Pinch*, Ph.D. Thesis, University of Wisconsin-Madison (1999).
23. D.J. Den Hartog, D. Craig, G. Fiksel, Poster from the *Bulletin of the American Physical Society*, Long Beach, California (2001).
24. D. Craig, G. Fiksel, D.J. Den Hartog, Private communications.
25. S. Terry, W. Ding, Private communications.
26. U. Shah, K.A. Connor, J. Lei, P.M. Schoch, D.R. Demers, J.G. Schatz, Poster from the *Bulletin of the American Physical Society*, Long Beach, California (2001).

27. J.B. Taylor, Rev. of Modern Physics, **58** (3), 741-763 (1986).
28. D. Craig, Private communication.
29. J.S. Sarff, Private communication.
30. J.S. Sarff, A.F. Almagri, J.K. Anderson, B.E. Chapman, D. Craig, C.S. Chiang, N.A. Crocker, D.J. Den Hartog, G. Fiksel, A.K. Hansen, S.C. Prager, Czech. Jour. Phys., **50** (12), 1471-1476 (2000).
31. H. Sakakita, Y. Yagi, Y. Hirano, T. Shimada, S. Sekine, T. Hirota, Y. Maejima, H. Koguchi, T.J. Baig, Jpn. J. Appl. Phys., **38** (7A), 4187-4193 (1999).
32. D.J. Den Hartog, A.F. Almagri, J.T. Chapman, G. Fiksel, C.C. Hegna, S.C. Prager, presented at the 9<sup>th</sup> National Topical Conference on High-Temperature Plasma Diagnostics, St. Petersburg, Russia (1997).
33. D. Craig, Private communication.
34. V. Antoni, R. Cavazzana, L. Fattorini, E. Martines, G. Serianni, M. Spolaore, L. Tramontin, and N. Vianello, Plasma Phys. Control. Fusion, **42**, 893-904 (2000).
35. U. Shah, Private communication.
36. R.W. Harvey, M.G. McCoy, J.Y. Hsu, A.A. Mirin, Phys. Rev. Let., **47** (2), 102-105 (1981).
37. B.E. Chapman, A.F. Almagri, J.K. Anderson, C.S. Chiang, D. Craig, G. Fiksel, N.E. Lanier, S.C. Prager, M.R. Stoneking, and P.W. Terry, Phys. Plasmas, **5** (5), 1848-1854 (1998).



Let our people travel light and free on their bicycles!

--Edward Abbey, *Desert Solitaire*

## Transport through the Sawtooth Cycle

Based on the kinetic profile measurements that were presented in the previous chapter, the movement of heat and particles throughout the plasma is estimated. First, at the plasma edge, 0-dimensional quantifications of global transport will be shown through the sawtooth cycle:  $\chi_{e,e}$  and  $\chi_p$ . Then the measured profiles presented in the previous chapter will be used to develop 1-D measures of transport:  $\chi_e$  and  $D_e$ . The primary results are: 1) A heat transport barrier exists near the edge of the plasma, which governs the whole-plasma confinement. 2) The overall heat transport in the core and mid-radius region is higher before the crash, even though  $\tilde{B}^2$  peaks after the crash. 3) Energy transport is primarily conductive ( $\chi_e \sim 400 \text{ m}^2/\text{s}$  and  $D_e \sim 5 \text{ m}^2/\text{s}$ ).

### 4.1 Energy Confinement Time

#### 4.1.1 Total Energy Confinement Time

Before presenting the detail of a 1-D transport analysis, an important figure of merit is the energy confinement time, which is a measure of how long a unit of thermal energy stays in the plasma. The energy confinement time is defined by the relation:

$$\tau_E = \frac{W}{P_{\square} \chi \frac{\partial W}{\partial a}}, \quad (25)$$

where  $W$  is the stored thermal energy and  $P_{\square}$  is the total Ohmic input power:

$$W = W_e + W_i = \int_0^a \left[ \frac{3}{2} n_e T_e + \frac{3}{2} n_i T_i \right] \frac{\partial V}{\partial \square} d\square. \quad (26)$$

$W$  and  $P_{\square}$  are found by integrating out to the edge of the plasma, giving a 0-D measure of the global plasma performance. Finding the stored thermal energy is straightforward, given the profiles of  $n_e$ ,  $T_e$ ,  $n_i$ , and  $T_i$  that were discussed above. Since these profiles were measured at 12 time slices throughout the sawtooth cycle, the  $\frac{\partial W}{\partial t}$  ( $= \dot{W}$ ) term can be estimated by calculating a 3-point, finite-time derivative from two adjacent time slices. This process can be improved somewhat since the density is measured at a much higher data-rate. Hence the time derivative of the density data itself can be ensembled and binned to 100  $\mu$ s as the density data is. Separating the terms:

$$\dot{W} = \dot{W}_e + \dot{W}_i = \int_0^a \left[ \frac{3}{2} n_e \frac{\partial T_e}{\partial t} + T_e \frac{\partial n_e}{\partial t} + n_i \frac{\partial T_i}{\partial t} + T_i \frac{\partial n_i}{\partial t} \right] \frac{\partial V}{\partial \square} d\square. \quad (27)$$

This yields slightly more accuracy in finding  $\dot{W}$ , when combined with the temperature data, which is estimated from finite-time derivatives.

Estimating  $P_{\square}|_a$  is the crux of accurately calculating the energy confinement time. One method of estimating the Ohmic input power at the edge is to apply Poynting's theorem:

$$P_{\square} = \int_{\text{Poynt.}} \int_{\text{mag}} \dot{W}_{\text{mag}} = \int_0^a \frac{1}{\mu_0} \oint_S (\mathbf{E} \times \mathbf{B}) \cdot d\mathbf{a} = \frac{\partial}{\partial t} \int_V \frac{1}{2} (\mu_0 E^2 + B^2 / \mu_0) dV. \quad (28)$$

At the edge of the MST, this expression reduces to:

$$P_{\text{a}} I_{\text{a}} = (I_{\text{p}} V_{\text{pg}} - \frac{R_0}{a} I_{\text{p}} V_{\text{pg}}) \dot{W}_{\text{mag}} - (I_{\text{p}} V_{\text{pg}} - \frac{R_0 B_0}{\mu_0 / 2} V_{\text{Tg}}) \dot{W}_{\text{mag}}, \quad (29)$$

where  $V_{\text{pg}}$  and  $V_{\text{Tg}}$  are the measured voltages across the poloidal and toroidal gaps, respectively,  $B_0$  is the on-axis toroidal magnetic field (measured by MSE), and  $R_0$  is the major radius of the shifted magnetic axis (calculable with MSTFit), or approximately the major radius of the torus. The remaining quantity needed for this technique is the time-change of electromagnetic energy. Since  $\mu_0$  is much, much smaller than  $1/\mu_0$ , the approximation can be easily made that:

$$\dot{W}_{\text{mag}} = \frac{\partial}{\partial t} \int_V \frac{1}{2} (\mu_0 E^2 + B^2 / \mu_0) dV - \frac{\partial}{\partial t} \int_V \frac{1}{2 \mu_0} B^2 dV. \quad (30)$$

Because the magnetic equilibrium has been reconstructed at 12 time slices separated by 0.5 ms throughout the sawtooth cycle, a finite time difference of the stored magnetic energy can be calculated to estimate this term. As long as the equilibrium magnetic fields are not changing much this term is a small correction.

It is customary in the day-to-day operation of the MST to calculate a toroidal “loop voltage” from the Ohmic input power and the measured plasma current:

$$P_{\text{a}} I_{\text{a}} = V_{\text{loop}} I_{\text{p}}. \quad (31)$$

During daily operation MSTFit reconstructions of the equilibrium fields are not available, so parameterized models (such as the  $\mu$ -model or the polynomial function model (PFM)) of the equilibrium plasma are used to calculate the Ohmic input power and the loop voltage.<sup>1</sup> These models differ from the method discussed above only in the way that the change in magnetic energy is calculated. Hence, all of these models work well for finding  $P_{\text{a}}$  if the plasma is in a

“strong” equilibrium, but they fail miserably if it is not, e.g. near the sawtooth crash, or during PPCD.<sup>2</sup> Comparisons between these models and MSTFit reconstructions are beyond the scope of this text, but calculations of  $P_{\square}$  are shown in Figure 4.1.

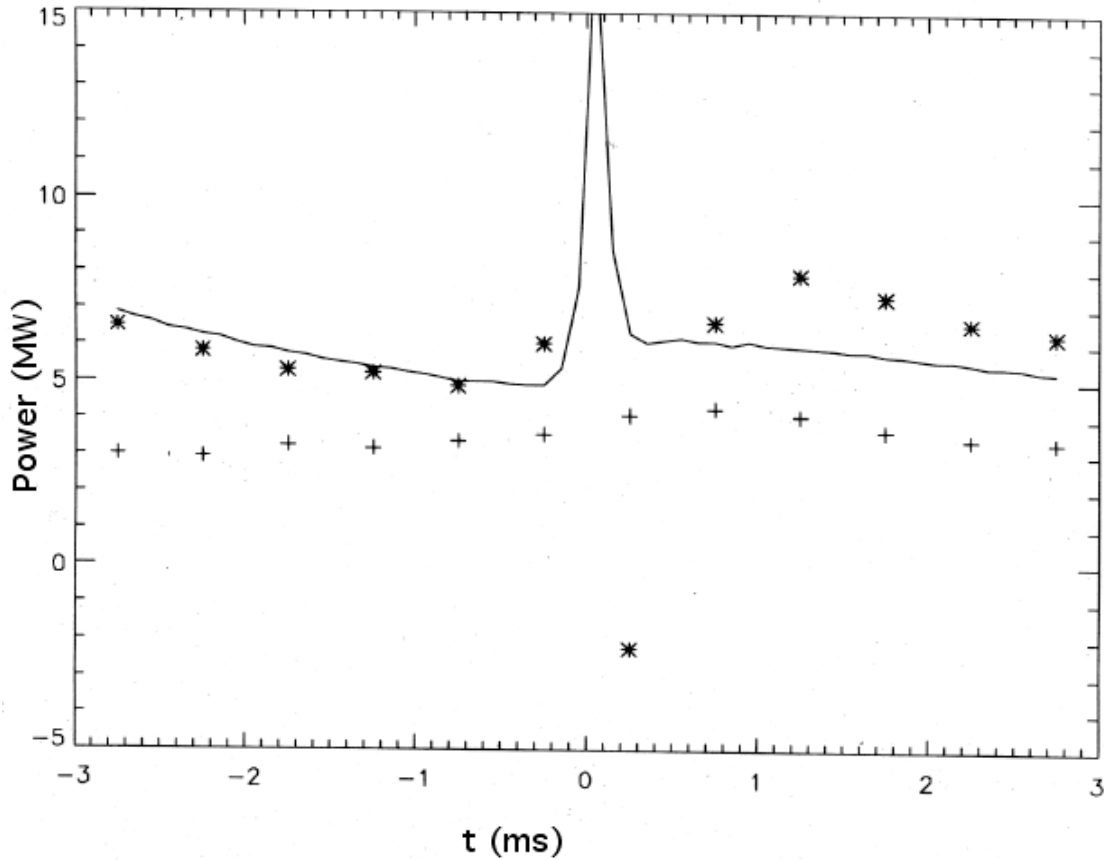


Figure 4.1 Comparison of the calculated Ohmic input power at the edge from the  $R$ -model (\*) and from finite time-slice MSTFit (solid line). For comparison, the value of  $\int j^2$  from MSTFit integrated over the volume is also shown (+) with flat  $Z_{\text{eff}}(r)=2$ .

It is a useful exercise to compare  $P_{\square}|_a$  from Poynting’s theorem to the integral of  $\int j^2$ , which should also be a measure of the Ohmic input power:

$$P_{\square} = \int (\mathbf{E} \cdot \mathbf{j}) \frac{\partial V}{\partial \square} \partial \square = \int (\square \mathbf{j} \cdot \mathbf{j}) \frac{\partial V}{\partial \square} \partial \square = \int (\square j^2) \frac{\partial V}{\partial \square} \partial \square. \quad (32)$$

This assumes that the electric field in the plasma obeys a simple Ohm's Law, i.e. that

$$E = \eta j, \quad (33)$$

which has been shown to be experimentally invalid during periods of intense plasma turbulence.<sup>3</sup> During these periods, e.g. particularly near the sawtooth crash or when magnetic fluctuations are large, the MHD dynamo plays an important role in redistributing flux and driving current in the plasma. Including the MHD dynamo, then

$$E = \eta j + \langle \tilde{v} \times \tilde{B} \rangle. \quad (34)$$

Here  $\langle \dots \rangle$  represents a flux-surface average over the dynamo driven fluctuating plasma velocity and magnetic field.<sup>4</sup> This correlated cross-product of fluctuating quantities has been measured in the past.<sup>3</sup> Away from the sawtooth crash, this term is small. Since the dynamo term was not measured explicitly in these experiments, any deviation from a simple Ohm's Law will be accounted for in an anomalous resistivity:

$$E = \eta^* j. \quad (35)$$

Moreover, it will be cast as a measure of the unknown quantity,  $Z_{\text{eff}}^*$ :

$$\eta^*(n_e(r), T_e(r), Z_{\text{eff}}(r)) = \eta(n_e(r), T_e(r), Z_{\text{eff}}^*(r)). \quad (36)$$

In the above expression the estimation of the plasma resistivity follows the neoclassical development of Hirschman and Sigmar.<sup>5</sup> In this manner,  $Z_{\text{eff}}^*$  is the value of  $Z_{\text{eff}}$  necessary in the resistivity calculation, such that

$$\left(\frac{\partial V}{\partial \alpha}\right)^2 = P_{\alpha} l_a V_{loop} I_p. \quad (37)$$

$Z_{eff}^*$  contains contributions to the resistivity from possible dynamo driven currents, from current carried by fast electrons, and from simple impurity effects. Practically,  $Z_{eff}^*$  is somewhat higher than MST experience would suggest for  $Z_{eff}$  ( $\sim 3.5$  instead of  $\sim 2$ ), which is why it is presented here as an “anomalous”  $Z_{eff}^*$ , rather than as a measurement of  $Z_{eff}$ . At present,  $Z_{eff}$  cannot be measured in the MST except in the most quiescent plasmas, i.e. during PPCD.<sup>6</sup> (As an aside, when this was attempted it was discovered that  $Z_{eff}$  in the core is  $\sim 5$ .) These PPCD plasmas are so radically different from Standard MST plasmas, that it is probably not useful to estimate  $Z_{eff}$  in Standard plasmas from PPCD plasmas. This will be discussed in further detail when the profiles of Ohmic power deposition are calculated in Section 4.3.

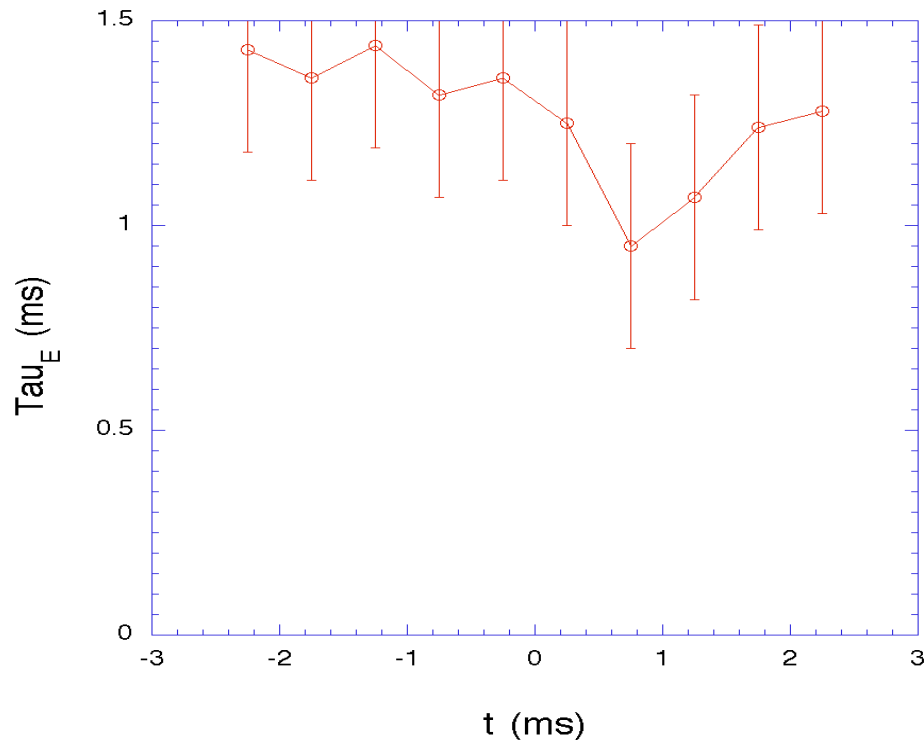


Figure 4.2 The total energy confinement time over a sawtooth cycle in Standard plasmas.

#### 4.1.2 Electron Energy Confinement Time

Before discussing the spatial variations in energy transport, it is useful to examine the global electron energy confinement time. That is, the period of time that a unit of energy specifically resides in the electrons. To do this it is necessary to examine how the input power is distributed between the ions and electrons and to understand how this power eventually leaves the plasma. These mechanisms of power distribution will be discussed further in Section 4.3. Because of their greater mobility, the Ohmic power is expected to flow into the electrons. The electrons are expected to lose energy to the ions through collisional heating and to the wall through line radiation. The ions, heated by the electrons, have an additional channel of energy loss through charge-exchanging collisions with cold neutral atoms. The radial particle flux, which can flow up a potential gradient, can be a source of significant power re-distribution between the electrons and ions as they move, but for Standard plasmas in the MST the structure of the radial electric field is such that any given particle will gain roughly as much energy as it loses by the time it reaches the edge of the plasma. (The power imbalance at the edge is  $\sim 1$  kW lost by the electrons, gained by the ions. For comparison, the Ohmic input power is on the order of 5 MW.) Examining the terms that only affect the electrons, the electron energy confinement time can be defined as:

$$\tau_{E,e} = \frac{W_e}{P_{\square} - P_{e \rightarrow i} - P_{\text{rad}} - \frac{\partial W_e}{\partial t}}. \quad (38)$$

Figure 4.3 shows the dependence of the electron energy confinement time over the sawtooth cycle. Since the radiated power increases dramatically after the crash, subtracting that term in the denominator results in an increase in the calculated confinement time. For comparison, the confinement time is also shown, without subtracting these “loss terms,”

which will be discussed in more detail in Section 4.3.2. Because of the way that  $Z_{\text{eff}}^*$  is defined above,  $P_{\square}$  contains any possible contributions of power that drives the MHD dynamo. This possible dynamo power will be more important when examining the ions, in Section 5.4.

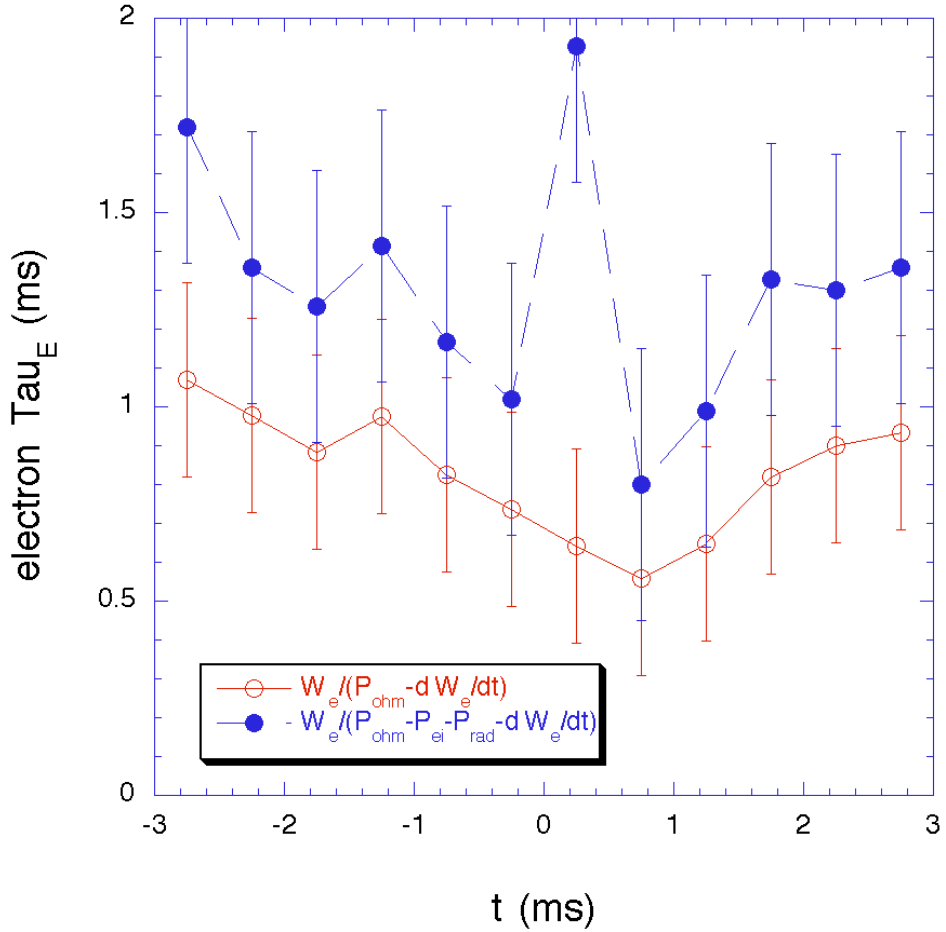


Figure 4.3 The electron energy confinement time over the sawtooth cycle in Standard plasmas.

### 4.2 Particle Confinement Time

Another figure of merit in any plasma device is the particle confinement time, which gives a measure of how long average plasma particles are confined in the machine. For electrons, it is defined as follows:

$$\tau_{p,e} = \frac{\int n_e \frac{\partial V}{\partial \Omega} d\Omega}{\int (S_{p,e} - \frac{\partial n_e}{\partial t}) \frac{\partial V}{\partial \Omega} d\Omega}. \quad (39)$$

Here  $S_{p,e}$  represents all sources of electrons. MST plasmas are largely fueled by neutral deuterium atoms from gas puffing and from wall recycling (although impurities may contribute). If  $dn_e/dt=0$  then the electron fueling rate must be equal to the electron loss rate. Or, including a change in the overall density,

$$S_{p,e} - \frac{\partial n_e}{\partial t} = S_{\text{loss},e}. \quad (40)$$

The emission of  $D_\alpha$  radiation is proportional to the ionization rate of neutral D, hence  $D_\alpha$  can be related to the neutral  $D_2$  density, and through further calculations to the particle source rate (which must approximately balance the loss rate.) Since there is no net current to the wall if the plasma remains overall charge neutral, electrons are lost from the plasma either directly to the wall at the same rate as ions, or through recombination with ions into neutral particles. Recombination is a relatively small contribution to the particle budget. For a more detailed discussion see the Ph.D. theses of Jay Anderson and/or Nick Lanier.<sup>6,7</sup> From the measured  $D_\alpha$  emission profile the electron source rate, and hence the denominator in the above equation, can be found, allowing the particle confinement time to be calculated. Technically, this is the particle confinement time for electrons, but for charge neutrality of the plasma to be maintained, the ion confinement time (averaged over the entire plasma) should be the same.<sup>8</sup>

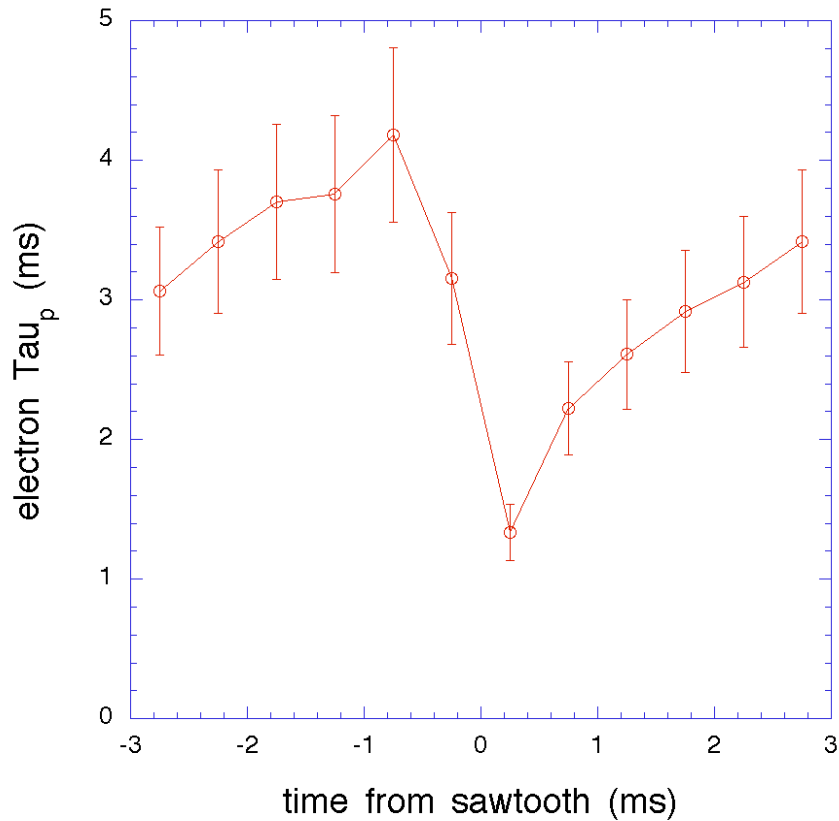


Figure 4.4 Particle confinement time through the sawtooth cycle for Standard plasmas.

Previous measurements have shown that the particle confinement time and the energy confinement time are nearly equal in Standard MST plasmas.<sup>7,9</sup> Comparing Figure 4.2 (or Figure 4.3) and Figure 4.4, however, shows that the measured particle confinement time is approximately 4 times greater than the energy confinement time. This may simply be the case, and no further discussion is necessary. The particle confinement time calculation is, however, heavily dependent on the calibration of the particle source measurement, i.e. the  $D_{\square}$  array of detectors. This calibration itself can change from week to week as the MST is run, since it has been observed that a thin hydrocarbon layer is deposited on the wall (and in particular on optical surfaces) of the machine over long periods of time. Decreased  $D_{\square}$  light in the diagnostic would be interpreted as a lower particle flux, and result in a higher

calculated particle confinement time, which is in the same direction as the trend indicated here.

### 4.3 Electron Heat and Particle Fluxes

#### 4.3.1 Particle Flux

The continuity equation for electrons is:

$$\frac{\partial n}{\partial t} = -\frac{1}{r} \frac{\partial}{\partial r}(r\Gamma) + S_p, \quad (41)$$

where  $S_p$  denotes the sum of possible “sources and sinks” of particles. The ionization rate can be estimated from  $D_{\alpha}$  arrays as discussed in the previous section, allowing the electron flux to be solved for:

$$\Gamma_e = \frac{1}{r} \int (S_{p,e} - \frac{\partial n_e}{\partial t}) r dr \quad (42)$$

Figure 4.5 shows the profile of electron particle flux at two different times during the sawtooth cycle. If the plasma is assumed to be quasi-neutral, and if the contributions from impurities are small ( $n_Z \sim 0.01n_e$  compared to  $n_i \sim 0.80n_e$  for a reasonable  $Z_{eff}$ ), then  $\Gamma_e \sim \Gamma_i$ . The particle flux is clearly larger after the sawtooth crash.

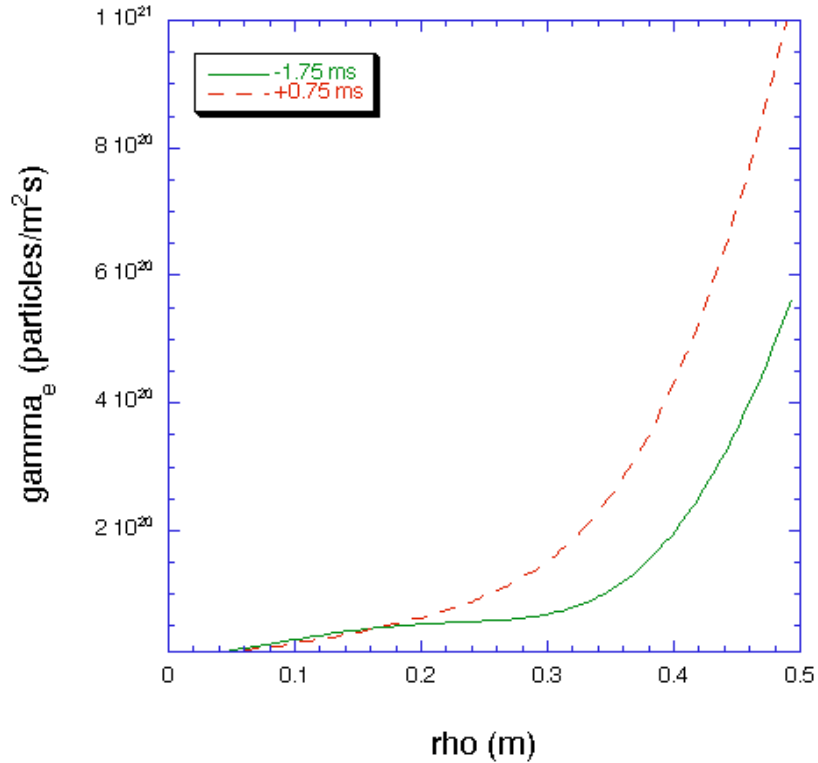


Figure 4.5 Measured electron flux profile at -1.75 ms and +0.75 ms relative to the sawtooth crash in Standard discharges.

#### 4.3.2 Power Deposition Profiles

Estimating the Ohmic input power profile,  $P_{\square}(r)$ , is the crux of accurately calculating the local electron power balance. One method of estimating  $P_{\square}$  is to apply Poynting's theorem:

$$P_{\square} = \square P_{\text{Poynt.}} \square \dot{W}_{\text{mag}} = \square \frac{1}{\square_0} \oint_{\square} (\mathbf{E} \square \mathbf{B}) \cdot d\mathbf{a} \square \frac{\partial}{\partial t} \left[ \frac{1}{2 \square_0} B^2 dV \right]. \quad (43)$$

If the profiles of the electric and magnetic fields,  $\mathbf{E}$  and  $\mathbf{B}$ , are known at each time, then  $P_{\square}(r)$  can be calculated without estimating the plasma resistivity.

The electric and magnetic fields can be found from the equilibrium reconstructions provided by MSTFit. MSTFit iteratively solves the Grad-Shafranov equation at each time slice for the poloidal and toroidal flux functions,  $\psi$  and  $\chi$ , which best fit the available data. It is straightforward to reconstruct the equilibrium current density and magnetic field at each time slice from these flux functions, using Maxwell's Equations. Moreover, utilizing Maxwell's Equations and finite difference time derivatives the electric field can be easily found from successive time slices:

$$E_{\psi} = -\frac{\partial \psi}{\partial t} = -\frac{1}{2R} \frac{\partial \chi}{\partial t}, \quad (44)$$

$$E_{\chi} = -\frac{\partial \chi}{\partial t} = -\frac{1}{R} \frac{\partial \psi}{\partial t}. \quad (45)$$

Likewise, the change in magnetic energy can easily be calculated:

$$\frac{\partial B^2}{\partial t} = \frac{\partial B^2}{\partial t}. \quad (46)$$

Finding the E and B fields in this manner allow  $P_{\psi}(r)$  to be calculated without measuring the plasma resistivity, or measuring  $Z_{\text{eff}}(r)$ .

For the sake of comparison, it is easy to assume a simplified Ohm's law with anomalous neoclassical resistivity, and to calculate the  $Z_{\text{eff}}$  that is implied:

$$P_{\psi} = \eta^* j^2. \quad (47)$$

The plasma current density profile is represented by  $j$ , and  $\eta^*$  is the anomalous resistivity profile. Again, the anomaly is cast in the form of  $Z_{\text{eff}}^*(r)$ , assuming neoclassical resistivity. Figure 4.6 shows the approximate  $Z_{\text{eff}}^*(r)$  parameterization profile that is necessary for the

power deposition profile to match the result of Poynting's theorem. This  $Z_{\text{eff}}^*$  contains effects from actual impurities, but also effects of MHD dynamo power re-distribution, and effects from bulk and fast electrons. It is perhaps worth noting that this  $Z_{\text{eff}}^*$  profile peaks where dynamo activity is expected to drive parallel current.<sup>10</sup>

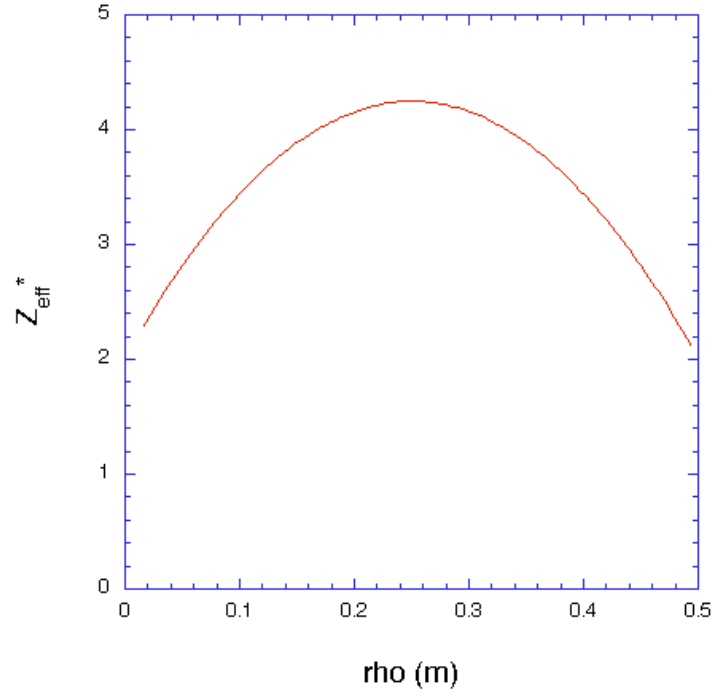


Figure 4.6 The parameterized profile of effective  $Z_{\text{eff}}$  in Standard plasmas away from the sawtooth crash.

Since  $E$  and  $B$  are not independently measured, the contribution of the MHD dynamo is implicitly included in the estimation of  $P_w$ . This can be seen by expanding  $E$ ,  $B$ , and  $j$  in terms of mean-field and fluctuating components within Poynting's Theorem:

$$\mathbf{E} \cdot \mathbf{j} = \frac{1}{2} \frac{\partial}{\partial t} \langle \mathbf{E}^2 \rangle + \frac{1}{\mu_0} \mathbf{B}^2 \langle \frac{1}{\mu_0} \rangle \cdot (\mathbf{E} \times \mathbf{B}). \quad (48)$$

This leads to the expression:

$$\langle p_{\square} \rangle = \bar{\mathbf{E}} \cdot \bar{\mathbf{j}} + \langle \tilde{\mathbf{E}} \cdot \tilde{\mathbf{j}} \rangle = \frac{1}{2\mu_0} \frac{\partial \bar{\mathbf{B}}^2}{\partial t} \frac{1}{\mu_0} \langle \bar{\mathbf{E}} \cdot \bar{\mathbf{B}} \rangle + \frac{1}{2\mu_0} \frac{\partial \tilde{\mathbf{B}}^2}{\partial t} \frac{1}{\mu_0} \langle \tilde{\mathbf{E}} \cdot \tilde{\mathbf{B}} \rangle. \quad (49)$$

Dynamo fluctuations result in an electro-motive force (EMF), which sums with the inductive electric field to drive current in the resistive plasma. The effects of this current are measured in the diagnostics that are used to constrain the MSTFit reconstruction of the equilibrium  $\mathbf{B}$  and  $\mathbf{j}$  and each time point. These time slices are then used to find  $\mathbf{E}$ . Hence the MHD dynamo contribution is included in the term represented by the mean electric field dotted into the mean current density. Because  $\mathbf{E}$  and  $\mathbf{B}$  are not measured independently, this term is identically equal to the sum of the first two terms on the right-hand side of the above equation. Any current fluctuations, e.g. from the magnetic tearing modes or the dynamo, come into play in the other terms above, and are probably small.

### 4.3.3 Heat Flux

Similarly, the electron heat flux can be approached. Including possible sources and sinks of energy,  $S_{E,e}$ , the energy balance equation is expressed as:

$$\frac{\partial}{\partial t} \left( \frac{3}{2} n_e T_e \right) = \frac{1}{r} \frac{\partial}{\partial r} (r Q_e) + S_{E,e} \quad (50)$$

This can be rewritten, solving for the heat flux:

$$Q_e = \frac{1}{r} \left[ S_{E,e} - \frac{\partial}{\partial t} \left( \frac{3}{2} n_e T_e \right) \right] r \quad (51)$$

For the electrons, the main sources and sinks can be expressed in the following equation:

$$S_{E,e} = P_{\square} - P_{ei} - P_{ez} - P_{rad} - eE_r \quad (52)$$

The source of energy for the electrons is the Ohmic input power,  $P_{\square}$ , as discussed in detail in the previous section.

Sinks of energy for the electrons are the energy (power density) lost through collisions with both the majority and impurity ions,  $P_{ei}$  and  $P_{ez}$ , the electron radiated power,  $P_{rad}$ , and the energy lost by motion along the radial electric field,  $-eE_r$ .

$$P_{ei} = \frac{m_e}{m_i} n_i n_e e^4 \frac{\ln(\square)}{4L_0} (T_e - T_i) \sqrt{2/\square^3 m_e T_e^3} \quad (53)$$

$$P_{ez} = \frac{m_e}{m_z} n_z n_e Z^2 e^4 \frac{\ln(\square)}{4L_0} (T_e - T_z) \sqrt{2/\square^3 m_e T_e^3} \quad (54)$$

These terms represent the main channels of heating for the ions and impurities, but are a small correction to the power budget of the electrons. The ion energy budget will be discussed in more detail in Section 5.4.  $P_{rad}$  is approximated as a profile dependent fraction of the Ohmic input power density,<sup>11</sup>

$$P_{rad} = C_{rad} (r/a)^8 P_{\square} \quad (55)$$

From this expression, the radiated power density is “edge peaked,” and depends on the parameter  $C_{rad}$ , which is adjusted such that the total radiated power matches bolometer measurements at the edge of the plasma. Finally, the radial electric field (Shown in Figure 3.33) is measured to be positive in the core and negative in the edge. Thus, in the core, outward moving electrons must do work (and hence lose energy) until they reach the edge of the plasma. This energy is imparted to the ions, which are in turn accelerated as they move

radially, until they reach the edge of the plasma, where the radial electric field changes sign. The volume-integrated terms in the electron power budget are shown in Figure 4.7 at  $-1.75$  ms away from the sawtooth crash. Clearly the energy loss terms are much smaller than the Ohmic heating of the electrons. In the core, the energy lost from the electrons due to motion along the radial electric field is about an order of magnitude less than the energy lost from collisional heating to the ions.

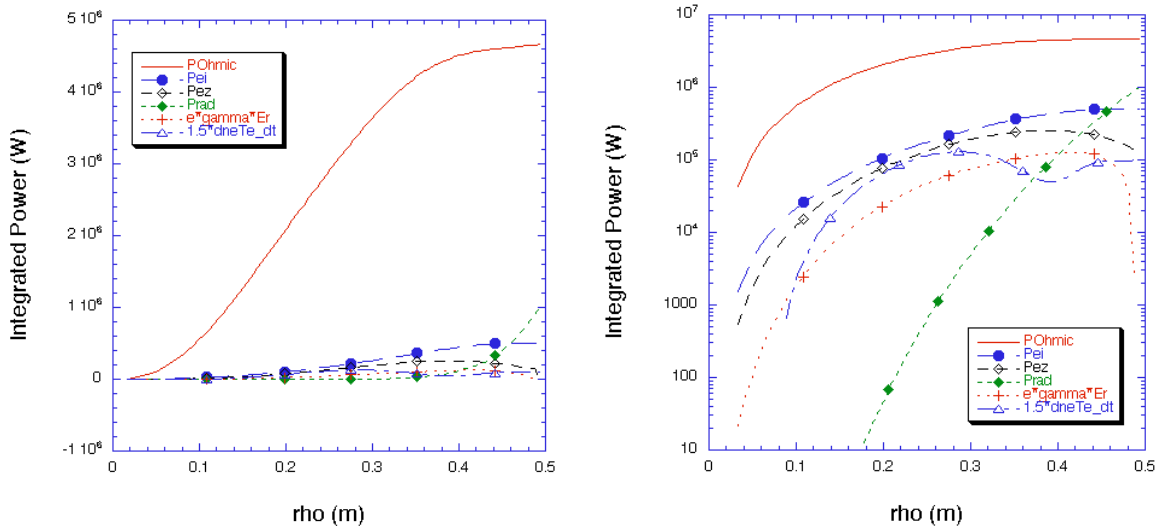


Figure 4.7 The electron energy budget at  $-1.75$  ms in the sawtooth cycle of Standard plasmas on linear and logarithmic scales (to show detail).

Combining these “source and sink” terms, the implied electron heat fluxes at two different times during the sawtooth cycle are shown as the solid lines in Figure 4.8. Clearly the heat flux is larger after the sawtooth crash, which is consistent with the lower energy confinement time during that phase. Also shown in Figure 4.8 are the convective and conductive components of the heat flux. Since the particle flux has been measured, it is straightforward to separate the convective heat flux from the total, yielding as remainder the conductive heat flux:

$$Q_e = Q_e^{\text{conv}} + Q_e^{\text{cond}} = \frac{5}{2} n_e T_e \left[ \frac{1}{2} n_e \left( \frac{1}{r} T_e \right) \right], \quad (56)$$

Separating the power in this fashion shows that heat transport in the MST is a dominantly conductive process from the core to the edge. Even at the edge of the plasma, where the temperature and (more importantly) the density gradients are large, the convective heat flux from electrons remains less than about 10% of the total electron heat flux, consistent with previous measurements.<sup>12,13</sup> The total heat flux at the edge is also in rough agreement with probe measurements in earlier experiments.<sup>14</sup>

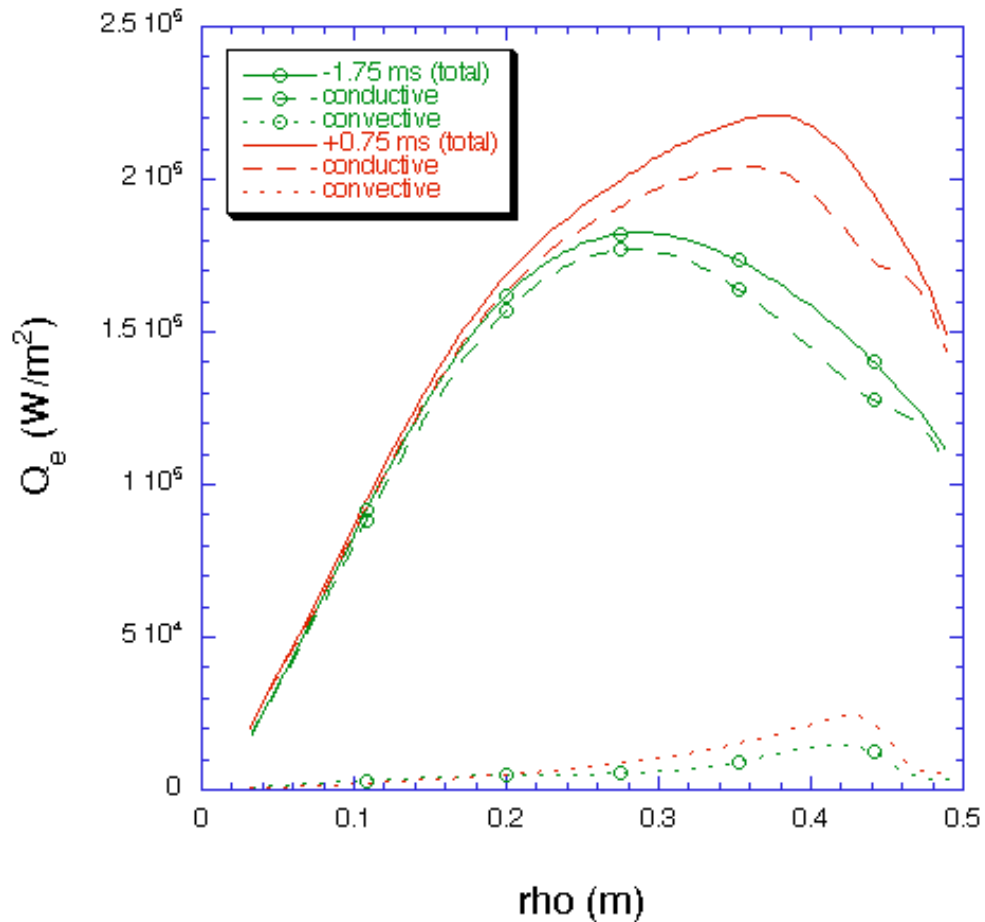


Figure 4.8 Electron heat flux (total: conductive and convective)  $-1.75$  ms away and  $+0.75$  ms after the sawtooth crash in Standard plasmas.

## 4.4 Thermal Conductivity Coefficients

### 4.4.1 Measured Electron Conductivity Profiles

Separating the heat flux in this manner allows for the coefficient of thermal conductivity to be extracted from the conductive heat flux profile:

$$Q_e^{\text{cond}} = -\kappa_e n_e \nabla_r T_e, \quad (57)$$

The measured electron thermal conductivity,  $\kappa_e$ , is shown in Figure 4.9 for two time slices in the sawtooth cycle:  $-1.25$  ms before the sawtooth crash, and  $+0.75$  ms after the crash. This analysis indicates that there is a slight drop in the overall thermal conductivity of the plasma between these two time slices. This is consistent with the observation that the electron temperature begins to decrease before the crash and increase after the crash. Also apparent from the profiles in Figure 4.9 is the presence of a transport barrier at the edge of the plasma, particularly in the region where the electron temperature gradient is large. This barrier persists throughout the sawtooth cycle, and has been observed in other RFP's.<sup>15,16</sup> Recent simulations of RFP plasmas have also reproduced this edge transport barrier.<sup>17</sup>

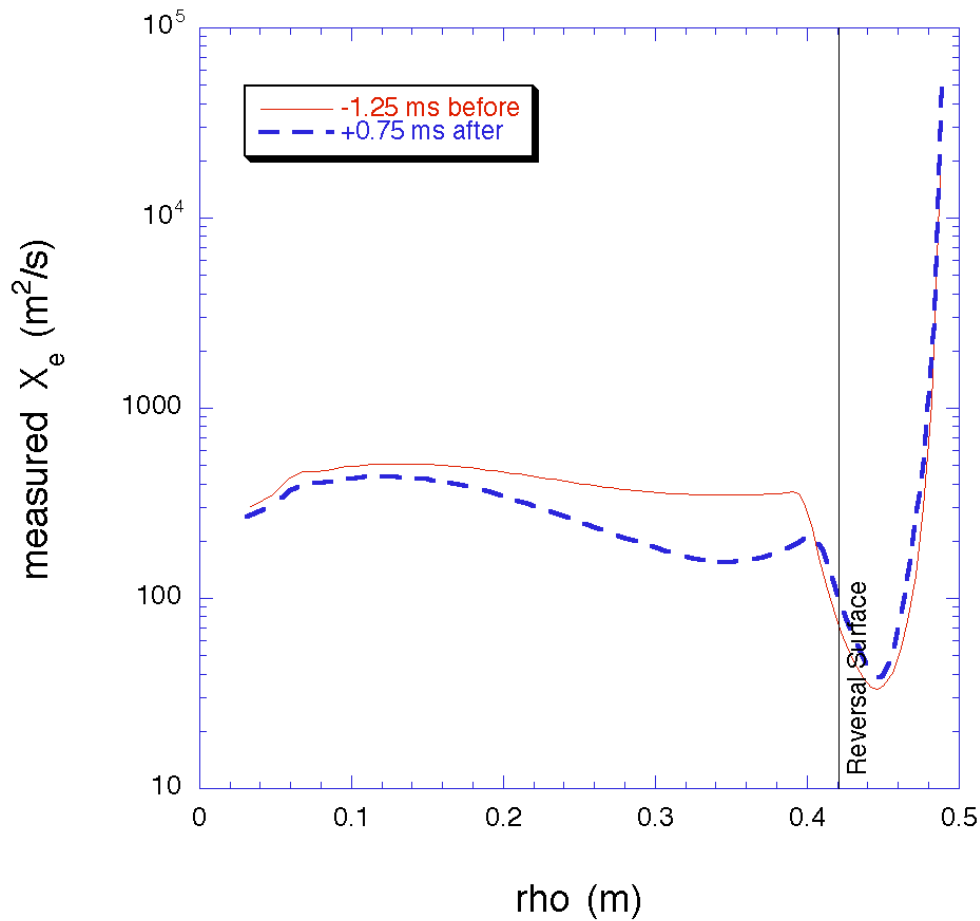


Figure 4.9 Measured electron thermal conductivity profiles at -1.25 ms (solid) and +0.75 ms (dashed) in Standard plasmas.

#### 4.4.2 Electron Conductivity through the Sawtooth Cycle

To examine the dynamics of the electron thermal conductivity over the sawtooth cycle, it is useful to define a “core-averaged”  $\chi_e$ . In the following discussion, the “measured, core-averaged thermal conductivity” is defined to be the volume average of the conductive heat flux divided by the electron density and the average gradient of the electron temperature between the radii of  $0.05 < \rho < 0.30$  m, i.e. about 60% of the plasma radius. The temperature gradient is preemptively averaged to remove structure from the radial profile, where it can be zero or negative. More explicitly:

$$q_e = \frac{\int_{0.05}^{0.30} q_e \frac{\partial V}{\partial \rho} \partial \rho}{\int_{0.05}^{0.30} \frac{\partial V}{\partial \rho} \partial \rho} = \frac{\int_{0.05}^{0.30} \frac{Q_e^{cond.}}{n_e (\langle T_e \rangle)^{avg}} \frac{\partial V}{\partial \rho} \partial \rho}{\int_{0.05}^{0.30} \frac{\partial V}{\partial \rho} \partial \rho}. \tag{58}$$

This radial range is chosen to cover the region that the magnetic field is expected to be most stochastic. This is the region where the (m=1) n=6-15 magnetic tearing modes are resonant (and overlapping) as seen in Figure 4.10.

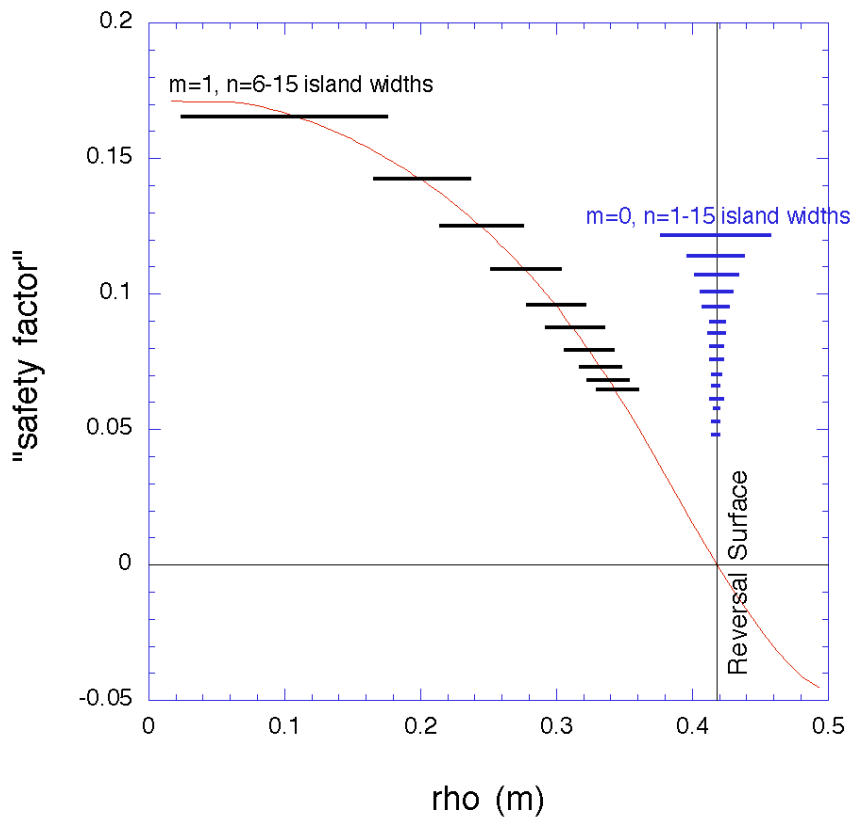


Figure 4.10 The q-profile at -1.75 ms in Standard plasmas, including island widths, which are derived from modeling in Chapter 5.

The time dependence of the core-averaged value and the reversal surface value of  $q_e$  is shown in Figure 4.11. Over the sawtooth cycle, the thermal conductivity averaged over the core of the plasma varies by a factor of roughly 5, consistent with observations of the

temperature profile, which drops considerably during the time period that the measured conductivity is high. The value of  $\chi_e$  at the reversal surface is representative of the depth of the transport barrier at the edge. Through the sawtooth cycle, the depth of this barrier changes little. On the surface the behavior of the core-averaged  $\chi_e$  in Figure 4.11 is qualitatively similar to the time traces of so many quantities over the sawtooth cycle: i.e. “Everything gets big at the crash.” But as is seen in the following figures the increase in measured  $\chi_e$  precedes the increase in total magnetic fluctuation amplitude (as measured by pickup coils at the wall). Magnetic fluctuation amplitudes in the MST are regarded as important indicators of the overall performance of the plasma.<sup>18</sup> When the fluctuation amplitude is low, the highest temperatures are observed.<sup>19</sup> An important distinction between Figure 4.11 and Figure 4.12 is that the magnetic fluctuation amplitudes peak (on this timescale) a full 0.5 ms later than the measured electron conductivity, i.e. after the crash, as compared to before. Plotting measured  $\chi_e$  vs. the square of the total magnetic fluctuation amplitude, previous experiments suggest a linear dependence.<sup>20,21</sup> This is, however, not the case, as shown in Figure 4.13 as a trajectory over the sawtooth cycle. Prior to the sawtooth crash, the core-averaged value of  $\chi_e$  appears to increase, even though the fluctuation level remains small. This suggests that the total fluctuation level by itself is not sufficient to explain the transport of heat in the pre-crash phase. After the crash,  $\chi_e$  behaves more as expected, qualitatively decreasing as the fluctuations subside. This trajectory can be improved (i.e. further collapsed into a linear relation), if instead of the total fluctuation amplitude (all m, all n), only the m=1(all n) mode amplitudes are considered, since the m=1 modes are resonant throughout the core of the plasma. But as will become clear in the next chapter, the dependant quantity that underlies the dynamics isn’t necessarily the strength of the magnetic mode fluctuations, but is the fundamental stochasticity of the magnetic field.

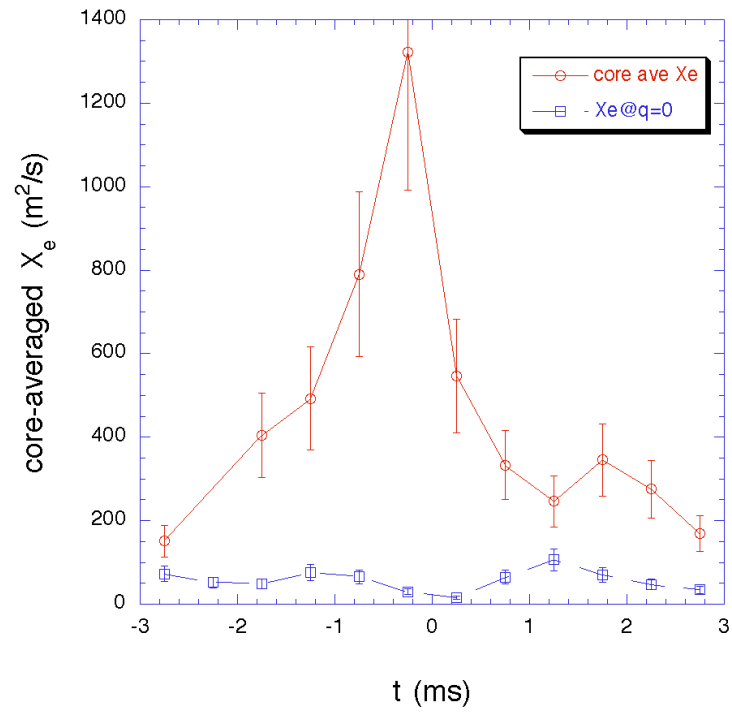


Figure 4.11 Behavior of thermal conductivity over the sawtooth crash in Standard plasmas.

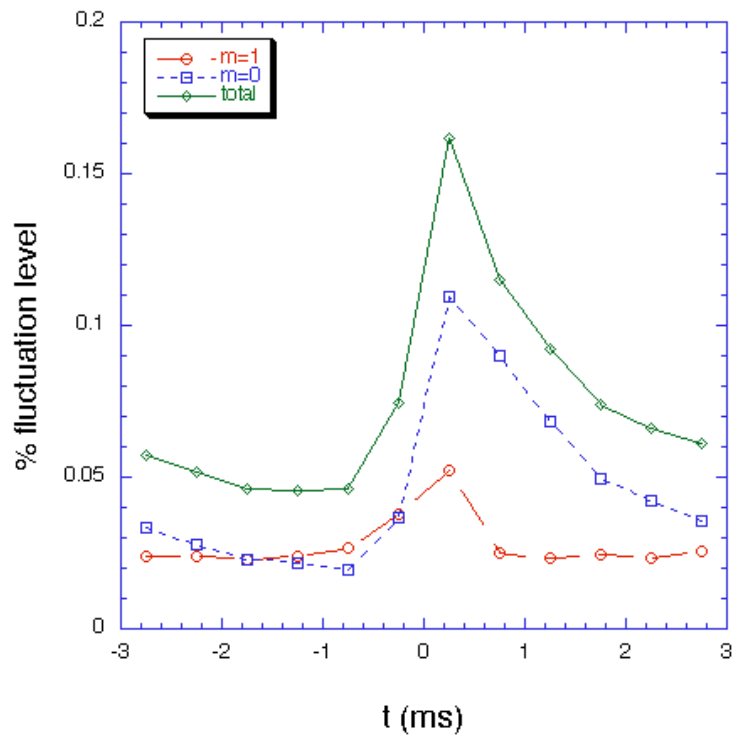


Figure 4.12 Total magnetic fluctuation amplitude as measured at the wall (summed over  $n$ ) through the sawtooth cycle in Standard plasmas.

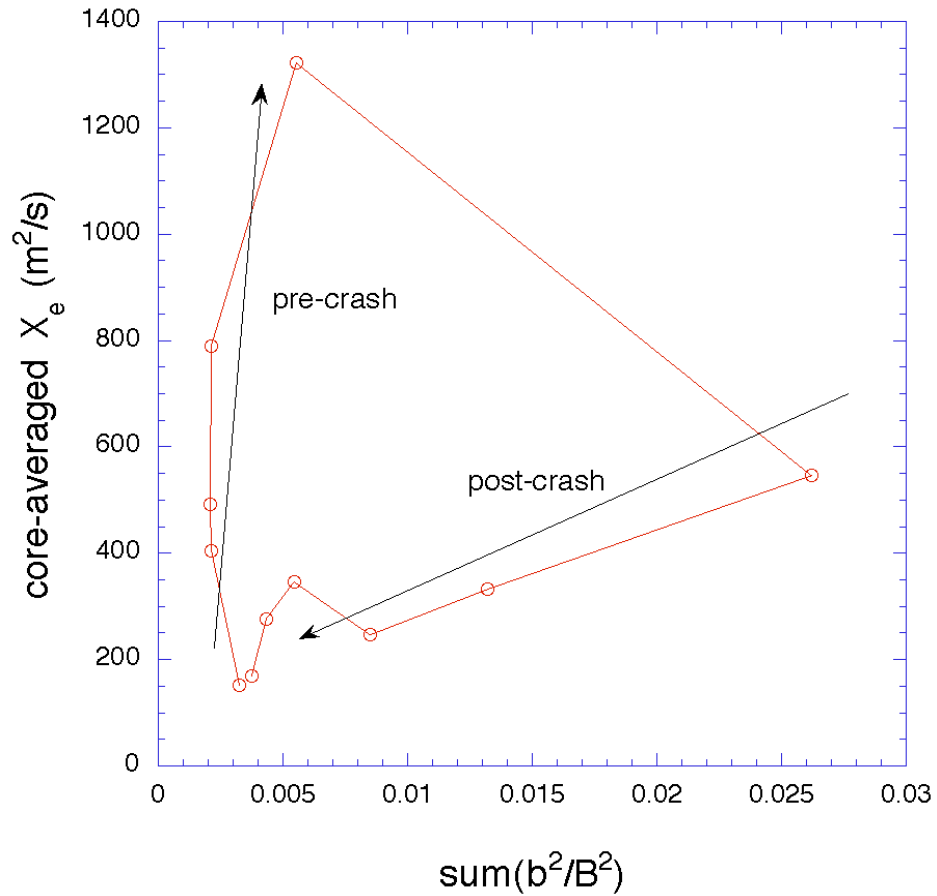


Figure 4.13 A trajectory of the measured thermal conductivity over the sawtooth cycle shows that total magnetic fluctuation level is not sufficient by itself to explain the transport of heat in Standard plasmas.

## 4.5 Particle Diffusion Coefficients

### 4.5.1 Measured Electron Diffusivity Profiles

Fick's Law for the diffusion of particles is:

$$\vec{j} = -D_{\text{Fick}} \nabla n. \quad (59)$$

Here  $\Gamma$  is the flux of particles,  $n$  is the number density of particles, and  $D_{\text{Fick}}$  is the diffusion coefficient, which is familiar to most plasma physicists.  $D_{\text{Fick}}$  is usually experimentally determined by measuring the other quantities in this relation. Fick's Law as written above can be derived from the fluid equation of motion, including collisions, under the assumption that the plasma is isothermal, in the absence of electric and magnetic fields:<sup>22</sup>

$$m n \frac{d\mathbf{v}}{dt} = m n \frac{\partial \mathbf{v}}{\partial t} + (\mathbf{v} \cdot \nabla) \mathbf{v} = q n \mathbf{E} - \nabla p - m n \nu \mathbf{v}. \quad (60)$$

In this equation  $m$  is the mass of the particle,  $\mathbf{v}$  is the velocity,  $q$  is the charge of the particle,  $\mathbf{E}$  is the electric field,  $p$  is the thermodynamic plasma pressure, and  $\nu$  is the collision frequency. Note that in this formalism,  $D_{\text{Fick}}$  has the simple form:

$$D_{\text{Fick}} \equiv \frac{T}{m \nu}. \quad (61)$$

Dimensional analysis shows that  $D$  has units of  $\text{m}^2/\text{s}$ , which is effectively the “step size” squared, divided by the time. Conceptually, for a randomly diffusive process, this is the distance (squared) that a given particle moves during the time between collisions. The constraints above are stringent, and generally too restrictive for fusion plasmas. In fact, this definition of the diffusion coefficient causes difficulties in interpreting MST Standard discharge data, since as shown in Section 3.4 the density profile can be flat-to-hollow in the core. This results in an infinite-to-negative value of  $D_{\text{Fick}}$ , as shown in Figure 4.14.

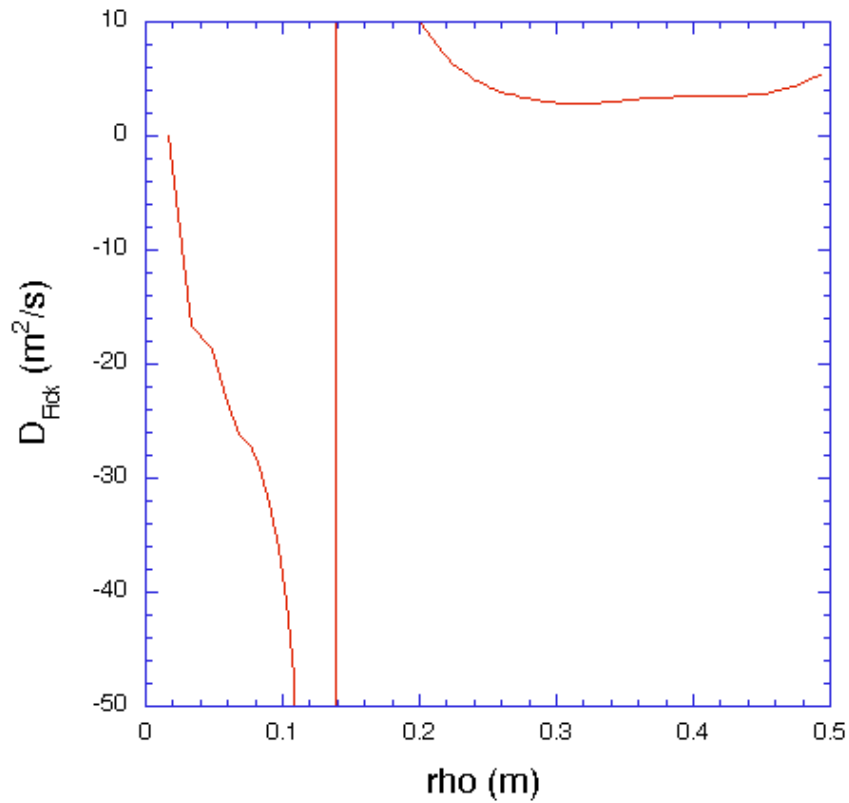


Figure 4.14 The electron diffusion coefficient derived from Fick's Law at -1.75 ms in Standard discharges.

An equation for the particle flux in a non-isothermal plasma can be derived without loss of generality from the above equation of motion:

$$\vec{j} = -D_{n,i} \frac{\nabla p}{T} = -D_{n,i} n \left[ \frac{\nabla n}{n} + \frac{\nabla T}{T} \right] \quad (62)$$

This expression yields another experimentally determined diffusion coefficient,  $D_{n,i}$ , similar to Fick's Law but for a non-isothermal plasma. Clearly, if the temperature gradient is zero, this expression reduces to Fick's Law, and the diffusion coefficients are identical.  $D_{\text{Fick}}$  and  $D_{n,i}$  are compared in Figure 4.15.

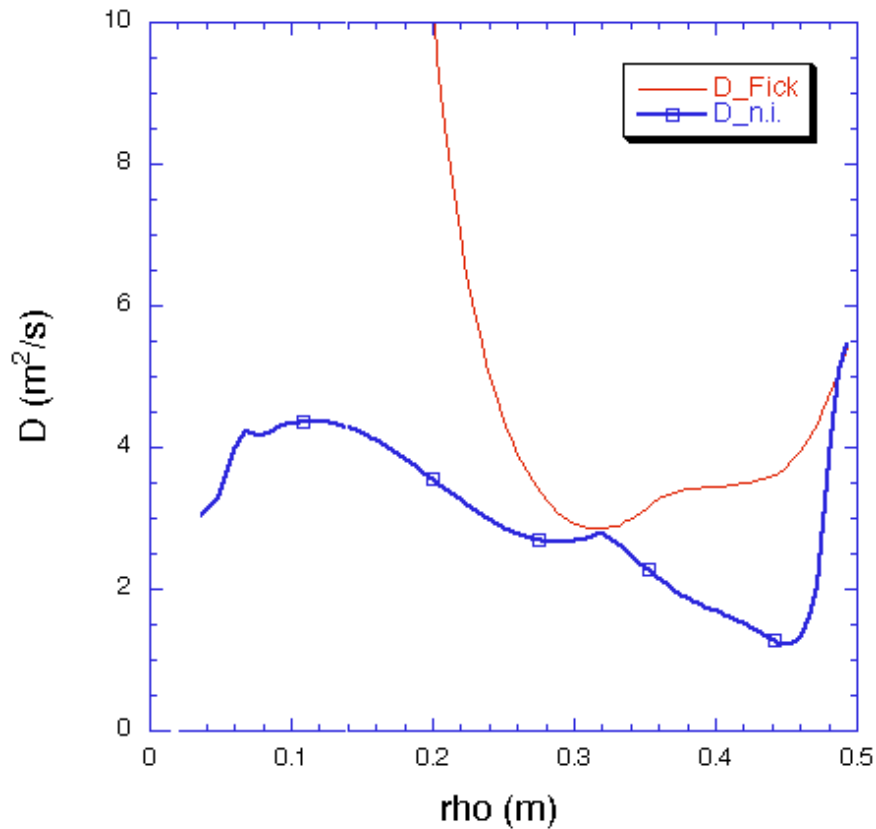


Figure 4.15 The electron diffusion coefficient including temperature gradient effects in Standard discharges at  $-1.75$  ms.

#### 4.5.2 Electron Diffusivity through the Sawtooth Cycle

Similarly to the electron thermal conductivity, a core-average ( $0.05 < \rho < 0.30$  m) of the density and temperature gradients is defined to investigate particle diffusion on a more global scale. Figure 4.11 shows that  $\bar{\rho}_e$  peaks up leading to the sawtooth crash. In comparison, the core-averaged electron diffusivity shows no clear trend (Figure 4.16). Because the density gradient in the core is flat or hollow following the crash,  $D_{\text{Fick}}$  is poorly defined, becoming hollow or negative. In contrast,  $D_{n,i}$  appears to hover around a core-averaged value of  $\sim 5$   $\text{m}^2/\text{s}$ .

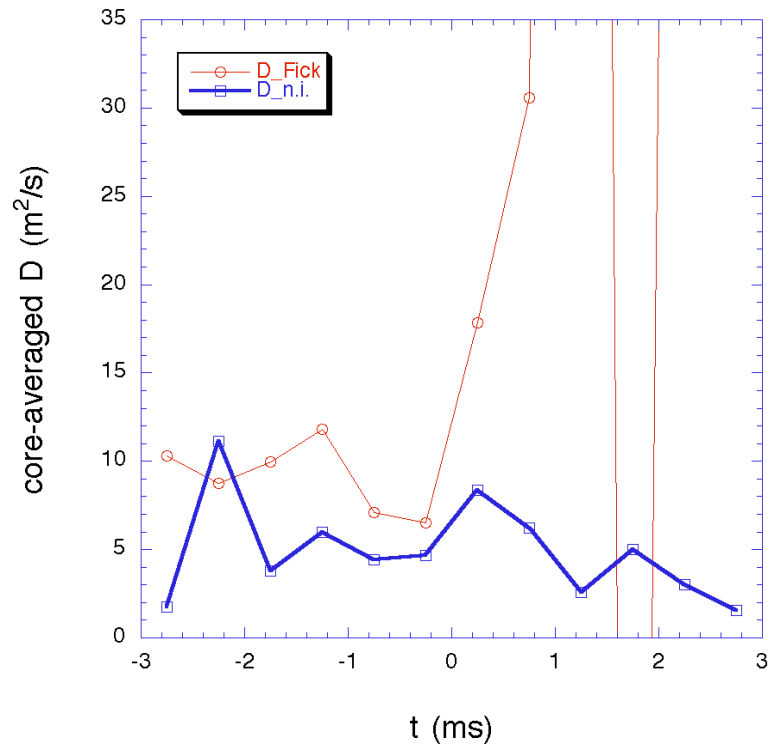


Figure 4.16 Core-averaged values of the electron diffusivity for Standard plasmas.

Since the majority of the density (and pressure) gradient is in the edge of the plasma, an edge-averaged ( $0.30 < r < 0.50$  m) value of these diffusion coefficients should be calculated. (Recall that the plasma minor radius is 0.52 m.) The result is shown in Figure 4.17. These traces are reminiscent of the variation of the magnetic fluctuation amplitude over the sawtooth cycle. In fact, plotting the sawtooth trajectory of the edge-averaged value of the electron diffusion coefficients against the total magnetic fluctuation amplitude shows a narrow trend (Figure 4.18), especially in comparison to the same trajectory for the thermal conductivity (Figure 4.13). Referring to Figure 4.12, the magnetic fluctuation spectrum is dominated by  $m=0$  modes after the crash, which are resonant at the reversal surface (in the edge.) This “narrowness” suggests that magnetic fluctuations may be sufficient to explain the observed particle dynamics at the edge, which is where the majority of the electron density gradient resides.

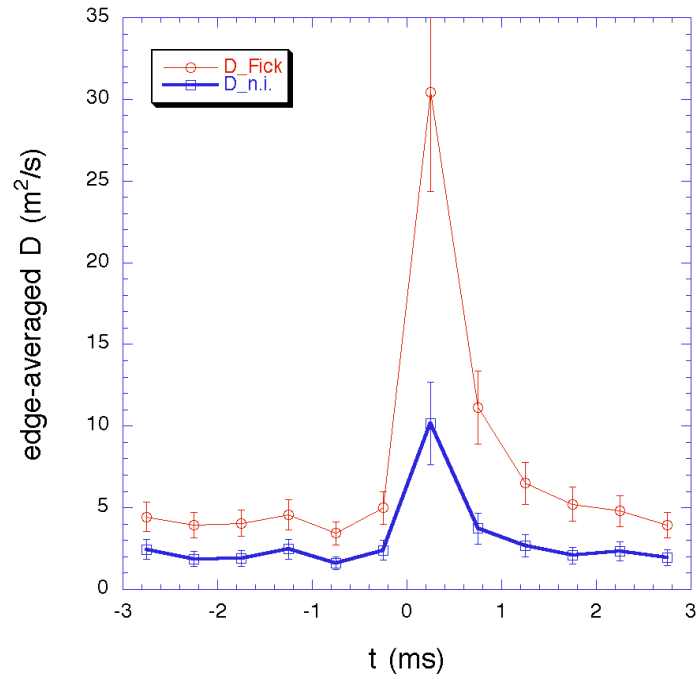


Figure 4.17 Edge-averaged values of the electron diffusivity for Standard plasmas.

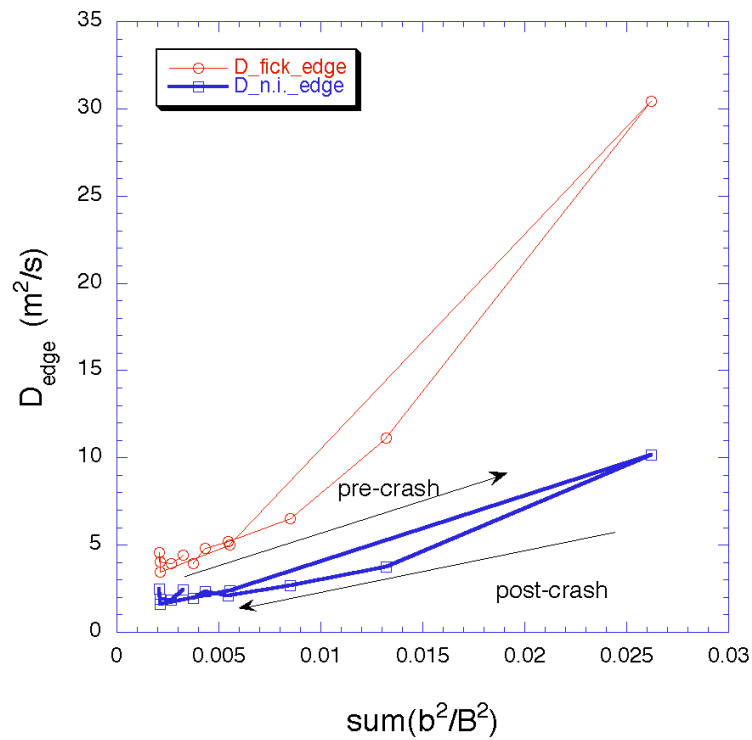


Figure 4.18 Trajectory of edge-averaged electron diffusion coefficients over the sawtooth cycle in Standard plasmas.

## 4.6 Summary

The movement of heat and particles within the plasma follows a complicated trajectory over the sawtooth cycle. The electron energy confinement time witnesses a strong but systematic variation throughout the sawtooth cycle, reaching a minimum around the sawtooth crash and peaking 1/2 sawtooth period later. In contrast the particle confinement time shows steady improvement from a given sawtooth crash, dropping suddenly at the next crash.

In 1-D analysis, conductive transport of heat is clearly the dominant process across all radii, with convective transport accounting for less than 10% at the edge of the plasma. Correspondingly, the electron thermal conductivity ( $\sim 400 \text{ m}^2/\text{s}$ ) is an order of magnitude larger than the electron diffusion coefficient in the core ( $\sim 5 \text{ m}^2/\text{s}$ ), though there is a strong thermal transport barrier at the edge of the plasma, which persists throughout the sawtooth cycle. Both total heat and particle fluxes for electrons are observed to increase, comparing before and after the sawtooth crash. Whereas the heat flux increases over the crash, the electron thermal conductivity in the core is observed to decrease sharply following the sawtooth crash. Because of the densely packed mode-rational surfaces of the RFP, stochastic magnetic fields may play a role in determining the dynamics of heat transport in the MST. Comparing the total magnetic fluctuation level with the measured electron thermal conductivity, however, the underlying dynamics are not apparently captured. In the next chapter it is shown that to capture the fundamental dynamics of heat transport it is necessary to characterize the inherent stochasticity of the field, not merely the fluctuation level.

## References

1. See for example the line comments that accompany the  $\square$ -model code, J.S. Sarff, University of Wisconsin-Madison.
2. J. Anderson and C. Forest, Private communications.
3. J.T. Chapman, *Spectroscopic Measurements of the MHD Dynamo in the MST Reversed Field Pinch*, Ph.D. Thesis, University of Wisconsin-Madison (1998).
4. Z. Yoshida, *Physics of Fluids B*, **4** (6), 1534-1538 (1992).
5. S.P. Hirschman and D.J. Sigmar, *Nuclear Fusion* **21**, 1079 (1981).
6. J.K. Anderson, *Measurement of the Electrical Resistivity Profile in the Madison Symmetric Torus*, Ph.D. Thesis, University of Wisconsin-Madison (2001).
7. N.E. Lanier, *Electron Density Fluctuations and Fluctuation-Induced Transport in the Reversed-Field Pinch*, Ph.D. Thesis, University of Wisconsin-Madison (1999).
8. T.D. Rempel, A.F. Almagri, S. Assadi, D.J. Den Hartog, S.A. Hokin, S.C. Prager, J.S. Sarff, W. Shen, K.L. Sidikman, C.W. Spragins, J.C. Sprott, M.R. Stoneking and E.J. Zita, *Phys. Fluids B*, **4** (7), 2136 (1992).
9. N.E. Lanier, D. Craig, J.K. Anderson, T.M. Biewer, B.E. Chapman, D.J. Den Hartog, C.B. Forest, and S.C. Prager, *Phys. Rev. Lett.*, **85** (10), 2120-2123 (2000).
10. J.K. Anderson, Private communication.
11. S.A. Hokin, *Nuclear Fusion*, **37** (11), 1615-1627 (1997).
11. H. Ji, H. Toyama, K. Miyamoto, S. Shinohara, and A. Fujisawa, *Phys. Rev. Lett.*, **67** (1), 62-65 (1991).
12. T.D. Rempel, C.W. Spragins, S.C. Prager, S. Assadi, D.J. Den Hartog and S.A. Hokin, *Phys. Rev. Lett.*, **67** (11), 1438 (1991).
13. M.R. Stoneking, S.A. Hokin, S.C. Prager, G. Fiksel, H. Ji and D.J. Den Hartog, *Phys. Rev. Lett.*, **73** (4), 549 (1994).

14. G. Fiksel, S.C. Prager, W. Shen and M. Stoneking, *Phys. Rev. Lett.*, **72**, 1028 (1994).
15. R. Bartiromo, V. Antoni, T. Bolzonella, A. Buffa, L. Marrelli, P. Martin, E. Martines, S. Martini, R. Pasqualotto, Presented at the 40<sup>th</sup> Annual Meeting of the Division of Plasma Physics, New Orleans, Louisiana, (1998).
16. D.A. Baker, C.J. Buchenauer, L.C. Burkhardt, et al., in *10<sup>th</sup> International Conference on Plasmas Physics and Controlled Nuclear Fusion Research*, London., Vol. 2, IAEA, Vienna (1984) 2-9.
17. E.D. Held, J.D. Callen, C.C. Hegna, C.R. Sovenic, *Physics of Plasmas*, **8** (4), 1171-1179 (2001).
18. B.E. Chapman, *Fluctuation Reduction and Enhanced Confinement in the MST Reversed-Field Pinch*, Ph.D. Thesis, University of Wisconsin-Madison (1997).
19. B.E. Chapman, A.F. Almagri, J.K. Anderson, C.S. Chiang, D. Craig, G. Fiksel, N.E. Lanier, S.C. Prager, M.R. Stoneking, and P.W. Terry, *Phys. Plasmas*, **5** (5), 1848-1854 (1998).
20. M. Cekic, J.S. Sarff, D.J. Den Hartog, S.C. Prager, "Magnetic Fluctuation Induced Energy Transport During Sawtooth Events in the MST Reversed-Field Pinch," MST Group internal report, University of Wisconsin-Madison.
21. J.S. Sarff, "Control of Magnetic Fluctuations and Transport in the MST," PLP Report 1225, University of Wisconsin-Madison, (1999).
22. F.F. Chen, *Introduction to Plasma Physics and Controlled Fusion*, Plenum Press, New York, NY, 1984.

## Chapter 5

---

Those who wish to control their own lives and move beyond existence as mere clients and consumers- those people ride a bike.

--Wolfgang Sachs, *For the Love of the Automobile*

### Comparisons to Rechester-Rosenbluth Theory

Measured values of  $\chi_e$  are compared to estimates of the thermal conductivity from Rechester-Rosenbluth theory for transport of heat in a stochastic magnetic field (in the limit of high stochasticity). For this comparison, the unmeasured amplitudes of radial magnetic fluctuations at the rational surfaces are needed; these were estimated by nonlinear MHD simulation using the DEBS code. The predicted radial fluctuation eigenfunctions, based on calculations at  $S \sim 10^6$ , were scaled to match fluctuations measured at the edge. The overall stochasticity of the magnetic field is calculated, and is essential to understanding the dynamics of measured thermal conductivity profiles in Standard MST plasmas. General agreement with stochastic transport of electrons has significant implications for ion transport, which is briefly explored.

#### 5.1 Rechester-Rosenbluth Model for Thermal Transport in a Stochastic Field

In their 1978 paper, Rechester and Rosenbluth expand the work of Callen to suggest that the thermal conductivity of plasmas in stochastic magnetic fields is given by the product of a stochastic magnetic field line diffusion coefficient and a parallel streaming velocity.<sup>1,2</sup> Plasma particles stream along magnetic field-lines; radial transport of particles and heat will

be enhanced if the magnetic field line itself wanders radially because the field is stochastic. It will be shown below, that in the MST the field is stochastic in regions where flux surfaces are destroyed by the overlap of magnetic tearing mode islands.<sup>3,4</sup> Rechester-Rosenbluth type thermal diffusion for electrons is expected to behave as:

$$\chi_{R\parallel R} \approx D_{st} v_{te}. \quad (63)$$

Here  $D_{st}$  is the stochastic diffusion coefficient of magnetic field-lines, and  $v_{te}$  is the electron thermal velocity. In the limit of strong island overlap (see the stochasticity parameter defined below), Rechester and Rosenbluth define

$$D_{st}(r) \approx \sum_{m,n} \frac{|b_{m,nr}(r)|^2}{B^2(r)} \delta\left(\frac{m}{q(r)} - n\right). \quad (64)$$

Here  $b_{m,nr}(r)$  is the radial component of the symmetry breaking magnetic field perturbation. The  $\delta$ -function implies that the diffusion is only large near the rational surfaces. This equation is often interpreted for individual modes as:

$$D_{st}(r_{m,n}) \approx \sum L_{eff} \frac{|\tilde{b}_r(r_{m,n})|^2}{B^2(r_{m,n})}. \quad (65)$$

Here  $L_{eff}$  is the effective autocorrelation length of the stochastic magnetic field:

$$L_{eff}^{\parallel} = L_{A.C.}^{\parallel} + \sum_{mfp}^{\parallel}. \quad (66)$$

In the MST under these plasma conditions, the collisional mean free path,  $\sum_{mfp}^{\parallel}$ , is on the order of 10's of meters. Field-line tracing for these experimental conditions (which will be

discussed further below) find that the autocorrelation length results in an  $L_{\text{eff}} \sim 0.7-1.0$  m. This calculated length is in agreement with previous results.<sup>5</sup> It is worth pointing out that the major radius of the MST is 1.5 m. To estimate the theoretical value of  $\Delta_e$  requires knowledge of the thermal velocity (electron temperature), the value of the radial fluctuations at the rational surfaces, the equilibrium magnetic field, and  $L_{\text{eff}}$ .

Rechester and Rosenbluth go on to say in their paper that the thermal conductivity of the plasma will be enhanced by a stochastic magnetic field, provided that the stochasticity is high enough. To be more quantitative, they define a “stochasticity parameter,”  $s$ , as:

$$s = \frac{1}{2} \frac{(w_{m,n} \Delta w_{m',n'})}{|r_{m,n} - r_{m',n'}|}. \quad (67)$$

This is essentially the Chirikov island overlap criterion.<sup>6</sup> Here  $w_{m,n}$  is the width of the  $m,n$ -magnetic tearing mode island,<sup>7</sup>

$$w_{m,n} = 4 \sqrt{\frac{r_{m,n} (b_r)_{m,n}}{nB_0 \left| \frac{\partial q}{\partial r} \right|_{r_{m,n}}}}, \quad (68)$$

and  $|r_{m,n} - r_{m',n'}|$  is the distance between two islands. It is worth noting that the island width (and hence the stochasticity,  $s$ ) depends on both the normalized, radial fluctuation amplitude at the resonant surface, and on the shear of the  $q$ -profile. Returning to the stochasticity, they state:

If  $s \geq 1$ , then magnetic surfaces are destroyed in the region between  $r_{mn}$  and  $r_{m'n'}$ , and the field lines wander ergodically.  $s=1$  corresponds to overlapping of islands of different helicity. The transition region is complicated and we will be discussing mainly the case of high stochasticity,  $s \gg 1$ , with dense rational surfaces.

The condition that the stochasticity, as defined here, be large will be important as the analysis progresses. The thermal conductivity calculated in this manner from the fluctuation amplitude represents an enhancement to the erstwhile conductivity by the radial, stochastic wandering of a magnetic field-line. If the stochasticity is not large, i.e. that  $s \sim 1$ , then it is reasonable to expect that the enhancement to the thermal conductivity due to magnetic fluctuations would be reduced by some intermediate factor. In a limiting sense, if the field were not stochastic at all,  $s < 1$  (corresponding to non-overlapping magnetic islands), then there will be no enhancement of transport by magnetic fluctuations, and the measured thermal conductivity will be less than that predicted by Rechester-Rosenbluth from a measure of the magnetic fluctuation amplitude.

## 5.2 DEBS Simulations of Standard Plasmas

The radial magnetic fluctuation amplitude is needed at the resonance location to compare the measured  $\chi_e$  to  $\chi_{RR}$ . In the MST the magnetic fluctuation amplitudes are measured with magnetic pick-up coils at the wall. More specifically, the toroidal and poloidal components of the magnetic fluctuations are measured, as the radial component is essentially zero, as discussed in Section 3.6.1. Modeling is required so that the value of the radial fluctuation eigenmodes deep in the core of the plasma can be estimated based on the edge measurements. Simulations of this type first revealed the stochastic core of an RFP on the ZT-40M experiment.<sup>8</sup>

The equilibrium fields and resistivity profile were used to initialize a DEBS code simulation, which models the nonlinear interaction of the turbulence in MST plasmas. DEBS is an initial value, 3-D code that solves the normalized non-linear resistive MHD equations in doubly periodic cylindrical geometry.<sup>9</sup> The governing equations are:

$$\rho(\partial \mathbf{v} / \partial t + S \mathbf{v} \cdot \nabla \mathbf{v}) = S \mathbf{j} \times \mathbf{B} + P_m \nabla^2 \mathbf{v}, \quad (69)$$

$$\partial A / \partial t = \nabla E, \quad (70)$$

$$E + S \mathbf{v} \times \mathbf{B} = \nabla j. \quad (71)$$

Here,  $\mathbf{A}$  is the magnetic vector potential,  $P_m$  is the magnetic Prandtl number ( $P_m = \rho / \eta$ ), and  $S$  is the Lundquist number. The Lundquist number is defined as the ratio of the resistive time to the Alfvén time:

$$S = \frac{\tau_{\text{res}}}{\tau_{\text{Alf}}} = \frac{\mu_0 a^2 / \eta}{a \sqrt{\mu_0 m_e n_e} / B} = \frac{a B}{\eta} \sqrt{\frac{\mu_0}{m_e n_e}}. \quad (72)$$

DEBS uses finite difference in the radial direction and is pseudo-spectral in the poloidal and axial directions. The code can be used to study small amplitude linear waves, large amplitude non-linear effects, and the interaction of waves with tearing mode turbulence all in the same framework.<sup>10</sup> Since the linearly unstable tearing modes saturate as they grow, it is important to model the plasma with a non-linear code such as DEBS, rather than a simple, linear code such as RESTER. DEBS was run for these experiments with a Lundquist number of  $S=10^6$ .<sup>#</sup> This is currently the highest  $S$  RFP-plasma simulated to date, and many of the dynamics are qualitatively similar to the actual experiment, for which  $S \sim 3 \times 10^6$ , as shown in Figure 5.1. In Figure 5.2 the  $q$ -profile representation of the equilibrium magnetic fields for

---

<sup>#</sup> Simulation run by John Wright.

the experiment (between sawtooth events) is compared to the q-profile that is calculated by the DEBS code at a given instant, showing relatively good agreement. It is worth pointing out that this is an instantaneous time slice during the simulation. As such, the “wiggly” structure is probably not significant. Averaging the simulation for a longer period of time (equivalent to  $\sim 1$  ms), would likely yield a smoother result.<sup>10</sup> For comparison, the DEBS simulation has  $F=-0.26$  and  $\bar{q}=1.72$ , while the between-sawteeth level in the experiment is  $F=-0.22$  and  $\bar{q}=1.76$ .

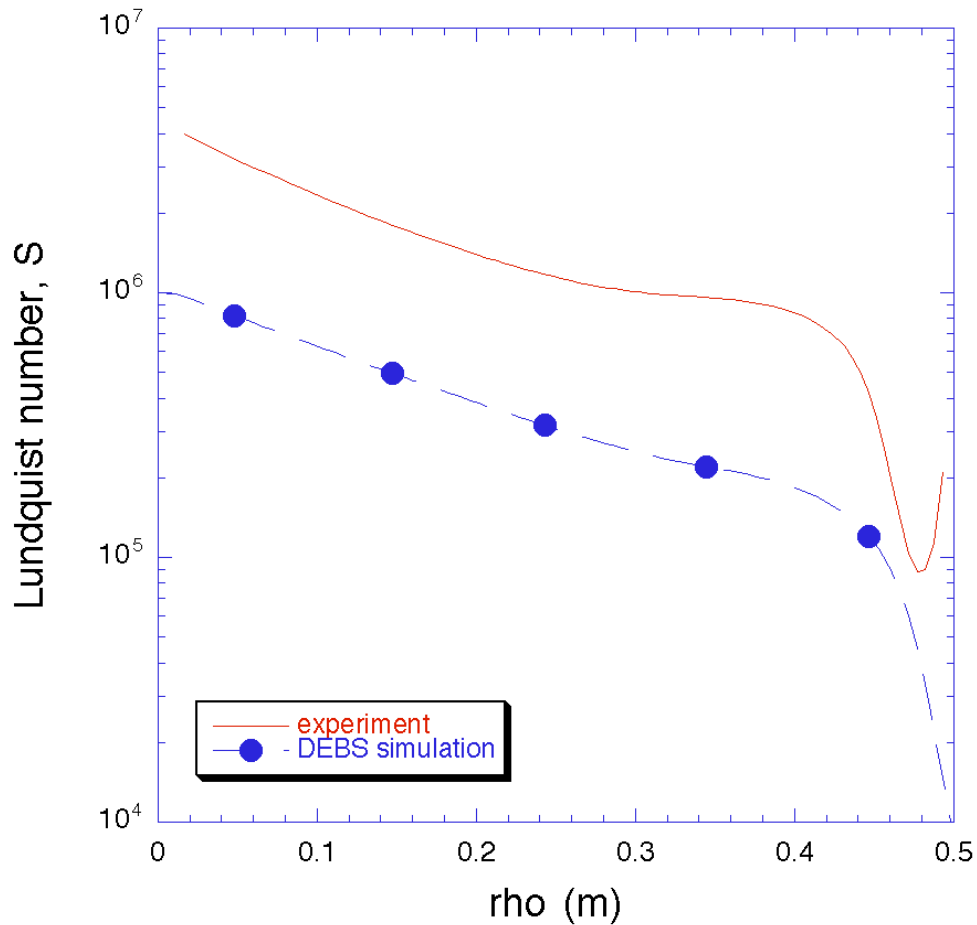


Figure 5.1 The experimental Lundquist number profile for Standard MST plasmas compared to the Lundquist number profile of the DEBS simulation.

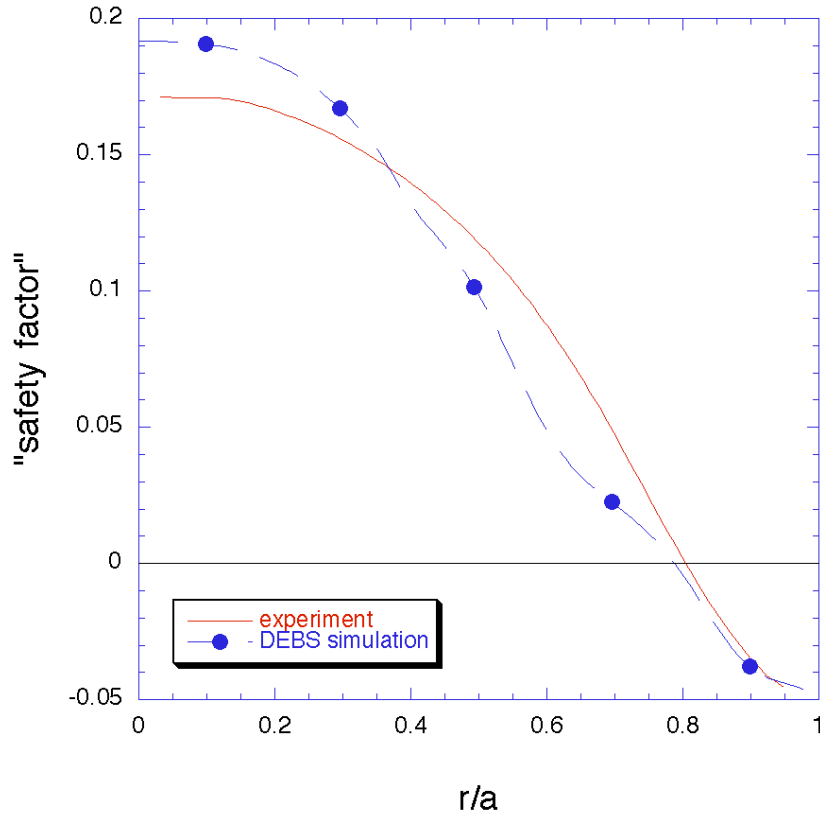


Figure 5.2 Comparison of the q-profiles from experiment (-1.75 ms before sawtooth crash) and from DEBS simulation at  $S \sim 10^6$ .

The effects of sawteeth on the magnetic modes that are observed in the experiment are also present in the DEBS simulation. This can be seen in Figure 5.3, where the value of the total magnetic fluctuation at the edge of the simulated plasma is shown, normalized by the axial magnetic field. In the experiment, magnetic pick-up coil triplets at the wall measure the magnetic fluctuation amplitudes (Figure 3.30). Two sawteeth are shown from the simulation, whose time axis is normalized by the resistive time scale of the simulated plasma. (Since  $\tau_{es}$  is between 1.0 and 0.5 s, the sawtooth period is between 3 and 6 ms in the simulation, which is in approximate agreement with the measured period of 6 ms.) Both experiment and simulation show the total fluctuation amplitude peaking at the sawtooth crash. Though qualitatively similar, there are some differences between the simulation and experiment. The  $m=0$  modes are clearly dominant over the entire sawtooth period of the

simulation. Experimentally, during Standard MST plasmas, it is observed that the  $m=0$  modes dominate following the sawtooth crash, then become comparable with the  $m=1$  modes. The toroidal mode spectrum of the DEBS simulation at a particular time (Figure 5.4) shows that there is more energy in the  $m=0$  modes (particularly at low  $n$ -numbers) than is observed in the experiment (Figure 3.29). Since the  $m=0$  modes are resonant at the edge of the plasma, they affect the transport of energy and particles in the edge, but have lesser effect in the core and mid-radius regions of the plasma. It is primarily the  $m=1$  modes, which are resonant in these regions, that are of concern.

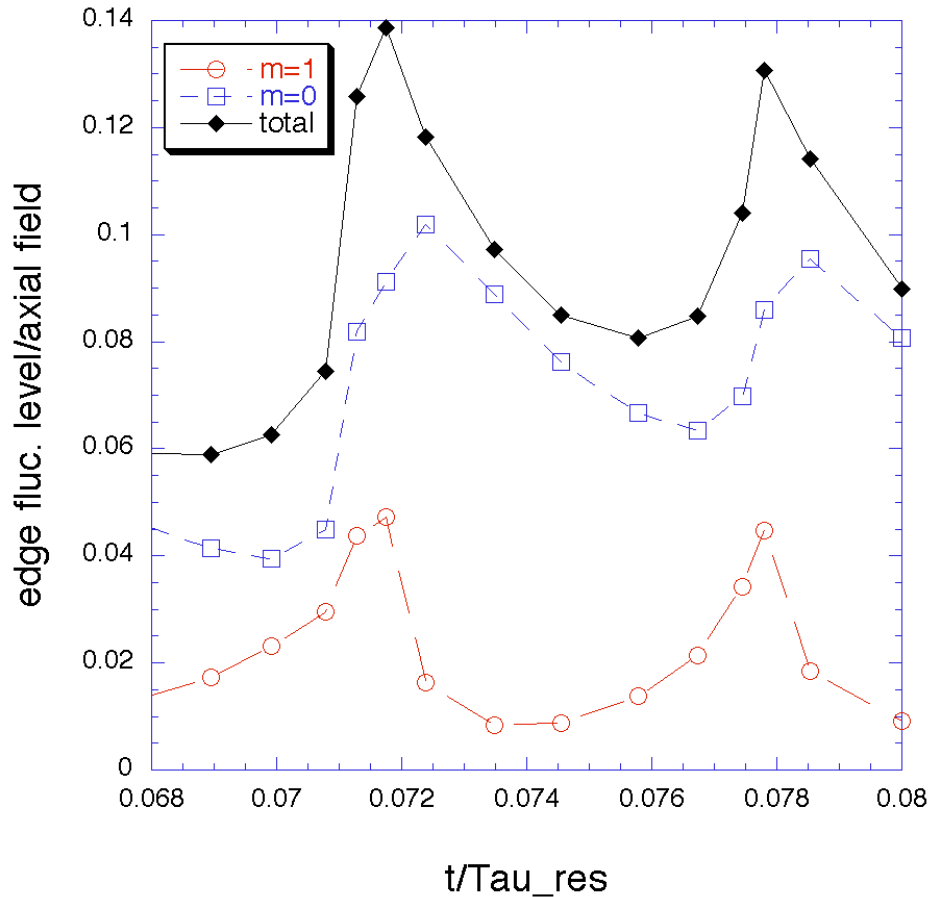


Figure 5.3 The behavior of the magnetic modes, as “measured” in the edge of the DEBS simulation, is qualitatively similar to the behavior observed in Standard MST plasmas (Figure 4.12). A full sawtooth cycle is shown. Since  $\tau_{es}$  is between 1.0-0.5 s, the sawtooth period is between 3-6 ms, which is in approximate agreement with the MST period of 6 ms.

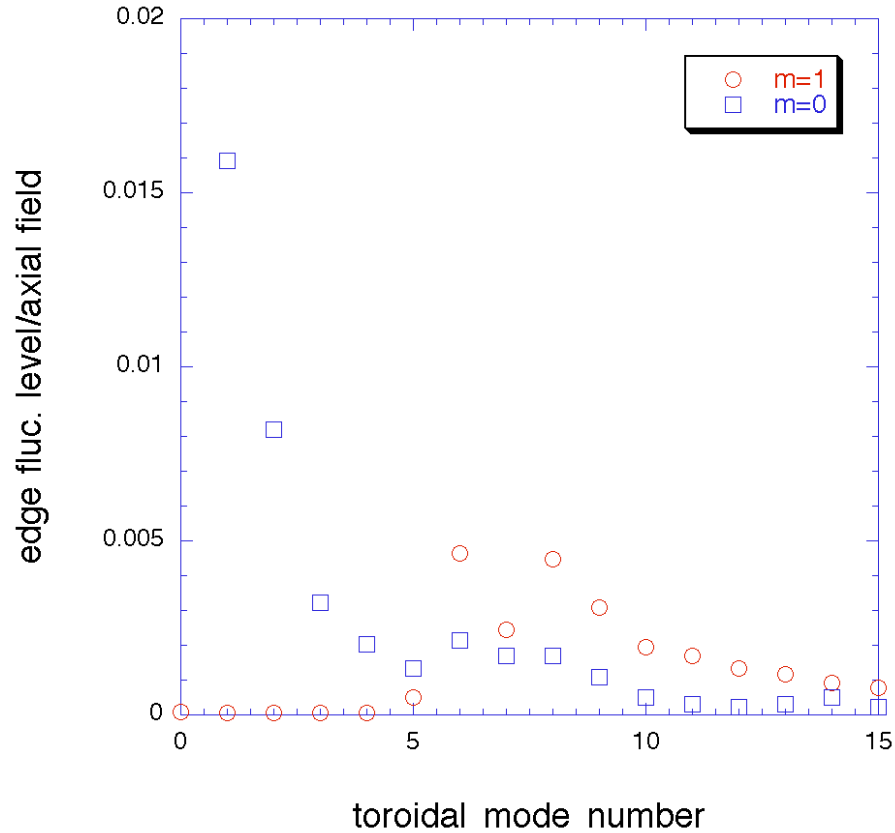


Figure 5.4 The  $n$ -spectra of  $m=0$  and  $m=1$  modes in the edge of the DEBS simulation is qualitatively similar to the spectra of Standard MST plasmas (Figure 3.29).

DEBS was used to generate the eigenfunctions of toroidal, poloidal, and radial magnetic fluctuations. The magnitudes of the toroidal and poloidal eigenfunctions were normalized to the measured fluctuation amplitudes at the wall of the MST. These scaling factors were then applied to the radial eigenfunctions, giving the radial fluctuation amplitudes internal to the plasma, as shown in Figure 5.5. The normalized radial eigenfunctions were also used in the MAL code, which follows particles and field-lines<sup>8</sup> to calculate correlation lengths.<sup>#</sup> This will be discussed in more detail below, but to summarize, these DEBS simulations have shown that the radial fluctuation amplitude at the rational surface is on the order of  $\sim 1.5$  to  $\sim 2$  times the value of the total fluctuation at the edge,

<sup>#</sup> MAL was run by Ben Hudson.

consistent with previous results.<sup>11</sup> With that caveat, the measured fluctuation levels at the wall were scaled to estimate the radial fluctuation level internal to the plasma, and used to calculate the Rechester-Rosenbluth thermal conductivity, the magnetic island widths, and the field stochasticity.

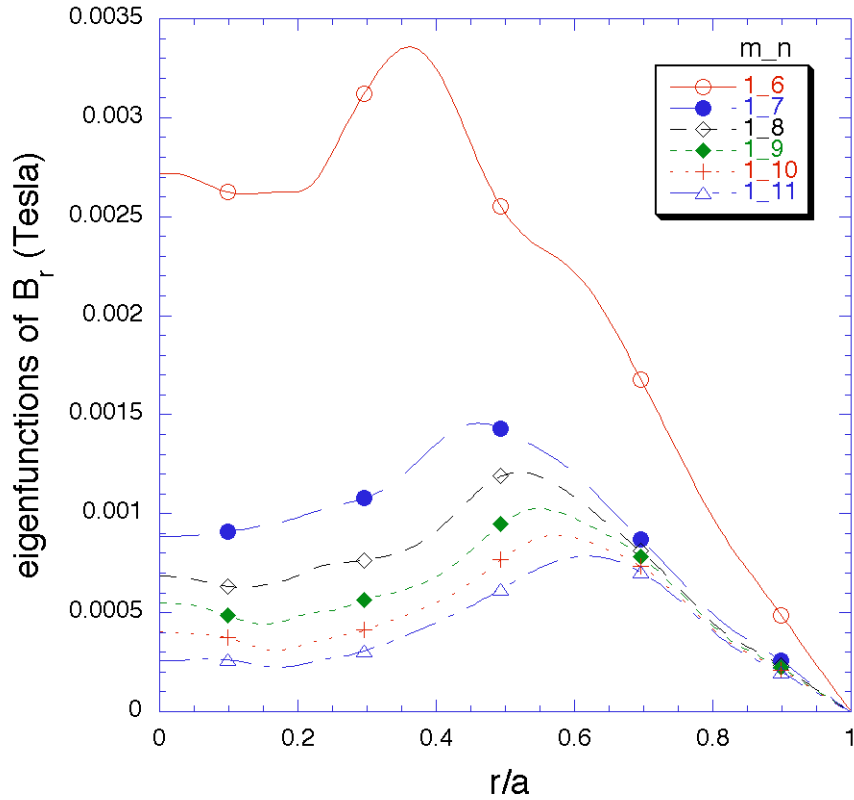


Figure 5.5 Radial fluctuation eigenfunctions as calculated by DEBS, scaled by the measured fluctuation amplitudes at the wall.

This paragraph outlines the exact process of deriving the radial fluctuation amplitude from the edge-measured modes. For a given mode the toroidal and poloidal fluctuation amplitudes are measured at the wall with magnetic pick-up coils. This measurement can be related to the value of the radial fluctuation amplitude internal to the plasma through some scaling function,  $F_n(r)$ :

$$\tilde{B}_r^{\text{exp.}}(r) = F_n(r) \tilde{B}_{\text{Tot.}}^{\text{exp.}}(a). \quad (73)$$

(Note that, a scaling function will exist for each mode in the spectrum. Superfluous n-subscripts have been dropped to avoid cluttering the expressions. They will be reinstated in the final relation.) Recall from Section 3.6.1 that for a given n-mode the total m=1 fluctuation amplitude at the wall is:

$$\tilde{B}_{\text{Tot.}}^{\text{exp.}}(a) \propto \sqrt{1 + \left(\frac{na}{R}\right)^2} \tilde{B}_p^{\text{exp.}}(a). \quad (74)$$

Hence, the scaling function can be defined as:

$$F_n(r) = \frac{\tilde{B}_r^{\text{exp.}}(r)}{\sqrt{1 + \left(\frac{na}{R}\right)^2} \tilde{B}_p^{\text{exp.}}(a)}. \quad (75)$$

The radial fluctuation eigenfunction in the experiment is not measured, but can presumably be related to the radial fluctuation eigenfunction in the DEBS simulation by some scaling parameter,  $C^{\text{DEBS}}$ :

$$\tilde{B}_r^{\text{exp.}}(r) = C_n^{\text{DEBS}} \tilde{B}_r^{\text{sim.}}(r). \quad (76)$$

For each mode,  $C^{\text{DEBS}}$  can be estimated from either the toroidal or poloidal fluctuation eigenfunction, since these eigenfunctions can be directly compared to toroidal or poloidal fluctuations measured at the edge of the plasma:

$$C_n^{\text{DEBS}} = \frac{\tilde{B}_p^{\text{exp.}}(a)}{\tilde{B}_p^{\text{sim.}}(a)}. \quad (77)$$

Implicit in this relation is the assumption that for a given mode, the  $C^{\text{DEBS}}$  scaling parameter is equally applicable to the poloidal, toroidal, and radial eigenfunction in turn. This assumption can be checked by comparing, mode-by-mode, the values of  $C^{\text{DEBS}}$  that are calculated from the toroidal and poloidal components. If these two numbers (for a given mode) are similar, it lends credence to the assumption that  $C^{\text{DEBS}}$  may be applied to the radial eigenfunctions. The values of  $C^{\text{DEBS}}$  for this  $S \sim 10^6$  simulation are shown in Table 5.1.

m=1, n	Toroidal $C^{\text{DEBS}}$	Poloidal $C^{\text{DEBS}}$	Infer. Radial $C^{\text{DEBS}}$
6	0.6467	0.6119	0.6293
7	0.4749	0.4071	0.4410
8	0.5095	0.4309	0.4702
9	0.5191	0.4351	0.4771
10	0.5417	0.4479	0.4948
11	0.5198	0.4545	0.4872

Table 5.1 Comparison of toroidally and poloidally calculated scaling factors from DEBS simulation to experiment. The radial scaling factors are the average of the toroidal and poloidal factors.

Thus for every mode, the scaling function can be calculated according to the relation:

$$F_n(r) = \frac{C_n^{\text{DEBS}} (\tilde{B}_r^{\text{sim.}}(r))_n}{\sqrt{1 + \left(\frac{na}{R}\right)^2} (\tilde{B}_p^{\text{exp.}}(a))_n}. \quad (78)$$

The scaling functions as calculated in this manner are shown in Figure 5.6. The important result from this figure is the value of the  $n^{\text{th}}$  scaling function at the  $n^{\text{th}}$  rational surface. These values are the multiplicative factors that must be applied to the edge-measured fluctuation amplitudes to yield the radial fluctuation amplitudes at the rational surfaces, which are then used to calculate the island widths, the field stochasticity, and the Rechester-Rosenbluth estimated thermal conductivity.

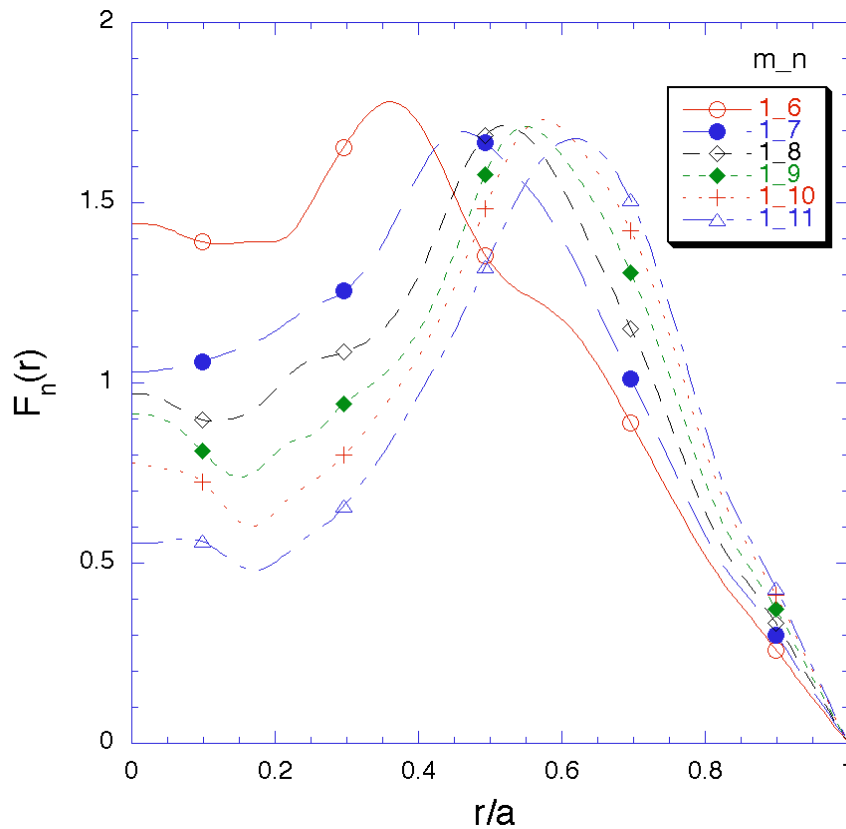


Figure 5.6 Calculated scaling functions for  $m=1$ ,  $n=6-11$  radial eigenmodes.

### 5.3 Comparing Measured $\chi_e$ to $\chi_{RR}$ in Standard Plasmas

Before comparing  $\chi_e$  to  $\chi_{RR}$  it is enlightening to examine the stochasticity of the magnetic field. The island widths have already been shown in conjunction with the  $q$ -profile

in Figure 4.10. It was shown above to motivate that the magnetic tearing mode islands overlap in the MST. That this overlap of islands destroys flux surfaces and leads to a stochastically wandering magnetic field is confirmed in the field-line tracing results from the MAL code, shown below in Figure 5.7. Puncture plots of the magnetic field line trajectories indicate that these Standard MST plasmas are highly stochastic in the mid-radius region, where the resonant surfaces begin to bunch together because of increased  $q$ -shear. In the core, where the stochasticity is low since the  $m=1, n=6$  island is largely isolated, field-line tracing reveals the  $n=6$  island structure. This simulation also suggests that good flux surfaces may be present around the reversal surface ( $r/a \sim 0.75$ ).

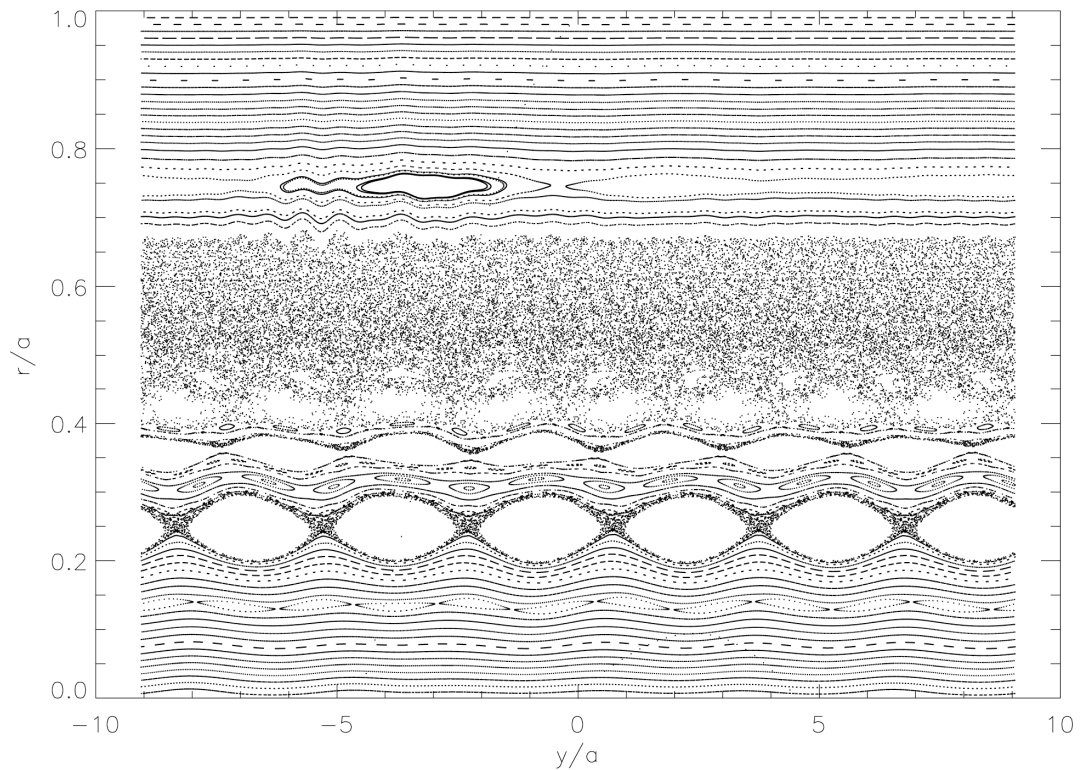


Figure 5.7 Puncture plot of magnetic field lines in Standard plasmas between sawteeth from DEBS/MAL simulation. Figure courtesy of Ben Hudson.

The stochasticity of the field can be made more quantifiable, by calculating the stochasticity parameter,  $s$ , as defined in the previous section. Table 5.2 shows the value of  $s$  for Standard MST plasmas. The fraction  $1/s^2$  can be thought of as the fraction of the original mode amplitude that is necessary to reduce the island overlap to “just touching.” For example,  $s=1.9$  for the  $n=6$  and  $n=7$  modes, then  $1/s^2=0.28$ ; or if the 6 and 7 mode amplitudes were reduced to less than 28% of their original value, then they would no longer be overlapping, all other things being equal.

m=1, n-number	$\Delta_{m,n}$ (cm)	island width (cm)	s	$1/s^2$
1-5	Not resonant			
6	10.3	22.4		
			1.9	0.28
7	20.0	11.6		
			2.3	0.19
8	24.5	9.3		
			2.8	0.12
9	27.5	7.8		
			3.8	0.07
10	29.4	6.7		
			4.2	0.06
11	30.9	6.0		
			4.9	0.04
12	32.1	5.4		
			6.5	0.02
13	32.9	4.7		
			5.8	0.03
14	33.7	4.5		
			11.0	0.01
15	34.1	4.3		

Table 5.2 The calculated stochasticity parameters for magnetic islands in Standard MST plasmas at  $-1.75$  ms in the sawtooth cycle.

Rechester-Rosenbluth type thermal conductivity, i.e. enhanced due to a stochastic magnetic field, is asserted to occur for regions in which the stochasticity parameter,  $s \gg 1$ .

From Table 5.2 it can be seen that even though the magnetic islands overlap in the core of of MST Standard plasmas, the stochasticity is on the order of 1. Therefore, it is not surprising that the measured  $\chi_e$  in the core of the MST is lower than the estimated  $\chi_{RR}$ , shown in Figure 5.8. Moving radially outward from the core, the island overlap increases, as does the corresponding stochasticity. Likewise, the measured  $\chi_e$  and the estimated  $\chi_{RR}$  come more into agreement, as the stochasticity in that region increases.

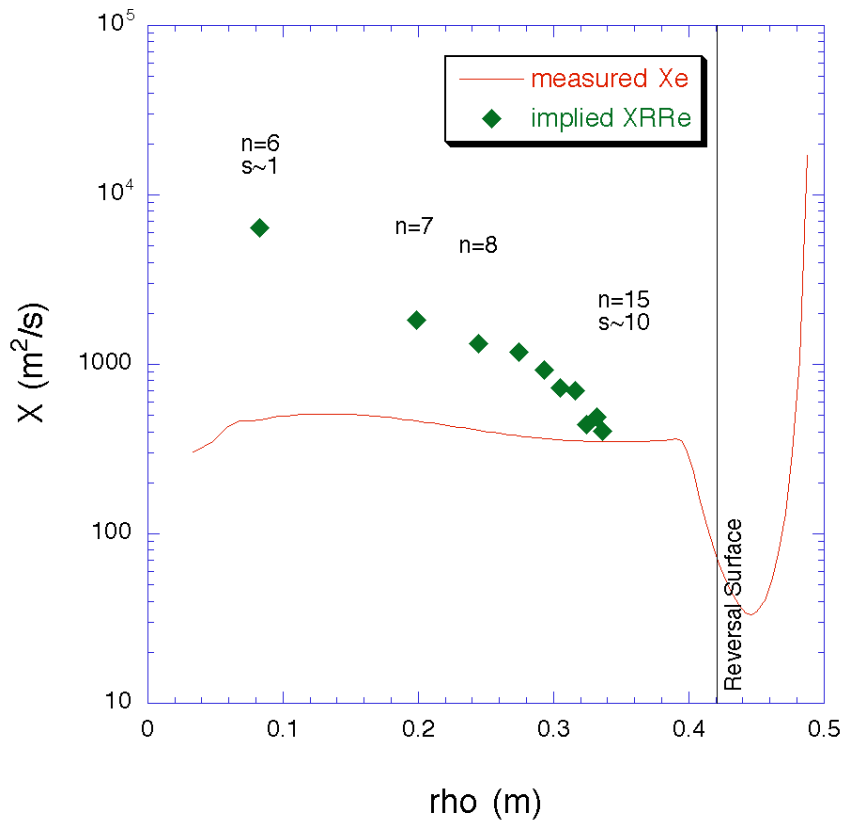


Figure 5.8 Profile of measured  $\chi_e$  -1.25 ms away from the sawtooth crash in Standard plasmas, compared to the calculated Rechester-Rosenbluth expected conductivity from the measured fluctuation level.

The variation of the magnetic field stochasticity serves to nominally divide the plasma into three regions: the core, the mid-radius, and the edge region. In the core, the q-

profile is very flat, and consequently there is little  $q$ -shear. This leads to a wide tearing-mode island (the  $m=1, n=6$  island), and also a large radial separation between neighboring resonant surfaces. Even though the  $n=6$  and  $n=7$  fluctuation amplitudes are measured to be the largest amplitudes in the discharge, there is only a weak overlap of the corresponding magnetic islands. Hence the stochasticity in the core is very low, and the measured thermal conductivity is (not surprisingly) far below that which is predicted from the fluctuation amplitudes. In the mid-radius region of the plasma, the  $q$ -shear increases, leading to closer packing of the mode-rational surfaces and ultimately to greater overlap of magnetic islands. Even though the fluctuation amplitudes are small for  $n=9$  through  $n=15$  modes, there is strong overlap of the magnetic islands, which implies a much greater field stochasticity. In this region, there is very good agreement between the measured thermal conductivity and that which is predicted by Rechester-Rosenbluth theory. Because the mid-radius region is a much larger volume of plasma than the core, the stochastic transport of this region dominates the core transport of heat. The edge region of the plasma is not well-diagnosed in these measurements, but because of the steep temperature gradient, a large reduction in thermal conductivity is implied. A lower  $\chi_e$  at the edge has been observed in other RFP experiments<sup>12,13</sup> and simulations.<sup>14</sup> Large  $m=0$  islands are present in this region and impede the transport of heat and particles from the mid-radius plasma to the edge.

Calculating a plasma-volume-averaged  $\chi_{RR}$  over the same radial range where the measured  $\chi_e$  is averaged facilitates a comparison between the two. Because of the volume averaging, this process weights the mid-radius region in which the stochasticity parameter is high. The result is shown in Figure 5.9. Excluding the time point immediately following the sawtooth crash (+0.25 ms) the data shows a linear dependence. It is not surprising that the slope of this line is  $<1$ , since included in the averaging is the core region, which does not agree with stochastic transport. The mid-radius region is more strongly weighted than the core region by the volume averaging though, and dominates the dynamics of the entire

region. The implication from these results is that stochastically wandering field-lines in the core and mid-radius region (taken as a whole) of Standard MST plasmas are responsible for the transport of heat, as expected from Rechester-Rosenbluth theory.<sup>3</sup>

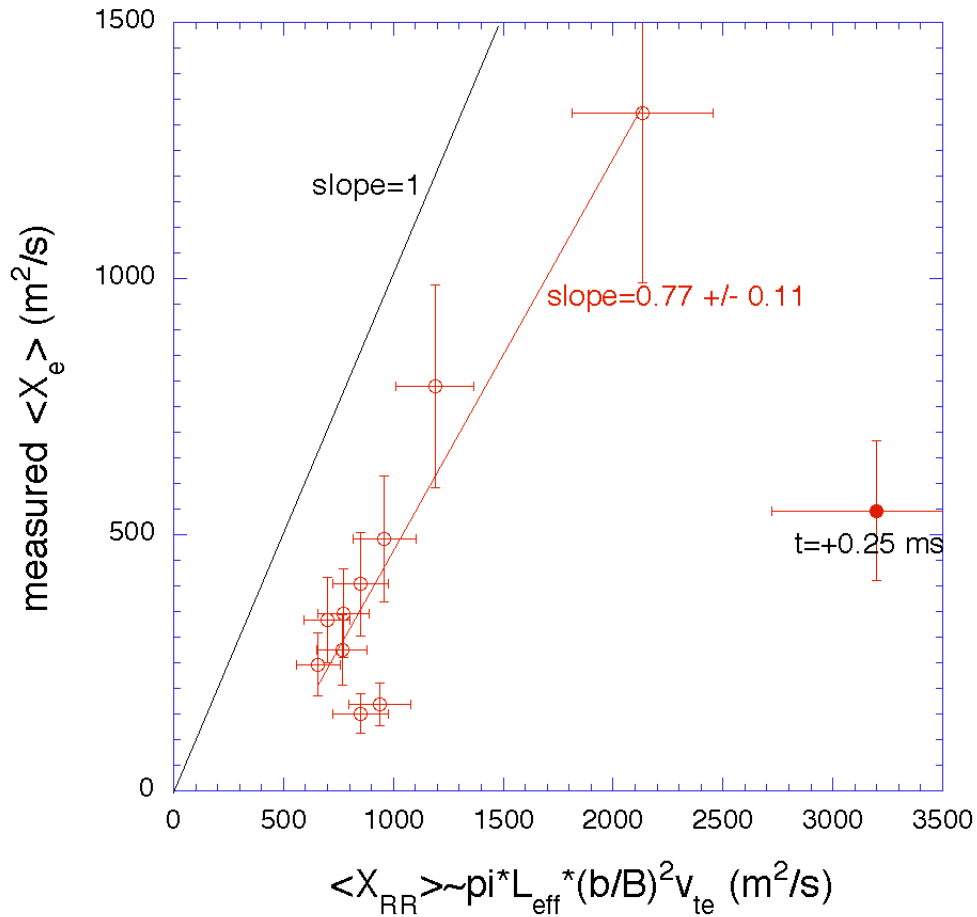


Figure 5.9 Linear scaling of core-averaged, measured thermal conductivity versus Rechester-Rosenbluth like thermal conductivity shows good agreement.

The overall stochasticity of the core plasma is a good indicator of the core electron thermal conductivity. Still outstanding from the above trend is the single time point at +0.25 ms, right after the sawtooth crash. This point lies well away from the fluctuation amplitude based scaling of Rechester-Rosenbluth. The calculated  $\langle X_{RR} \rangle$  depends both on the square of the (local) radial fluctuation amplitude and on the thermal velocity, which has a weak

temperature dependence. It does not take into account the local degree of stochasticity, instead assuming a fully stochastic field. The stochasticity has a weak, inverse dependence on the q-profile shear. In Section 3.5.6, Figure 3.25, it was shown that after the sawtooth crash the current profile has relaxed,  $\beta_e$  has become flatter, and the q-shear has increased. This suggests that the stochasticity after the sawtooth crash is less than the stochasticity before, if the fluctuation amplitudes are comparable. Plotting the core-averaged, measured  $\beta_e$  against the volume-averaged stochasticity over the sawtooth cycle supports this trend, even across different plasma discharge types, as shown in Figure 5.10. Of particular note is that the time point at +0.25 ms (the filled circle) is now much more in-line with the rest of the data, though the agreement is not perfect.

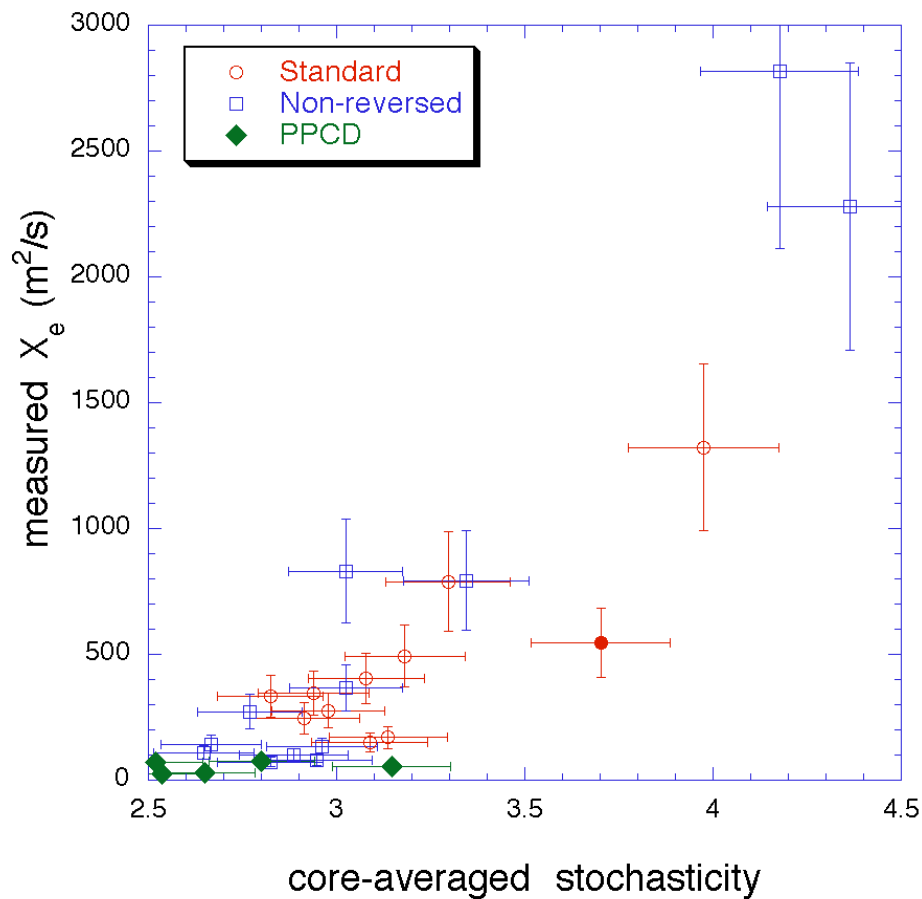


Figure 5.10 Measured, core-averaged conductivity increases with stochasticity across various plasmas discharge types.

## 5.4 Implications for Ion Heating

### 5.4.1 Ion Energy Confinement Time

The ion energy confinement time can be defined as:

$$\tau_{E,i} = \frac{W_i}{P_{e\text{to}i} - P_{CX} - \frac{\partial W_i}{\partial t}} \quad (79)$$

Calculating this term is difficult for Standard MST plasmas because the measured sources and sinks in the denominator are comparable, and the difference between them is near zero. This results in an ion energy confinement time, which can be large in magnitude and often negative. Averaging over the sawtooth cycle, the ion energy confinement time is about  $-6$  ms. A confinement time less than zero is, of course, unphysical, and suggests that the energy budget terms which are being considered here are not complete. As a lower bound, it is reasonable to assume that the ion energy confinement time is equal to the total energy confinement time (about 1.5 ms),<sup>15</sup> which is slightly higher than the electron energy confinement time (about 1 ms). (See Figure 4.2 and Figure 4.3.) Since the stored thermal energy in the ions is about 2.3 kJ, a “back of the envelope” calculation suggests that there is an (upper bound) ion-heating budget of about 1.5 MW. Since the collisional heating is about 450 kW, charge exchange losses are about 645 kW, and the change in ion stored thermal energy provides an additional 57kW of heating, there is a remaining (upper bound) “anomalous” ion heating power of about 1.7 MW necessary. If the ion energy confinement time is about 10 ms,<sup>15</sup> then only 370 kW of anomalous power are needed. For comparison the total, Ohmic input power to the plasma is on the order of 5 MW. Assuming an ion energy confinement time of 10 ms, the anomalous power required over the sawtooth cycle is shown

in Figure 5.11. This anomalous power should be subtracted from the electron energy budget, but represents a small correction (unless the ion and electron energy confinement times are similar.) The source of this “anomalous” power is unknown at this point, but the MHD dynamo is suspected.<sup>16, 17</sup>

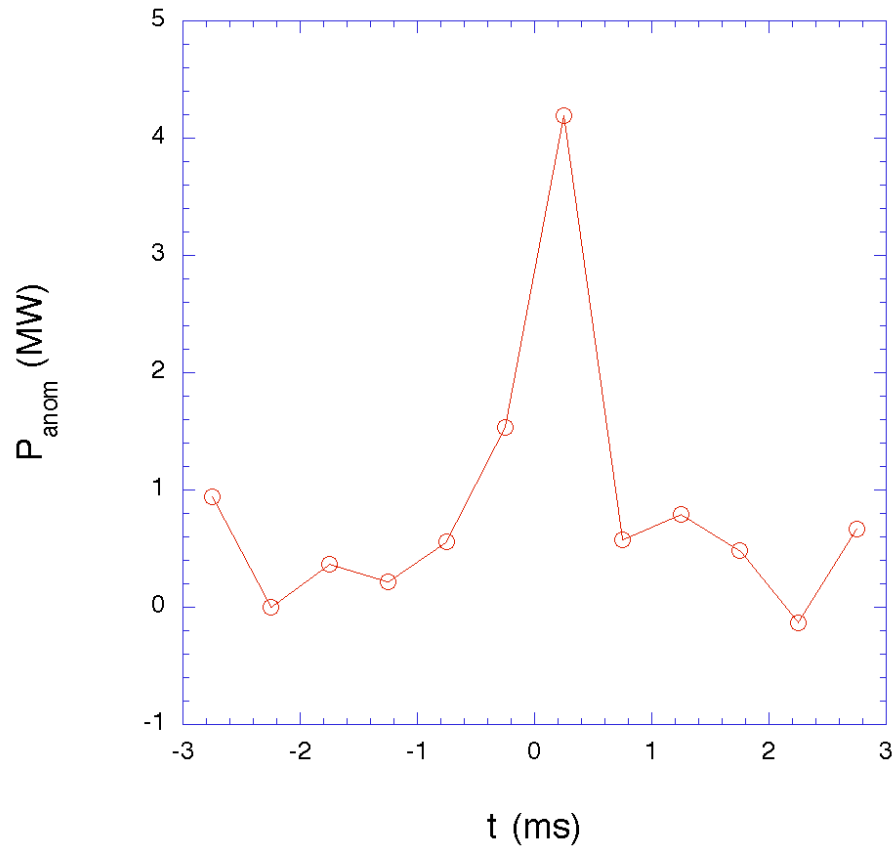


Figure 5.11 Anomalous power required if the ions have a 10 ms energy confinement time.

#### 5.4.2 Comments on Ion Thermal Conductivity

Referring to Figure 5.9, averaged over the core, i.e. where the magnetic field is stochastic to varying degrees, the measured electron thermal conductivity is in approximate agreement with the amount of conductivity that would be expected according to Rechester-Rosenbluth arguments from a stochastic magnetic field. Again, this is averaged over the

core. If parallel electron streaming along the stochastic field is responsible for electron heat transport (averaged over the core), then it is reasonable to expect that parallel ion streaming along the stochastic field is responsible for ion heat transport.<sup>18</sup> In that case, the core-averaged value of the ion thermal conductivity can be calculated, since in Rechester-Rosenbluth's model<sup>1</sup> the difference in transport is simply the ratio of the ion to electron thermal speeds:

$$\kappa_i = \kappa_e \sqrt{\frac{T_i m_e}{T_e m_i}}. \quad (80)$$

Under this assumption, the amount of anomalous ion heating can be deduced from the relations for ion power balance:

$$Q_i^{\text{cond}} = 2\kappa_i n_i \nabla_r T_i, \quad (81)$$

$$Q_i = Q_i^{\text{conv}} + Q_i^{\text{cond}} = 2\kappa_i T_i \nabla_r n_i, \quad (82)$$

$$Q_i = \frac{1}{4\pi} \int S_{E,i} \nabla \left( \frac{3}{2} n_i T_i \right) dV. \quad (83)$$

Implicit here is the assumption that the electron and ion fluxes are equal, which is essentially the condition of ambipolarity (assuming the impurity flux is negligible.) For the ions, the main sources and sinks can be expressed in the following equation:

$$S_{E,i} = P_{ei} + e \int E_r \nabla P_{CX} + P_{\text{anom}} \quad (84)$$

The magnitudes of these terms are shown in Figure 5.12. The solid lines in Figure 5.12 are nominally “source” terms and the dashed lines are nominally “sink” terms. A negative sink term is effectively a source, and vice versa. Essentially, if  $\rho_i$  can be found from the “stochastically driven transport in the core” assumption, then the anomalous ion heating power (for  $0 < \rho < 0.35$  m) can be deduced. This amount of power can then be compared (in Figure 5.13) to the result from the previous section, which is the total amount of anomalous power needed in the entire plasma. It is worth pointing out that  $\rho = 0.35$  m represents about 70% of the plasma radius, and about 50% of the plasma volume.

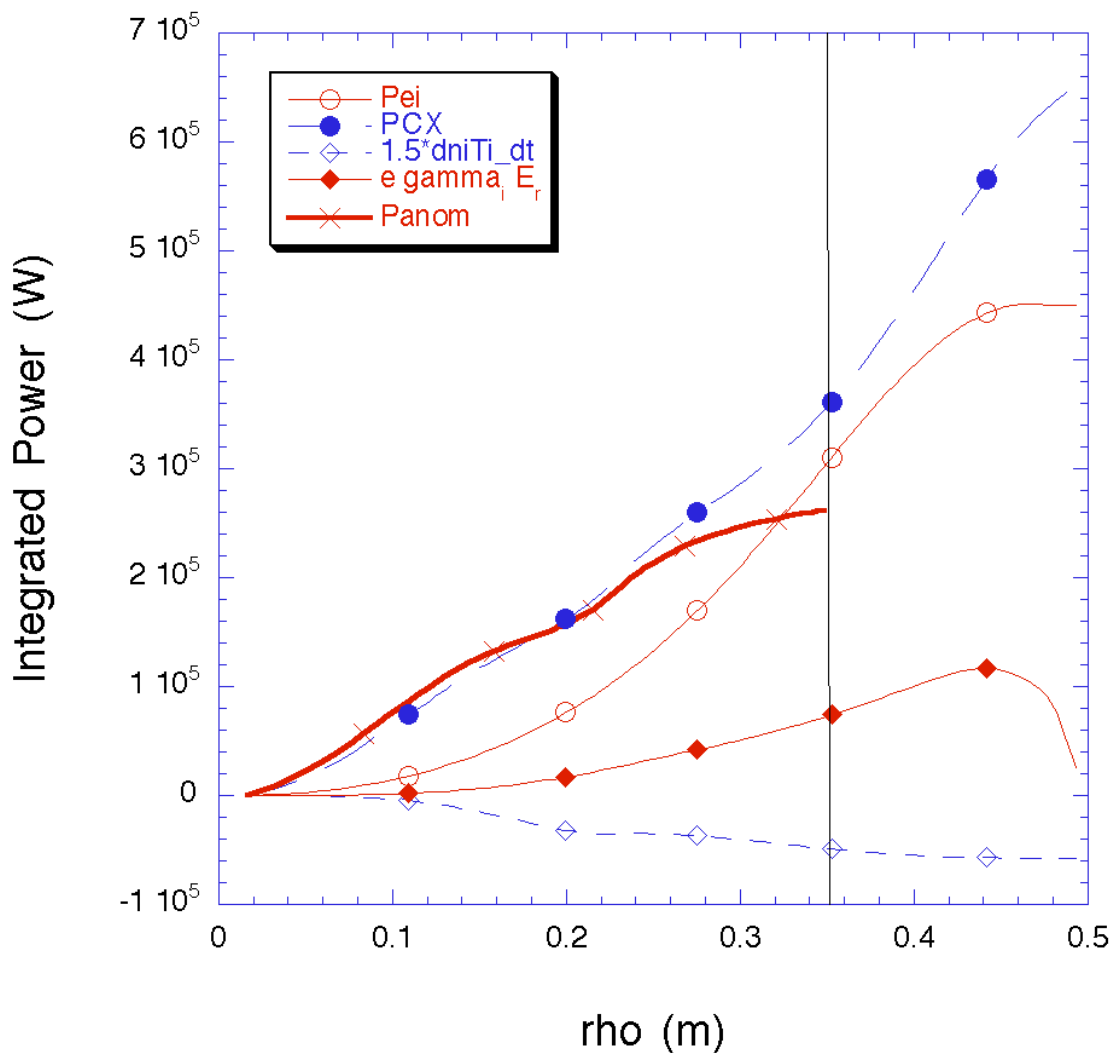


Figure 5.12 Ion energy budget at -1.75 ms in Standard plasmas.

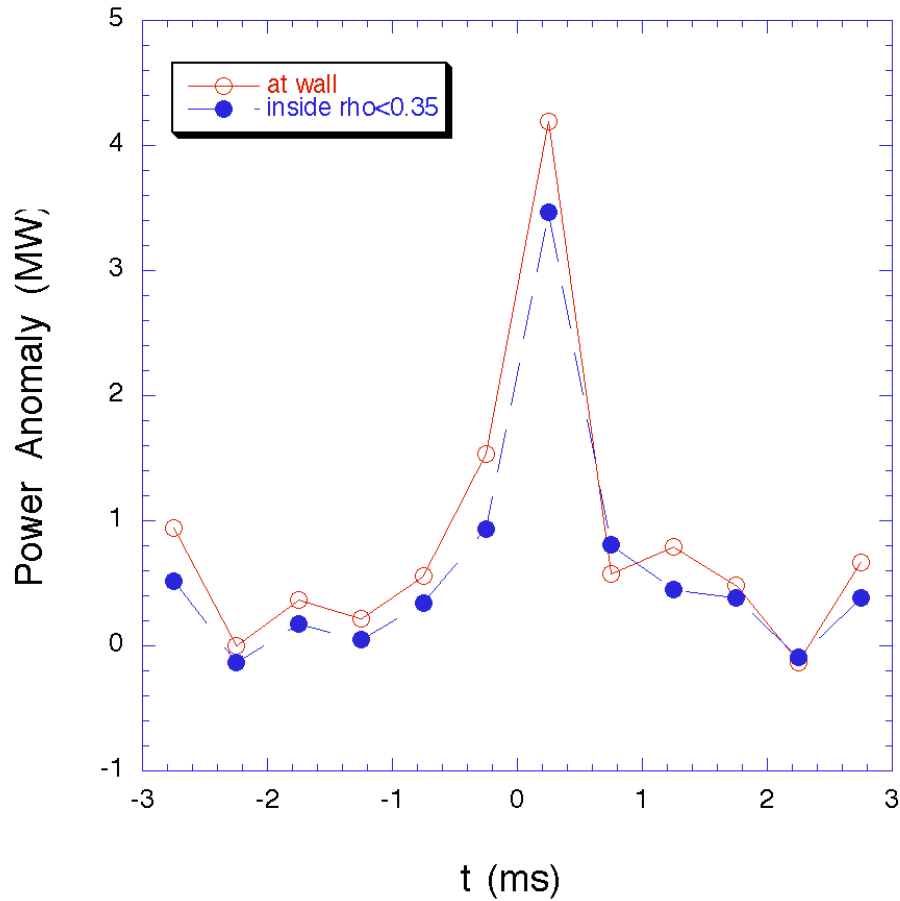


Figure 5.13 Comparison between core&mid-radius and whole plasma of the amount of expected anomalous ion heating.

On the surface, Figure 5.13 is a comparison of how the anomalous power is distributed between the mid-radius and the edge. In this sense, since the curves are nearly equal, it suggests that the majority of anomalous ion heating occurs inside of the mid-radius region of the plasma. If that is physically true, then there is a more subtle implication: that the ion energy confinement time is indeed  $\sim 10$  ms, as assumed in the previous section. In contrast, the “stochastic field” assumption used to determine  $\tau_i$ , is probably a lower bound. A larger actual  $\tau_i$  would require a larger amount of anomalous ion heating inside the mid-radius region, since the other terms are measured. Without ion-cooling in the edge, there cannot be greater ion-heating inside the mid-radius region than is measured in the entire

plasma (at the wall). Thus, the strongest conclusions that can be drawn comparing these two curves is that  $\chi_i$  from this stochastic field assumption is a lower bound on ion heat transport, and the ion energy confinement time is less than 10 ms.

## 5.5 Summary

Non-linear DEBS calculations at a Lundquist number of  $10^6$  have been done for the first time for MST plasmas, and are used to determine the eigenfunctions of radial magnetic fluctuations. These eigenfunctions, when properly normalized by experimental measurements of fluctuation amplitudes at the edge, allow the plasma stochasticity, island widths, and thermal conductivity to be calculated, based on the framework of Rechester-Rosenbluth theory. These theoretical calculations of the thermal conductivity show that where the magnetic field stochasticity is high, as in the mid-radius region of the plasma, there is good agreement between the predicted and measured value of electron thermal conductivity. If the stochasticity is low, as it is in the core of MST Standard plasmas, then the predicted conductivity overestimates the measured conductivity. Rechester-Rosenbluth theory for transport in a stochastic magnetic field is only valid if the stochasticity is high. Hence the deviation is not surprising.

Averaging over the core and mid-radius regions ( $0.05 < r < 0.30$  m), the measured electron thermal conductivity scales roughly linearly with the plasma-volume-averaged Rechester-Rosenbluth conductivity. The scaling slope is slightly less than 1, which would be perfect agreement. Since the stochasticity averaged over this region is not particularly large, however, it is reasonable that the scaling slope would be less than 1. Comparing the core-averaged measured electron thermal conductivity with the core-averaged stochasticity, there is a strong scaling. When the stochasticity is high, so is the measured electron conductivity, underscoring the notion that the stochasticity of the magnetic field is at the heart of

determining heat transport in the MST. This trend with stochasticity persists across various discharge types, from PPCD, to Standard, to Non-Reversed discharges, which will be discussed in the next chapter.

Finally, since the stochastic magnetic field is responsible for electron heat transport, it is perhaps reasonable to assume that it is also responsible for ion heat transport. This assumption ultimately necessitates an “anomalous” power source for the ions, and constrains the ion energy confinement time to be less than  $\sim 10$  ms during Standard MST discharges.

## References

1. A.B. Rechester and M.N. Rosenbluth, *Physical Review Letters*, **40** (1), 38-41 (1978).
2. J.D. Callen, *Physical Review Letters*, **39** (24), 1540-1543 (1977).
3. J.S. Sarff, "Control of Magnetic Fluctuations and Transport in the MST," PLP Report 1225, University of Wisconsin-Madison, (1999).
4. F. D'Angelo, R. Paccagnella, *Physics of Plasmas*, **3** (6), 2353-2364 (1996).
5. M.R. Stoneking, J.T. Chapman, D.J. Den Hartog, S.C. Prager and J.S. Sarff, *Phys. Plasmas*, **5** (4), 1004-1014 (1998).
6. G.M. Zaslavsky and B.V. Chirikov, *Sov. Phys. Usp.* **14**, 549 (1972).
7. A.F. Almagri, *The Effects of Magnetic Field Errors on Reversed Field Pinch Plasmas*, *Ph.D. Thesis*, University of Wisconsin-Madison (1990).
9. D.D. Schnack, D.C. Barnes, Z. Mikic, D.S. Harned, E.J. Caramana, *Journal of Computational Physics*, **70**, 330-354 (1987).
10. J.C. Wright, Personal communication.
11. J.T. Chapman, *Spectroscopic Measurements of the MHD Dynamo in the MST Reversed Field Pinch*, *Ph.D. Thesis*, University of Wisconsin-Madison (1998).
12. R. Bartiromo, V. Antoni, T. Bolzonella, A. Buffa, L. Marrelli, P. Martin, E. Martines, S. Martini, R. Pasqualotto, Presented at the 40<sup>th</sup> Annual Meeting of the Division of Plasma Physics, New Orleans, Louisiana, (1998).
13. D.A. Baker, C.J. Buchenauer, L.C. Burkhardt, et al., in *10<sup>th</sup> International Conference on Plasmas Physics and Controlled Nuclear Fusion Research*, London., Vol. 2, IAEA, Vienna (1984) 2-9.
14. E.D. Held, J.D. Callen, C.C. Hegna, C.R. Sovenic, *Physics of Plasmas*, **8** (4), 1171-1179 (2001).

15. E. Scime, M. Cekic, D.J. Den Hartog, S. Hokin, D. Holly, and C. Watts, *Phys Fluids B*, **4**, 4062 (1992).
16. E. Scime, S. Hokin, N. Mattor, and C. Watts, *Phys. Rev. Lett.*, **68**, 2165 (1992).
17. S. Hokin, A. Almagri, M. Cekic, B. Chapman, N. Crocker, D.J. Den Hartog, G. Fiksel, J. Henry, H. Ji, S. Prager, J. Sarff, E. Scime, W. Shen, M. Stoneking and C. Watts, *Journal of Fusion Energy*, **12** (3), 281-287 (1993).
18. J.M. McChesney, P.M. Bellan, R.A. Stern, *Physics of Fluids B*, **3** (12), 3363-3378 (1991).

Let me tell you what I think of bicycling. I think it has done more to emancipate women than anything else in the world.

-- Susan B. Anthony

## **Comparisons to Other MST Plasmas**

The MST can be run in a wide range of operating modes, which correspond to a variety of magnetic field configurations, and hence have a variety of confinement and transport characteristics. Comparing these characteristics can yield some general insight into RFP plasmas. In this chapter are the results from 5 separate experiments. For simplicity the plasma current and density were held relatively constant. To coarsely differentiate between these experiments the reversal parameter,  $F$ , was varied. Profiles for  $T_e$ ,  $T_i$ , and  $n_e$  are used to calculate the pressure profile, which is compared to the reconstructed  $q$ -profile to examine stability to ideal interchange modes. Zero-D and 1-D heat transport is compared through the different discharges. Changes in magnetic field stochasticity could explain the variation of confinement among the different discharges.

### **6.1 Introduction to the Experiments**

#### 6.1.1 Overview

The “Standard” MST plasma discharge has been expounded upon in some detail in the previous three chapters. As suggested early in Chapter 3, the MST is capable of producing plasma discharges, which differ significantly from the Standard discharge. To

investigate the transport characteristics of some of these other plasma discharges, a series of experiments were performed and subjected to analysis using the same routines as applied above.

The MST is a Reversed Field Pinch (RFP), meaning that the toroidal magnetic field reverses direction at the edge of the plasma, as compared to its direction in the core of the plasma. Moving radially outward from the core, since the toroidal field reverses direction, there must be a radius at which the toroidal field is zero. This is called the reversal radius; and in flux surface coordinates, it defines a reversal surface. In a Standard plasma the reversal surface can be between 6 to 10 cm into the plasma, measured from the last closed flux surface. In the case studied here, with  $I_p \sim 375$  kA,  $F \sim -0.22$ , the reversal surface is about 8 cm into the plasma, as shown above in Figure 4.10. The parameter  $F$  is the ratio of the toroidal magnetic field at the edge of the plasma to the average magnetic field over the entire plasma. As such,  $F$  is a coarse measure of the depth of the reversal surface in the plasma. As  $F$  is made more positive, the reversal surface approaches the edge of the plasma. For a discharge in which  $F=0$ , the reversal surface is found at the extreme edge of the plasma, i.e. the toroidal magnetic field is zero at the wall of the MST. An  $F=0$  discharge in the MST is referred to as a “Non-Reversed” plasma discharge. Because  $m=0$  magnetic modes, which contribute to the overall magnetic fluctuation level and hence presumably enhance radial (cross-field) plasma transport, are resonant at the reversal surface, the benefit of a Non-Reversed discharge is that the  $m=0$  modes are excluded from the plasma. A Non-Reversed plasma, then, is expected to have better confinement properties, all other things being equal. An  $F=0$ , Non-Reversed discharge is one of the cases studied below.

If  $F$  is further increased and becomes positive, i.e. the toroidal magnetic field remains in the same direction as it is in the core of the plasma, the MST is no longer a “reversed field” pinch in the sense of these discharges. Naming these plasmas is of some debate, but for the purposes of this thesis, they will simply be referred to as “ $F>0$  discharges,” or

“positive  $F$  plasmas.” Experimentally it is observed that the confinement properties of these plasmas are greatly degraded with respect to Standard ( $F < 0$ ) and even to Non-Reversed ( $F = 0$ ) plasmas. Moreover, the plasma discharges degrade quickly as  $F$  is made more positive. The results for two discharge conditions,  $F = +0.02$  and  $F = +0.03$  are shown below.

The final discharge condition examined in this chapter is a MST plasma under the influence of pulsed-poloidal current drive (PPCD.) The principles of PPCD have been developed elsewhere, but a cursory explanation is provided here.<sup>1,2,3</sup> The MHD dynamo refers to the spontaneous generation of magnetic field, caused by a resistive plasma flowing in an existing magnetic field. The dynamo driven current in the MST provides additional poloidal current at the edge of the plasma, with respect to the Ohmically driven current. Because this “dynamo current” arises from nonlinear interactions within the plasma, it is often associated with increased magnetic mode activity, which leads to increased cross-field (radial) transport, and decreased plasma (particle and energy) confinement. The idea behind PPCD is that if this additional poloidal current, erstwhile driven by the MHD dynamo fluctuations, is instead supplied by external capacitor banks, then the overall level of magnetic fluctuations in the plasma will be reduced and confinement will be improved. Experimentally, confinement is observed to improve dramatically with the application of PPCD, though the mechanism proposed above has yet to be clearly identified as responsible. The application of PPCD significantly alters the plasma, and it is unclear that the reduction in the MHD dynamo is the only effect resulting in improved confinement. Moreover, it is unclear even what represents “cause” and what represents “effect.” Still, it is clear that confinement is improved and magnetic fluctuations are reduced, compared to Standard plasma discharges, as will be shown below.

### 6.1.2 Experiment Sample Shots

By way of introducing the differences between the diverse plasma discharges available with the MST, sample shots will be shown of the 5 discharges studied in this thesis. The Standard plasma discharge has already been shown in Figure 3.1, but is reproduced here for convenience in Figure 6.1. The four traces shown in each of the figures, Figure 6.1 through Figure 6.5, will be useful for elucidating the basic ways the plasma discharges differ. The top trace is the plasma current, which in all 5 discharge types was around 385 kA. Similarly, the plasma density was held at roughly the same level,  $\sim 1 \times 10^{13} \text{ cm}^{-3}$ , as shown in the second trace. The third trace shows the voltage across the toroidal gap. Sawtooth events can be clearly seen as “spikes” in the toroidal gap voltage. The fourth trace shows the field reversal parameter,  $F$ . Comparing this trace among the 5 discharge types shows how  $F$  varies from  $-0.22$  (Standard), through  $0$  (Non-Reversed), to  $+0.02$ , and up to  $+0.03$ . In Figure 6.4 the plasma degradation can be clearly seen, e.g. in the sudden termination of the plasma. Note that Figure 6.1 through Figure 6.5 are on somewhat different time scales. PPCD is inherently transitory, and its pulsed nature can be seen in the  $F$ -trace of Figure 6.5. The auxiliary current drive is applied at 9.5 ms into the discharge, and shots were selected such that the last MHD burst occurs at  $\sim 15$  ms.  $F$  reaches a minimum of  $\sim -1$  around 18 ms into the discharge. The reduction of magnetic fluctuations while PPCD is applied is readily apparent in the trace of toroidal gap voltage. This fluctuation reduction is observed during PPCD on other machines as well.<sup>4</sup>

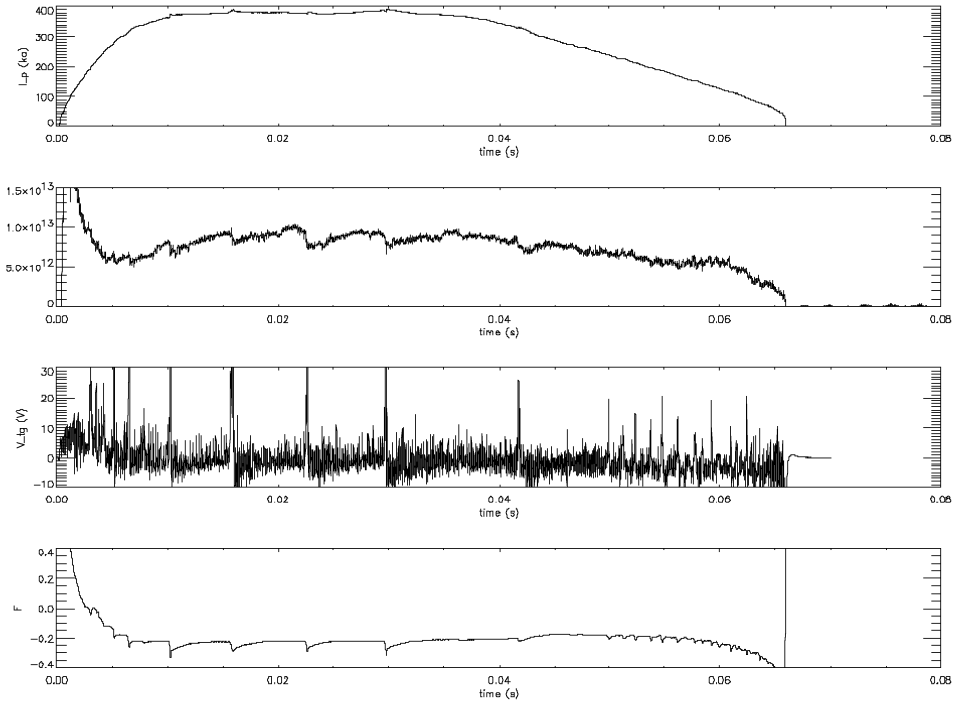


Figure 6.1 Shot 69 from November 13<sup>th</sup>, 2000 showing a typical “Standard” MST plasma.

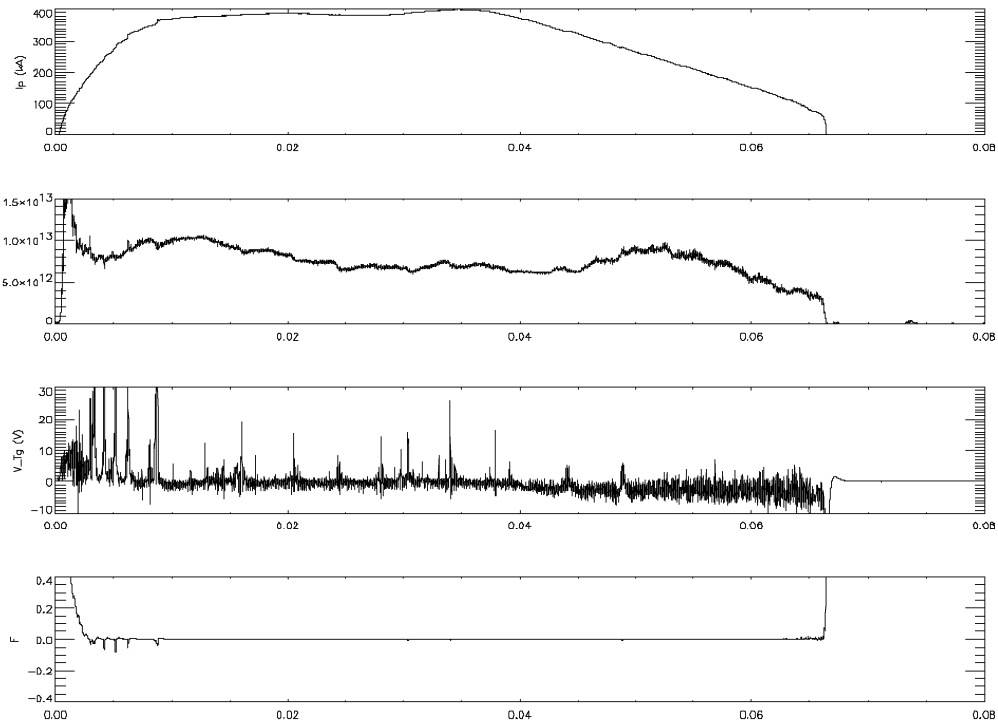


Figure 6.2 Shot 80 from March 30<sup>th</sup>, 2001 showing a typical “Non-Reversed” MST plasma.

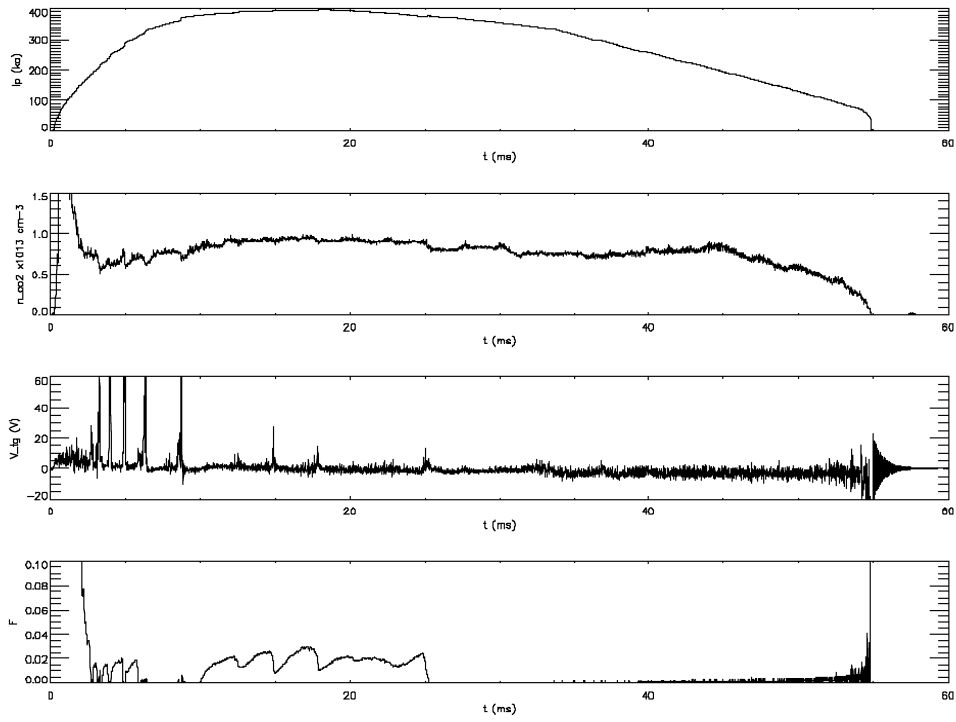


Figure 6.3 Shot 51 from April 3<sup>rd</sup>, 2001 showing a typical “F= +0.02” MST plasma.

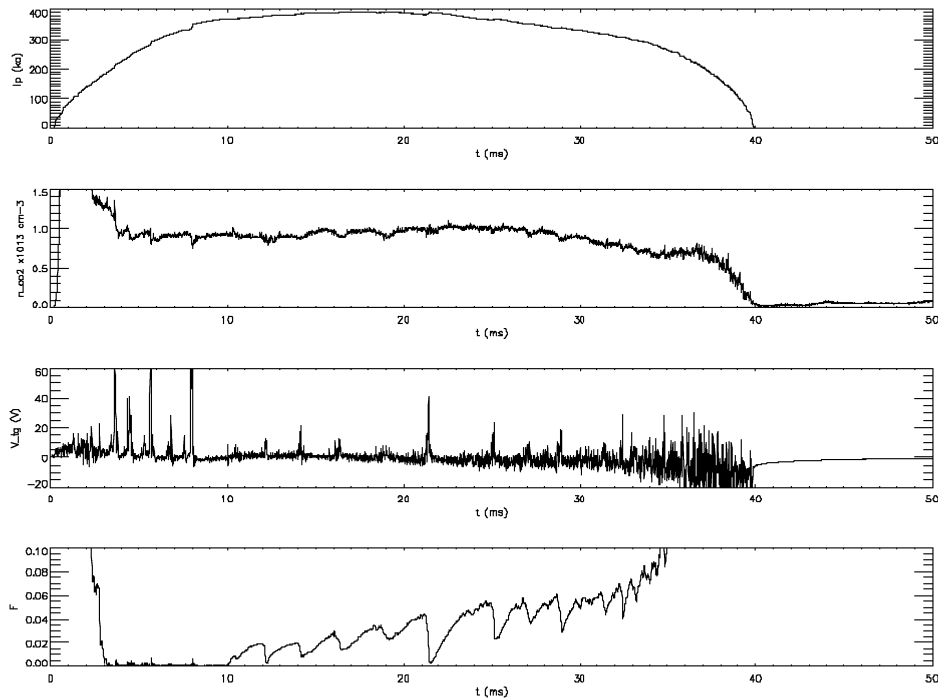


Figure 6.4 Shot 69 from April 2<sup>nd</sup>, 2001 showing a typical “F= +0.03” MST plasma: a small increase in F leads to a rapid degradation of the plasma.

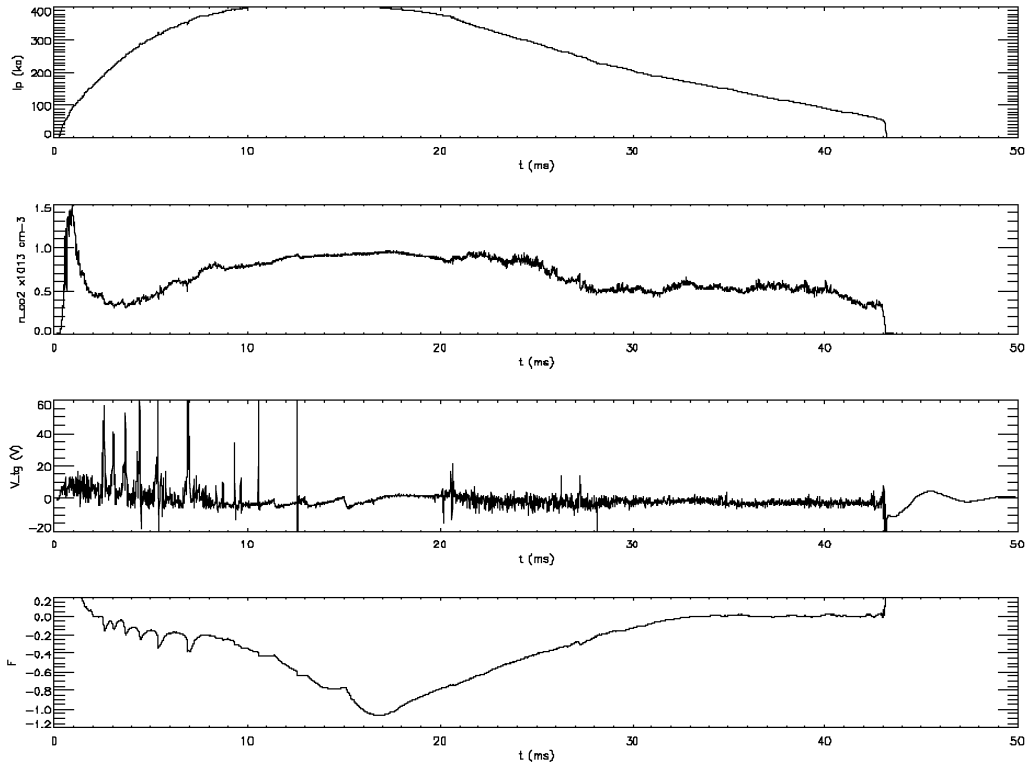


Figure 6.5 Shot 50 from March 24<sup>th</sup>, 2001 showing a typical “PPCD” MST plasma and the consequent reduction in magnetic fluctuations. Note that discharges were selected such that the last MHD burst occurs near  $\sim 15$  ms.

While the differences between these plasmas will be developed further in this chapter, it is useful to include an introductory summary table here. Table 6.1 gives a quick comparison of the basic plasma parameters at a time relative to the sawtooth crash indicated in the last column. For the PPCD case the information is shown at a time relative to the beginning of the plasma discharge, since sawteeth are generally not present while PPCD is applied. The approximate sawtooth period for the other 4 cases is shown in the sixth column. As such, the data in this table is generally “away” from the sawtooth crash. The table is arranged by increasing  $F$ . Both the plasma current and density are roughly equal for all cases, as intended. In all experiments deuterium was the working gas. The fifth column gives an indication of how many discharges each experiment includes in its ensemble. The

remaining columns allow the electron and ion temperatures, as well as the on-axis magnetic field, to be compared across experiments.

			CO <sub>2</sub>			TS	RS	MSE	
Name	F	I <sub>p</sub>	n <sub>e</sub>	n <sub>shots</sub>	τ <sub>sawt.</sub>	T <sub>e</sub>	T <sub>i</sub>	B <sub>0</sub>	t <sub>rel.</sub>
		kA	10 <sup>13</sup> cm <sup>-3</sup>		ms	eV	eV	T	ms
PPCD	-0.97	383	1.00	389	NA	825	410	0.395	18
Stan.	-0.22	375	0.89	475	6	310	239	0.347	-1.75
N.Rev.	0	374	1.01	401	6	350	187	0.306	-1.75
F>0	+0.02	390	0.93	336	4	250	230	0.329	-1.75
F>>0	+0.03	386	1.02	221	3	250	250	0.310	-1.25

Table 6.1 Overview of the experimental conditions. Deuterium was the working gas in all experiments.

## 6.2 Stability of the Pressure Profile

### 6.2.1 The Suydam Criterion

One type of instability for a high temperature plasma in a magnetic field arises from a detailed consideration of whether or not it is energetically more favorable for a tube of magnetic flux to move down the pressure gradient into a region of greater field curvature.<sup>5</sup> Whether or not the plasma is stable to this ideal interchange mode can be assessed by what is known as Suydam’s criterion:

$$\frac{rB_T^2}{B_0} \frac{dq}{dr} + 8p > 0. \tag{85}$$

Here  $B_T$  is the toroidal magnetic field,  $q$  is the “safety factor” representation of the magnetic field profiles, and  $p$  is the thermodynamic pressure. The safety factor,  $q$ , is given by the relation

$$q = \frac{rB_T}{RB_p}. \quad (86)$$

Here  $r$  is the minor radius,  $R$  is the major radius, and  $B_p$  is the poloidal magnetic field. Suydam’s criterion is a necessary but not sufficient condition for stability. This relation can be used to define a critical pressure gradient. If the measured pressure gradient is greater than this critical value, then the plasma could be unstable to ideal interchange modes. To assess whether or not MST plasmas are stable to these modes, it is necessary to have measurements of both the pressure gradient and the equilibrium magnetic fields.

### 6.2.2 Measured Pressure Profiles

The thermodynamic pressure profile is made up of the sum of the electron and ion pressure profiles. As will be shown below, the ion pressure varies only moderately between these 5 experiments. Though the ion pressure is included in the stability and transport analysis, most of the variation in the pressure between experiments comes from the electron terms. The electron density (and presumably ion density) was held roughly constant by design, hence any variation in electron pressure between experiments is due primarily to a change in electron temperature. Figure 6.6 shows the electron temperature profiles for these 5 experiments (away from the sawtooth crash.) Figure 6.7 shows the electron density profiles. The pressure profile is shown in Figure 6.8. Immediately apparent is the dramatic

increase of the electron temperature in PPCD plasma discharges. The electron temperature more than doubles during PPCD, even though the electron density changes little.

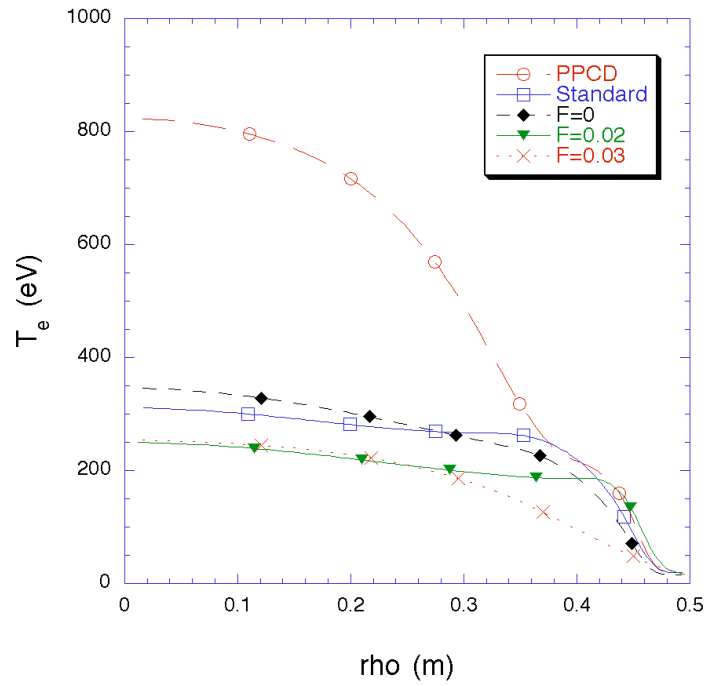


Figure 6.6 The electron temperature profile away from the nearest sawtooth crash.

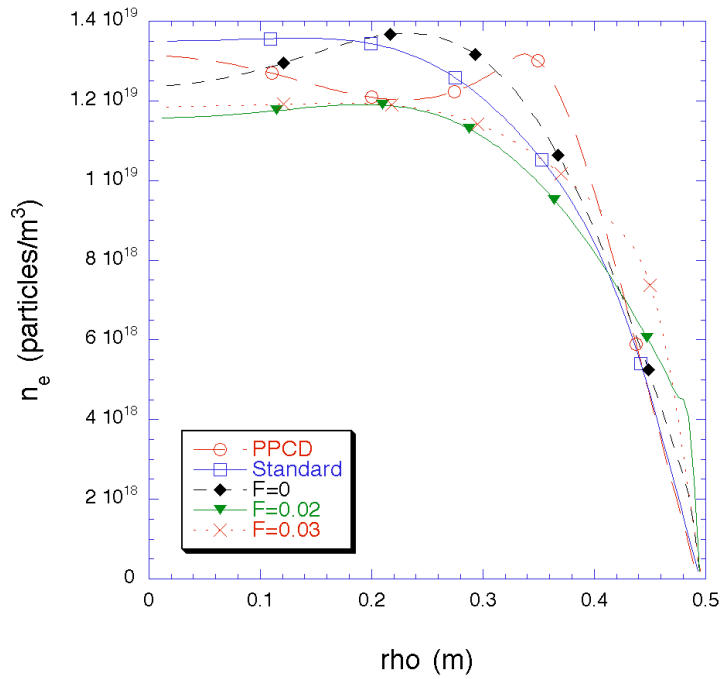


Figure 6.7 The electron density profile away from the nearest sawtooth crash.

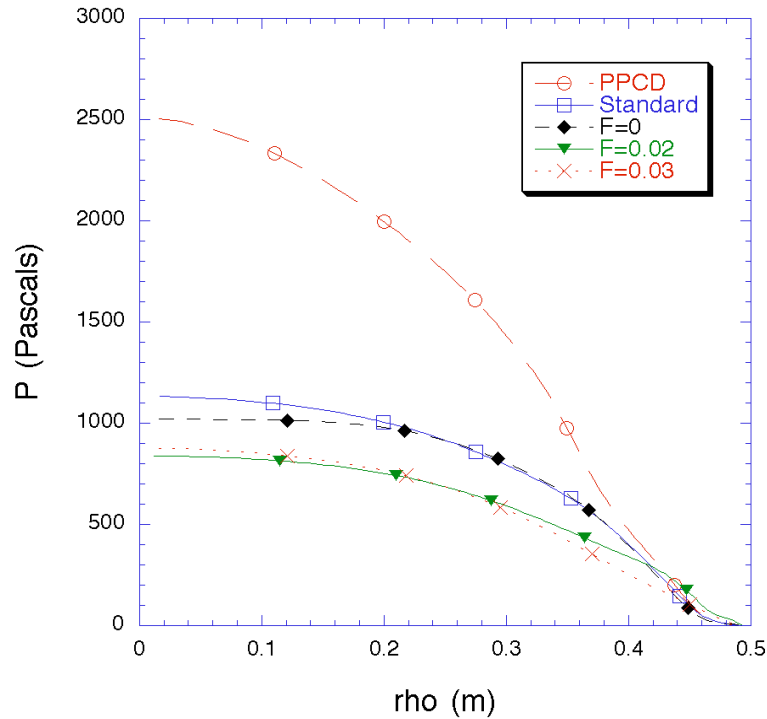


Figure 6.8 The pressure profile away from the nearest sawtooth crash.

### 6.2.3 Current Density and q-Profiles

The equilibrium magnetic field profiles in MST plasmas, and hence the q-profiles, are essentially determined by the current density profiles. MSTFit reconstructed current density profiles are strongly constrained by the measured Faraday rotation angle from FIR polarimetry, by the on-axis measured magnetic field from the motional Stark effect diagnostic, by the total plasma current from flux loops, and from deflections in a poloidal array of Mirnov probes. The current density profiles for all 5 experiments are shown in Figure 6.9. Because  $I_p$  is similar for all 5 cases, the volume integral of the current density must be approximately equal in all cases. I.e. small differences in edge current density are as significant as large differences in core current density. One observation is that Non-Reversed plasmas have a significantly broader current density profile compared to Standard plasmas.

This results in a more peaked  $q$ -profile and a flatter  $\beta$ -profile. A flatter  $\beta$ -profile implies that the plasma is closer to a Taylor minimum-energy state,<sup>6</sup> which may be significant when considering dynamo driven heating of the ions, as discussed in Section 6.3.

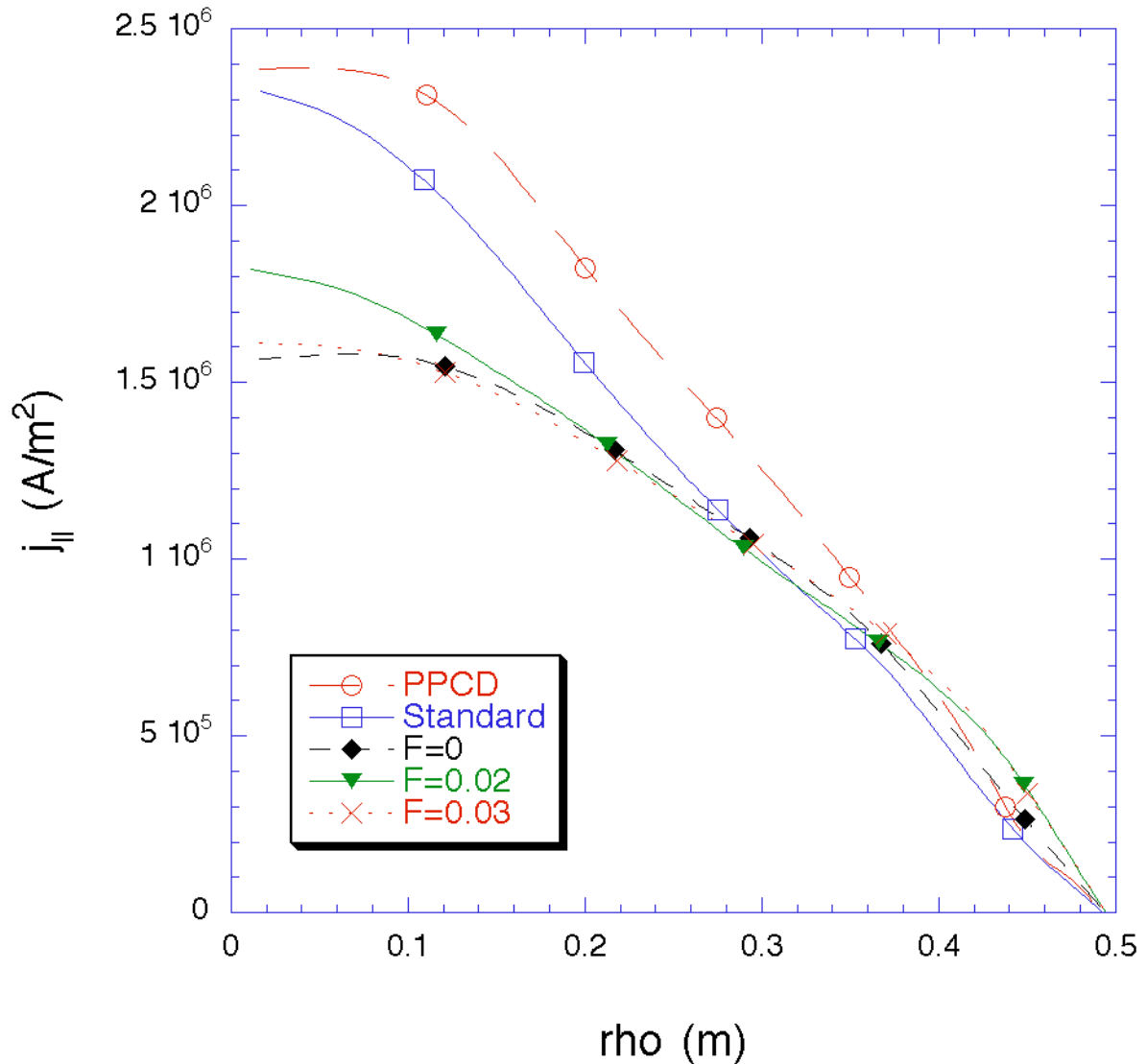


Figure 6.9 The current profile away from the sawtooth crash.

The safety factor profile for all of the experiments is shown in Figure 6.10, away from the sawtooth crash. As mentioned in the previous section, the reversal parameter  $F$  can be treated as a coarse measure of the depth of the reversal surface in the plasma. The more

negative  $F$  is, the further from the wall the reversal surface is located. Equilibrium reconstruction allows the location of the reversal surface to be asserted more quantitatively. Figure 6.10 indicates that as  $F$  is increased the reversal surface moves towards the wall, as expected.

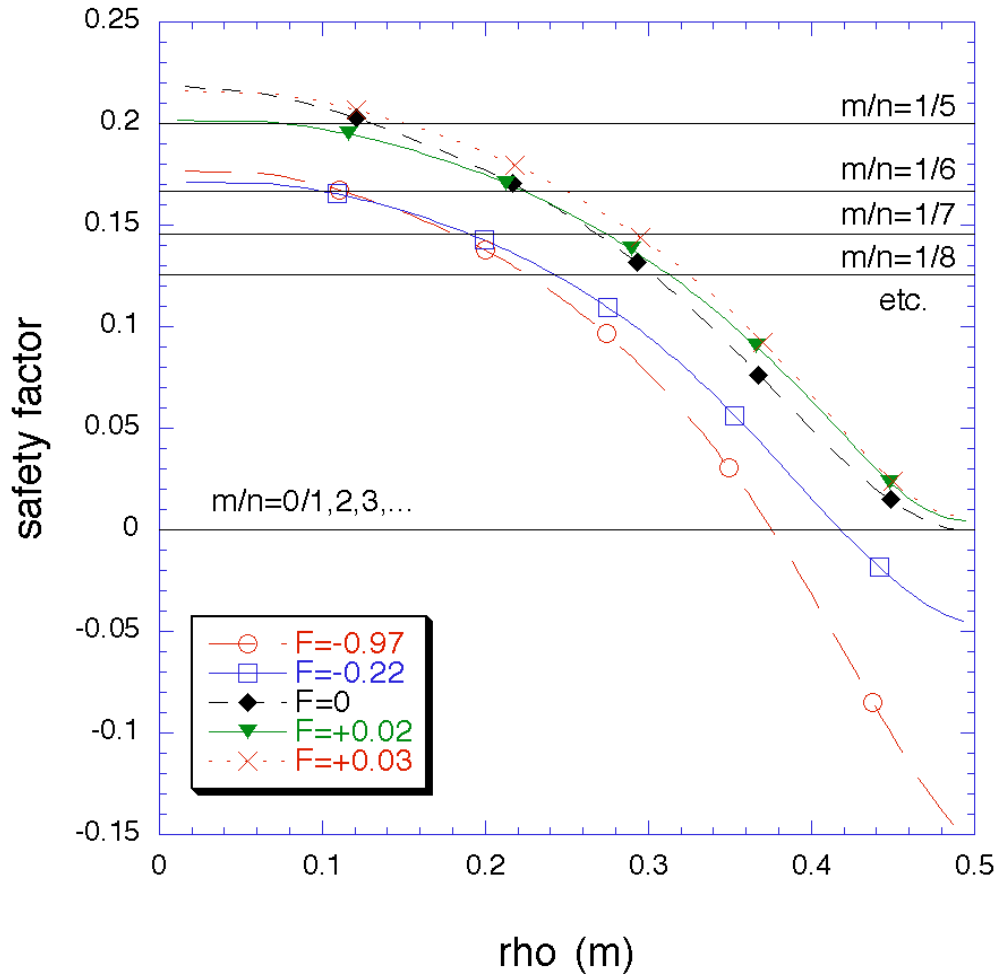


Figure 6.10 The safety factor profile away from the nearest sawtooth crash for all 5 plasma discharge types.

Also indicated in Figure 6.10 are the values for which the safety factor is a rational number, i.e. the ratio of two integers. Consider a magnetic field line that has a helical structure as it wraps around the torus. Let  $n$  be the number of times the field line completes a toroidal transit in a number- $m$  complete poloidal transits. Since in an RFP the toroidal and

poloidal magnetic fields are on the same order of magnitude, and since the MST has an inverse aspect ratio ( $a/R$ ) of about  $1/3$ , a reasonable value of  $q$  on axis of the MST would be on the order of  $0.3$ . This limits the spectrum of magnetic modes that have resonant surfaces (where  $q=m/n$ ) in the MST. Experimentally it is observed that the dominant magnetic modes are  $m=1$  and  $n=5, 6, 7-10$ . This is consistent with the  $q$ -profiles shown in Figure 6.10. The resonant surfaces for the  $m=1$  modes are located in the core region of the plasma, and hence are referred to as “core modes,” particularly low  $n$ -modes (5, 6, 7). In plasmas which contain a reversal surface,  $m=0$  mode activity is also observed. Since the reversal surface is local to the edge region of the plasma,  $m=0$  modes (with any  $n$ ) are referred to as “edge modes.” In  $F \geq 0$  plasmas, the  $q=0$  surface is removed from the plasma, eliminating the  $m=0$  resonant surface. Since the  $m=0$  modes contribute to the overall level of magnetic fluctuations, and hence presumably cross-field transport, confinement should be improved in Non-Reversed and  $F > 0$  plasmas. This will be examined more thoroughly in Section 6.4.

Before leaving the discussion of Figure 6.10, it is worthwhile to draw out some differences between Standard and PPCD plasma discharges. Immediately obvious is that the reversal surface is much deeper in PPCD plasmas. While both  $q$ -profiles have approximately the same value on axis, the edge- $q$  during PPCD is much lower than that of Standard plasmas. Besides a deeper reversal surface, this also implies that the shear in  $q$  is greater during PPCD. Greater field shear during PPCD is also observed on other machines, in particular RFX.<sup>4</sup> Increased  $q$ -shear implies an increased stability to ideal interchange modes. Since ideal interchange modes limit the pressure gradient, if they were stabilized in some way (by the application of PPCD), a larger pressure gradient could be sustained. Indeed, even though the edge pressure gradient is about the same in Standard and PPCD plasmas, the pressure gradient remains large deeper into PPCD plasmas than it does in Standard plasmas, where the pressure profile becomes flat.

## 6.2.4 Discussion

Except for PPCD plasmas, the edge pressure gradients are limited by interchange modes as shown in Figure 6.11. That is to say, the measured edge pressure gradients for non-PPCD plasmas in the MST approach the calculated Suydam critical pressure gradient for ideal interchange modes. In all cases, the flattening of the temperature profile in the mid-radius region is not explained by a Suydam, critical pressure gradient, i.e. the measured gradient becomes small (or zero) even though the calculated ideal interchange mode stability limit could support a larger gradient. This suggests that another process (other than ideal interchange) is limiting the pressure gradient, and ultimately the electron temperature, in the MST. Good candidates are the tearing modes.

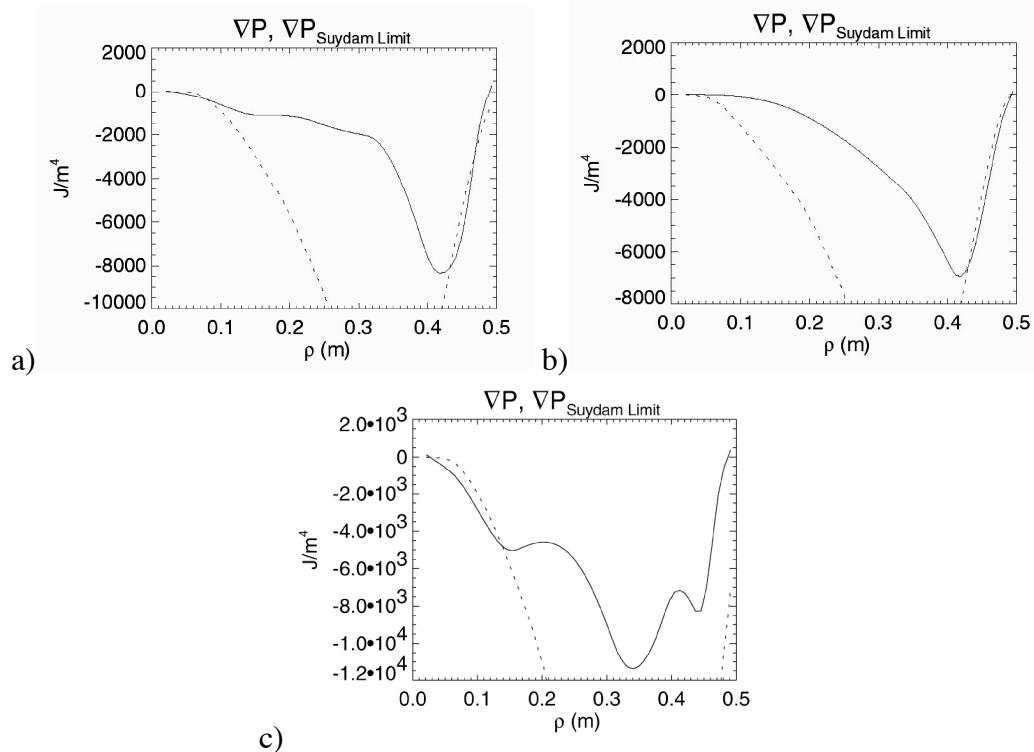


Figure 6.11 Comparison of the measured pressure gradient (solid line) with the calculated Suydam pressure gradient limit (dashed line) to ideal interchange modes: a) Standard ( $F=-0.22$ ) plasma (-1.75 ms), b) Non-Reversed ( $F=0$ ) plasma (-1.75 ms), c) PPCD plasma (18 ms).

Tearing modes tend to create magnetic islands at the mode rational surfaces ( $q=1/5$ ,  $1/6$ ,  $1/7$ , ...) The width of the  $m/n=1/5$  islands (for example) is again related to the shear of  $q$ . If the  $q$  profile is flat, there is a large radial region where the  $1/5$  mode is near resonance. Hence the  $1/5$  island would be “wide.” If the next nearest island, in this case the  $1/6$ , is also “wide,” it is possible for the two islands to overlap radially, which leads to stochastically wandering (radially) magnetic field lines and hence poor flux surfaces. The presence of overlapping magnetic islands is thought to flatten the temperature profile through increased radial transport of particles following stochastic magnetic field lines. This appears to be the case for non-PPCD plasmas in the MST. The temperature profile is flat, because a gradient cannot be maintained against the enhanced transport of overlapping  $m=1$  islands which extend from near the core of the plasma to essentially the reversal surface. Tearing modes limit the temperature in the core of the MST by enhancing radial transport of heat and particles.

By increasing the shear of  $q$ , the island widths become narrower and more localized. Also, the radial locations of mode rational surfaces become closer together in regions of increased  $q$ -shear. If a “happy medium” can be found, such that the magnetic islands do not overlap, then good flux surfaces can be restored to the plasma and radial transport can be reduced. This appears to be the case in PPCD plasmas. Even though the same  $m=1$  tearing modes are present that are in non-PPCD plasmas, the increased  $q$ -shear narrows the magnetic islands enough (combined with an overall lower fluctuation level) that they do not overlap, and hence the temperature gradient can be maintained against transport, leading to high electron temperatures in the core of the plasma.

Further evidence that good flux surfaces exist in PPCD plasmas comes from hard x-ray measurements. Hard x-rays up to energies of 100 keV have been observed in the MST during PPCD.<sup>7,8</sup> The only way that x-rays of this high energy can be produced is if run-away

electrons are accelerated over many toroidal transits of the torus. This can only happen if good flux surfaces exist, preventing the high-energy run-away electrons from straying into regions of high collisionality. Such high energy hard x-rays are not observed in other plasma discharges. Fast-electron transport along weakly stochastic magnetic field lines has been cited as a major sink of energy in other devices.<sup>9</sup>

Though not shown here, it is worth pointing out that not all PPCD discharges result in reduced magnetic fluctuations, better confinement, and higher electron temperatures. In the parlance of the MST experimental control room, these are referred to simply as “good” and “bad” PPCD discharges. From an external viewpoint, though all capacitor-bank charging levels and firing times are essentially identical, the plasma behavior can vary wildly between these extremes. This suggests that some critical aspect is being surpassed to result in “good” PPCD rather than “bad” PPCD. Perhaps that critical aspect is the shear in  $q$ . As stated above, increased  $q$ -shear narrows the island width, but it also brings the island centers closer together. These are competing processes in eliminating island overlap, one stabilizing, the other destabilizing, respectively. A thorough examination of “bad” PPCD plasmas should be done to determine if variation in the resultant  $q$ -profiles can account for the differences between “good” and “bad” PPCD discharges.

The shear in  $q$  is not the whole story in understanding possible island overlap issues. Whereas increased  $q$ -shear does tend to reduce island widths, the island width is also narrowed by reducing the amplitude of the relevant tearing mode fluctuation. The shear in  $q$  depends on the shape of the  $q$ -profile. The  $q$ -profile is a representation of the magnetic field profiles. And the magnetic field profiles are due to the current profile within the plasma. Currents flowing in the plasma can be Ohmically driven, or they can be driven through MHD dynamo action. Dynamo driven current inherently generates increased magnetic fluctuations, because it arises from nonlinear interactions within a resistive plasma flowing across a magnetic field. Hence, tearing mode amplitudes are larger in plasmas with a large amount of

dynamo activity. The impetus behind confinement improvements from PPCD is that PPCD theoretically reduces the need for dynamo driven current by externally providing (from capacitor banks) edge current erstwhile driven by the dynamo. Thus reducing magnetic fluctuations (reducing the tearing mode amplitudes), narrowing the island widths, eliminating overlap, restoring good flux surfaces, and improving confinement, presumably in that order of causality. From an island overlap standpoint then, PPCD does two things which combine to result in better confined plasmas: the currents driven to produce PPCD 1) reduce the MHD dynamo and subsequently the tearing mode amplitudes, leading to narrower magnetic islands, and 2) result in a highly sheared q-profile, which further narrows magnetic islands, but also unfortunately brings the island centers closer to one another. A case for further study which could separate the importance of these two effects is a Standard plasma at very deep reversal. Experimentally, it is observed that as the reversal surface is made deeper, spontaneous periods of enhanced confinement (EC) appear, during which magnetic fluctuations decrease and the electron temperature increases (as inferred from soft x-ray diagnostics).<sup>10</sup> Unfortunately, these “EC” plasmas have not been examined in the same detail as the experiments presented here.

### **6.3 Anomalous Ion Heating**

#### 6.3.1 Standard v. Non-Reversed Plasmas

During Standard discharges it has been experimentally observed that the majority and impurity ion temperatures increase dramatically following the sawtooth crash (Figure 6.12),<sup>11</sup> however this ion heating is not observed in Non-Reversed plasmas (Figure 6.13). It was originally thought since the electron temperature falls at the sawtooth during Standard discharges, that thermal energy was being channeled from the electrons to the ions.<sup>12</sup>

However, the temperature increase evident in the Standard discharge ions can be much larger than what is lost by the electrons, particularly within the impurity ions. Moreover, during Non-Reversed discharges the electron temperature still falls at the sawtooth crash, while the ion temperature remains constant. From the analysis of transport in Standard discharges given in Chapters 4 and 5, the variation in the electron temperature can be accounted for by an increase in stochastic transport of heat to the wall. Another mechanism is then necessary to account for the observed ion heating of Standard plasmas at the sawtooth. Since this sawtooth ion-heating is not observed in Non-Reversed plasmas, Non-Reversed discharges can yield useful clues to this investigation.

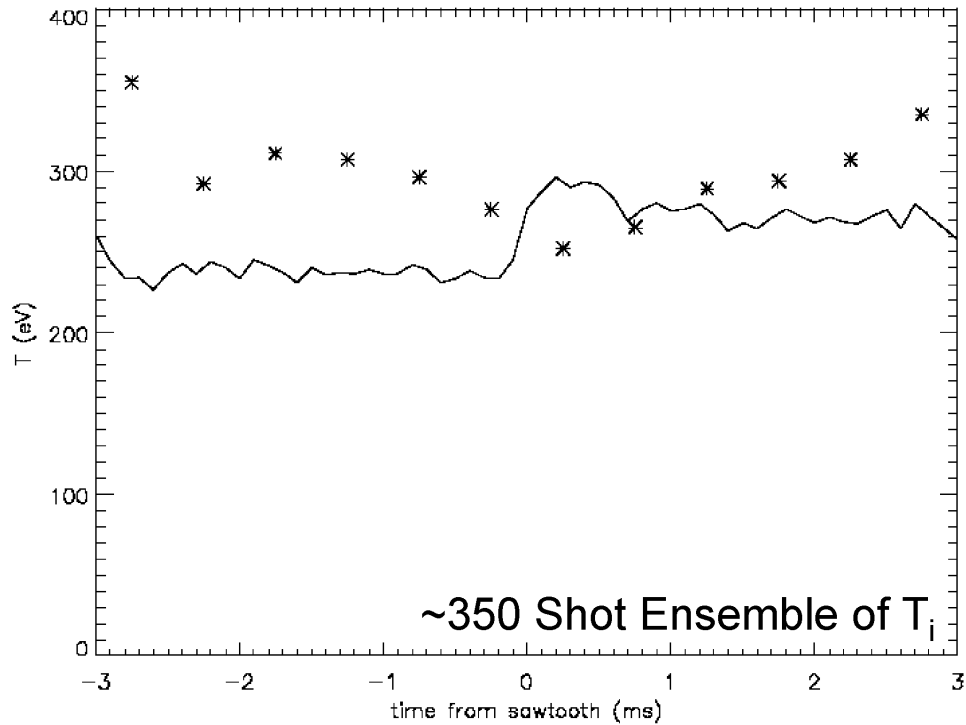


Figure 6.12 Anomalous ion heating at the sawtooth crash in Standard plasma, as measured by Rutherford scattering (solid), compared to the Thomson scattering measured electron temperature (stars.)

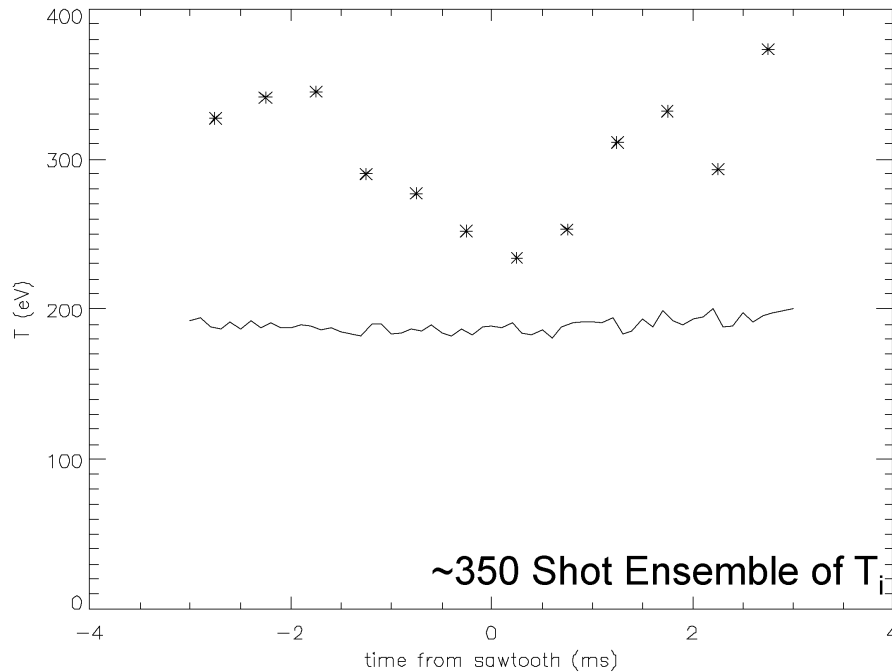


Figure 6.13 The RS measured ion temperature (solid) remains flat throughout the sawtooth cycle, i.e. a lack of anomalous ion heating. The peak electron temperature (stars) is also shown.

A possible explanation for the lack of ion heating in Non-Reversed discharges is found by examining MSTFit equilibrium reconstructions, particularly the  $\psi$ -profiles. From Figure 6.14, in Non-Reversed plasmas the current density profile preceding the sawtooth crash is broader than Standard plasmas, and hence the corresponding  $\psi$ -profile is flatter. As discussed earlier, a flat  $\psi$ -profile represents the Taylor minimum-energy state for RFP plasmas.<sup>6</sup> While the mechanism for sawtooth ion heating is not understood,<sup>15-18</sup> the “free energy” to drive the ion heating process at the sawtooth crash may come from the relaxation of the current profile. In Non-Reversed discharges, the plasma is already near a Taylor minimum energy state (flat  $\psi$ ) preceding the crash, hence there may not be as much free energy available for ion heating at the sawtooth crash as there is for Standard plasmas.

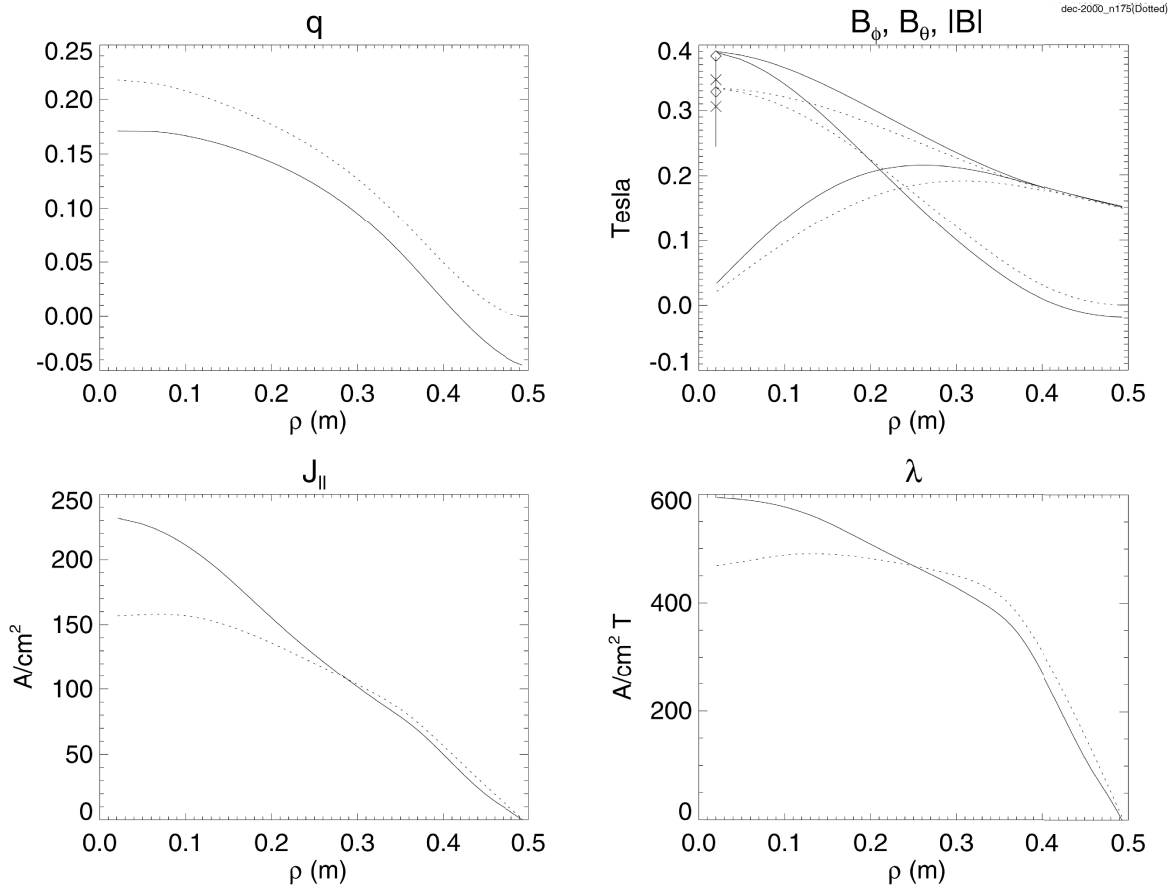


Figure 6.14 Comparison of equilibrium reconstructed profiles between Standard (solid) and Non-Reversed plasmas (dotted) shows a much flatter  $q$ -profile.

### 6.3.2 Standard v. PPCD Plasmas

Ion heating during PPCD plasmas can be explained as the result of collisional heating from the electrons. The electron temperature increases dramatically during the application of PPCD, as shown in Section 6.2. The ion temperature profiles in the MST are measured by Rutherford scattering (RS), ion-dynamic spectroscopy (IDS), and/or by charge-exchange recombination spectroscopy (CHERS.) Both IDS and CHERS are measurements of the impurity ( $C^V$ ) ion temperature. CHERS is a localized measurement, while IDS is chord averaged. Rutherford scattering is a local measurement of the majority ion temperature. The

bulk ion temperature profile is compared to the electron temperature profile for a PPCD discharge in Figure 6.15. The time evolution of the central electron and ion temperatures is shown in Figure 6.16. Following the calculation of the ion energy confinement time, as laid out in Section 5.4.1, no anomalous power is required to balance the terms in the ion energy budget, and at 18 ms the ion energy confinement time is measured to be 10.23 ms. (Recall that PPCD is applied at 9.5 ms., and the last MHD burst occurs at  $\sim 15$  ms.) As will be shown in the next section, this is  $\sim 2.5$  times greater than the total energy confinement time during PPCD plasmas.

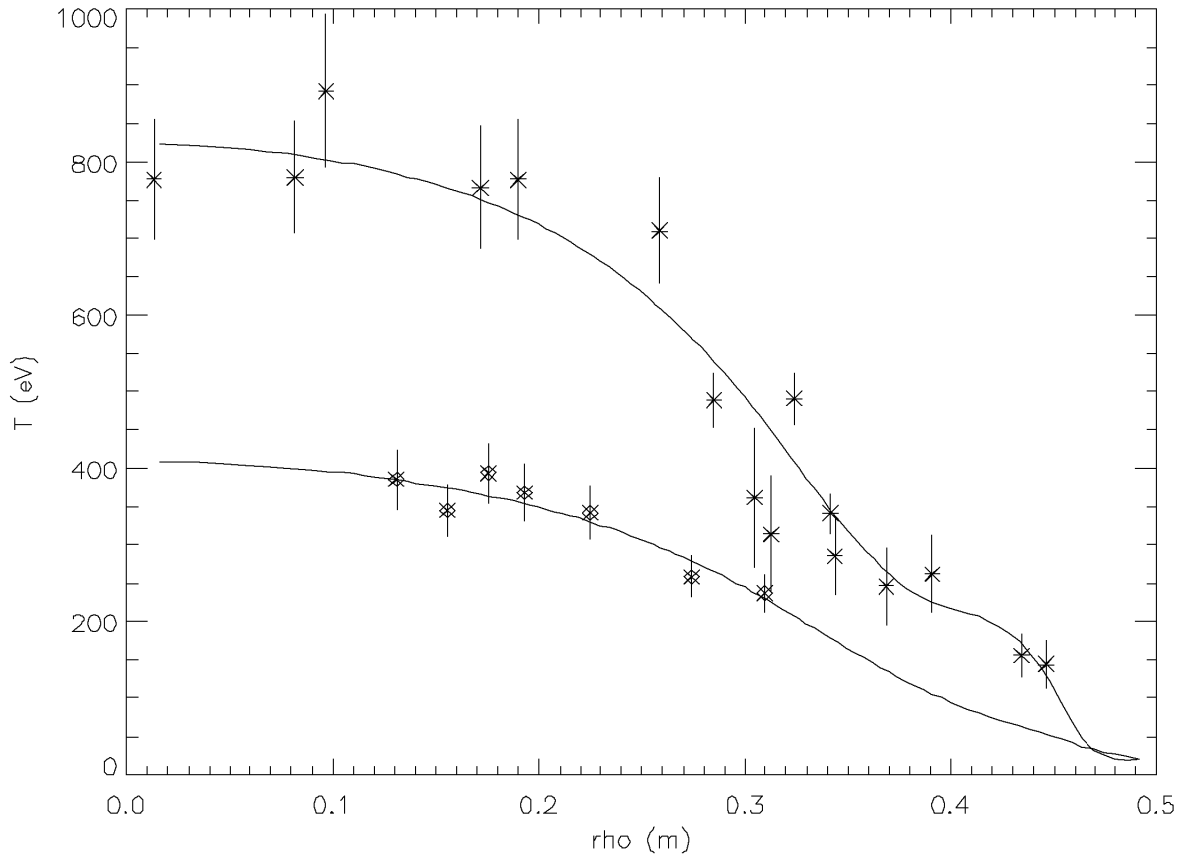


Figure 6.15 Electron and ion temperature profiles at 18 ms, during PPCD plasma discharges.

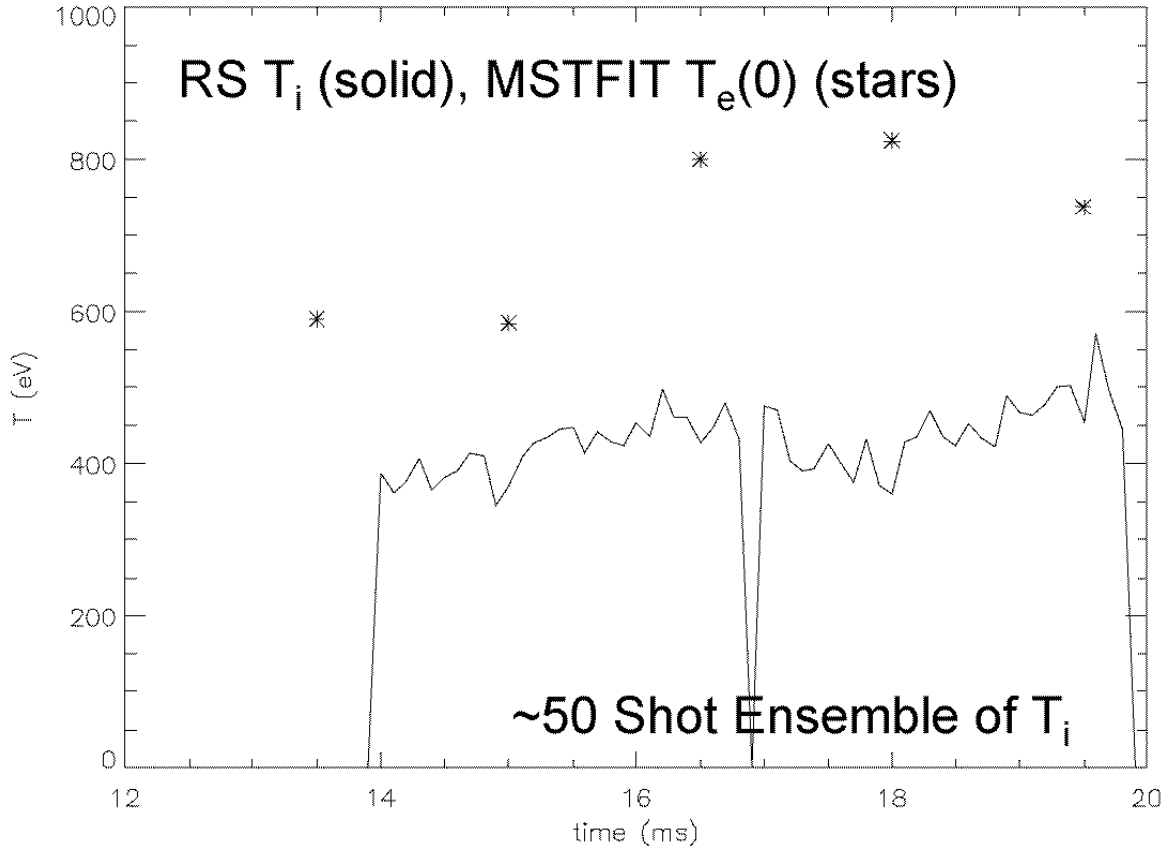


Figure 6.16 Electron and ion temperature evolution during PPCD discharges.

## 6.4 Transport

### 6.4.1 Zero-D: $\beta_p$ and Plasma $\beta$

Plasma  $\beta$  is a volume-averaged measure of the ratio of the thermodynamic pressure to the magnetic field pressure:

$$\beta_{\text{tot}} = \frac{\int (n_e T_e + n_i T_i) \frac{\partial V}{\partial \Omega} \partial \Omega}{\frac{1}{2\mu_0} \int B^2 \frac{\partial V}{\partial \Omega} \partial \Omega}. \quad (87)$$

As such,  $\beta$  is often used as a figure-of-merit when comparing magnetically confined plasmas. A high  $\beta$  suggests that the confining magnetic field is “efficient,” in a sense, at containing a high temperature plasma. Confinement and heating go hand-in-hand, since poorly confined plasmas will never reach the high temperatures necessary for fusion to occur. Figure 6.17 shows the behavior of total  $\beta$  over a sawtooth cycle for Standard MST discharges.

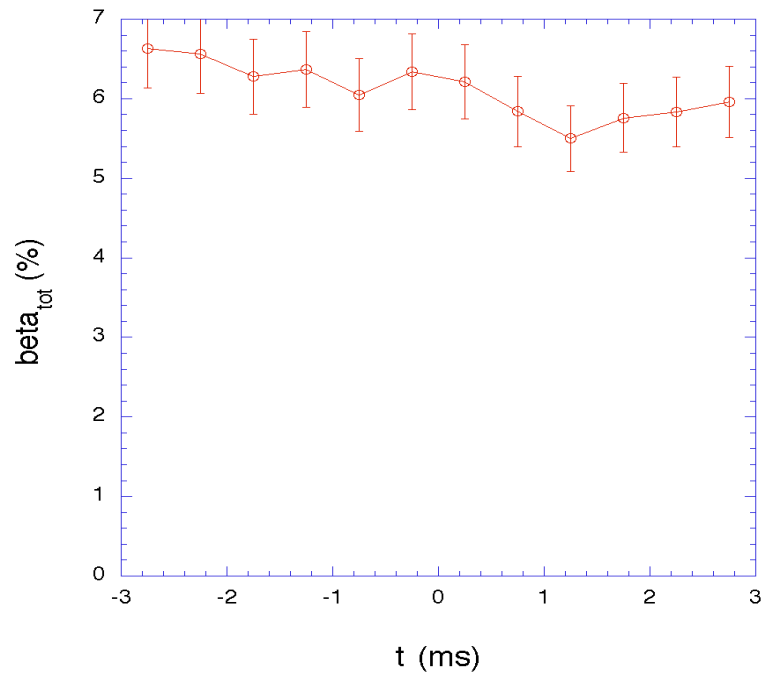


Figure 6.17 Total  $\beta$  over the sawtooth cycle for Standard plasmas.

The energy confinement time has been defined in Section 4.1, and  $\beta$  is defined here.  $\beta_e$  gives a measure of the global plasma energy confinement at the wall, and  $\beta$  is a measure of how the machine energy budget is distributed between thermal energy and confining fields. These parameters are plotted in Figure 6.18 and Figure 6.19 for the 5 discharge conditions. PPCD plasmas show a clear increase in confinement and  $\beta$ . Note that PPCD is applied at 9.5 ms into the discharge. For Non-Reversed plasmas, confinement improves slightly at  $F=0$ , then degrades rapidly as  $F$  is raised. The sawtooth period also shortens considerably. The

values of  $\beta$  and  $\beta_E$  measured for Standard MST plasmas are in agreement with measurements from other similarly-sized RFP's at this current.<sup>13,14</sup>

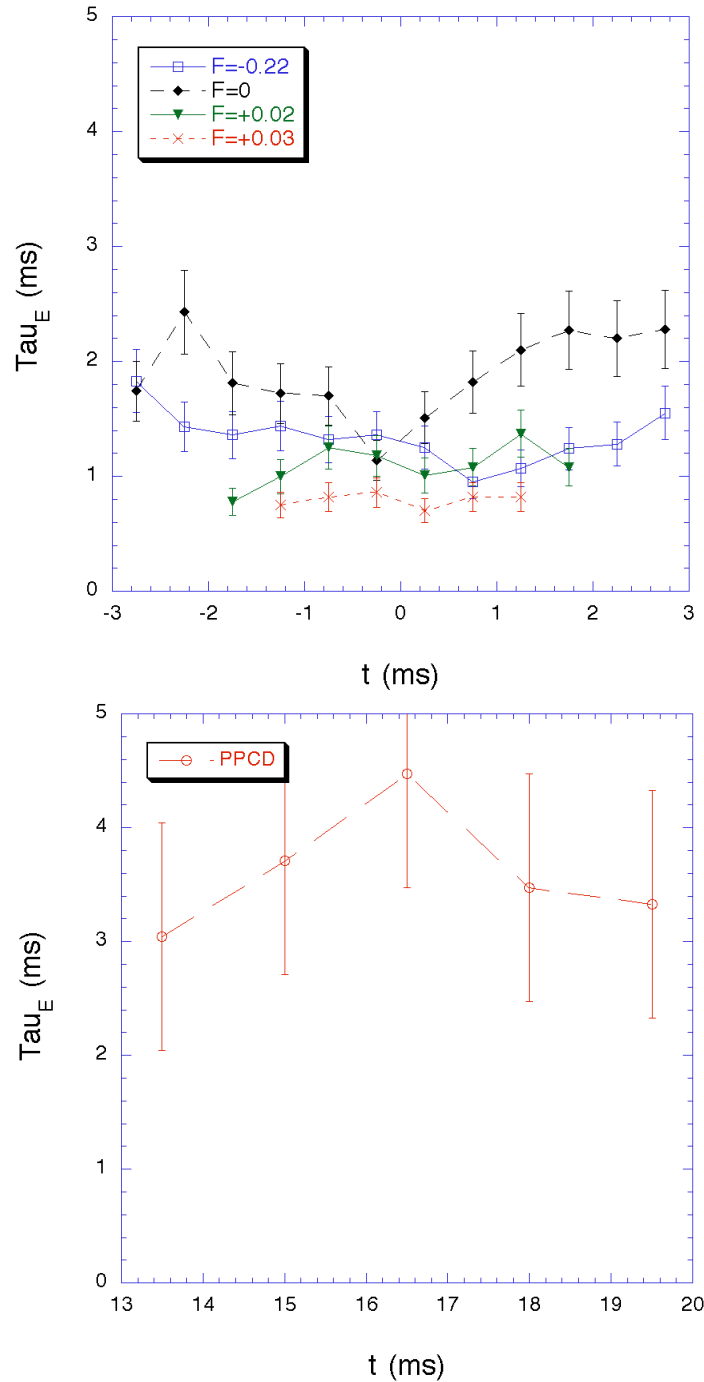


Figure 6.18 Energy confinement time over a sawtooth cycle for  $-0.22 < F < +0.03$  and during PPCD. Confinement improves at  $F=0$ , but degrades rapidly for  $F>0$ . The total energy confinement during PPCD is about a factor of 3 higher.

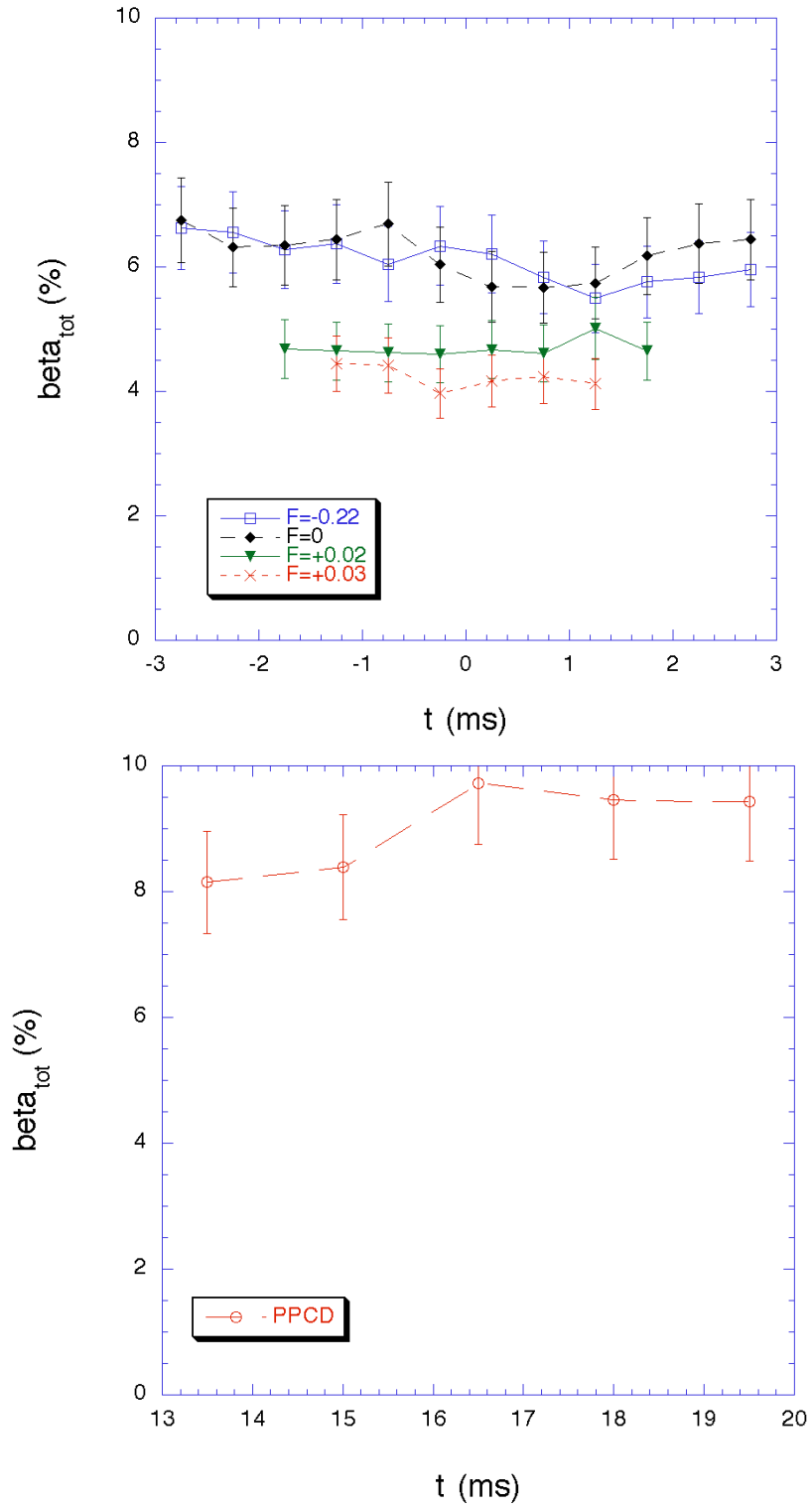


Figure 6.19 Total  $\beta$  over a sawtooth cycle for  $-0.22 < F < +0.03$  plasmas, and during PPCD.

Magnetic fluctuations play an important role in heat transport during MST discharges. This was shown in Chapters 4 and 5. Specifically, in Chapter 5 it was shown that heat transport in Standard plasmas is governed by the overall stochasticity of the magnetic field, particularly in the mid-radius region, where magnetic tearing mode islands overlap strongly. The stochasticity of the magnetic field depends both on the amplitudes of the magnetic fluctuations and on the shape of the  $q$ -profile. For a given  $q$ -profile (and subsequent resonant mode spacing) if the fluctuation level is reduced, the stochasticity will be reduced. Figure 6.20 shows the total  $m=0$  and  $m=1$  magnetic fluctuation levels, normalized to the equilibrium field, in the MST discharges that are being discussed in this chapter. In Non-Reversed plasmas the reversal surface is at the wall, stabilizing  $m=0$  modes. A significant reduction in the  $m=0$  fluctuation amplitude is observed, while there is little change in the  $m=1$  fluctuation amplitude. Raising  $F$  above zero shows an even larger decrease in the total magnetic fluctuation level. PPCD plasmas exhibit the lowest fluctuation levels of all MST discharges, which agrees with observations from other RFP's that utilize PPCD.<sup>4</sup> From an energy confinement perspective, this suggests that PPCD plasmas would have the highest confinement, which is observed (Figure 6.18). The magnetic fluctuation level also suggests that  $F=0$  plasmas would be better confined than Standard plasmas, which is likewise observed. However, it is observed that  $F>0$  plasmas have poorer confinement than Standard plasmas despite lower fluctuation levels, suggesting that magnetic fluctuations are no longer the dominate process for energy transport in these plasmas.

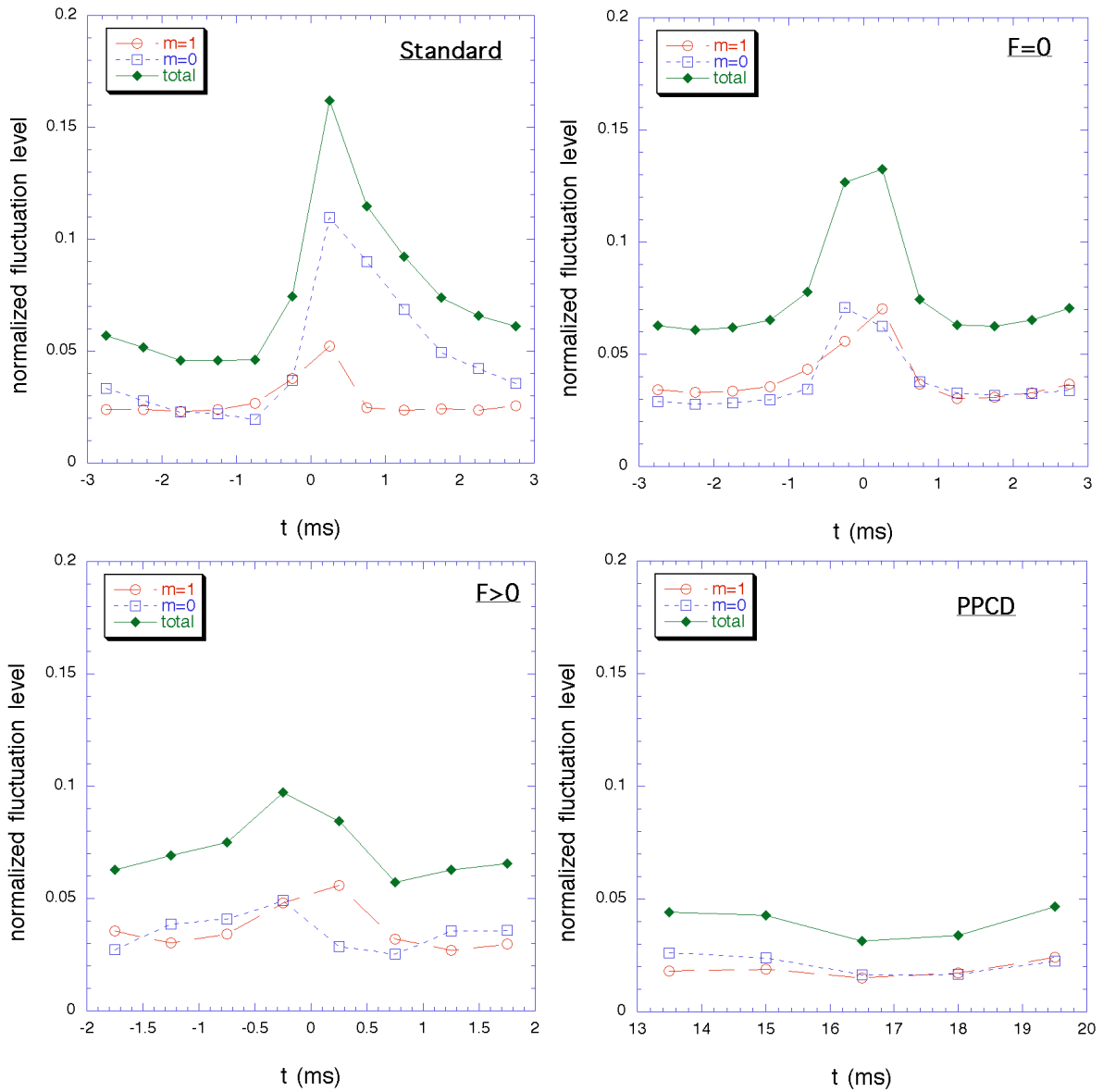


Figure 6.20 Magnetic fluctuation levels normalized to the equilibrium magnetic field for different discharge conditions.

#### 6.4.2 One-D: $\bar{n}_e$ through the Discharge

As outlined by the procedure in Chapter 4, the electron thermal conductivity profile for the various MST discharges can be calculated, as shown in Figure 6.21. The profiles are shown away from the sawtooth crash, or (for the PPCD case) at 18 ms into the discharge.

The edge transport barrier that is observed for Standard plasmas is also present for  $F=0$  and PPCD plasmas, but is absent for  $F>0$  plasmas, collaborating the energy confinement time degradation when  $F$  is raised above zero. Also, comparing Standard to  $F=0$  plasmas,  $\chi_e$  is a factor of 5 lower for Non-Reversed plasmas, qualitatively consistent with its higher energy confinement time. The electron thermal conductivity of PPCD plasmas is an order of magnitude lower than Standard plasmas, and has a value across the profile, which is comparable to the value established by the edge transport barrier. This reduction of core transport to edge values during PPCD has also been observed on the RFX RFP.<sup>15</sup>

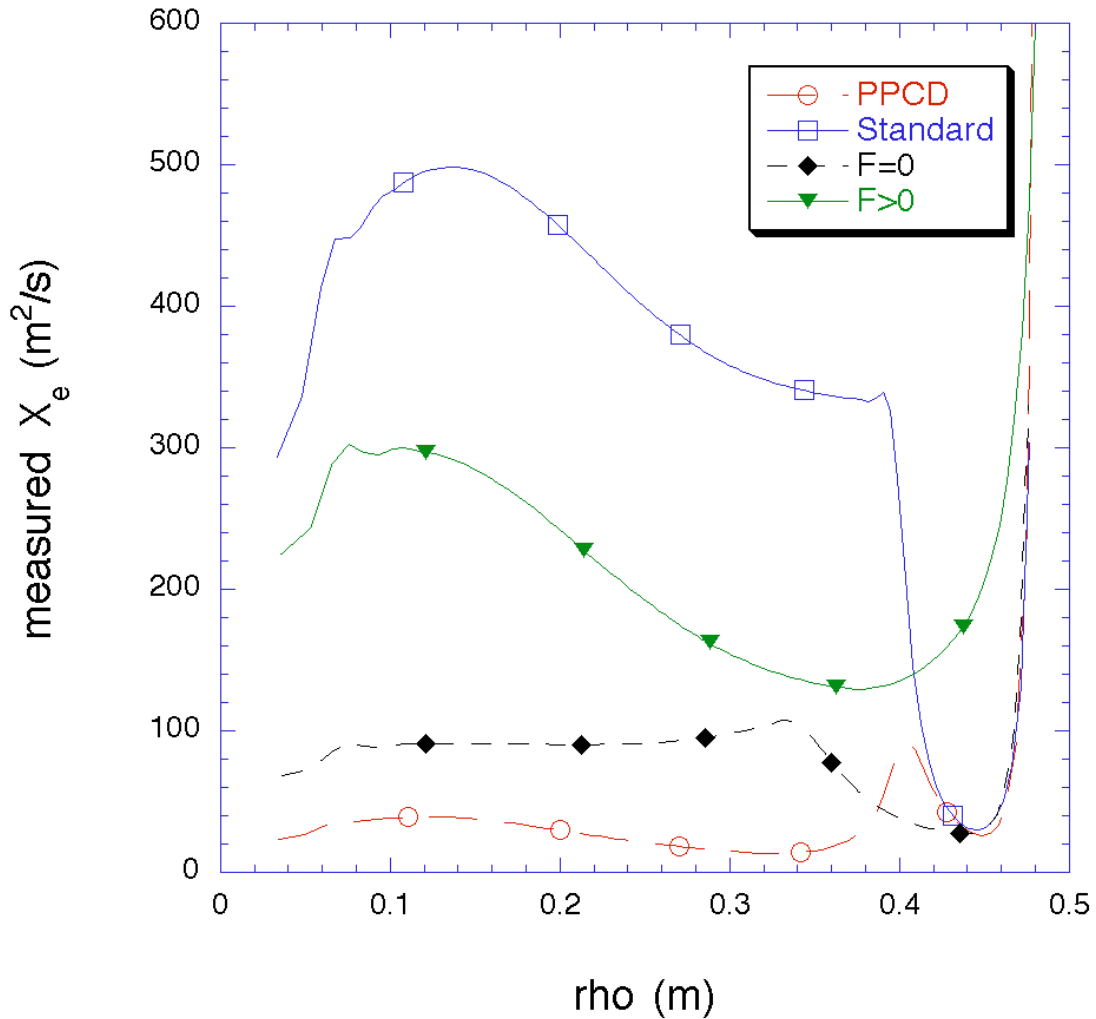


Figure 6.21 Profiles of electron thermal conductivity for different MST discharge types away from the sawtooth crash (where applicable). PPCD discharge is shown at 18 ms.

By averaging over the core and mid-radius region, the evolution of the average electron thermal conductivity through the discharge can be studied, as shown in Figure 6.22. During PPCD discharges the electron heat transport from the core and mid-radius region remains very low. The general trend that the heat transport increases at the sawtooth crash is true for Standard, Non-Reversed, and F>0 plasmas. Even though the magnetic fluctuation amplitudes exhibit the smallest increase at the sawtooth for F>0 discharges,  $\chi_e$  shows the largest increase at the sawtooth for F>0 discharges. This can be explained by referring back to the observed current density profile relaxation in Standard discharges. In Standard discharges the current profile relaxes at the crash, leading to a more sheared q-profile, and to a lower measured stochasticity parameter. Hence the magnetic field is less stochastic after the crash even though the magnetic fluctuations increase. For Non-Reversed discharges, there is little relaxation of the current density profile and essentially no increase in the q-shear stabilization. Hence the increase in magnetic fluctuations result directly in an increase in the field stochasticity for F>0 plasmas, which leads to an increase in the measured  $\chi_e$ .

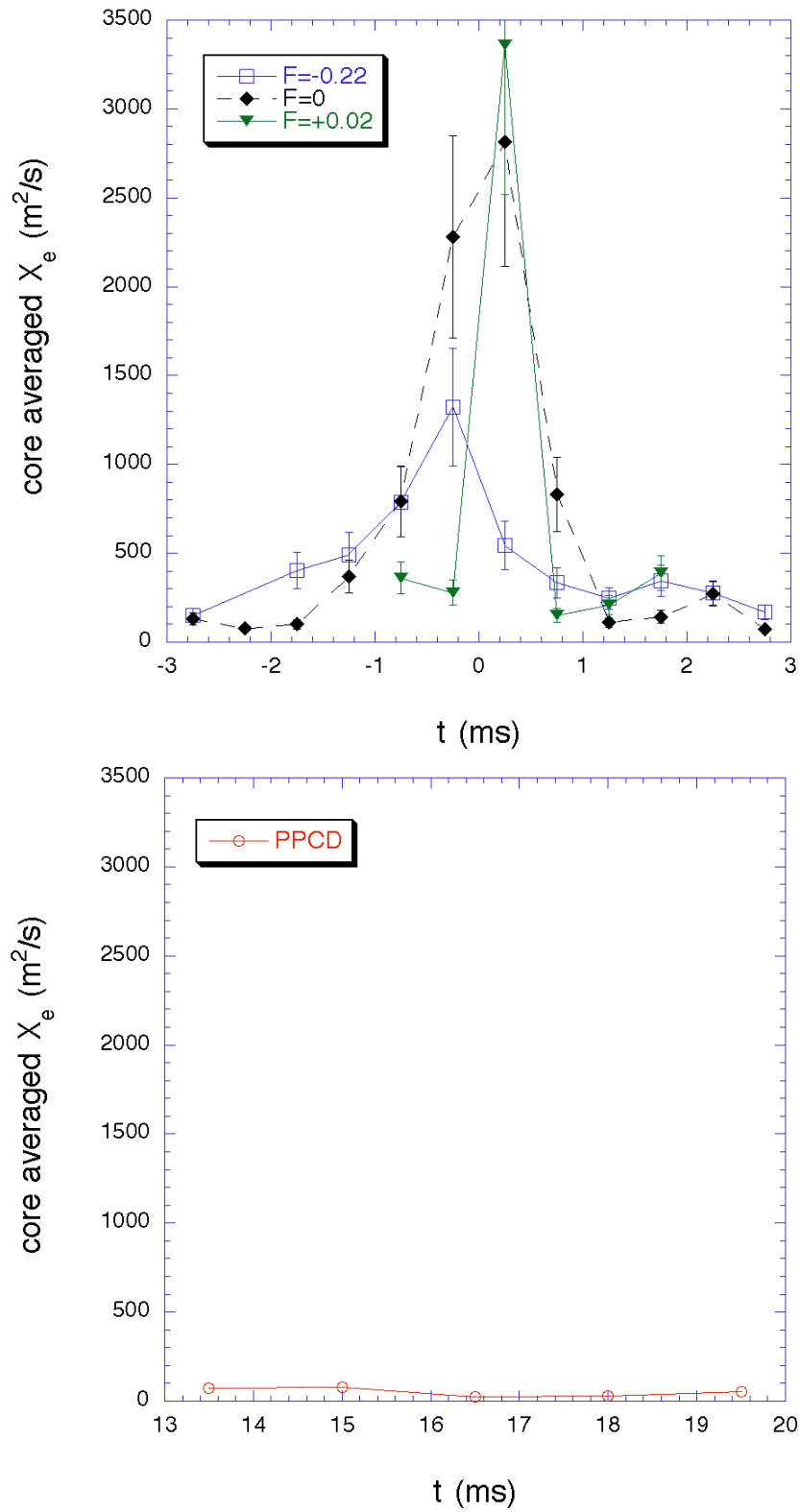


Figure 6.22 Electron thermal conductivity variation over the sawtooth cycle for  $-0.22 < F < +0.02$  plasmas, and during PPCD plasmas.

Since DEBS simulations have not yet been run for the various different discharge types, the increase in field stochasticity during other-than-Standard discharges is speculation. If the assumption is used, that the radial eigenfunctions do not change drastically from the Standard case, then they can be applied to the other discharges to yield an approximate stochasticity parameter. The core-averaged stochasticity is compared for the various discharge types in Figure 6.23. This figure was already shown in Chapter 5, but is reproduced here. The trend of enhanced electron thermal conductivity with increasing stochasticity is apparent.

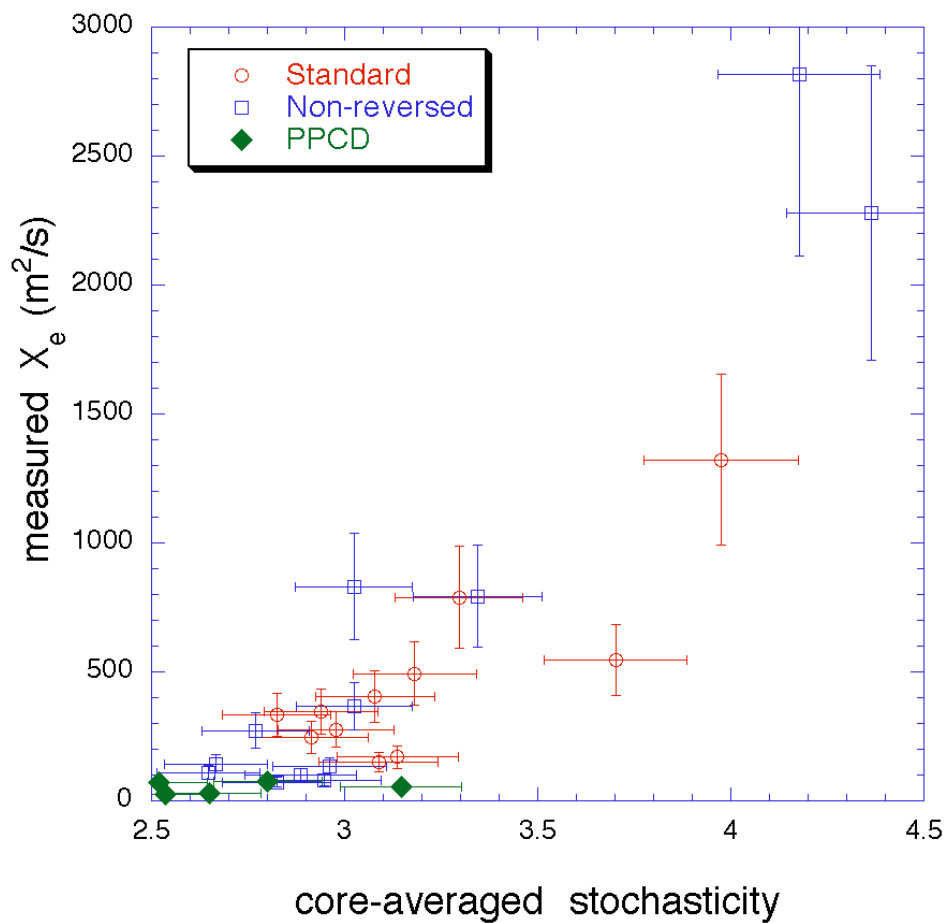


Figure 6.23 Measured, core-averaged conductivity increases with stochasticity across various plasmas discharge types.

## 6.5 Summary

Five different MST discharge types have been compared: Standard ( $F=-0.22$ ), Non-Reversed ( $F=0$ ),  $F=+0.02$ ,  $F=+0.03$ , and PPCD plasmas. A quick summary of their basic plasma parameters and 0-D transport quantities is given in Table 6.2. All discharge types were at a plasma current of  $\sim 385$  kA, and an electron density of  $1.1 \times 10^{13}$  cm $^{-3}$ . PPCD was applied at 9.5 ms into the discharge, and plasma shots were selected which had a final MHD burst around 15 ms.

			FIR	TS	RS	MSE		
name	F	$I_p$	$n_e$	$T_e$	$T_i$	$B_0$	$\tau_E$	$\tau_{tot}$
		kA	$10^{19}$ m $^{-3}$	eV	eV	T	ms	%
PPCD	-0.97	383	1.10	825	410	0.395	4.0	10
Stan	-0.22	375	1.10	310	240	0.347	1.50	6.5
N.Rev.	0	374	1.10	350	190	0.306	2.0	6.5
F>0	+0.02	390	1.00	250	225	0.329	1.25	4.75
F>>0	+0.03	386	1.03	250	225	0.310	0.75	4.25

Table 6.2 Summary table of 0-D transport quantities.

The stability of these plasmas was compared to the Suydam criterion for ideal interchange modes. The measured pressure gradients are compared to the  $q$ -shear calculated from MSTFit equilibrium reconstructions of the magnetic field profiles. In the edge, the pressure gradients are comparable between the different plasma discharges, and, except for PPCD plasmas, are approximately equal to the Suydam critical pressure gradient for stability

to ideal interchange modes. Because the  $q$ -profile is much more sheared in PPCD plasmas, the measured pressure gradient is well below the Suydam critical gradient in the edge. This large pressure gradient is maintained through the mid-radius region, into the core, of PPCD plasmas. In Standard and Non-Reversed plasmas the pressure gradient flattens out sharply in the mid-radius region, in the area where  $m=1$  tearing modes are resonant. This suggests that tearing mode activity, through the overlap of magnetic islands, increases heat transport such that a temperature gradient cannot be sustained.

The current density profiles for these plasmas shed some light on the underlying dynamics. The current density profile is most peaked for Standard discharges, resulting in plasmas which are furthest from a Taylor minimum-energy state. At the sawtooth crash, the current density profile relaxes, and the  $q$ -profile flattens. The  $q$ -profile for Non-Reversed plasmas (at all times) is very similar to the after-sawtooth profile of Standard plasmas. Substantial ion heating at the sawtooth is observed for Standard plasmas, but is absent for Non-Reversed plasmas. Whereas the mechanism for ion heating at the sawtooth crash is not yet understood, this result suggests that the energy to drive sawtooth ion heating of Standard plasmas comes from the relaxation of the current density profile. This is a different mechanism than the anomalous power for between-sawtooth ion heating that was discussed in Chapter 4. During PPCD plasmas, which are sawtooth free, measurements of power balance for the ions suggest that no anomalous heating power is needed to explain the observed ion temperature, and that the ion energy confinement time is on the order of 10 ms.

Energy is better confined in PPCD plasmas than in other cases. The total (ion and electron) energy confinement time for PPCD plasmas is a factor of 2 to 3 higher than for Standard plasmas, reaching 4 ms. Plasma  $\beta$  is correspondingly about 10%, compared to 6.5% for Standard plasmas. The energy confinement time for Non-Reversed plasmas is slightly higher than Standard plasmas, but degrades rapidly as the reversal parameter is made

more positive. Plasma  $\chi$  is roughly equal for Standard and Non-Reversed plasmas, but drops to  $\sim 4\%$  for  $F > 0$  plasmas.

Profiles of electron thermal conductivity have also been measured in the different discharges. Away from sawteeth the edge transport barrier that appears in Standard plasmas also appears in Non-Reversed and PPCD plasmas, and has about the same depth. When  $F$  is made positive, this transport barrier disappears, explaining the observed overall lower confinement. For PPCD plasmas the electron thermal conductivity remains low over the bulk of the minor radius, while for Standard, Non-Reversed, and  $F > 0$  plasmas it is larger in the mid-radius and core regions, where  $m=1$  tearing modes are resonant.

Calculating a volume average over the core and mid-radius regions allows the time dependence of the electron thermal conductivity to be studied. For PPCD plasmas, the volume-averaged  $\chi_e$  remains very low, without much variation from 13.5 ms to 19.5 ms., i.e. the range over which measurements were made. PPCD was applied at 9.5 ms into the discharge. The other cases exhibit qualitatively similar behavior to each other,  $\chi_e$  spiking upward near the sawtooth crash along with the edge-measured magnetic fluctuation levels. Quantitatively, the measured  $\chi_e$  for the  $F \geq 0$  cases increases to a higher level than the Standard case, even though the fluctuation increase at the crash is less. This can likely be explained by considering the relaxation of the current density profile, which is observed for Standard plasmas. This relaxation results in greater  $q$ -shear, which is a stabilizing factor for the tearing mode islands and suggests lower field stochasticity (and subsequently lower heat transport.) Since this current density profile relaxation does not occur for  $F \geq 0$  plasmas, any increase in magnetic fluctuations leads to an increase in stochasticity, and hence transport. Variation of the core-averaged electron thermal conductivity with the core-averaged stochasticity parameter shows a linear relation over multiple plasma discharge types.

## References

1. J.S. Sarff, "Control of Magnetic Fluctuations and Transport in the MST," PLP Report 1225, University of Wisconsin-Madison, (1999).
2. B.E. Chapman, A.F. Almagri, J.K. Anderson, C.S. Chiang, D. Craig, G. Fiksel, N.E. Lanier, S.C. Prager, M.R. Stoneking, and P.W. Terry, *Phys. Plasmas*, **5** (5), 1848-1854 (1998).
3. B.E. Chapman, *Fluctuation Reduction and Enhanced Confinement in the MST Reversed-Field Pinch*, Ph.D. Thesis, University of Wisconsin-Madison (1997).
4. V. Antoni, R. Cavazzana, L. Fattorini, E. Martines, G. Serianni, M. Spolaore, L. Tramontin, and N. Vianello, *Plasma Phys. Control. Fusion*, **42**, 893-904 (2000).
5. J.P. Freidberg, *Ideal Magnetohydrodynamics*, Plenum Press, New York (1987), 295.
6. J.B. Taylor, *Rev. of Modern Physics*, **58** (3), 741-763 (1986).
7. R. O'Connell, Private communication.
8. J.K. Anderson, *Measurement of the Electrical Resistivity Profile in the Madison Symmetric Torus*, Ph.D. Thesis, University of Wisconsin-Madison (2001).
9. P.G. Weber, K.F. Schoenberg, J.C. Ingraham, et al., in *13<sup>th</sup> International Conference on Plasmas Physics and Controlled Nuclear Fusion Research*, Washington D.C., Vol. 2, IAEA, Vienna (1990) 509-517.
10. B.E. Chapman, M. Cekic, J.T. Chapman, C.S. Chiang, D.J. Den Hartog, N.E. Lanier, S.C. Prager, M.R. Stoneking, Poster from the *Bulletin of the American Physical Society*, Denver, Colorado (1996).
11. D.J. Den Hartog, D. Craig, "Isotropy of ion heading during a sawtooth crash in a Reversed-Field Pinch," MST Group internal report, University of Wisconsin-Madison (2000).

12. E. Scime, M. Cekic, D.J. Den Hartog, S. Hokin, D. Holly, and C. Watts, *Phys Fluids B*, **4**, 4062 (1992).
13. Y. Yagi, *Nuclear Fusion*, **40** (11), 1933-1942 (2000).
14. R. Bartiromo, V. Antoni, T. Bolzonella, A. Buffa, L. Marrelli, P. Martin, E. Martines, S. Martini, R. Pasqualotto, Presented at the 40<sup>th</sup> Annual Meeting of the Division of Plasma Physics, New Orleans, Louisiana, (1998).
15. P.G. Carolan, A.R. Field, A. Lazaros, M.G. Rusbridge, H.Y.W. Tsui, and M.V. Bevir, *Proceedings of the 14<sup>th</sup> European Conference on Controlled Fusion and Plasma Physics*, Madrid, EPS, Petit-Lancy, **2**, 469 (1987).
16. G.A. Wurden, P.G. Weber, K.F. Schoenberg, et al., in *15<sup>th</sup> European Conference on Controlled Fusion and Plasmas Physics*, Vol. 12B, 533 (European Physical Society, Dubrovnik, 1988).
17. A. Ejiri, K. Miyamoto, *Plasma Physics and Controlled Fusion*, **37**, 43-56 (1995).
18. J.M. McChesney, P.M. Bellan, R.A. Stern, *Physics of Fluids B*, **3** (12), 3363-3378 (1991).



When I see an adult on a bicycle, I do not despair for the future of the human race.

--H.G. Wells

## Conclusions

### 7.1 Summary and Conclusions

To understand electron transport in the MST requires detailed measurements of many fundamental plasma parameters. These measurements have been made at multiple times throughout the sawtooth cycle. No attempt is made to explain the mechanisms that cause the sawtooth crash. The sawtooth cycle is examined as an *a priori*, time-evolving condition that is affecting the plasma equilibrium and consequently the transport of heat and particles. The current density peaks up as the sawtooth crash is approached. This current peaking pushes the plasma farther away from the Taylor minimum-energy state and causes (possibly dynamo driven) tearing instabilities to grow. At the crash the current density profile broadens, resulting in a flatter  $\beta$ -profile, and a plasma that is closer to a Taylor minimum-energy state. Another effect of the peaking current density is a broadening of the q-profile. Lower q-shear results in a more stochastic magnetic field in the region where tearing mode islands overlap. Greater field stochasticity leads to enhanced transport of heat and particles by the electrons, and the electron temperature is observed to drop. After the sawtooth crash, the current density broadens, the q-profile peaks, the q-shear is increased in the region of overlapping islands, the field stochasticity is reduced, and the electron heat transport falls.

Diagnostic upgrades and additions have expanded the ability of experimentalists to accurately characterize the dynamics of plasmas in the MST. Time evolved profiles over the

sawtooth cycle of the electron temperature and electron density have been shown in Chapter 3 for “Standard” MST plasmas, defined as  $I_p \sim 380$  kA,  $n_{e,0} \sim 1.1 \times 10^{23}$  particles/cm<sup>3</sup>, and  $F \sim -0.22$ . Time evolved profiles of the majority ion temperature have also been shown. Whereas the electron temperature is observed to decrease up to a ms before the sawtooth crash, the ion temperature is observed to increase dramatically at the crash, to temperatures above the electron temperature. The development of the MSTFit equilibrium reconstruction code played no small role in interpreting and understanding the implications of this data. A consistent set of measurements has been made during Standard MST plasmas, allowing the time dependence of the current density profile through the sawtooth cycle to be characterized. The current density profile evolution plays a major role in understanding the energy-budget of the plasma, since MST plasmas are Ohmically heated.

Charged particle transport is highly susceptible to the presence of electric fields. Quasi-neutral plasmas will establish radial electric fields in response to the ambipolar movement of electrons and ions, which have differing mobilities. The radial electric field has been measured for the first time in the MST using the HIBP diagnostic. It agrees well with the calculated radial electric field that is expected from ion momentum balance, and appears to be ambipolar in nature.

The movement of heat and particles within the plasma follows a complicated trajectory over the sawtooth cycle. From a “whole plasma”, 0-D perspective the total plasma  $\beta$  remains relatively constant, between 6 and 7%, in these Standard discharges. This is due both to the circuitous redistribution of heat from electrons to ions at the sawtooth crash seen in Chapter 3, and to changes in the equilibrium magnetic fields. The electron energy confinement time witnesses a strong but systematic variation throughout the sawtooth cycle, reaching a minimum around the sawtooth crash and peaking 1/2 sawtooth period later. In contrast the particle confinement time shows steady improvement from a given sawtooth

crash, dropping suddenly at the next crash. This suggests that convective transfer of particles and energy is not the governing dynamics.

This is born out in 1-D analysis by partitioning the measured electron heat flux into convective and conductive parts. Conductive transport of heat is clearly the dominant process across all radii, with convective transport accounting for less than 10% at the edge of the plasma. Correspondingly, the electron thermal conductivity is more than an order of magnitude larger than the electron diffusion coefficient in the core, though there is a strong thermal transport barrier at the edge of the plasma, which persists throughout the sawtooth cycle. Both total heat and particle fluxes for electrons are observed to increase, comparing before and after the sawtooth crash. However, whereas the heat flux increases over the crash, the electron thermal conductivity in the core is observed to decrease sharply following the sawtooth crash. Because of the densely packed mode-rational surfaces of the RFP, stochastic magnetic fields play a role in determining the dynamics of heat transport in the MST. This is underscored by comparing the total magnetic fluctuation level with the measured electron thermal conductivity, since the underlying dynamics are not apparently captured.

In Chapter 5 it was shown that it is necessary to characterize the inherent stochasticity of the field, not merely the fluctuation level, to capture the fundamental dynamics. Non-linear DEBS calculations at a Lundquist number of  $10^6$  have been done for the first time for MST plasmas, and are used to determine the eigenfunctions of radial magnetic fluctuations. These eigenfunctions, when properly normalized by experimental measurements of fluctuation amplitudes at the edge, allow the plasma stochasticity, island widths, and thermal conductivity to be calculated, based on the framework of Rechester-Rosenbluth theory. These theoretical calculations of the thermal conductivity show that where the magnetic field stochasticity is high, as in the mid-radius region of the plasma, there is good agreement between the predicted and measured value of electron thermal conductivity. If the stochasticity is low, as it is in the core of MST Standard plasmas, then the predicted

conductivity overestimates the measured conductivity. Rechester-Rosenbluth theory for transport in a stochastic magnetic field is only valid if the stochasticity is high. Hence the deviation is not surprising.

Averaging over the core and mid-radius regions ( $0.05 < r < 0.30$  m), the measured electron thermal conductivity scales roughly linearly with the plasma-volume-averaged Rechester-Rosenbluth conductivity. The scaling slope is slightly less than 1, which would be perfect agreement. Since the stochasticity averaged over this region is not particularly large, however, it is reasonable that the scaling slope would be less than 1. Comparing the core-averaged measured electron thermal conductivity with the core-averaged stochasticity, there is a strong scaling. When the stochasticity is high, so is the measured electron conductivity, underscoring the notion that the stochasticity of the magnetic field is at the heart of determining heat transport in the MST. This trend with stochasticity persists across various discharge types, from PPCD, to Standard, to Non-Reversed discharges. Since the stochastic magnetic field is responsible for electron heat transport, it is perhaps reasonable to assume that it is also responsible for ion heat transport. This assumption ultimately necessitates an “anomalous” power source for the ions, and constrains the ion energy confinement time to be less than  $\sim 10$  ms during Standard MST discharges.

Five different MST discharge types have been compared: Standard ( $F=-0.22$ ), Non-Reversed ( $F=0$ ),  $F=+0.02$ ,  $F=+0.03$ , and PPCD plasmas. A quick summary of their basic plasma parameters and 0-D transport quantities is given in Table 7.1. All discharge types were at a plasma current of  $\sim 385$  kA, and an electron density of  $1.1 \times 10^{13}$  cm<sup>-3</sup>. PPCD was applied at 9.5 ms into the discharge, and plasma shots were selected which had a final MHD burst around 15 ms.

			FIR	TS	RS	MSE		
name	F	$I_p$	$n_e$	$T_e$	$T_i$	$B_0$	$\tau_E$	$\tau_{tot}$
		kA	$10^{19} \text{ m}^{-3}$	eV	eV	T	ms	%
PPCD	-0.97	383	1.10	825	410	0.395	4.0	10
Stan	-0.22	375	1.10	310	240	0.347	1.50	6.5
N.Rev.	0	374	1.10	350	190	0.306	2.0	6.5
F>0	+0.02	390	1.00	250	225	0.329	1.25	4.75
F>>0	+0.03	386	1.03	250	225	0.310	0.75	4.25

Table 7.1 Summary table of 0-D transport quantities.

The stability of these plasmas was compared to the Suydam criterion for ideal interchange modes. The measured pressure gradients are compared to the q-shear calculated from MSTFit equilibrium reconstructions of the magnetic field profiles. In the edge, the pressure gradients are comparable between the different plasma discharges, and, except for PPCD plasmas, are approximately equal to the Suydam critical pressure gradient for stability to ideal interchange modes. Because the q-profile is much more sheared in PPCD plasmas, the measured pressure gradient is well below the Suydam critical gradient in the edge. This large pressure gradient is maintained through the mid-radius region, into the core, of PPCD plasmas. In Standard and Non-Reversed plasmas the pressure gradient flattens out sharply in the mid-radius region, in the area where  $m=1$  tearing modes are resonant. This suggests that tearing mode activity, through the overlap of magnetic islands, increases heat transport such that a temperature gradient cannot be sustained.

The current density profiles for these plasmas shed some light on the underlying dynamics. The current density profile is most peaked for Standard discharges, resulting in plasmas which are furthest from a Taylor minimum-energy state. At the sawtooth crash, the

current density profile relaxes, and the  $n$ -profile flattens. The  $n$ -profile for Non-Reversed plasmas (at all times) is very similar to the after-sawtooth profile of Standard plasmas. Substantial ion heating at the sawtooth is observed for Standard plasmas, but is absent for Non-Reversed plasmas. Whereas the mechanism for ion heating at the sawtooth crash is not yet understood, this result suggests that the energy to drive sawtooth ion heating of Standard plasmas comes from the relaxation of the current density profile. This is a different mechanism than the anomalous power for between-sawtooth ion heating that was discussed in Chapter 4. During PPCD plasmas, which are sawtooth free, measurements of power balance for the ions suggest that no anomalous heating power is needed to explain the observed ion temperature, and that the ion energy confinement time is on the order of 10 ms.

Energy is better confined in PPCD plasmas than in other cases. The total (ion and electron) energy confinement time for PPCD plasmas is a factor of 2 to 3 higher than for Standard plasmas, reaching 4 ms. Plasma  $\beta$  is correspondingly about 10%, compared to 6.5% for Standard plasmas. The energy confinement time for Non-Reversed plasmas is slightly higher than Standard plasmas, but it degrades rapidly as the reversal parameter is made more positive. Plasma  $\beta$  is roughly equal for Standard and Non-Reversed plasmas, but drops to  $\sim 4\%$  for  $F > 0$  plasmas.

Profiles of electron thermal conductivity have also been measured in the different discharges. Away from sawteeth the edge transport barrier that appears in Standard plasmas also appears in Non-Reversed and PPCD plasmas, and has about the same depth. When  $F$  is made positive, this transport barrier disappears, explaining the observed overall lower confinement. For PPCD plasmas the electron thermal conductivity remains low over the bulk of the minor radius, while for Standard, Non-Reversed, and  $F > 0$  plasmas it is larger in the mid-radius and core regions, where  $m=1$  tearing modes are resonant.

Calculating a volume average over the core and mid-radius regions allows the time dependence of the electron thermal conductivity to be studied. For PPCD plasmas, the

volume-averaged  $\chi_e$  remained very low, without much variation from 13.5 ms to 19.5 ms., i.e. the range over which measurements were made. PPCD was applied at 9.5 ms into the discharge. The other cases exhibited qualitatively similar behavior to each other,  $\chi_e$  spiking upward near the sawtooth crash along with the edge-measured magnetic fluctuation levels. Quantitatively, the measured  $\chi_e$  for the  $F \geq 0$  cases increases to a higher level than the Standard case, even though the fluctuation increase at the crash is less. This can likely be explained by considering the relaxation of the current density profile, which is observed for Standard plasmas. This relaxation results in greater q-shear, which is a stabilizing factor for the tearing mode islands and suggests lower field stochasticity (and subsequently lower heat transport.) Since this current density profile relaxation does not occur for  $F \geq 0$  plasmas, any increase in magnetic fluctuation leads to an increase in stochasticity, and hence transport. Variation of the core-averaged electron thermal conductivity with the core-averaged stochasticity parameter shows a linear relation over multiple plasma discharge types.

## 7.2 Future Work

Electron heat and particle transport through the sawtooth cycle have been extensively studied for “Standard” MST discharges. The same analysis framework has been applied to a variety of other discharge types, including PPCD plasmas, Non-Reversed plasmas, and  $F > 0$  plasmas. These experiments were all carried out at a plasma current of  $\sim 380$  kA and an electron density of  $\sim 1.1 \times 10^{13}$  cm<sup>-3</sup>. It has been experimentally shown elsewhere, that PPCD effects a greater change in confinement at lower current ( $\sim 200$  kA). Repeating this extensive analysis of the conductivity and stochasticity at other currents and densities would yield insights into the scaling of RFP plasma dynamics. These current and density scaling relations are inherently necessary when attempting to project the RFP concept (ultimately) onto a fusion reactor.

Moreover, the number of operating modes of the MST RFP seems to be ever expanding, most recently with the addition of Oscillating Field Current Drive (OFCD), and the experimental observation of spontaneous Enhanced Confinement (EC) operation. These EC discharges occur at “deep-F,” particularly at low density, suggesting that a traditional F-scan may yield surprising results. When the magnetic field structure is deeply reversed (similar to PPCD, but without the external drive circuitry), it is likely that there is greater shear in the  $q$ -profile. As shown above, greater  $q$ -shear leads to lower stochasticity, and improved confinement. This is likely the process that is occurring in EC discharges. It remains to be experimentally shown, however.

Neutral-beam heating has been added to the MST since the experiments presented in this dissertation were performed. Any external heating could prove to be a useful tool in probing the conductivity measurements, representing extra terms in the energy balance equation that do not intimately rely on the equilibrium reconstruction of the plasma. To this end, the proposed addition of electron Bernstein wave (EBW) heating of MST plasmas will be equally as interesting.

The experiments suggested above will be much easier to carry out once the multi-point multi-pulse Thomson scattering system is operational. The electron temperature profiles, which featured prominently in this analysis, required many hundreds of discharges to build up for each plasma discharge case. The prospect of being able to measure those profiles in a single shot, or more likely in a single day of running the MST, is inherently pleasing. The single shot profile measurement removes the uncertainty of machine condition variability over extended run-campaigns. And the multi-pulse aspect opens up an entire realm of temperature fluctuation studies, which were systematically avoided in the campaigns presented here.

Apart from additional experiments, comparisons remain to be made between non-Standard plasmas and their corresponding DEBS simulations. Because of the limitations of

computing power, a single simulation at  $S \sim 10^6$  can take multiple weeks to complete. Much information stands to be gained by undertaking these simulations though, especially in terms of visualizing the reduction of magnetic field stochasticity during PPCD that is implied by these experimental results.

Other experimentally observed phenomena beg investigation by the techniques outlined in this thesis, in particular quasi-single helicity (QSH) discharges, so-called “bad” PPCD discharges, and so-called “super” PPCD discharges. (“Super” PPCD plasmas typically have their last MHD burst around 12 ms, as compared to 15 ms for the “good” PPCD plasmas studied here.) These discharges may arise from Standard and PPCD discharges simply through small variations in the plasma q-profile, derived ultimately from the current density profile. In QSH discharges it is observed that there is a single magnetic mode dominating the mode spectrum. This mode is usually the core-most resonant mode. The QSH state can occur in both Standard and PPCD plasmas. Chapter 5 showed that in Standard plasmas, the core-most island (i.e. the  $m=1, n=6$ ) overlaps only slightly the closest resonant island (i.e. the  $n=7$ ). This overlap allows energy (heat) to flow from one island to the next; for higher n-modes heat flows rapidly radially outward since the islands strongly overlap and the magnetic field is highly stochastic by Rechester-Rosenbluth’s formalism. If the q-profile were sheared sufficiently, the core-most magnetic island could conceivably cease to overlap its closest neighbor. As a result energy from the core-most mode would be “trapped,” allowing the mode to remain relatively larger than its neighbors, which would cascade energy to each other through enhanced transport. Since the machine wall serves to stabilize tearing modes, the core-most mode is larger than its neighbor, being farther from the wall. QSH discharges would not necessarily exhibit better confinement (in either Standard or PPCD plasmas), since the transport of heat out of the mid-radius region is determined by the stochastic field from closely packed magnetic islands in that region, i.e. not by the largely independent mode in the core. Similarly, as discussed in Chapter 6, the differences between

“good, bad, and super” PPCD may be small variations in the current density profile, which lead to favorable variations in the q-profile. By appropriately “mining” the larger datasets that the Standard and PPCD ensemble plasmas were culled from, sufficient data may already exist to determine if indeed q-shear is playing a role in the differentiation of QSH plasmas and “bad” PPCD plasmas from their counterparts. As so much of science goes, one needs only to look to see if it is true.



\*\*\*\*\*  
 Left June 27<sup>th</sup> back Aug. 22<sup>nd</sup> 1968  
 JOHN BIEWER RETURNS FROM CONTINENT

Congratulations to John Biewer upon successful completion of a sixty-day bicycle trip through Europe. Under his own steam, John traveled through England, France, Switzerland, Austria, Germany, and Belgium. We hope to hear more of John's experiences later.  
 \*\*\*\*\*



Last week I forgot how to ride a bicycle.

-- Steven Wright

## **Magnetic Mode Amplitudes and Velocities**

This appendix contains plots of the time histories of the magnetic modes for each of the 5 experiments detailed: Standard ( $F=-0.22$ ), Non-Reversed ( $F=0$ ),  $F=+0.02$ ,  $F=+0.03$ , and PPCD plasmas. The data is measured by a toroidal array of 32 edge magnetic pickup coil-sets, i.e. Mirnov probes. Each coil set contains a triplet of coils, respectively sensitive to radial, poloidal, and toroidal fluctuations and capable of resolving the mode spectrum for  $n=1-15$ . Because the radial fluctuation amplitude at the wall must be identically zero, the data from the radial mode amplitude coils is not shown. Each section is organized as follows: The first figure is the poloidal fluctuation amplitude vs. time for  $n=1-15$  from the toroidal array. The second figure is the toroidal fluctuation amplitude vs. time for the toroidal array. The third and fourth figures plot at each time slice the poloidal and toroidal fluctuation amplitude spectra, respectively. The fifth and sixth figures are the corresponding measured mode velocities (which should be equal for the poloidal and toroidal components of the toroidal array). For low amplitude modes ( $n=1-4, 10-15$ ), the mode velocity may not be representative of the actual mode speed, due to low signal levels and low phase resolution.

A.1 Standard Plasmas

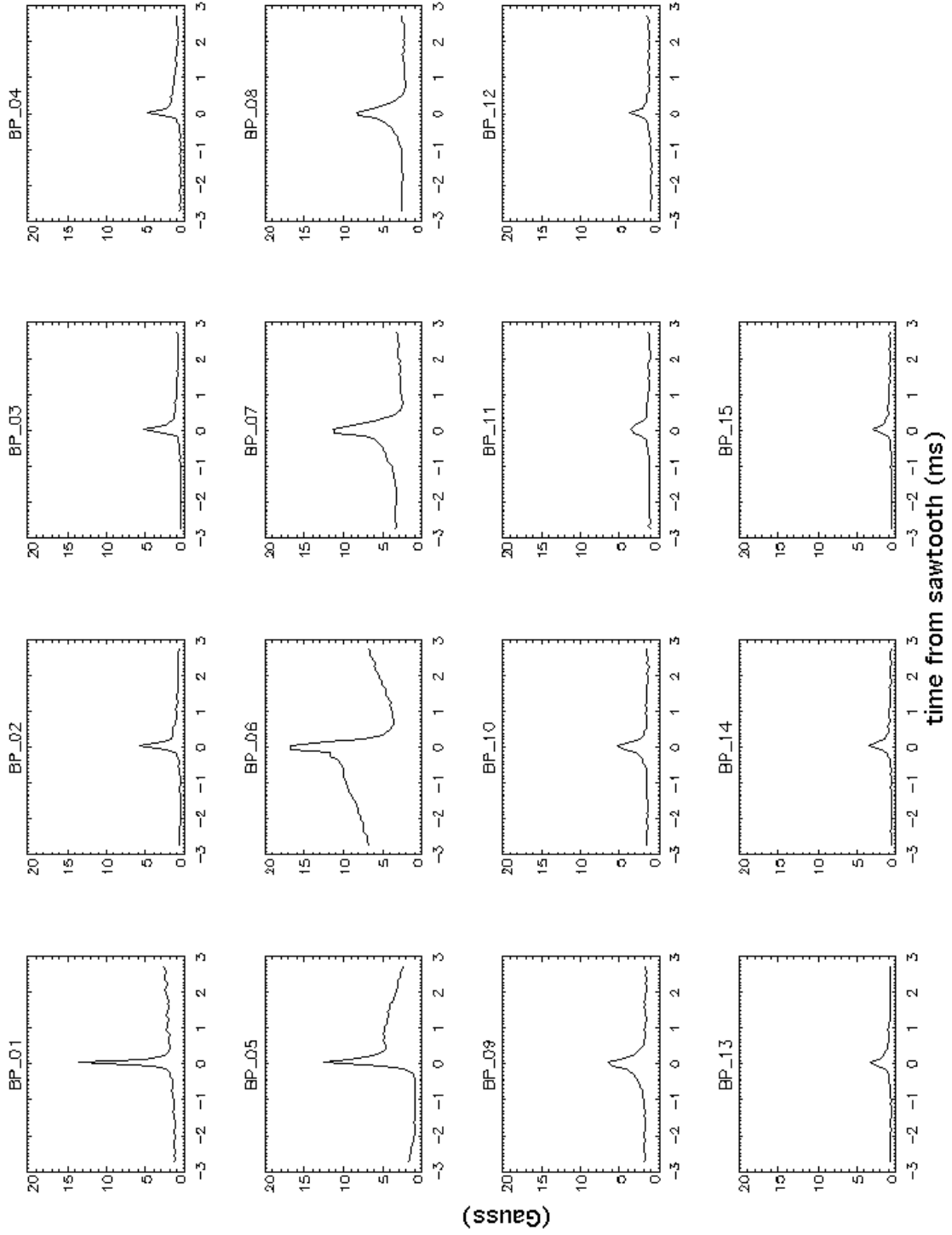


Figure A.1 Poloidal fluctuation amplitude spectrum for Standard plasmas.

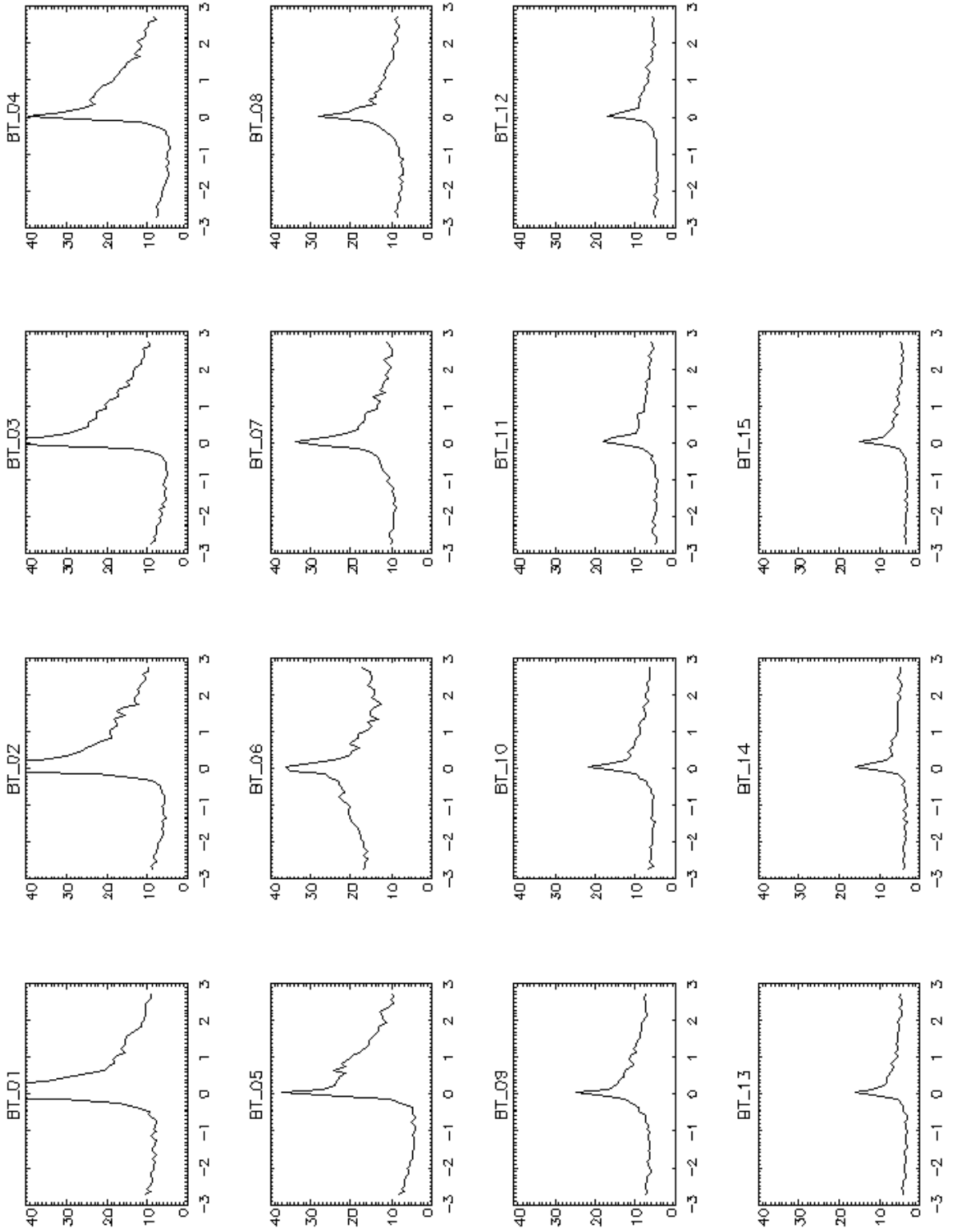


Figure 8.2 Toroidal fluctuation amplitude spectrum for Standard plasmas.

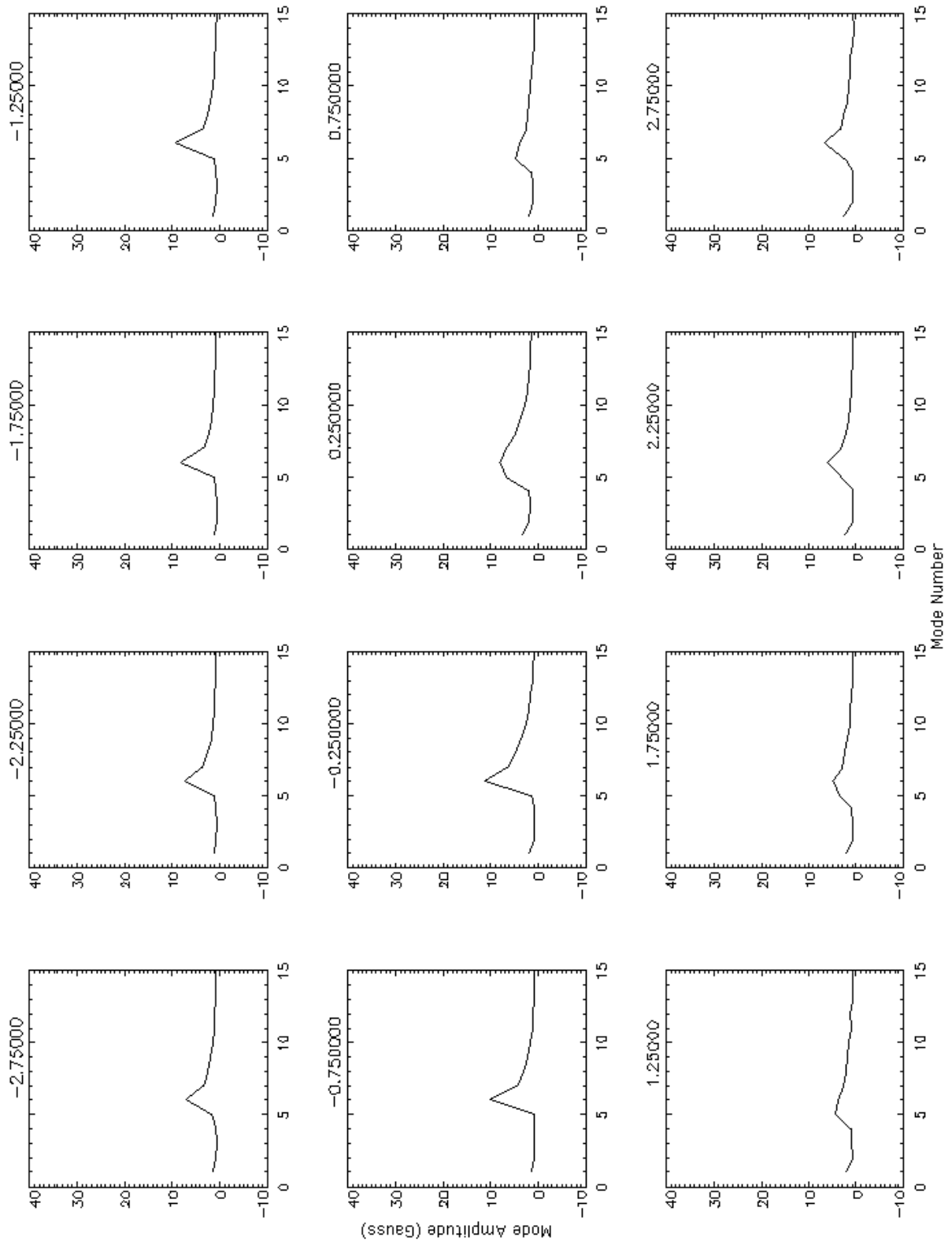


Figure 8.3 Poloidal fluctuation amplitudes at select times during F=-0.22 plasmas.

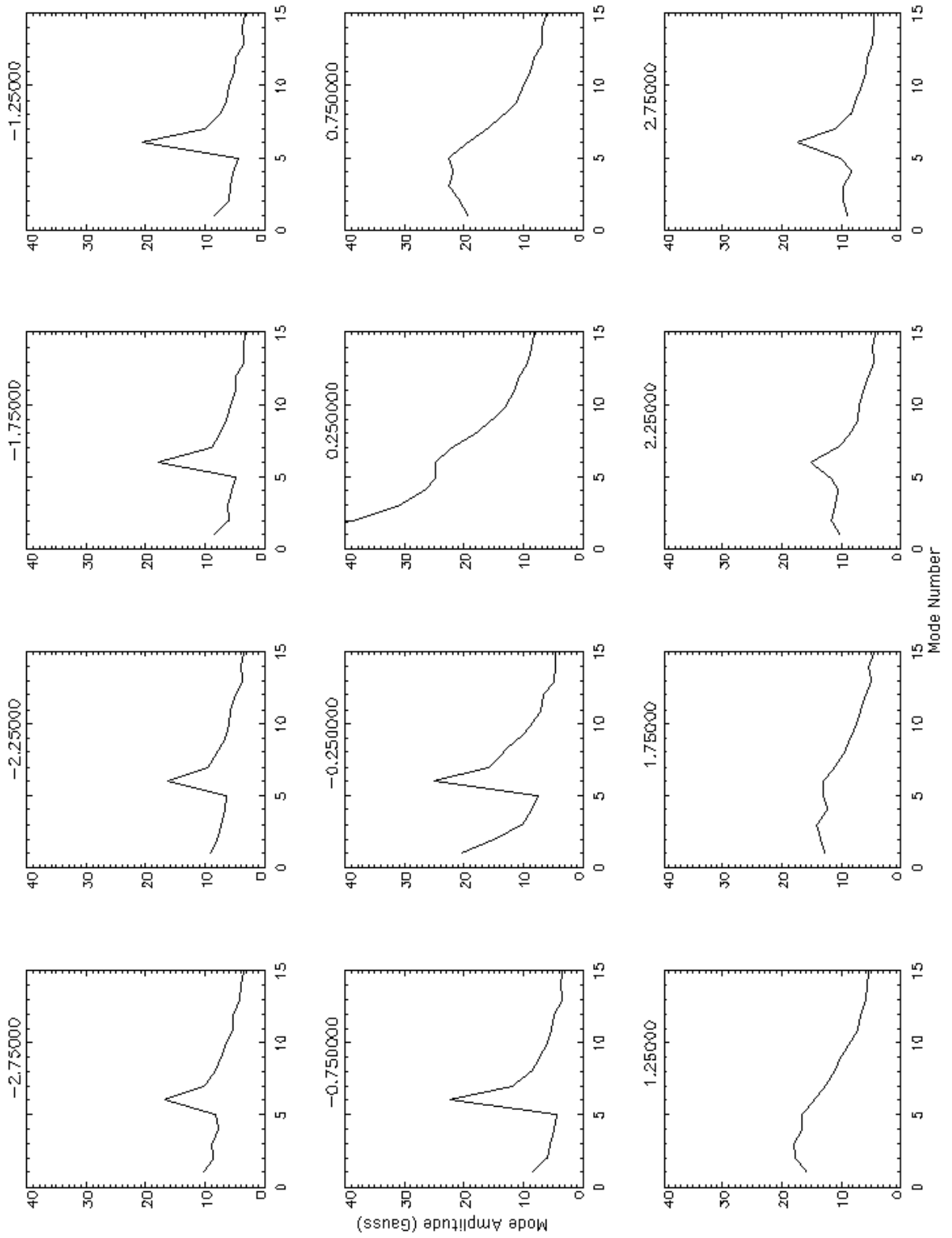


Figure 8.4 Toroidal fluctuation amplitude at select times during F=-0.22 plasmas.

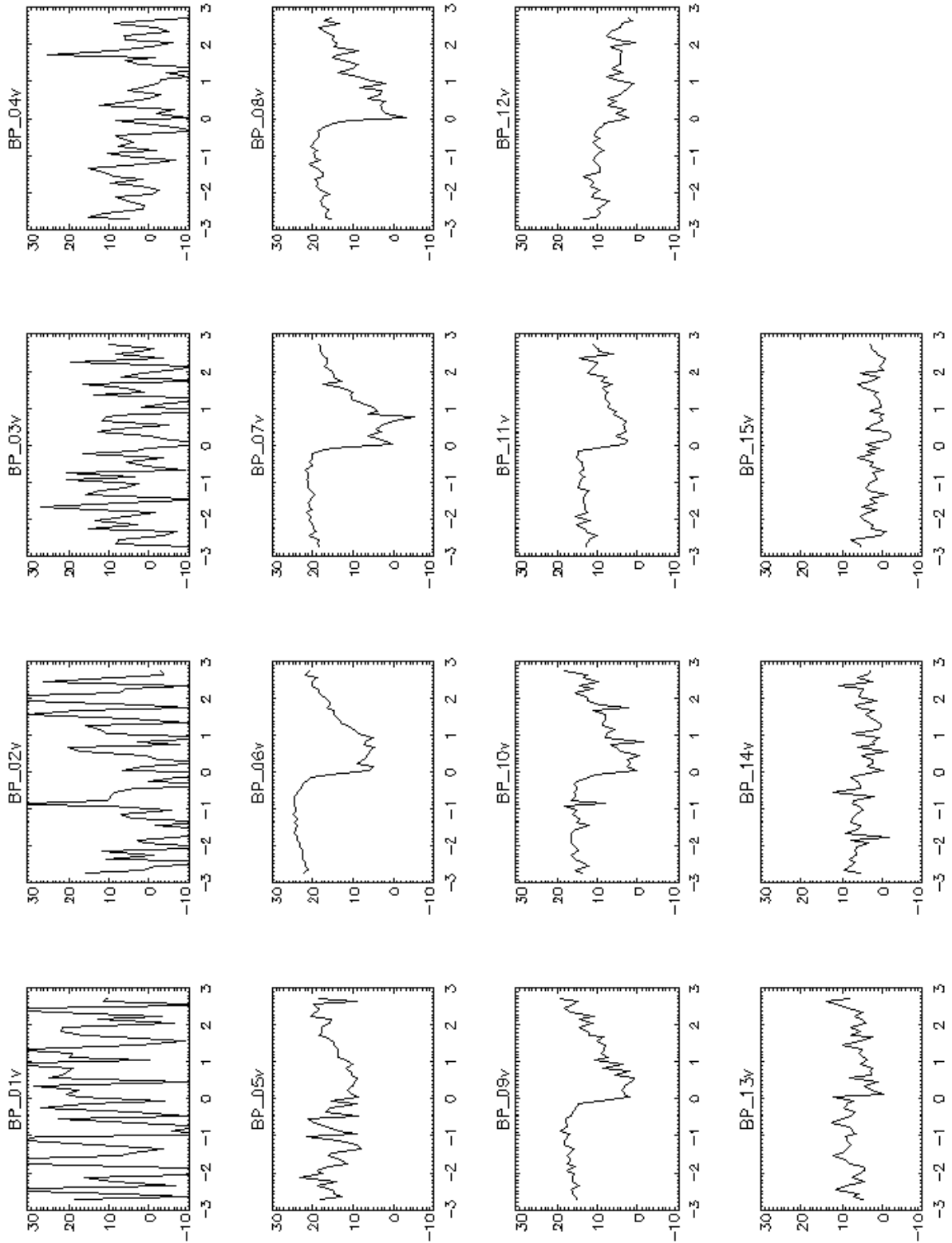


Figure 8.5 Poloidally derived mode velocity spectrum (km/s) for Standard plasmas.

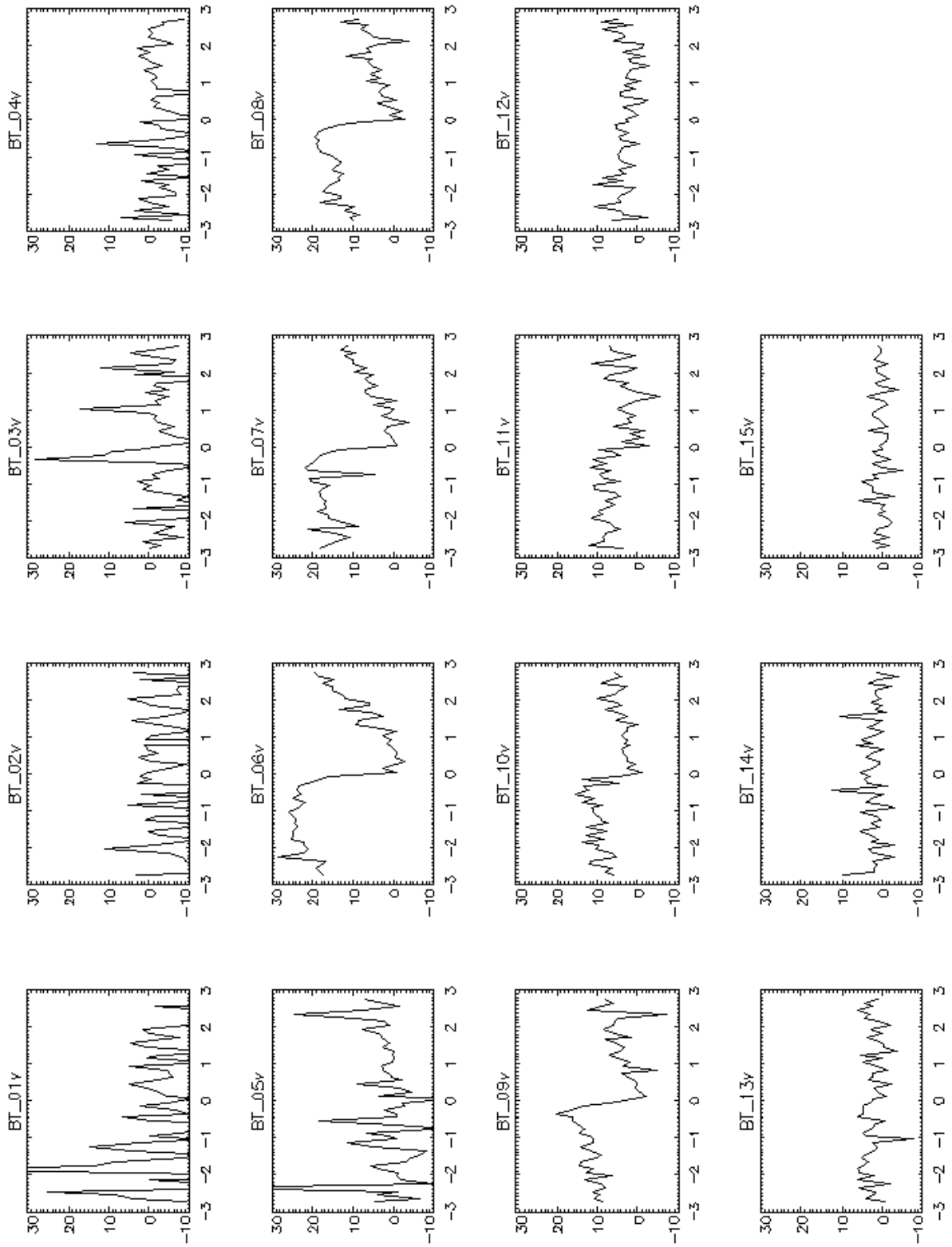


Figure 8.6 Toroidally derived mode velocity spectrum (km/s) for Standard plasmas.

## A.2 Non-Reversed Plasmas

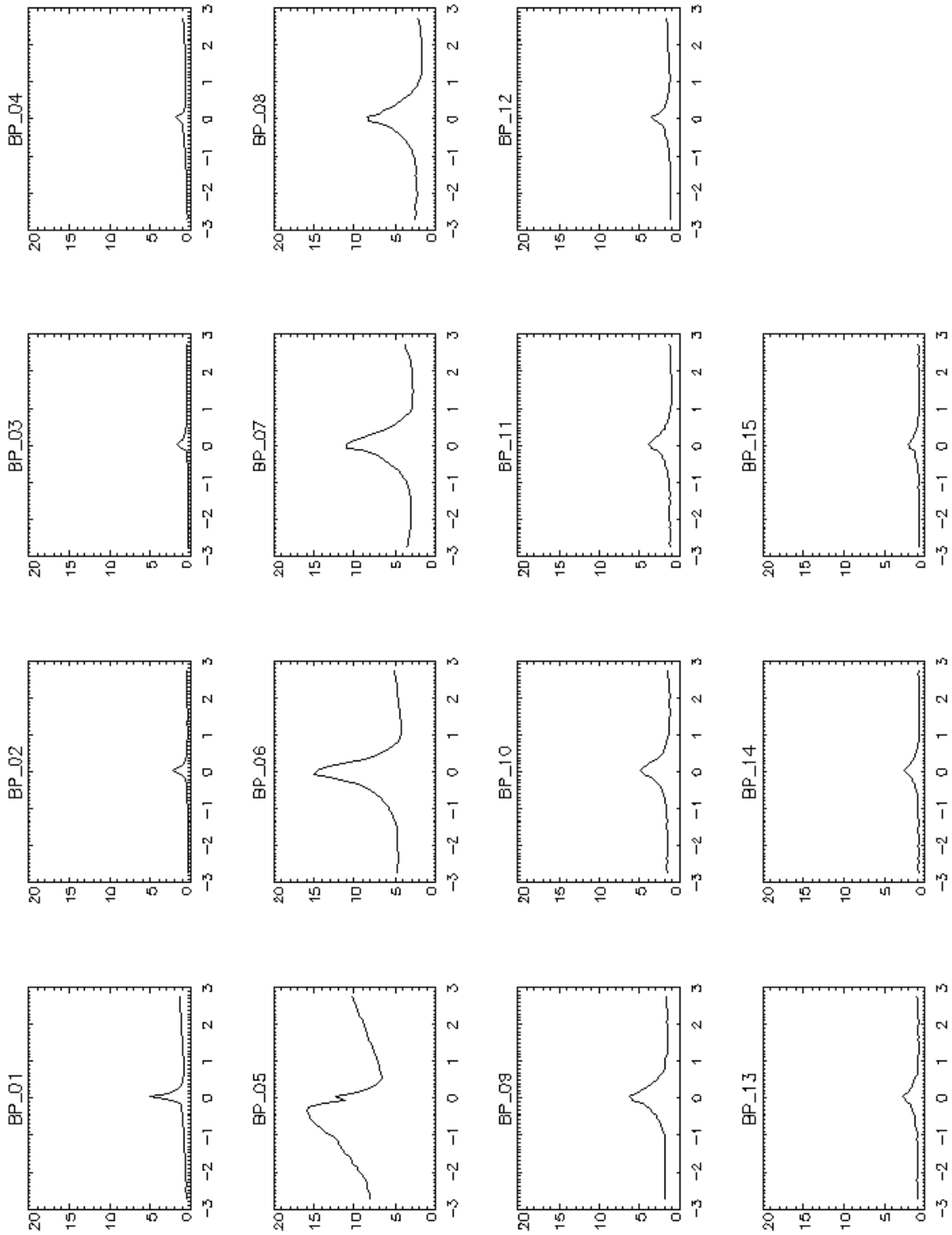


Figure 8.7 Poloidal mode amplitude spectrum for Non-Reversed plasmas.

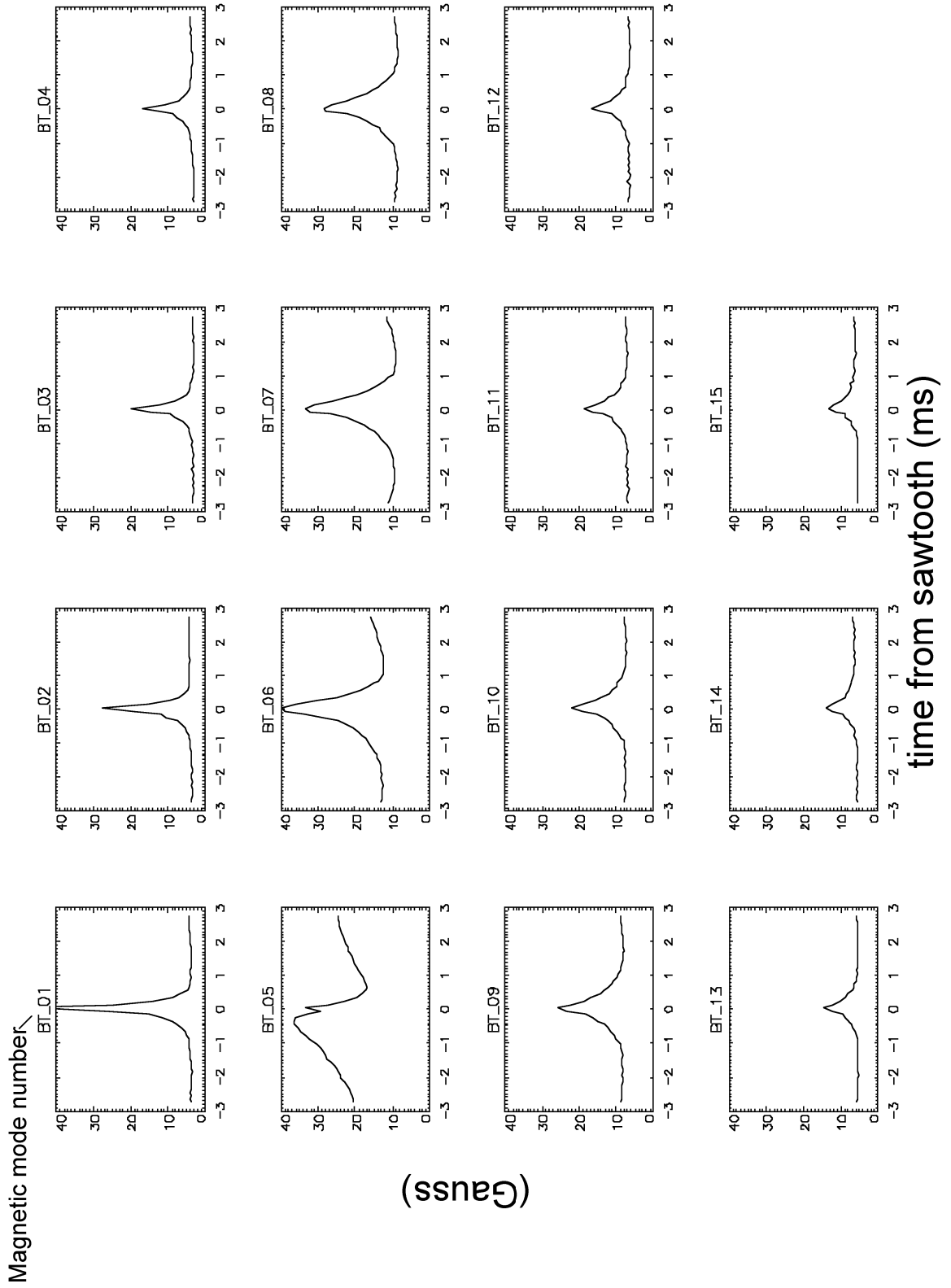


Figure A.8 Toroidally derived mode amplitude spectrum for Non-Reversed plasmas.

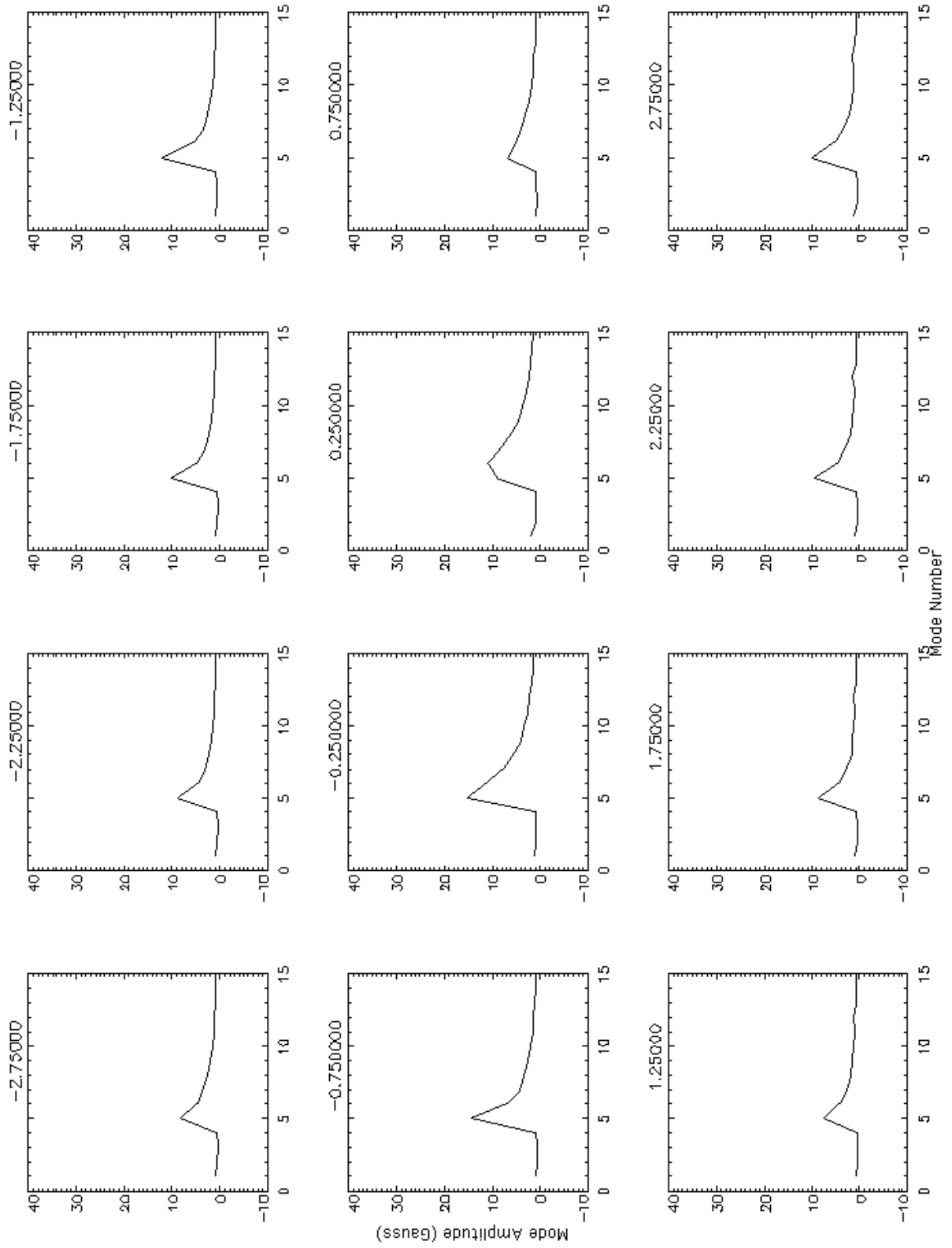


Figure 8.9 Poloidal mode amplitudes for select times during F=0 plasmas.

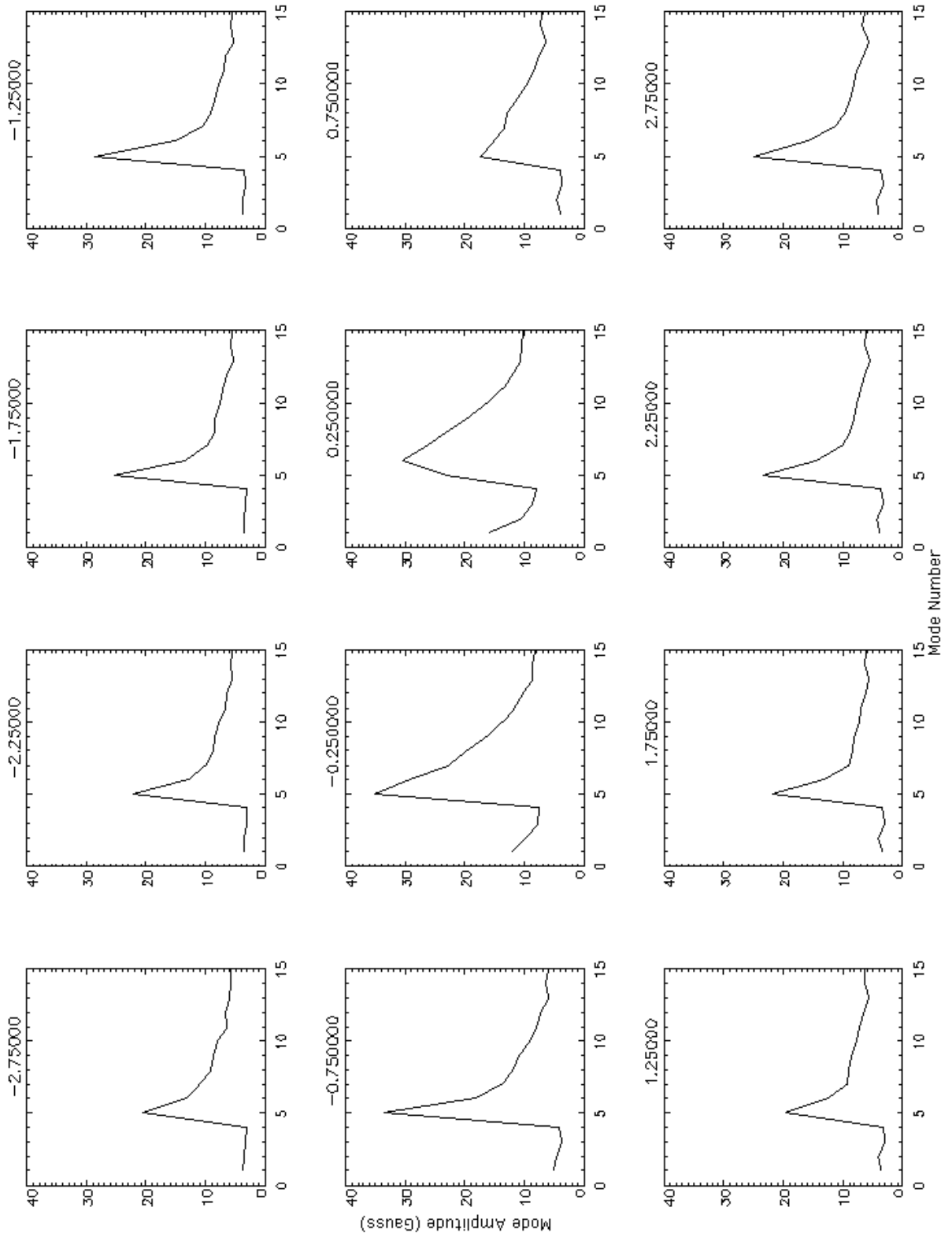


Figure 8.10 Toroidal mode amplitude at select times during F=0 plasmas.

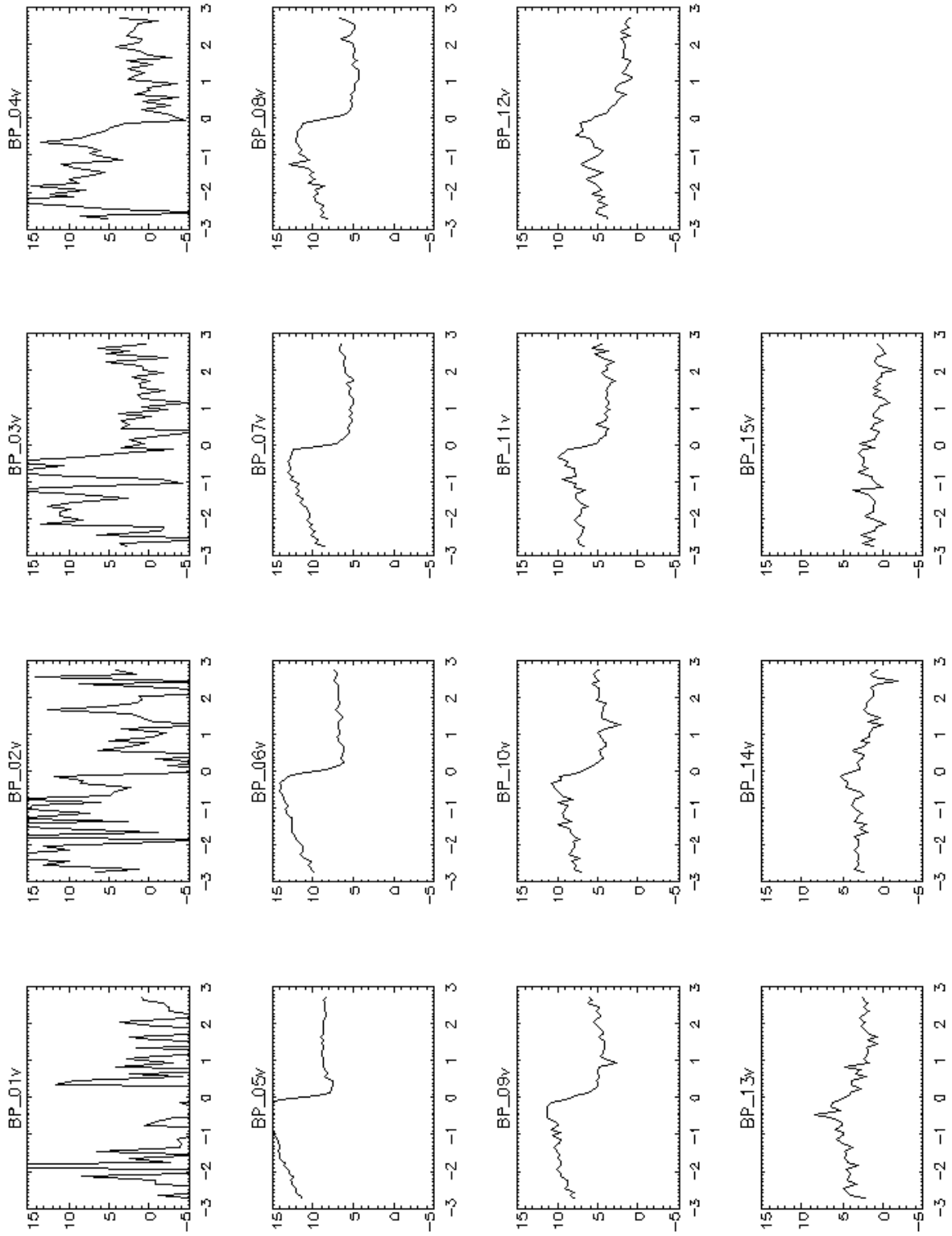


Figure 8.11 Poloidally derived mode velocity spectrum (km/s) for Non-Reversed plasmas.

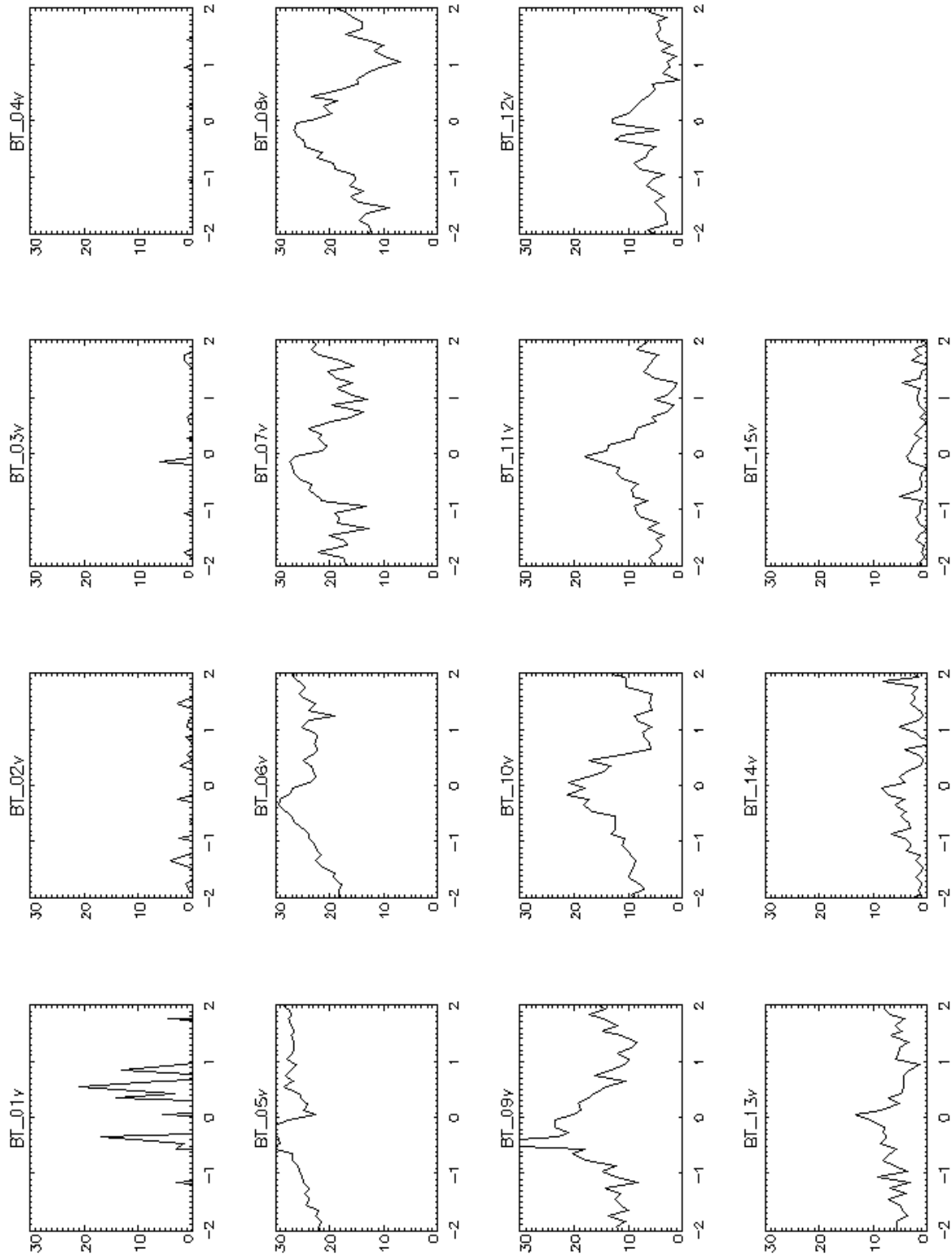
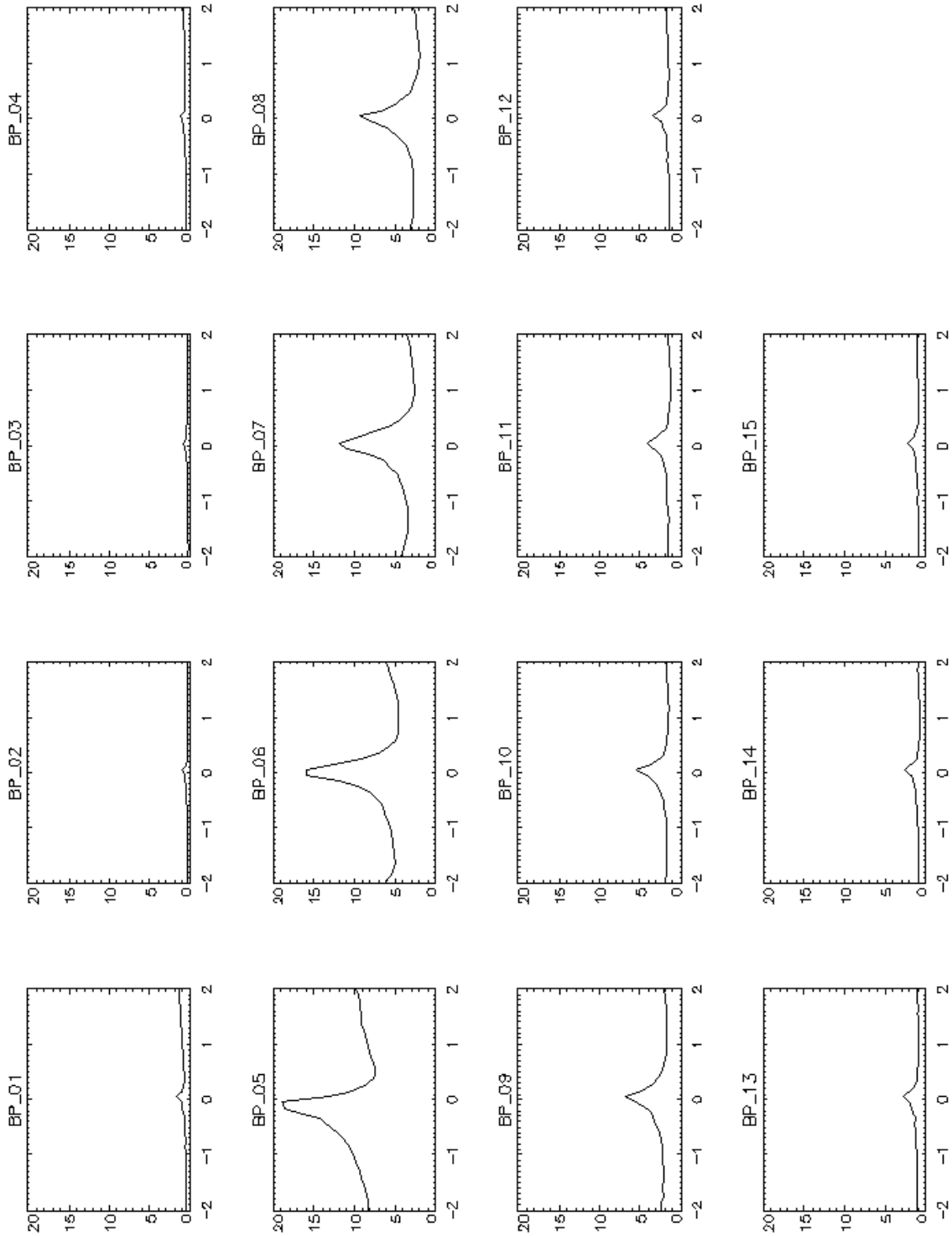


Figure 8.12 Toroidally derived mode velocity spectrum (km/s) for Non-Reversed plasmas.

A.3  $F=+0.02$  PlasmasFigure 8.13 Poloidally derived mode amplitude spectrum for  $F=+0.02$  plasmas.

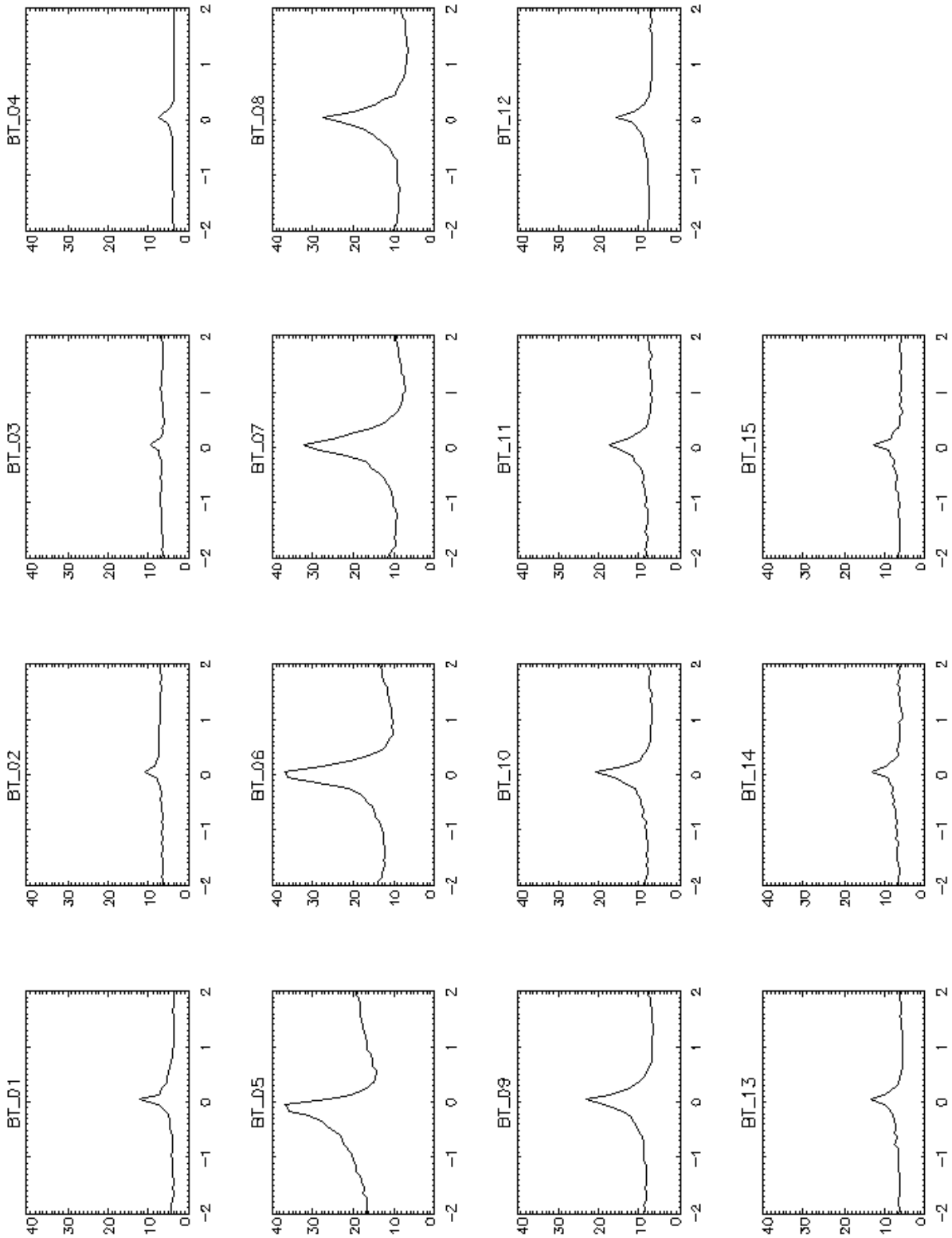


Figure 8.14 Toroidally derived mode amplitude spectrum for  $F=+0.02$  plasmas.

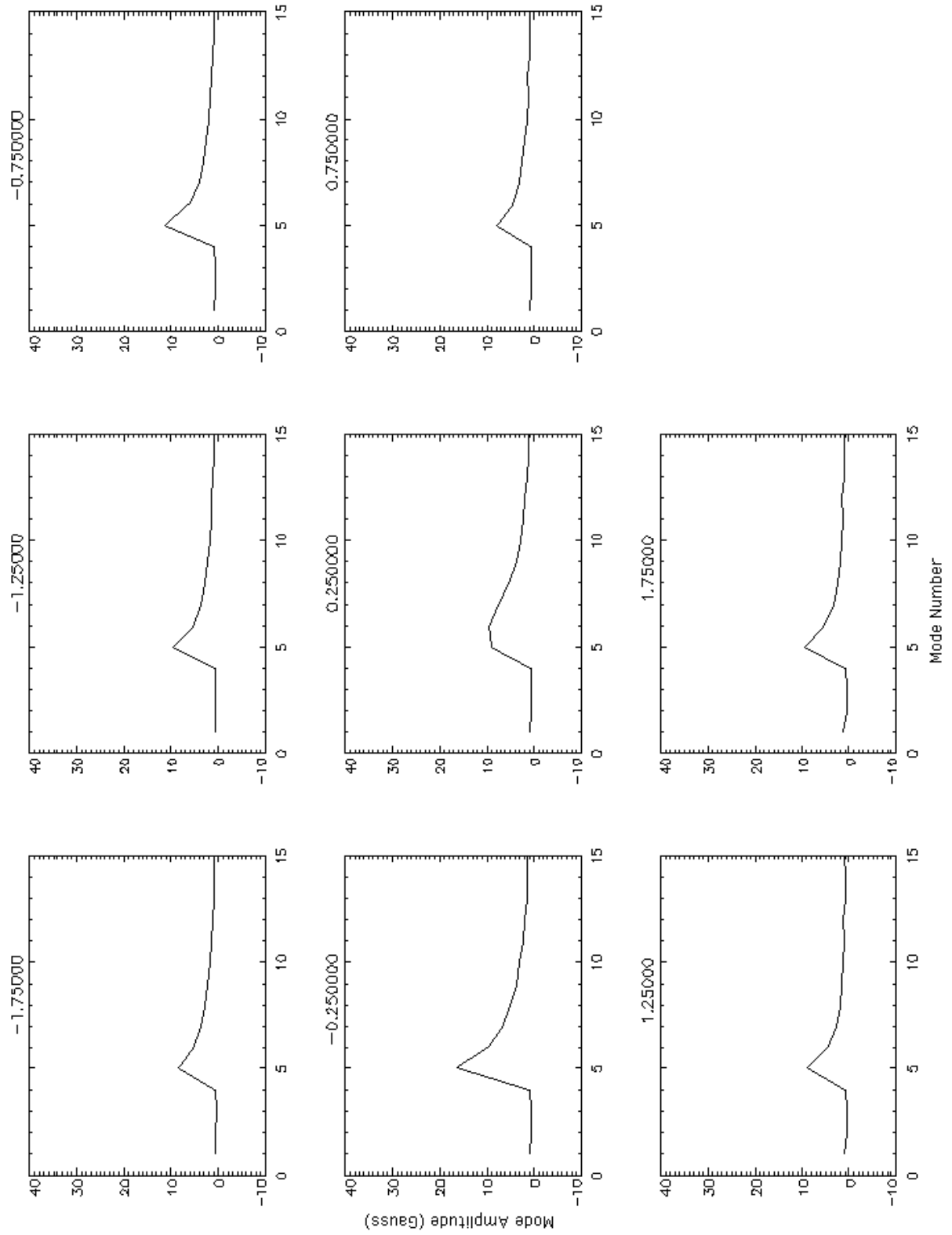


Figure 8.15 Poloidal mode amplitude for select times during  $F=+0.02$  plasmas.

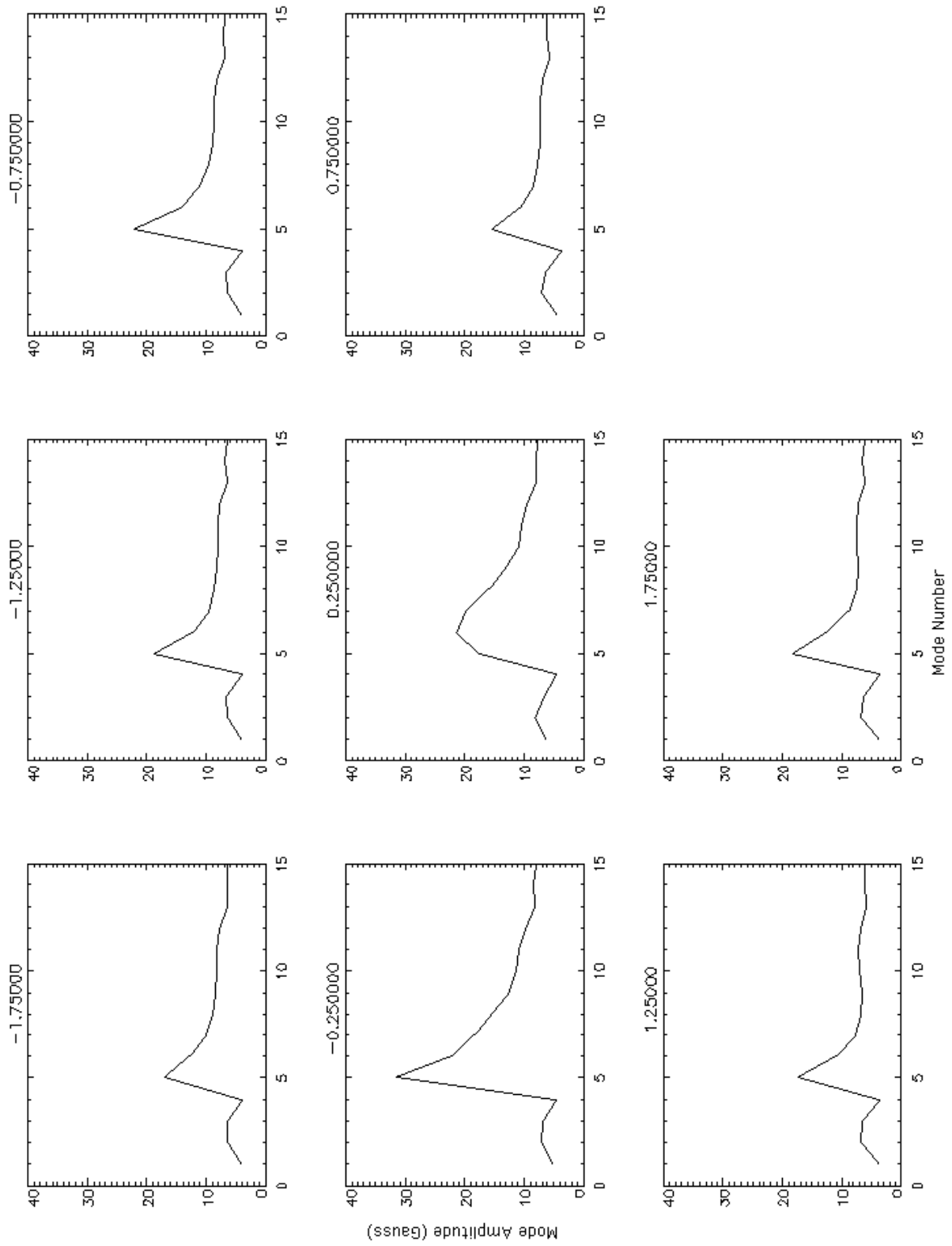


Figure 8.16 Toroidal mode amplitude for select times during F=+0.02 plasmas.

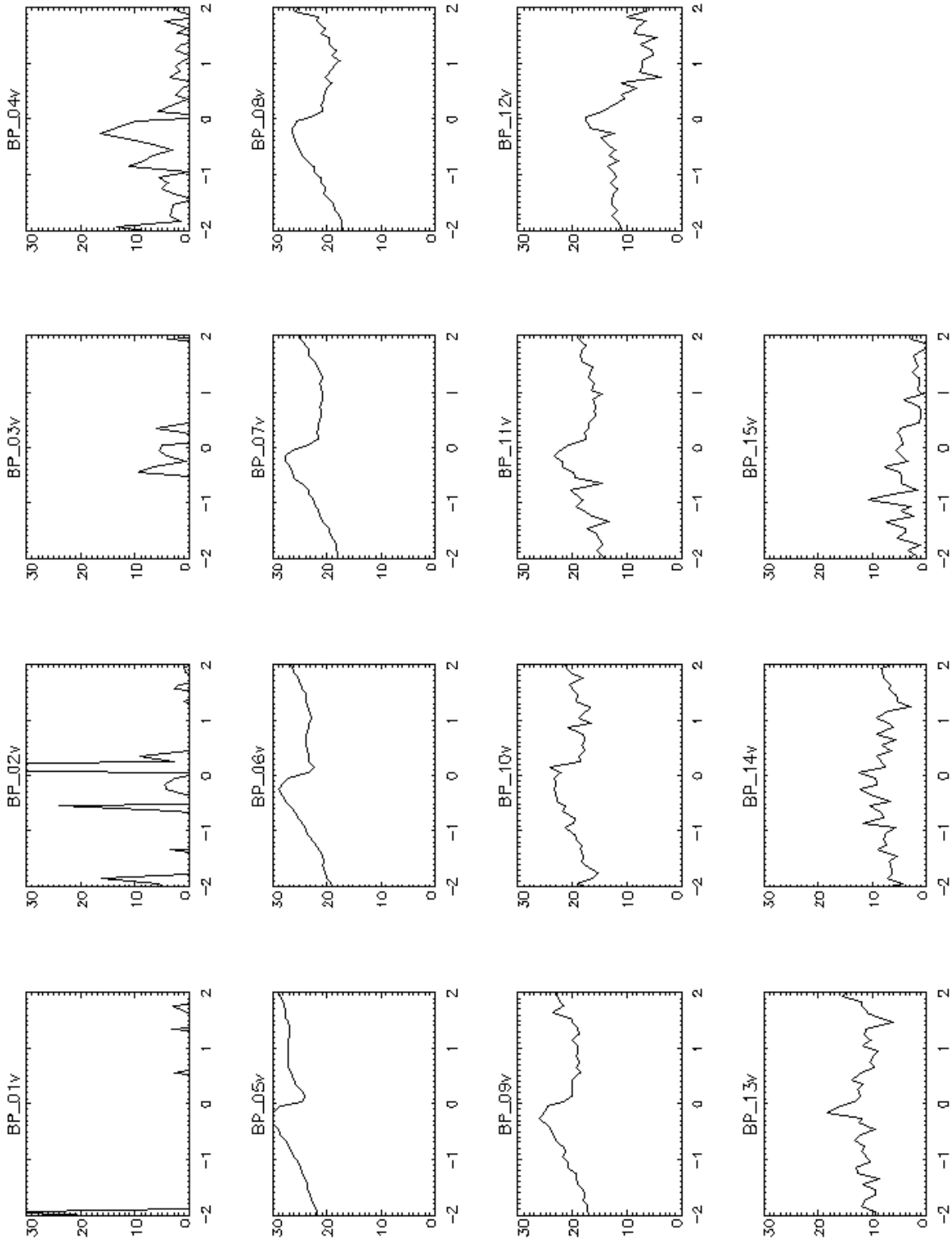


Figure 8.17 Poloidally derived mode velocity spectrum (km/s) for  $F=+0.02$  plasmas.

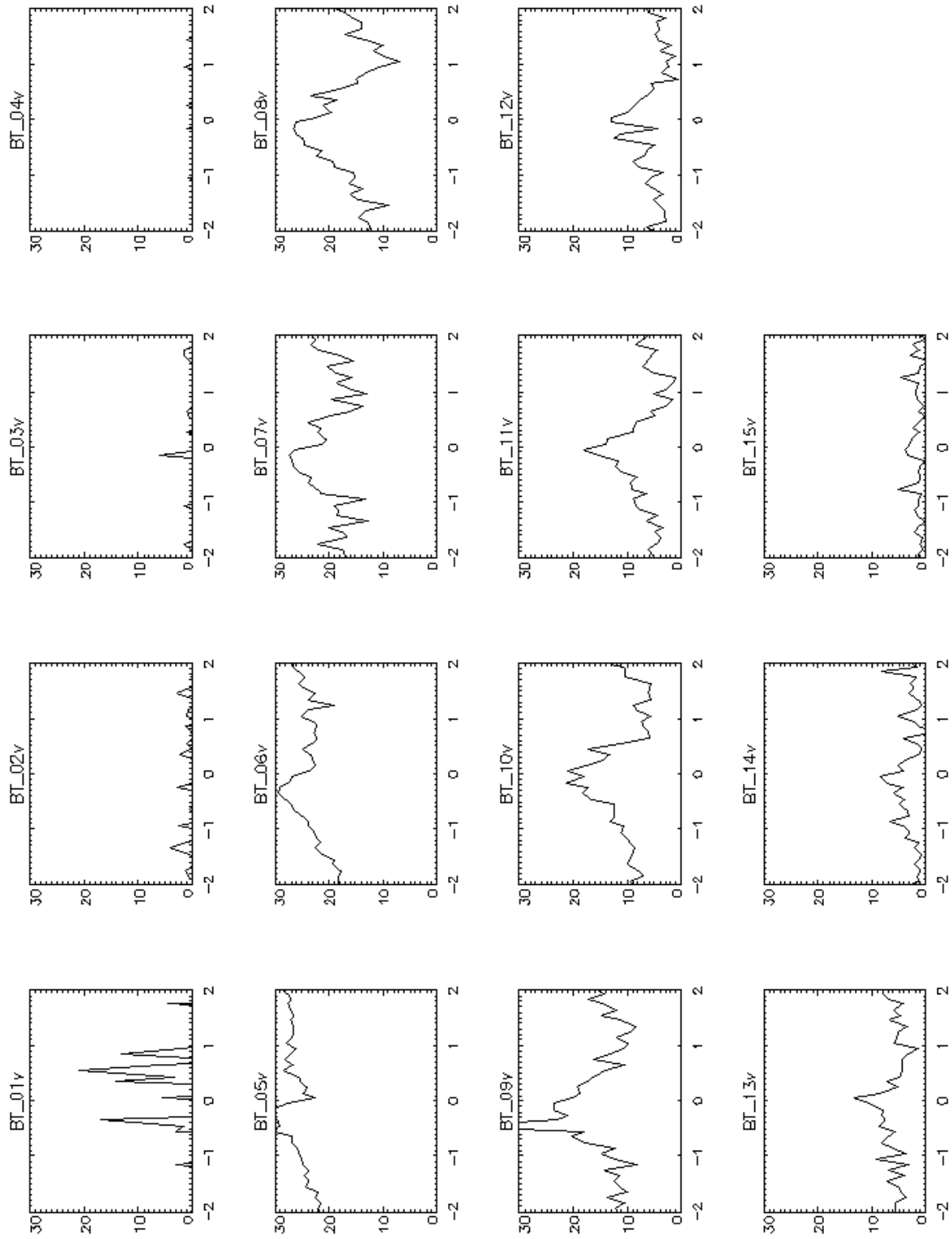


Figure 8.18 Toroidally derived mode velocity (km/s) for  $F=+0.02$  plasmas.

A.4  $F=+0.03$  Plasmas

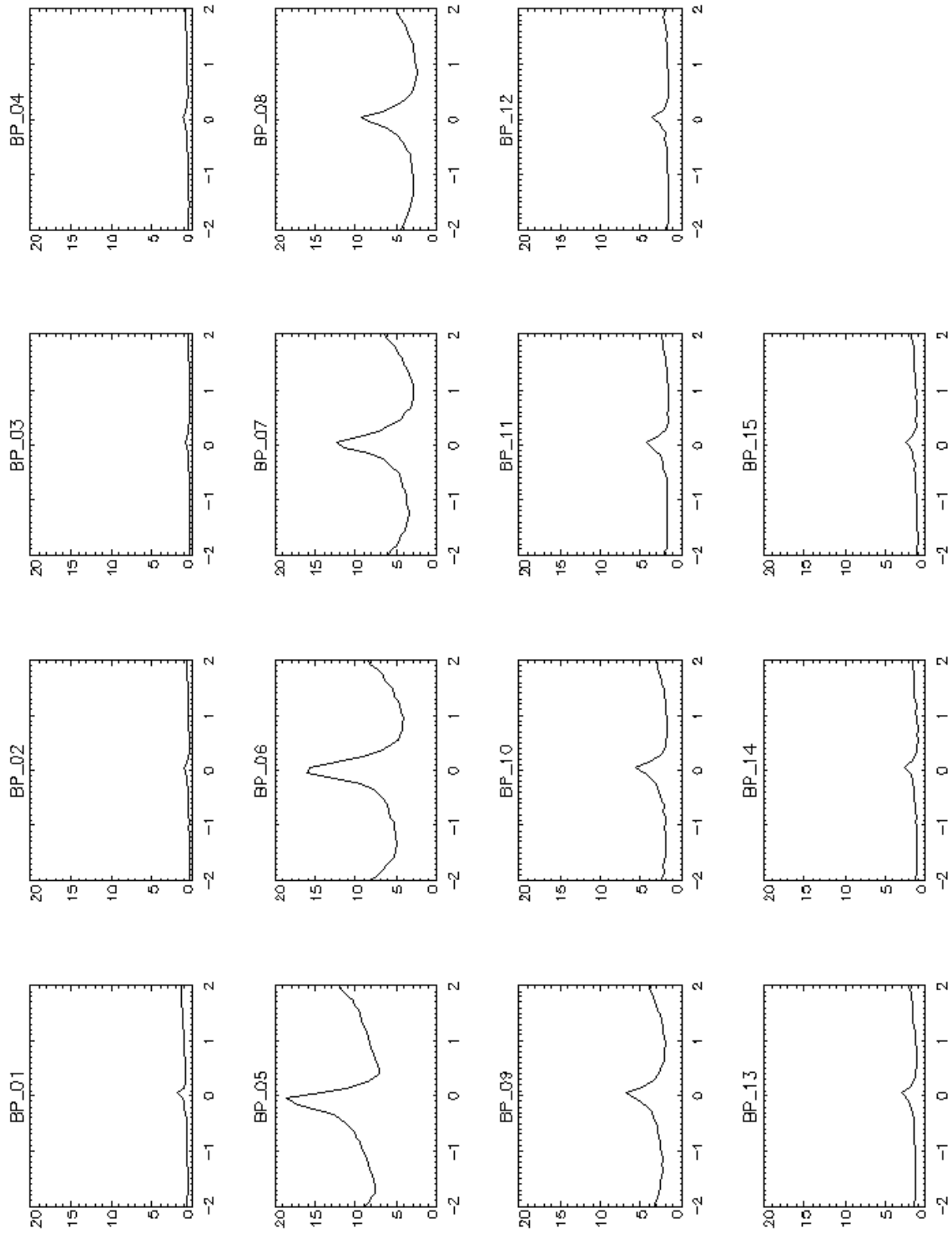


Figure 8.19 Poloidally derived mode amplitude spectrum for  $F=+0.03$  plasmas.

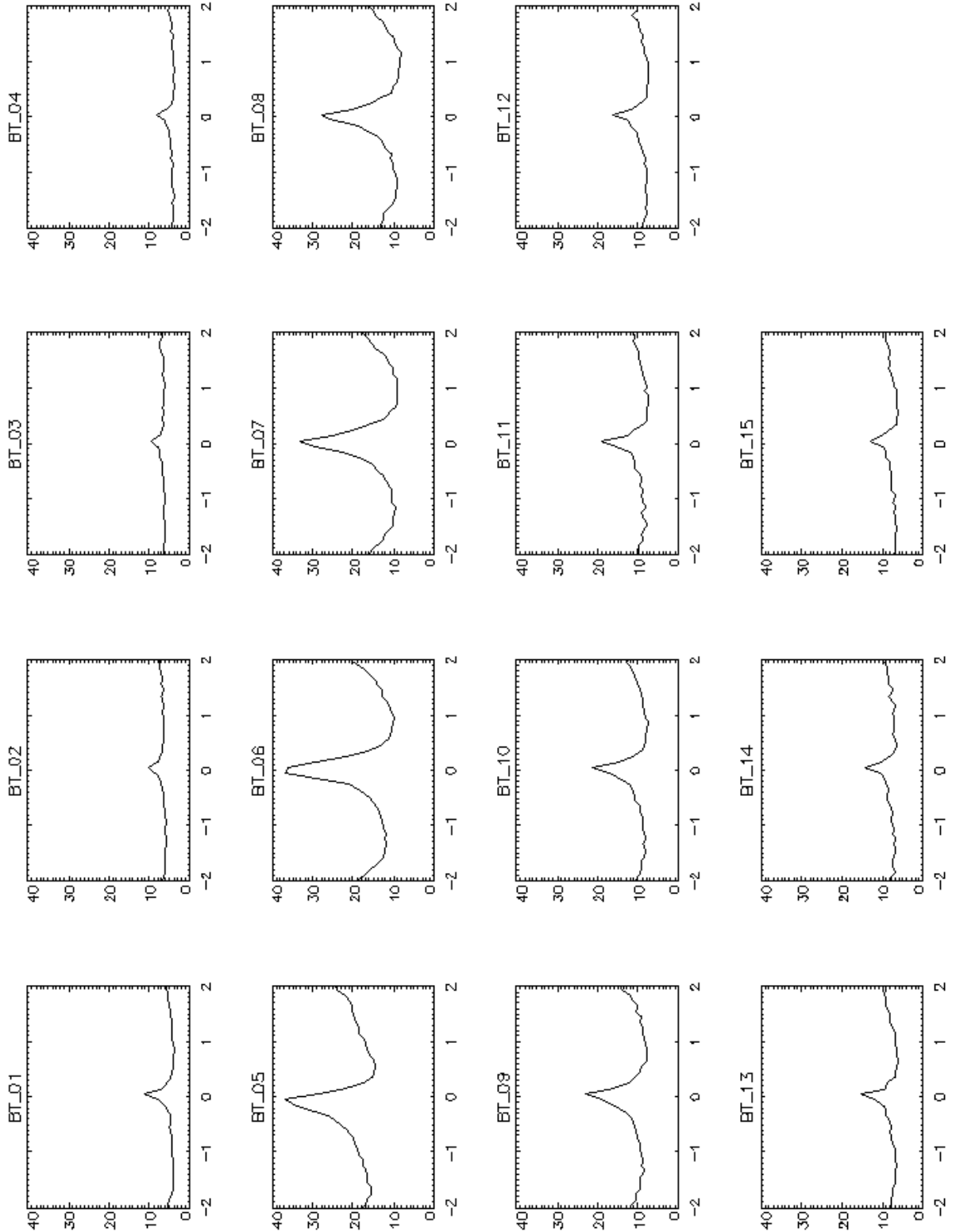


Figure 8.20 Toroidally derived mode amplitude for  $F=+0.03$  plasmas.

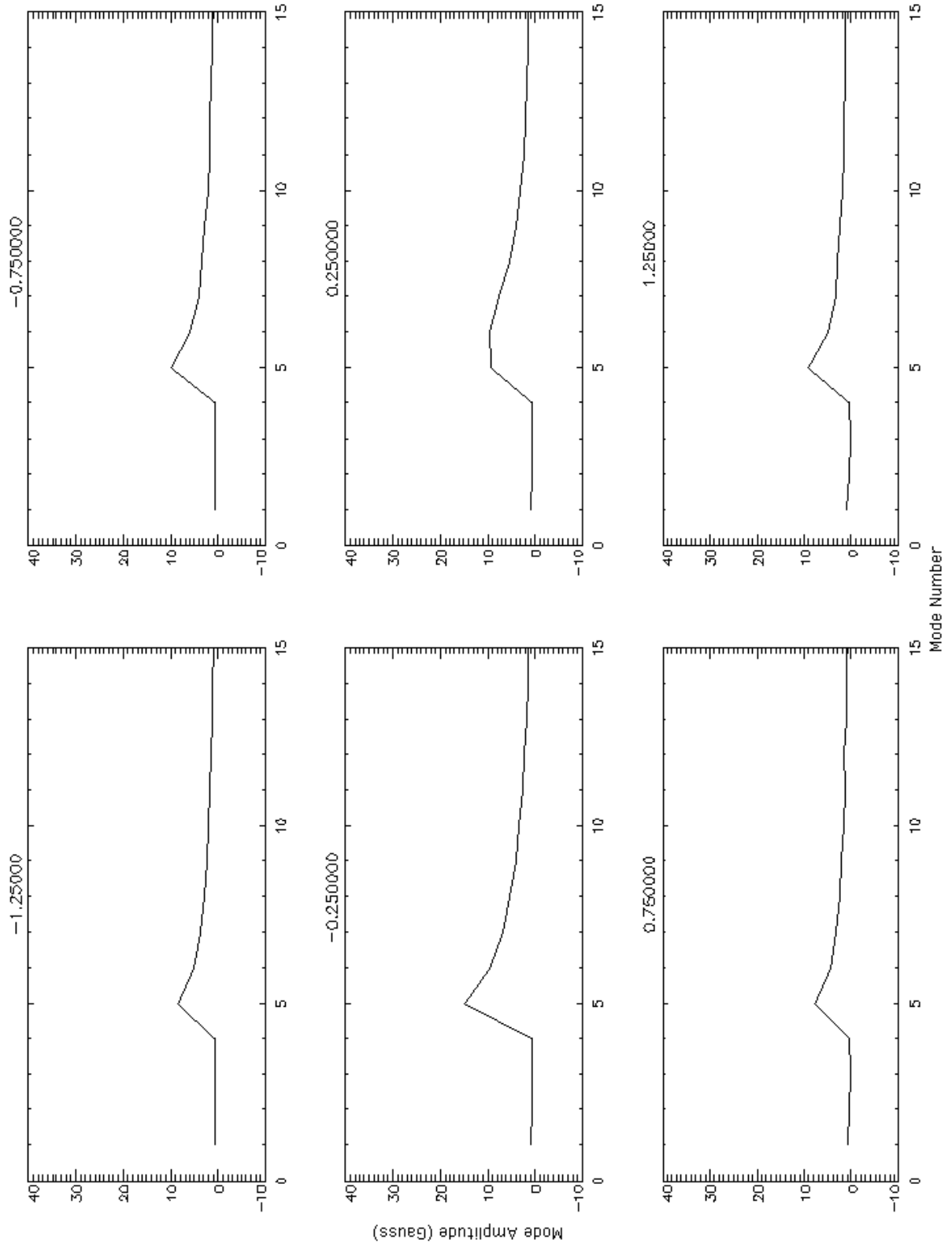


Figure 8.21 Poloidal mode amplitudes at select times for F=+0.03 plasmas.

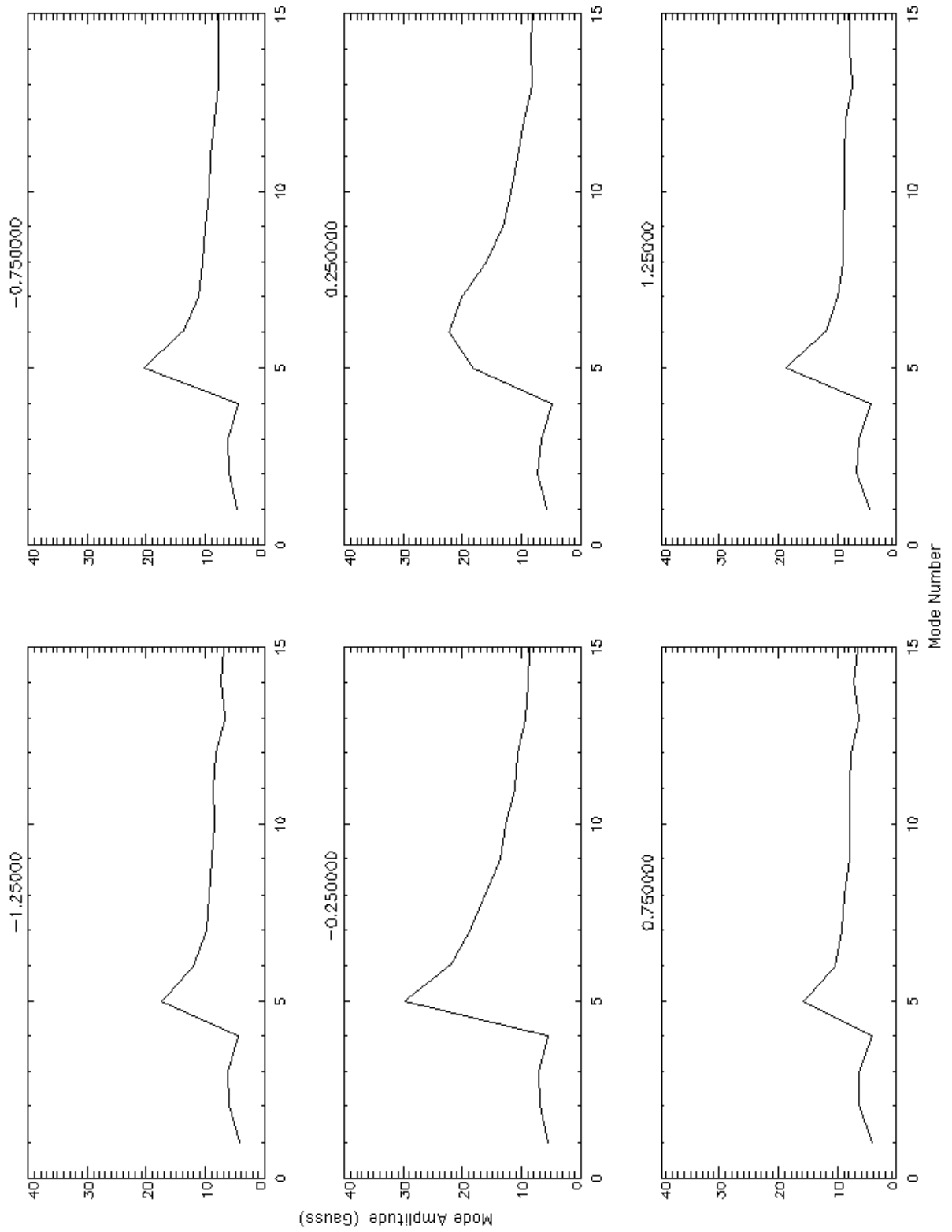


Figure 8.22 Toroidal mode amplitudes at select times for  $F=+0.03$  plasmas.

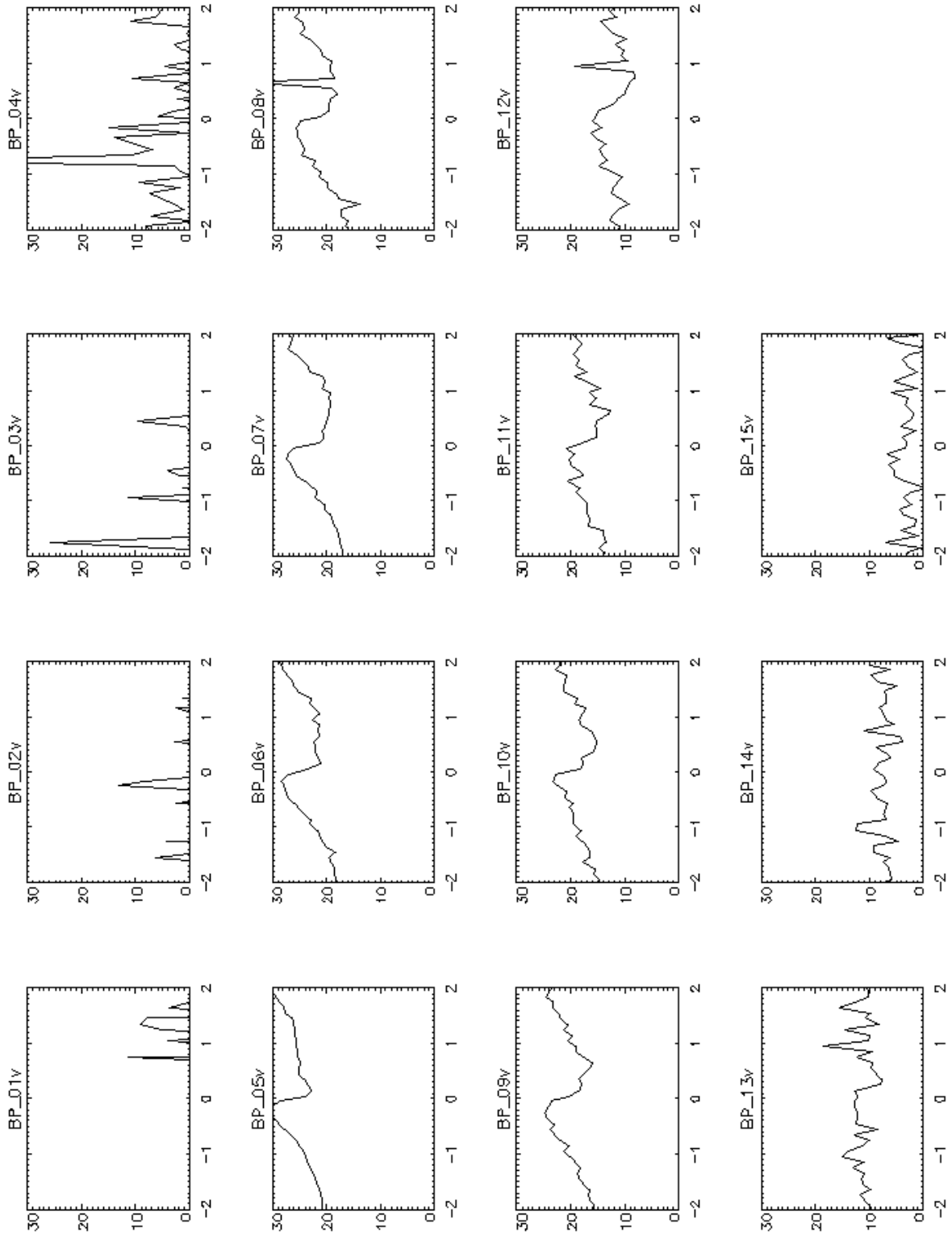


Figure 8.23 Poloidally derived mode velocity spectrum (km/s) for  $F=+0.03$  plasmas.

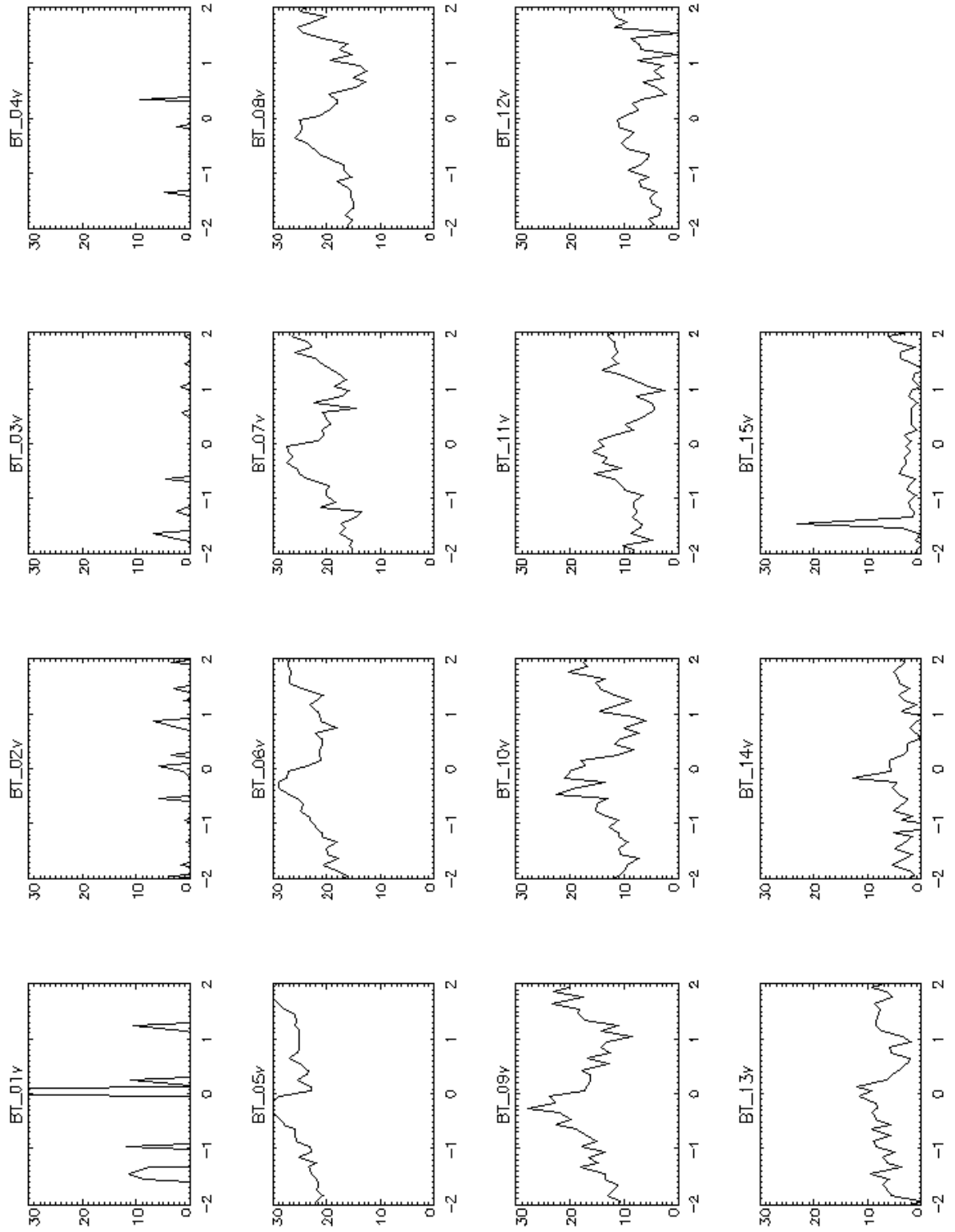


Figure 8.24 Toroidally derived mode velocity spectrum (km/s) for  $F=+0.03$  plasmas.

### A.5 PPCD Plasmas

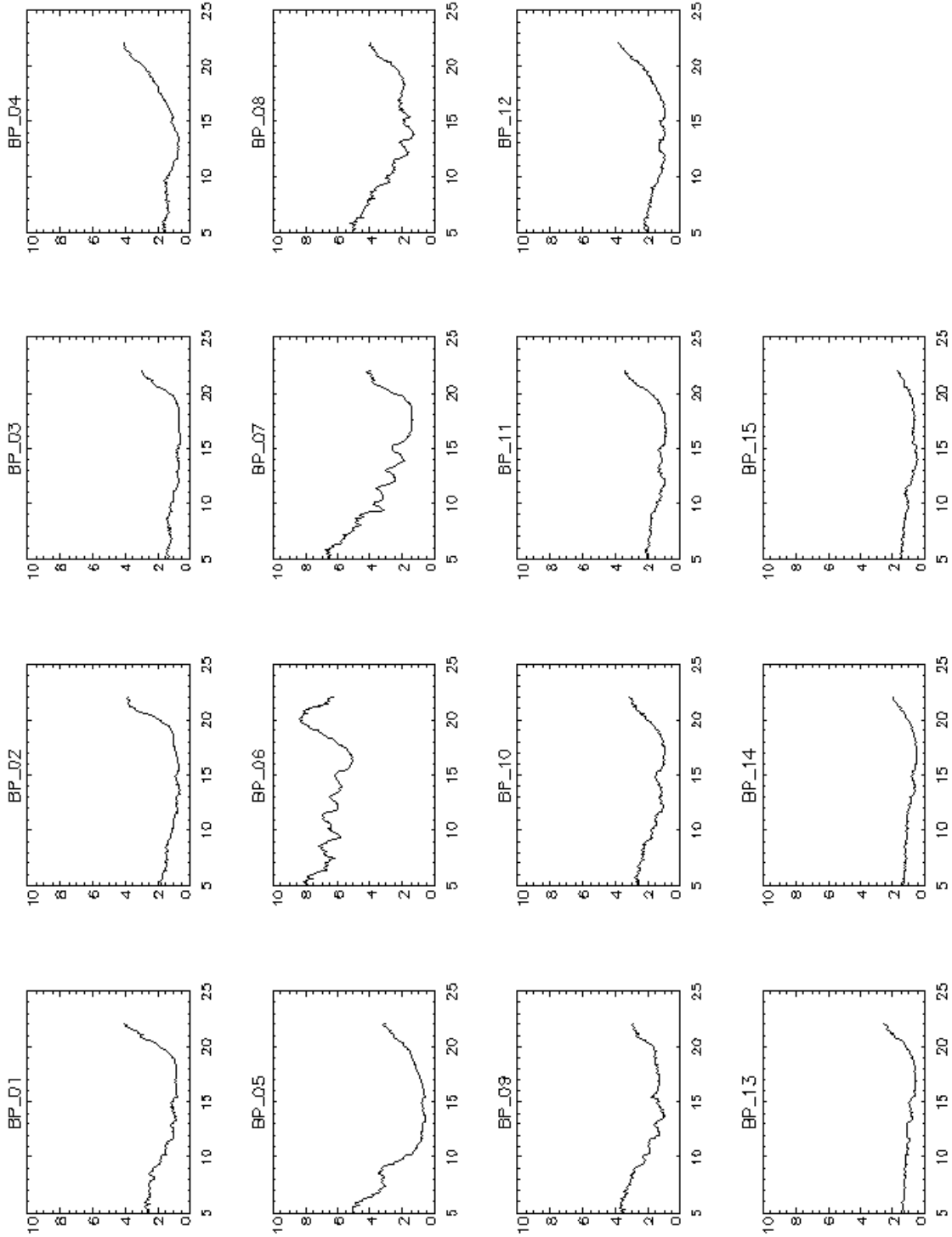


Figure 8.25 Poloidally derived mode amplitude spectrum for PPCD plasmas.

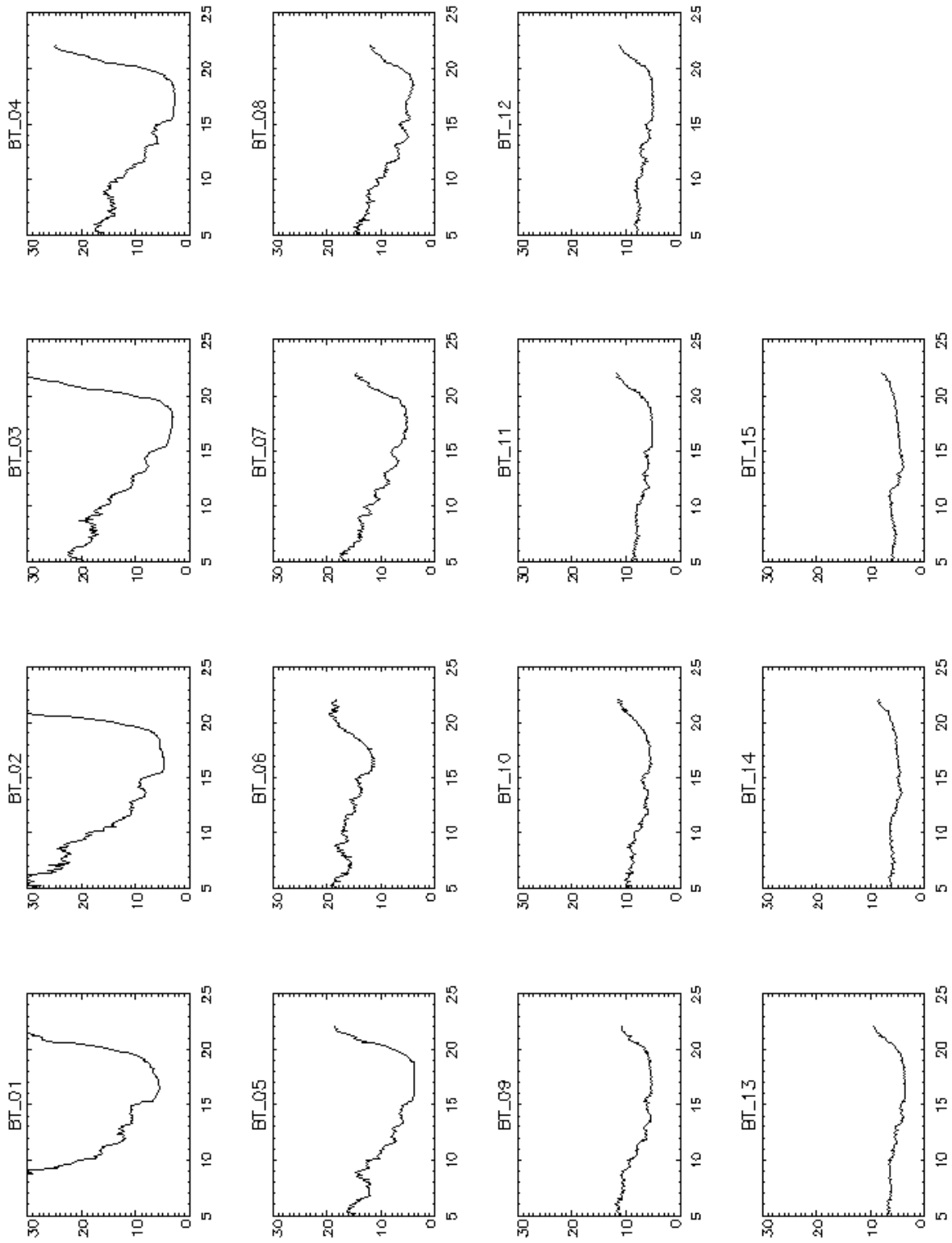


Figure 8.26 Toroidally derived mode amplitude spectrum for PPCD plasmas.

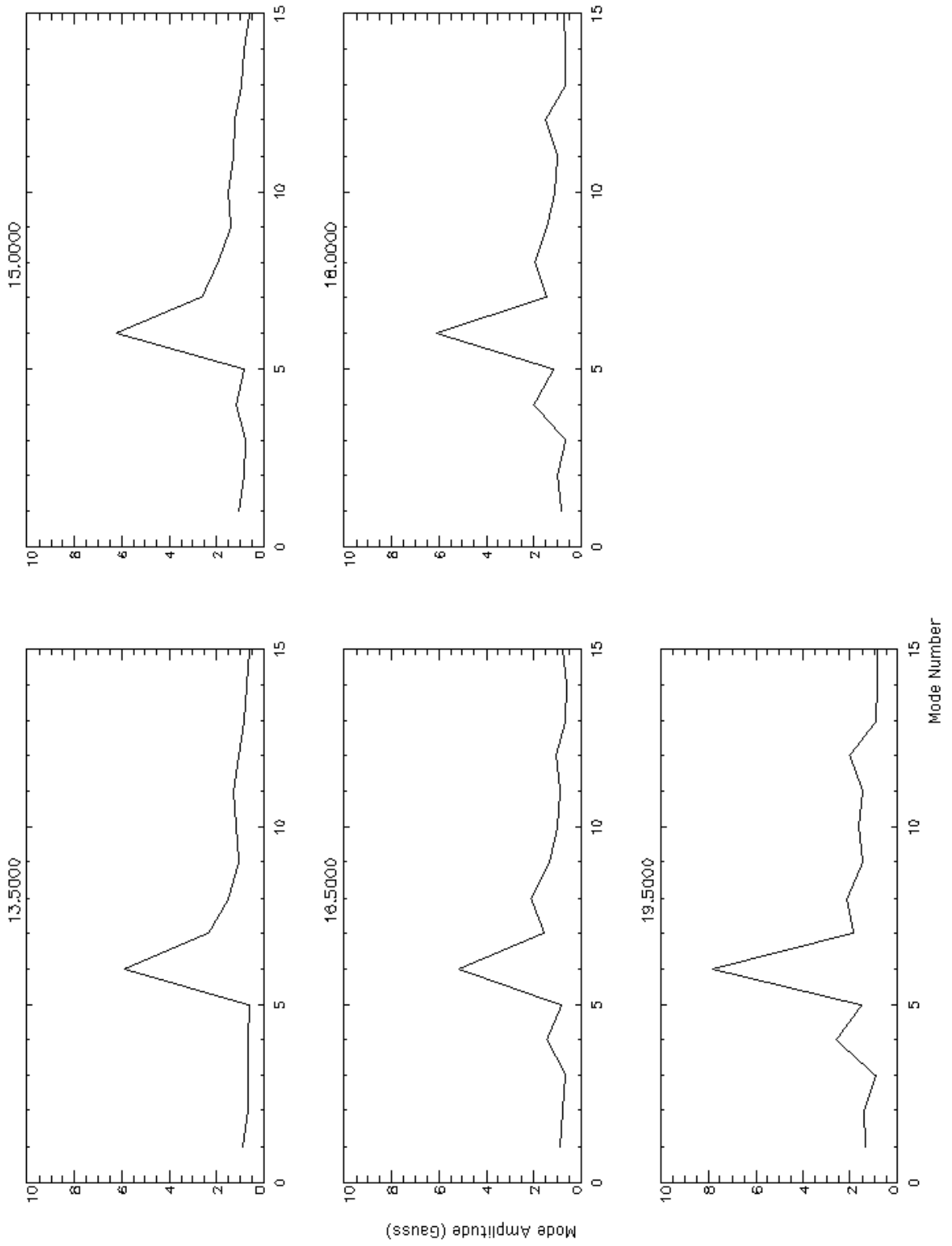


Figure 8.27 Poloidal mode spectrum at select times for PPCD plasmas.

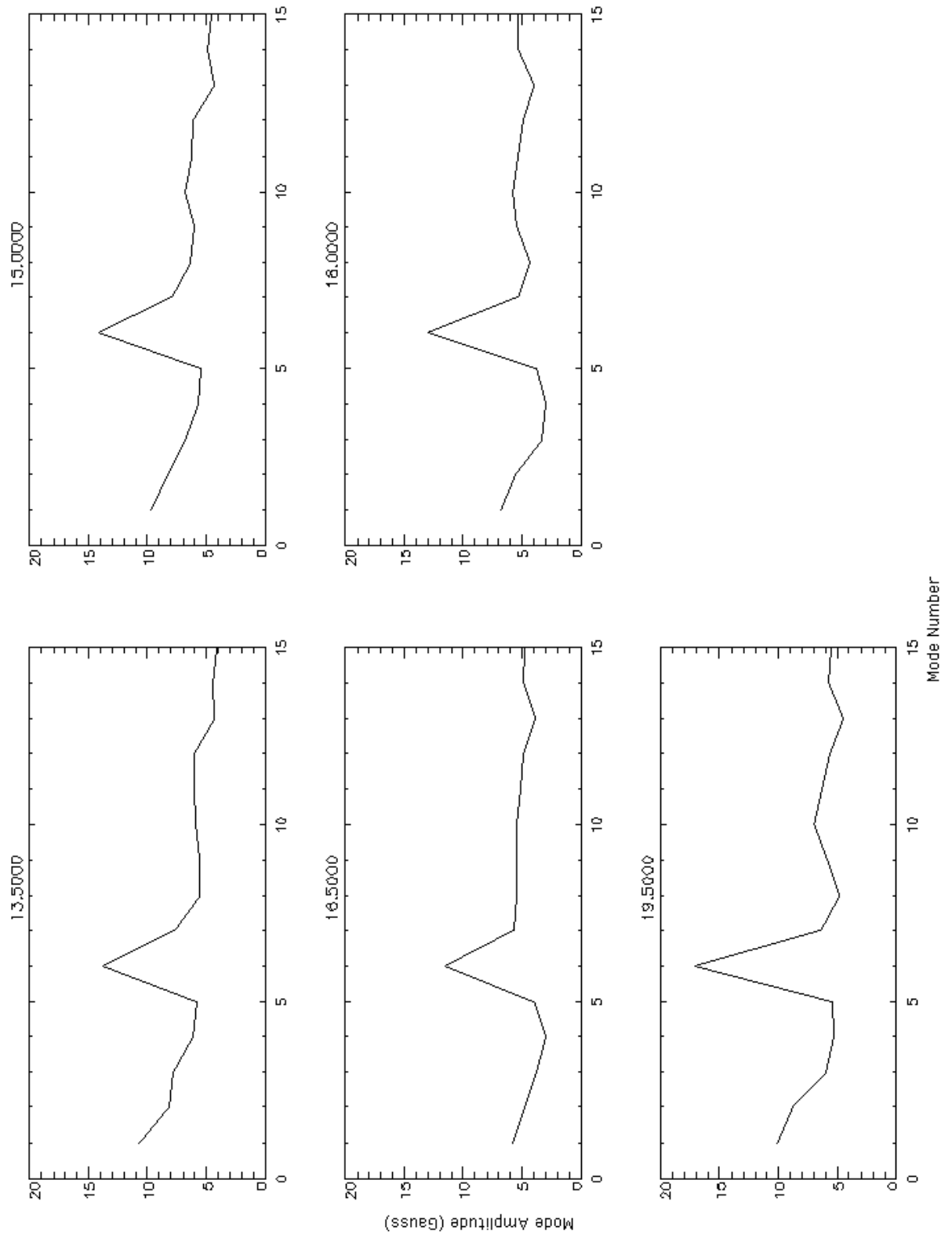


Figure 8.28 Toroidal mode spectrum at select times for PPCD plasmas.

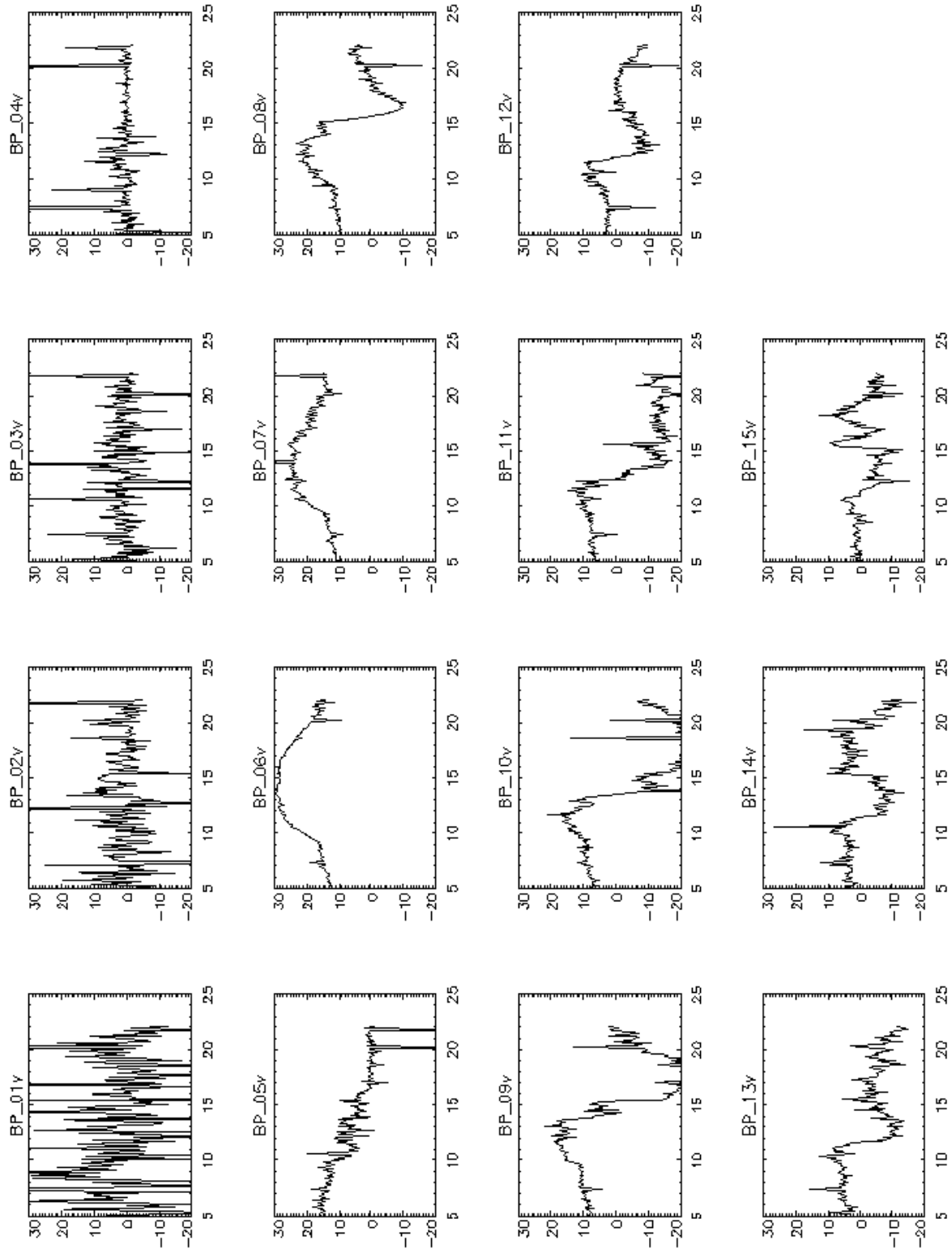


Figure 8.29 Poloidally derived mode velocity spectrum (km/s) for PPCD plasmas.

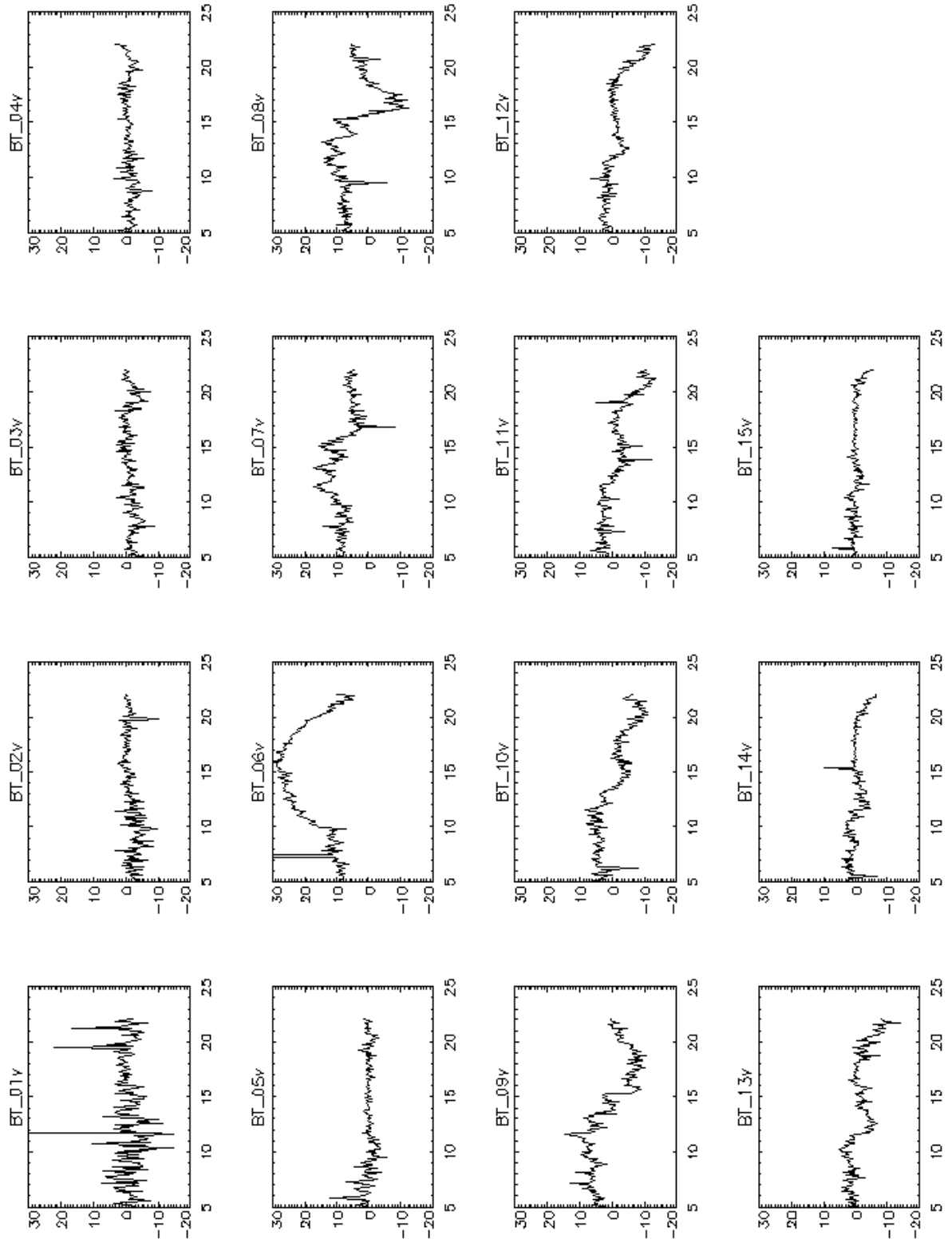


Figure 8.30 Toroidally derived mode velocity spectrum (km/s) for PPCD plasmas.